Hydrodynamics of vegetated compound channels

Model representations of estuarine mangrove squeeze in the Mekong Delta

Truong Hong, Son

DOI
10.4233/uuid:2b9ee3f5-010f-4dbe-b57f-1bb19eeb593e

Publication date
2018

Document Version
Final published version

Citation (APA)
Truong Hong, S. (2018). *Hydrodynamics of vegetated compound channels: Model representations of estuarine mangrove squeeze in the Mekong Delta*. [Dissertation (TU Delft), Delft University of Technology]. https://doi.org/10.4233/uuid:2b9ee3f5-010f-4dbe-b57f-1bb19eeb593e

Important note
To cite this publication, please use the final published version (if applicable).
Please check the document version above.

HYDRODYNAMICS OF VEGETATED COMPOUND CHANNELS

MODEL REPRESENTATIONS OF ESTUARINE MANGROVE SQUEEZE IN THE MEKONG DELTA

HYDRODYNAMICS OF VEGETATED COMPOUND CHANNELS

MODEL REPRESENTATIONS OF ESTUARINE MANGROVE SQUEEZE IN THE MEKONG DELTA

Proefschrift

ter verkrijging van de graad van doctor
aan de Technische Universiteit Delft,
op gezag van de Rector Magnificus Prof. dr. ir. T.H.J.J. van der Hagen,
voorzitter van het College voor Promoties,
in het openbaar te verdedigen op
Maandag 19 November 2018 om 12:30 uur

door

Hong Son TRUONG

Master of Science in Civil Engineering, Delft University of Technology
geboren te Ha Noi, Vietnam.

Dit proefschrift is goedgekeurd door de promotoren.

Samenstelling promotiecommissie bestaat uit:

Rector Magnificus,	voorzitter
prof. dr. M. J.F Stive	Technische Universiteit Delft, promotor
prof. dr. W. S.J Uijttewaal	Technische Universiteit Delft, promotor

Onafhankelijke leden:

Dr. E. Penning	Deltares
prof. dr. T. J Bouma	Royal Netherlands Institute for Sea Research (NIOZ)
prof. dr. H. M. Nepf	Massachusetts Institute of Technology (MIT), USA
prof. dr. P. M.J. Herman	Deltares
prof. dr. ir. A. J.H.M. Reniers	Technische Universiteit Delft

The work presented in this thesis was performed at the Department of Hydraulic Engineering of the Faculty of Civil Engineering and Geosciences of Delft University of Technology. This research was fund by the Vietnam International Education Cooperation Department (VIED) - Ministry of Education and Training.

Keywords: Estuarine mangroves, Compound vegetated channels, Large coherent structures.

Printed by: Son Truong Hong

Front & Back: Cylinder arrays and pink dye used to observe the large coherent structures in the water laboratory (by Truong Hong Son)

ISBN 978-94-6186-992-0

An electronic version of this dissertation is available at
http://repository.tudelft.nl/.

Enjoy doing these research as just go with the flow,
observing the facts and training the mind to think.

Contents

Summary ix

Samenvatting xiii

1 Introduction 1
- 1.1 Research context . . . 2
- 1.2 Research motivation . . . 4
- 1.3 Reserach questions . . . 6
- 1.4 Research methodology and outline . . . 7

2 Estuarine mangrove squeeze hypothesis 13
- 2.1 Introduction . . . 14
- 2.2 Method . . . 17
  - 2.2.1 Study Site in Global and Regional Context . . . 17
  - 2.2.2 Observations of Mangrove Width and River Bank Evolution . . . 20
  - 2.2.3 Flow Attenuation in the Mangrove Forest . . . 23
- 2.3 Results . . . 28
  - 2.3.1 General results . . . 29
  - 2.3.2 No Mangrove . . . 30
  - 2.3.3 Mangroves with different density . . . 30
  - 2.3.4 Mangrove with different width . . . 31
- 2.4 Discussion . . . 33
  - 2.4.1 Critical mangrove width and sedimentation . . . 33
  - 2.4.2 Critical mangrove width and restoration capability . . . 33
- 2.5 Conclusions . . . 36

3 Exchange processes in vegetated compound channels 43
- 3.1 Introduction . . . 44
- 3.2 Objective . . . 46
- 3.3 Experiment setup and measurements . . . 46
- 3.4 Results . . . 51
  - 3.4.1 Role of vegetation . . . 51
  - 3.4.2 Role of Large horizontal coherent structures . . . 55
  - 3.4.3 Role of vegetation width or Squeeze effect . . . 64
- 3.5 Discussion . . . 67
- 3.6 Conclusions . . . 69

4 Analytical modelling of transverse momentum exchange **75**
4.1 Introduction . . . 76
4.2 Objectives . . . 78
4.3 Methodology . . . 78
4.4 Governing Equations . . . 78
4.5 Existing Models of Transverse Exchange of Momentum . . . 81
4.6 Experiment set up and general results . . . 82
4.7 Quadrant analysis of the cycloid flow field under the effects of LHCSs . . . 84
4.8 Modelling Transverse Momentum Exchange in Vegetated Floodplain Channel . . . 87
4.9 Comparison with the experimental data . . . 90
4.10 Conclusions . . . 93

5 Numerical modelling **99**
5.1 Introduction . . . 100
5.2 Objectives and Methodology . . . 101
5.3 Physical model . . . 102
5.4 2DH model set-up . . . 102
5.5 Eddy viscosity models . . . 105
5.6 Results . . . 106
5.6.1 2DH model results with different eddy viscosity models . . . 106
5.6.2 The presence of LHCSs . . . 109
5.7 Discussions . . . 111
5.7.1 A 2DH model of schematised Tieu estuary river channel . . . 111
5.7.2 Squeeze effects . . . 117
5.8 Conclusions . . . 119

6 Conclusions and recommendations **123**
6.1 Mangrove Squeeze phenomenon . . . 124
6.2 Physical mechanisms . . . 125
6.3 Transverse momentum exchange - analytical model . . . 126
6.4 Numerical simulations . . . 126
6.5 Recommendations . . . 127

A Appendix Experimental Results **129**

B Appendix Hybrid eddy viscosity model validation **133**

Acknowledgements **145**

Curriculum Vitæ **147**

List of Publications **149**

Summary

Mangroves are an interesting species of vegetation, surviving and thriving at the interface of land and water, in the inter tidal brackish coastal waters between the mean sea level and mean high water. Mangroves are a highly productive and complex ecosystem, providing numerous services and goods to people and marine environment. Mangroves are home to a large variety of underwater animals. Mangrove wood is valuable because it is resistant to rot and insects and can be harvested for pulp or charcoal production. Most importantly, complex roots, stems and canopies of mangroves provide effective protective means for coastal and estuarine regions. Waves and tidal flows are significantly slowed down as they make their way into and through the roots, stems and canopies of the mangrove forest. Nutrients and sediments can be deposited, providing necessary conditions for a sustainable development of the mangrove ecological system in particular and a stable coastal area in general. However, despite the important role of mangroves along the Mekong delta estuary, a large part of the mangrove forests has been converted into fish farms. In many regions, only a narrow strip of mangroves remained and, as a consequence, mangrove forests degraded and banks and shorelines experience severe erosion. Although numerous attempts were implemented to restore the mangroves and to enhance the river bank stability, these were not really successful. A possible explanation may be that knowledge about the hydrodynamics and exchange processes in and around the mangrove forest vegetation area is still not yet rigorously researched. In order to understand the dynamics of mangroves, the remaining width of mangrove forests and erosion (accretion) rate were observed, collected and analysed in terms of a morphological perspective. It is found that the river bank erosion appears to relate to the width of mangrove forest. The larger the width of the mangroves, the less erosion of the river bank and vice versa. In this context, the concept “Squeeze Phenomenon,” explaining the degradation of mangroves together with the erosion of the river bank, is introduced. Based on a schematised numerical model, changes in hydrodynamics and exchange processes caused by the limited width of the forest are proposed to be the fundamental reason for the “Squeeze Phenomenon.”

It is noted that estuarine channels in the Mekong Delta usually include mangroves, dominating floodplain regions, transition areas with very a gentle slope of about 1:10, and a main channel. As such, hydrodynamics of estuarine mangroves appear similar to those of a vegetated compound channel. Therefore, a detailed laboratory study of a vegetated compound channel was conducted in a flume at the Water Laboratory of TU Delft. The experimental results theoretically clarified the fundamental role of hy-

drodynamic processes, especially Large Horizontal Coherent Structures (LHCSs), which are turbulent vortex structures at the channel-vegetation interface in relation to vegetation regions and vice versa. It is shown that in a compound vegetated channel with a gentle transverse slope, the shear layer properties are dominated by the presence of vegetation, rather than by the water depth difference. The vegetation significantly increases the gradient of the mean streamwise velocity, drawing more exchange toward the vegetation edge and pushing more flow into the floodplain region. The vegetation is also very effective in damping and shielding the flow within the mangrove forest from external boundary conditions. Furthermore, the presence of vegetation does enhance the occurrence of LHCSs as a dominant factor in forcing the exchange mechanism at the vegetation interface. The presence of LHCSs, which is much more pronounced in cases with vegetation, is the major factor contributing to the momentum exchange between the vegetated floodplain regions and the adjacent open channel. The experimental results also reveal that the region affected by the LHCSs, where large transverse fluctuations can occur, is much larger than the region of transverse momentum exchange which is connected to the penetration of the LHCSs into the vegetated floodplain region. The moving of the LHCSs along the vegetation interface is associated with the sweeps and ejections, as well as the stagnant and the reverse flows forming a so called cycloid motion. While the sweeps and ejections dominate the momentum exchange region and appear to link to the import and export mechanism of nutrients and sediments, the stagnant and reverse flows appear to dominate the region further inside the vegetation and are important for the deposition processes. It is important to note that, although the vegetation is very effective in damping and protecting the hydrodynamic conditions within the forest, the “squeeze effect” makes this protection much less successful. Reducing the forest width does influence the hydrodynamics in and around the cylinder arrays, especially the shear layer at the vegetation interface. Furthermore, the mean flow velocity needs a certain space to reach its uniform value inside the floodplain area and the vegetated region, affected by the LHCSs, can be even larger than the region into which the mixing layer can penetrate. Hence, a too narrow floodplain may diminish the affected area directly and makes it impossible for the flow field inside the vegetation to be able to reach its equilibrium state. As a result, the LHCSs in a “squeeze” condition occur more frequently but less regularly and the transverse exchange processes, induced by these LHCSs, can be strongly disturbed. The momentum fluxes are larger and the time and space for the sediment to be deposited is restricted. These conditions are hypothesized to be unfavorable for the nutrient and/or sediment deposition within the mangrove forest. It is also seen that the denser the vegetation, the less sensitive the mangrove forest is to the squeeze effects. This again shows the importance of the function of the vegetation in the protection of the river banks.

A quadrant analysis of the Reynolds shear stresses has been applied, showing the connection between the flow events and the LHCSs and their contribution to the transverse momentum exchange. It is suggested that local variability leads to differences in the transverse exchange of mass and momentum. Moreover, it is noted that although various exchange models have been developed, their applicability in different circumstances is still unclear as their validity is usually restricted to a narrowly ranging experimental data set. A proper model for this exchange of momentum in a compound chan-

nel geometry, with or without vegetation, is still lacking, especially in the context of the presence of the Large Horizontal Coherent Structures (LHCSs). In this context, the experimental data were used to verify state-of-the-art momentum exchange models. As the limitations of those models were analysed, for the first time a hybrid eddy viscosity model, based on the occurrence of LHCSs and on the presence of vegetation, was proposed and verification, using a variety of experimental data sets including a non-vegetated compound channel, a vegetated compound channel and a partially vegetated channel. The results show that, by varying only a coefficient of proportionality β which is related to the transverse slope between the main channel and the floodplain, the transverse momentum exchange can be well reproduced with the new eddy viscosity model for quite a range of different set-ups and scenarios.

Finally, as the generic applicability of the viscosity estimation has been demonstrated, it was consecutively used as a turbulence model representing the large scale structures in numerical simulations of compound channel flow. It is noted, that most knowledge obtained so far is primarily based on laboratory studies. Numerical models that can well reproduce the physics, cost high computational time in terms of practical engineering. Although depth averaged numerical models (2DH models) have widely been applied to model quasi-steady depth averaged flow patterns in rivers, estuaries and coasts, the applicability of a 2DH model in the context of the presence of the LHCSs has yet to be determined. Therefore, the capability of 2DH models in modelling the shallow flows in a compound vegetated channel was examined. The shallow water solver of Delft3D was used, and based on that a 2DH numerical model mimicking a physical model of a compound vegetated channel was constructed. The model results were then compared with the experimental results, showing the limitation of the 2DH models. Subsequently, the new hybrid eddy viscosity model was prescribed in the 2DH numerical simulations of vegetated compound channels to improve the prediction capability of the model in terms of the mean streamwise velocity and the transverse shear stresses. In this context, the utilization of the 2DH model for real-time scenarios of a vegetated compound channel was examined. The phenomena and lessons, learned at small-scale experiments, are important in the discussion on a larger real-time scale and its application by means of a scaled up numerical model.

Samenvatting

Mangroven zijn een interessante vegetatie, groeiend en bloeiend tussen land en water in de brakke kustwateren van het getij en tussen het gemiddelde niveau van het zeewater en het hoogwater. Mangroven zijn een zeer complex ecosysteem en voorzien in talrijke behoeftes van de mens en de maritieme omgeving. Mangroven vormen een thuisbasis voor een grote verscheidenheid aan onderwaterleven. Mangrovehout is waardevol omdat het is bestand tegen verrotting en insecten en het voor de productie van pulp of houtskool geoogst kan worden. Het belangrijkste aspect van mangroven zijn de complexe wortels, stengels en bladerdak welke een effectieve bescherming biedt aan kust en riviermondingen. Golven en getijde stroming worden aanzienlijk vertraagd op weg in en door de wortels, stengels en boomkronen van het mangrovebos. Voeding en sediment kunnen worden gedeponeerd; noodzakelijke voorwaarden voor een duurzame ontwikkeling van het ecologisch mangrove systeem in het bijzonder en een stabiel kustgebied in het algemeen. Echter, ondanks de belangrijke rol van de mangroven in de riviermondingen van de Mekong-delta, is een groot deel van de mangrovebossen omgebouwd tot viskwekerijen. In vele regio's is slechts een smalle strook van mangroves over gebleven en zijn mangrovebossen dientengevolge gedegradeerd en zijn de rivieroevers en de kust aan ernstige erosie onderhevig. Hoewel vele pogingen zijn ondernomen om de mangroven te herstellen en de stabiliteit van de rivieroevers te verbeteren, waren deze niet echt succesvol. Een mogelijke verklaring kan zijn dat de kennis over de hydrodynamica en uitwisselingsprocessen in en rond mangroven vegetatie nog niet grondig is onderzocht. Om de dynamiek van de mangroven te begrijpen, werd de mate van erosie (accretie) in relatie tot de resterende breedte van mangrovebossen geobserveerd en verzameld, en geanalyseerd in termen van een morfologische perspectief. Onmiskenbaar lijkt de erosie van de rivieroever gerelateerd te zijn tot de breedte van mangrovebossen. Hoe breder de strook van mangroven, hoe minder erosie van de rivieroever en vice versa. In deze context introduceren wij het concept 'Squeeze Fenomeen,' dat de afbraak van de mangroven in relatie tot de erosie van de rivieroever verklaart. Op basis van een geschematiseerd numeriek model, worden de veranderingen in de hydrodynamica en uitwisselingsprocessen voorgesteld als de fundamentele reden voor het "Squeeze Fenomeen".

Opgemerkt moet worden dat de riviermondingskanalen van de Mekong Delta een totaliteit vormen van mangrovebegroeiing, vlaktes waar overstromingen domineren, overgangsgebieden met een zeer lichte helling van ongeveer 1:10 en een hoofdkanaal. In deze conditie lijkt de hydrodynamica van mangroven in de riviermonding vergelijkbaar met die van een begroeid, gesegmenteerd kanaal (Engels:'compound channel'). Een ge-

detailleerde laboratoriumstudie van een begroeid, gesegmenteerd kanaal ('compound channel') is uitgevoerd in het Waterlaboratorium van de TU Delft. De experimentele resultaten gaven een theoretisch inzicht in de fundamentele rol van de hydrodynamische processen, met name de 'grote horizontale coherente structuren' (Engels: LHCSs), die de turbulente vortexstructuren vormen op het grensvlak van vegetatie in relatie tot begroeide gebieden, en omgekeerd. Aangetoond werd dat, in een begroeid kanaal ('compound channel') met een milde dwarshelling, de eigenschappen van de oevers vooral worden bepaald door de aanwezigheid van vegetatie en niet zozeer door het verschil in waterdiepte. De vegetatie verhoogt de gradiënt van de gemiddelde stroomsnelheid aanzienlijk, waardoor er toenemende uitwisseling plaatsvindt naar de rand van de vegetatie en de stroming meer naar de uiterwaarden wordt gestuwd. De vegetatie van het mangrovebos is ook zeer effectief in de demping van de externe stroming. Bovendien worden 'LHCSs' door de aanwezigheid van vegetatie een dominante factor in het uitwisselingsmechanisme op het niveau van de vegetatie. De aanwezigheid van 'LHCSs' is vooral bepalend in situaties met vegetatie en dit is de belangrijkste factor die bijdraagt aan de momentumuitwisseling tussen de begroeide uiterwaarden en het aangrenzende, open kanaal. De experimentele resultaten lieten ook zien, dat het gebied waar grote transversale fluctuaties kunnen optreden onder invloed van 'LHCSs', veel groter is dan het gebied van transversale momentumuitwisseling gerelateerd met het binnendringen van 'LHCSs' in het begroeide overstromingsgebied. De 'LHCSs' in het grensgebied van de vegetatie worden geassocieerd met zwaai- en werpbewegingen en vormen, samen met de stagnering en tegenstroming, een zogenaamde cycloïde beweging. Terwijl de zwaai- en werpbewegingen het gebied van momentumuitwisseling domineren en een verbinding ontstaat met het import- en exportmechanisme van voeding en sediment, lijken de stagnering en tegenstroming het gebied binnen de vegetatie te domineren en dit is belangrijk voor de depositie processen. Het is relevant om op te merken dat, hoewel de vegetatie zeer effectief is in het dempen en beschermen van de hydrodynamische omstandigheden in het bos, het "knijpeffect"(Engels: Squeeze Phenomenon) deze bescherming veel minder succesvol maakt. Het verkleinen van de breedte van het bos heeft invloed op de hydrodynamica in en rond de cilindermatrices, vooral op de oever op het niveau van de vegetatie. Verder heeft de gemiddelde stroomsnelheid een bepaalde ruimte nodig om zijn uniforme waarde binnen het gebied van de uiterwaarden te bereiken en het is mogelijk dat het begroeide gebied, beïnvloed door de 'LHCSs,' groter is dan het gebied waarin de gemengde laag kan doordringen. Vandaar dat een te smalle overstromingsstrook het aangetaste gebied nog verder kan verkleinen en het bereik van de stroming binnen de vegetatie onmogelijk is om een evenwichtstoestand te creëren. Dientengevolge komen de 'LHCSs' in 'knijp'-toestand vaker, maar minder regelmatig voor en de transversale uitwisselingsprocessen, geïnduceerd door deze 'LHCSs', kunnen hierdoor worden verstoord. De momentumfluxen zijn groter en de tijd en ruimte voor het afzetten van sediment is beperkt. De vooronderstelling is, dat deze omstandigheden ongunstige zijn voor de afzetting van voeding en/of sediment in het mangrovebos. We zien, dat hoe dichter de vegetatie, hoe minder gevoelig het mangrovebos is voor knijpeffecten. Dit toont opnieuw het belang en de functie van vegetatie aan bij de bescherming van rivieroevers.

Een kwadrant-analyse van de Reynolds afschuifspanningen is toegepast, die de verbinding van de stromingsgebeurtenissen en de 'LHCSs,' en hun aandeel aan de dwarse

momentumuitwisseling, aantoont. De suggestie is, dat lokale variabiliteit tot verschillen in de transversale uitwisseling van massa en momentum leidt. Bovendien wordt opgemerkt dat hoewel diverse uitwisselingsmodellen zijn ontwikkeld, hun toepasbaarheid in verschillende omstandigheden nog steeds onduidelijk is, aangezien hun geldigheid gewoonlijk beperkt is tot een beperkte set van experimentele gegevens. Een goed model voor deze uitwisseling van momentum in een samengestelde kanaalgeometrie, met of zonder vegetatie, ontbreekt nog steeds; vooral in de context van de aanwezigheid van de 'LHCSs'. In deze context werden de experimentele gegevens gebruikt om de 'state-of-the-art' momentumuitwisselingsmodellen te verifiëren. De analyse van de beperkingen van modellen, leidden tot het eerste hybride wervel-viscositeitsmodel dat is gebaseerd op het voorkomen van 'LHCSs' en op de aanwezigheid van vegetatie, en voorgesteld en gevalideerd met behulp van een verscheidenheid aan experimentele gegevens: een niet-begroeid kanaal, een begroeide samengesteld kanaal en een gedeeltelijk begroeid kanaal. De resultaten tonen aan dat, door slechts een proportionaliteitscoëfficiënt β te variëren, gerelateerd aan de transversale helling tussen het hoofdkanaal en de uiterwaarden, de transversale momentumwisseling goed gemodelleerd kan worden met het nieuwe wervelstromings-viscositeitsmodel voor een redelijk aantal verschillende 'set-ups' en scenario's.

Ten slotte, aangezien de generieke toepasbaarheid van de viscositeitsschatting is aangetoond, werd deze achtereenvolgens gebruikt als een turbulentie model dat de grootschalige structuren representeert in numerieke simulaties van de stroming van het samengestelde kanaal. Opgemerkt moet worden dat de meeste tot nu toe verkregen kennis voornamelijk gebaseerd is op laboratoriumonderzoeken. Numerieke modellen die de fysica goed kunnen reproduceren, kosten veel computertijd in termen van praktische engineering. Hoewel modelgemiddelde numerieke modellen (2DH-modellen) alom worden toegepast voor het modelleren van quasi-stabiele dieptegemiddelde stroompatronen in rivieren, estuaria en kusten, moet de toepasbaarheid van een 2DH-model in de context van de aanwezigheid van de 'LHCSs' nog worden bepaald. Daarom werd het vermogen van 2DH-modellen in het modelleren van de ondiepe stromingen in een samengesteld begroeide kanaal onderzocht. De "ondiep wateroplosser" van Delft3D werd gebruikt, op basis van een 2DH numeriek model dat een fysiek model nabootst van een samengesteld begroeide kanaal. De modelresultaten werden vervolgens vergeleken met de experimentele resultaten, die de beperking van de 2DH-modellen tonen. Vervolgens werd het nieuwe hybride wervelviscositeitsmodel voorgeschreven in de 2DH numerieke simulaties van begroeide kanalen om het voorspellingsvermogen van het model te verbeteren in termen van de gemiddelde stroomsnelheid en de transversale schuifspanningen. In deze context werd het gebruik van het 2DH model voor real-time scenario's van een begroeid samengesteld kanaal onderzocht. De verschijnselen en lessen, geleerd in kleinschalige experimenten, zijn belangrijk in de discussie over grotere real-time schaal toepassineng door middel van een opgeschaald numeriek model.

Chapter 1

Introduction

Mangrove trees live up to 100 years;
It only takes 1 day to destroy a whole forest.

USA – Graphic Artist Carly Hoover

Figure 1.1: Mangrove at the edge of land and water. Photo taken by Ethan Daniels, 2013.

1

The main purpose of this chapter is to present the problem, the research questions and the research methodology. Additionally, it is intended to provide an introduction to readers, who may not be familiar with the scientific knowledge.

1.1 Research context

THis thesis is a story about the degradation of mangrove forests due to the changes in hydrodynamics induced by human intervention. The focus is on the process of momentum exchange between the flow in the vegetation area and in the adjacent main river channel.

Mangroves are a group of trees and shrubs which usually live near the sea, in the intertidal areas such as along shores, rivers, and estuaries (Duke and Schmitt, 2016). Mangroves can not withstand cool temperature (about 10°C-20.6°C), so they develop mainly in the tropical and sub-tropical regions (Alongi, 2009). Mangrove forests can be well recognized by their dense tangle of roots wriggling out of the muddy soil (Figure 1.2) (Chapman, 1976). The complex system of the tangle of roots not only enables mangroves to adapt the sinusoidal changes of tidal water level, but also makes mangrove forests become an attractive home of many precious and distinctive aquatic organisms (Hong and San, 1993). Furthermore, by inhibiting and slowing down the tidal flow, the intricate root system of the mangrove forest can enable fine sediment to deposit and raise the muddy bottom (Kathiresan, 2003). In this way, mangrove forests can increase the stability and reduce the erosion of the along shore river bank and coastline by currents, waves and tides .

Figure 1.2: The complex system of roots, stems and canopy of the mangrove forest in the Mekong Delta, Vietnam. Photo taken by Marcel Stive, 2015.

However, mangrove forests are among the most threatened ecosystems of the world (Gilman et al., 2008). About 35% of the mangrove forests already disappeared, while in Vietnam this figure is as high as 50% (Makowski and Finkl, 2018). Human interventions, both direct and indirect, are considered to be the main reason of this degradation of mangrove forests all around the world. For instance,a mangrove forest is usually cleared for agriculture and infrastructure and over harvested to make construction wood or charcoal production (Larson, 2004; Makowski and Finkl, 2018; Polidoro et al., 2010). In addition, industrial waste, fertilizers and toxic chemicals dumped into the water resources can kill animals living in mangrove forests, and threaten the long-term survival of the whole mangrove eco-system (Starr, 2007) .

All changes and impacts from human intervention at first affect the hydrodynamics of the ecosystem *i.e.* the motion of fluid in and around the ecosystem in general and mangrove forest in particular (Elias, 2006; Nikora Vladimir, 2009; Van Andel and Aronson, 2006; Yu and Zhang, 2011). However, knowledge about this topic is incomplete, especially the existence of large turbulence structures formed in the mixing layer has been only recognized recently (Nakagawa and Nezu, 1993).

In general, the flow of water in coasts, river and estuaries is turbulent, which means that the fluid at those locations undergoes irregular fluctuating motions. The velocity of the fluid keeps changing in both magnitude and direction. For example, tidal flows in oceans and coastal areas, river flows and channel flows are turbulent. Initially, turbulence was believed to be an irregular, random, chaotic, and unpredictable phenomenon and only could be understood through statistical approaches (Pope, 2000). Thereafter, turbulence was viewed as a combination of small scale and large scale motion within the flow (Nikora, 2007). The former account for the dissipation of the turbulent energy, and the latter are determined by the geometry of the flow (Venditti et al., 2013). This view of turbulent flow implies that the turbulent energy is transferred from the mean flow to large-scale turbulent motions, which may develop in the flow, but eventually will resolve to smaller scales. In other words, although the motion of fluid in turbulent flow experiences chaotic changes in pressure and velocities, it contains periodical fluctuating motions, a circular character which are usually called “eddies”, “vortices”, “turbulence structure”or “coherent structure ”, at different time and space scales. The small-scale disorganised fluctuation of the motion of fluid can occur in larger organised patterns. This is a deterministic approach to understanding turbulent flows.

Since 1970s, the presence of self-organizing flow structures within the fluid has been recognized (Cantwell, 1981; Katul and Vidakovic, 1996; Townsend, 1976). These fundamental structures are “ coherent flow structures” arising from the internal flow instability and are considered to govern the structure of turbulent flows. These coherent flow structures can involve a wide range of vortex length scales, from micro-scale eddies to macro-scale horizontal coherent structures with horizontal length scales larger than the water depth. The existence of these large horizontal coherent structures (LHCSs) has been found to be a fundamental and typical characteristic of the shallow flow. For instance, the presence of such large horizontal coherent structures was well observed in cases of flow past river groynes, the confluence of more than two rivers, in the wakes of inslands, along the edge of vegetated channels, or at the interface of compound channels (Chen and Jirka, 1997; Nezu et al., 1999; Talstra, 2011; Uijttewaal and Booij, 2000;

Van Prooijen, 2004; van Prooijen et al., 2005; White and Nepf, 2007). They usually appear in the mixing layer, where there is a large difference in horizontal velocities of the shallow flow field. The presence of the large horizontal coherent structures increase the momentum exchange from "fast" regions to "slow" regions, which definitely plays an important factor from the environmental engineering aspects.

The story of this thesis involves a wide range of disciplines, from relative general subjects of ecology and environment to a very narrow, specific and fundamental subject of turbulence structure in fluid mechanics. The study therefore also required a wide range of approaches. The most fundamental key issue in this study is to understand the peculiar effects of the LHCSs on the shallow flow field of vegetated compound channels, which mimics the flow in mangrove forests along estuarine river channels.

1.2 Research motivation

Estuarine and coastal ecosystems are being seriously threatened from both landside and waterside. People tend to want to live close to the water, in the coastal region, next to the beach or by the riverside. Nowadays it is known that about 80 percent of the world's population lives within 60 miles of the coastline of an ocean, lake, or river (Cromwell et al., 2007). For example, over half of the American population lives within 50 miles of the coast, and more than a billion people live in low-lying coastal regions (Neumann et al., 2015). From the environmental perspective, this means that these people strongly depend on the coastal and marine ecosystems, habitats and resources for the essential things of life, such as fertile lands, food etc., as a consequence, the increasing amount of garbage, sewage and toxic wastes are dumped in these areas. This unquestionably damages the whole ecosystem, destroying the habitat and causing the extinction of many species. Besides, the warming climate since the mid-20th century causes the seawater to expand and the melting of ice over land, resulting in sea level rise (Riebeek, 2011). This water level rising induced by climate change has put more pressure on the ecological system at the interface region between land and water, which are already damaged due to intensive human activities.

The damaged ecosystem next to the water under the pressure of human activity and sea level rise means that there are more regions of forest degradation and inundation. Coastline and river bank erosion, as well as saltmarshes and mangrove disappearance, are visible consequences (Erlandson, 2008; Valiela et al., 2009; Zhang et al., 2004). People have been forced to find ways of coping with these threatens. From the practical engineering perspective, hard solutions, referring to the construction of protective concrete structures, are usually considered. However, as far as the environmental values are concerned, whether or not this is a long-term and sustainable approach is still controversial (Nordstrom, 2014). It is noted that the natural ecosystem has its own capability to deal with relative sea-level rise by retreating landward. However, the human intervention such as the construction often blocks this capability, making the situation sometimes even worse (Doody, 2004; Phan et al., 2015; Torio and Chmura, 2013).

Specifically, when travelling along the Mekong Delta estuaries, it is observed that in many regions, estuarine mangroves have degraded into a narrow strip and river banks at those locations are also usually observed to be suffering from strong erosion with a rate

of 2 to 4 m per year (SIWRR, 2010). The increasing demand of creating more space for local fish-farming is believed to be the main reason for this devastation of the mangrove system (Renaud and Kuenzer, 2012). There exist several attempts to restore the degraded mangrove system, both in the coastal and estuarine area. However, understanding the mutual interactions between the (fish-farm) constructions, the motion of the fluid and estuarine mangrove ecosystem is still poorly known. As a result, the general result of restoration campaigns is very limited. Thousands of mangrove trees have been planted, but most of the replanted mangrove forest cannot remain sustainable growth and usually drop after some seasons (Marchand, 2008; Seto and Fragkias, 2007). It is also noted that a mangrove forest may be able to be restored in some regions, but only through the recovery of monocultures of easy and fast-growing species such as Sonneratia, Avicenna or Rhizophora, other rare species and the whole mangrove ecosystems cannot be fully restored (Polidoro et al., 2010). More over, it is noticed that coastal mangroves and estuarine mangroves are forced differently. While coastal mangroves are controlled by wave attenuation, estuaries mangroves are governing by the lateral flow as the influences of waves in estuarine region are small and often neglected. The attention for the loss of mangroves are mainly focused on the coastal mangrove (Truong et al., 2017). As a result, understanding the hydrodynamics in the context of the protective role of estuarine mangroves is less well acknowledged.

Previous studies of the hydrodynamics of mangroves in general and mangroves in the Mekong Delta Estuaries in particular (Aucan and Ridd, 2000; Furukawa et al., 1997; Horstman, 2014; Mazda et al., 1995; Wattayakorn et al., 1990; Wolanski et al., 1980, 1990), are mostly based on a particular field setting. Moreover, these studies only considered a healthy riverine mangrove forest where mangrove width is not limited and is much larger than the lateral over-bank flow region. In reality, along the Mekong Delta Estuaries, only a very narrow strip of mangroves of about 50 m is often left (Phan et al., 2015; Truong et al., 2017). In this condition, the hydrodynamics of mangroves are similar to that of a vegetated channel. The presence of large vortex structures, which are termed large horizontal coherence structures (LHCSs), has never been taken into account in studies of hydrodynamics of estuarine mangrove forest. The exchange of mangrove seeds, nutrients and fine suspended sediments through this kind of structure can play an important part in the sustainable growth of the ecological system (White and Nepf, 2007).

In summary, the incomplete knowledge about mangroves in general and estuarine mangroves in particular make it difficult to understand their state and threats. Without such understanding, sustainable long term management strategies cannot be achieved. In this context, various common questions can be raised : (1) are the mangrove really dying and why they are death? (2) are there any hydrodynamic reasons cause the death of mangrove forests ?, (3) why regions with degraded mangrove are usually suffered from more erosion ?, (4) what can be done to recover the damaged mangrove forest ?, *etc.* These questions are indeed the original inspirations of this research trying to answer some of them by studying the mangrove ecosystem from the hydrodynamic scientific perspective, examine the possible physics lying behind and translate them to feasible engineering solutions.

1

1.3 Reserach questions

As indicated in the previous section, there are scientific knowledge gaps in (1) understanding the mangrove classification based on their hydrodynamic forces ; (2) the hydrodynamic of the estuarine mangrove system which is defined to be the mutual interaction between fish-farm constructions, motions of fluid and a mangrove forest ; and (3) the exchange processes (momentum and mass) between a mangrove forest and an adjacent open channel. In order to fill these knowledge gaps, in this section of the chapter, they will be translated into research questions which enables to study these one by one clearly and separately as much as possible.

According to this approach, the main research question of the research can be stated as follows: "How does the hydrodynamic processes occur in the squeezed estuarine mangroves ?". The term hydrodynamic processes refers to the motion of the fluid and the exchange processes induced by the large vortex structures, the term squeeze is related to the restricted width of the forest due to the construction of fish-farms land ward and the term estuarine mangrove is related to the type of vegetation and the typical geometry of the river channel. The estuarine river channel consisting of floodplains, transition slopes and an open main channel is usually termed a vegetated compound channel . Based on the main research question, several key and sub-key questions can be formulated.

Key question 1: "What are the characteristics of estuarine mangroves?" (Chapter 2)

- What are the differences between coastal and estuarine mangroves ?
- What are the hydrodynamic forces on estuarine mangroves ?

Key 2: "Why and how do estuarine mangrove forests degrade ?" (Chapter 2)

- What is the squeeze phenomenon ?
- What can be the explanation in terms of hydrodynamics for the squeeze effects ?

Key 3: "How does flow field in and around estuarine mangrove river channel occur ?" (Chapter 3)

- What is the effect of vegetation on the flow field ?
- What is the effect of the large horizontal coherent structures (LHCSs) on the flow field ?
- What is the effect of the squeeze phenomenon and hydrodynamics of a vegetated compound channel in general and on the LHCSs in particular ?

Key 4: "How does the transverse momentum occur in the compound channel flow ? "(Chapter 4)
Key 5 : "How and to what extent can the knowledge obtained be applied in reality ?" (Chapter 5)

1.4 Research methodology and outline

A variety of methods was applied to collect, observe and analyse the data in order to answer the research questions.

To begin with, mangrove settings in general and in the Mekong delta in particular has been studied through literature. The differences between coastal and estuarine mangroves were recognized and analysed. Then, a hypothesis of the squeeze phenomenon was proposed based on the empirical relationship between the width of mangrove and the erosion/accretion data collected through local investigation. The initial explanations were given based on the results of a schematised model, constructed with the state-of-the-art Delft 3D vegetation model.(Chapter 2)

Subsequently, in order to investigate the possible physics lying behind in more detail, a unique physical laboratory experiment mimicking the hydrodynamic of the estuarine mangrove in the Mekong Delta was conducted. The experimental data (the depth averaged mean streamwise velocity, instantaneous shallow flow field) were collected and analysed.(Chapter 3)

Governing equations of the vegetated compound channel were derived. Then, the transverse momentum exchange was studied in more detail. A quadrant analysis of the Reynold shear stress was applied to understand the flow events and their corresponding contribution to the lateral momentum exchange. Most state-of-the-art transverse momentum exchange models were analysed. Based on that, a new hybrid eddy viscosity model is proposed and validated using different experiment data sets (Chapter 4).

Furthermore, a numerical model mimicking the experiment was constructed, prescribed by different models of background eddy viscosity (Chapter 5). The knowledge derived was imposed again to the schematised model of Tieu estuary and the philosophies obtained on a small scale were discussed on a larger real scale. Finally, the effects of estuarine mangroves and river bank stability were considered in the context of the squeeze phenomenon. Conclusions were derived and recommendations were formulated.(Chapter 6)

References

Alongi, D. (2009). *The Energetics of Mangrove Forests*. SpringerLink: Springer e-Books. Springer Netherlands.

Aucan, J. and Ridd, P. V. (2000). Tidal asymmetry in creeks surrounded by saltflats and mangroves with small swamp slopes. *Wetlands Ecology and Management*, 8(4):223–232.

Cantwell, B. J. (1981). Organized Motion in Turbulent Flow. *Annual Review of Fluid Mechanics*, 13(1):457–515.

Chapman, V. J. (1976). *Mangrove vegetation*.

Chen, D. and Jirka, G. H. (1997). Absolute and convective instabilities of plane turbulent wakes in a shallow water layer. *Journal of Fluid Mechanics*, 338:157–172.

Cromwell, M., Edelman, S., Coulton, K., and McAfee, S. (2007). How many people live in coastal areas? *Journal of Coastal Research*, 23(5):iii–vi.

Doody, J. P. (2004). ?coastal squeeze?–an historical perspective. *Journal of Coastal Conservation*, 10(1):129–138.

Duke, N. C. and Schmitt, K. (2016). Mangroves: Unusual forests at the seas' edge. In *Tropical Forestry Handbook, Second Edition*, volume 2, pages 1693–1724.

Elias, E. (2006). *Morphodynamics of Texel Inlet*. Delft Hydraulics select series. IOS Press.

Erlandson, J. M. (2008). Racing a rising tide: Global warming, rising seas, and the erosion of human history.

Furukawa, K., Wolanski, E., and Muellerc, H. (1997). Currents and Sediment Transport in Mangrove\rForests. *Estuarine, Coastal and Shelf Science*, 44:301–310.

Gilman, E. L., Ellison, J., Duke, N. C., and Field, C. (2008). Threats to mangroves from climate change and adaptation options: A review.

Hong, P. and San, H. (1993). *Mangroves of Vietnam*. IUCN wetlands programme. IUCN.

Horstman, E. (2014). *The Mangrove Tangle: Short-term bio-physical interactions in coastal mangroves*. PhD thesis.

Kathiresan, K. (2003). How do mangrove forests induce sedimentation? *Revista de Biologia Tropical*, 51(2):355–359.

Katul, G. and Vidakovic, B. (1996). The partitioning of attached and detached eddy motion in the atmospheric surface layer using Lorentz wavelet filtering. *Boundary-Layer Meteorology*, 77(9):153–172.

Larson, J. S. (2004). Shrimp Farming and Mangrove Loss in Thailand. *Wetlands*, 24(4):913–913.

Makowski, C. and Finkl, C. (2018). *Threats to Mangrove Forests: Hazards, Vulnerability, and Management*. Coastal Research Library. Springer International Publishing.

Marchand, M. (2008). Mangrove restoration in vietnam, key considerations and a practical guide. Technical report, Deltares.

Mazda, Y., Kanazawa, N., and Wolanski, E. (1995). Tidal asymmetry in mangrove creeks. *Hydrobiologia*, 295(1-3):51–58.

Nakagawa, H. and Nezu, I. (1993). *Turbulence in Open Channel Flows*. IAHR Monographs. Taylor & Francis.

Neumann, B., Vafeidis, A. T., Zimmermann, J., and Nicholls, R. J. (2015). Future coastal population growth and exposure to sea-level rise and coastal flooding - A global assessment. *PLoS ONE*, 10(3).

Nezu, I., Onitsuka, K., and Iketani, K. (1999). Coherent horizontal vortices in compound open-channel flows. *Hydraulic Modeling (ed. VP Singh, IW Seo & JH Sonu)*, pages 17–32.

Nikora, V. (2007). 3 hydrodynamics of gravel-bed rivers: scale issues. In Habersack, H., Piegay, H., and Rinaldi, M., editors, *Gravel-Bed Rivers VI: From Process Understanding to River Restoration*, volume 11 of *Developments in Earth Surface Processes*, pages 61 – 81. Elsevier.

Nikora Vladimir (2009). Hydrodynamics of aquatic ecosystems. *River research and applications*, 26:367–384.

Nordstrom, K. F. (2014). Living with shore protection structures: A review. *Estuarine, Coastal and Shelf Science*, 150(PA):11–23.

Phan, L. K., van Thiel de Vries, J. S., and Stive, M. J. (2015). Coastal Mangrove Squeeze in the Mekong Delta. *Journal of Coastal Research*, 300:233–243.

Polidoro, B. A., Carpenter, K. E., Collins, L., Duke, N. C., Ellison, A. M., Ellison, J. C., Farnsworth, E. J., Fernando, E. S., Kathiresan, K., Koedam, N. E., Livingstone, S. R., Miyagi, T., Moore, G. E., Nam, V. N., Ong, J. E., Primavera, J. H., Salmo, S. G., Sanciangco, J. C., Sukardjo, S., Wang, Y., and Yong, J. W. H. (2010). The loss of species: Mangrove extinction risk and geographic areas of global concern. *PLoS ONE*, 5(4).

Pope, S. (2000). *Turbulent Flows*. Cambridge University Press.

Renaud, F. G. and Kuenzer, C. (2012). *The Mekong Delta System: Interdisciplinary Analyses of a River Delta*.

Riebeek, H. (2011). Global Warming : Feature Articles Global Warming.

Seto, K. C. and Fragkias, M. (2007). Mangrove conversion and aquaculture development in Vietnam: A remote sensing-based approach for evaluating the Ramsar Convention on Wetlands. *Global Environmental Change*, 17(3-4):486–500.

SIWRR (2010). Tien Estuary Investigation Report [in Vietnamese]. Technical report, Southern Institute of Water Resources Research, Ho Chi Minh, Vietnam: Ministry of Agriculture and Rural Development of Vietnam, 180 p.

Starr, C. (2007). *Biology: Concepts and Applications without Physiology*. Brooks/Cole biology series. Cengage Learning.

Talstra, H. (2011). *Large-scale turbulence structures in shallow separating flows*. PhD thesis.

Torio, D. D. and Chmura, G. L. (2013). Assessing Coastal Squeeze of Tidal Wetlands. *Journal of Coastal Research*, 290:1049–1061.

Townsend, A. (1976). *The Structure of Turbulent Shear Flow*. Cambridge Monographs on Mechanics. Cambridge University Press.

Truong, S. H., Ye, Q., and Stive, M. J. (2017). Estuarine mangrove squeeze in the mekong delta, vietnam. *Journal of Coastal Research*, pages 747–763.

Uijttewaal, W. and Booij, R. (2000). Effects of shallowness on the development of free-surface mixing layers. *Physics of fluids*, 12(2):392–402.

Valiela, I., Kinney, E., Culbertson, J., Peacock, E., and Smith, S. (2009). Global losses of mangroves and salt marshes. In *Global Loss of Coastal Habitats Rates, Causes and Consequences*, pages 107–142.

Van Andel, J. and Aronson, J. (2006). *Restoration ecology: the new frontier*, volume 14.

Van Prooijen, B. (2004). *Shallow mixing layers*. PhD thesis.

van Prooijen, B., Battjes, J. A., and Uijttewaal, W. (2005). Momentum Exchange in Straight Uniform Compound Channel Flow. *Journal of Hydraulic Engineering*, 131(3):175–183.

Venditti, J., Best, J., Church, M., and Hardy, R. (2013). *Coherent Flow Structures at Earth's Surface*. Wiley.

Wattayakorn, G., Wolanski, E., and Kjerfve, B. (1990). Mixing, trapping and outwelling in the Klong Ngao mangrove swamp, Thailand. *Estuarine, Coastal and Shelf Science*, 31(5):667–688.

White, B. L. and Nepf, H. M. (2007). Shear instability and coherent structures in shallow flow adjacent to a porous layer. *Journal of Fluid Mechanics*, 593:1–32.

Wolanski, E., Jones, M., and Bunt, J. S. (1980). Hydrodynamics of a tidal creek - mangrove swamp system. *Aust. J. Mar. Freshwater Res.*, 31(4):431–450.

Wolanski, E., Mazda, Y., King, B., and Gay, S. (1990). Dynamics, flushing and trapping in Hinchinbrook channel, a giant mangrove swamp, Australia. *Estuarine, Coastal and Shelf Science*, 31(5):555–579.

Yu, G. and Zhang, J. Y. (2011). Analysis of the impact on ecosystem and environment of marine reclamation-A case study in Jiaozhou Bay. In *Energy Procedia*, volume 5, pages 105–111.

Zhang, K. Q., Douglas, B. C., and Leatherman, S. P. (2004). Global warming and coastal erosion. *Climatic Change*, 64(1-2):41–58.

Chapter 2

Estuarine mangrove squeeze hypothesis

If you want different results;
do not do the same things

Albert Einstein

Along the Mekong estuaries, mangroves have rapidly been destroyed. In many regions, estuarine mangroves have degraded into a narrow strip of less than 50 m. River banks at those locations are usually observed to be suffering from erosion with a rate of 2 to 4 m per year. The main reason of this "estuarine mangrove squeeze" phenomenon is due to the increasing demand of creating more space for local fish-farming. Hence, "squeeze" is used in a broader sense than in the context of sea-level rise impact alone. The hypothesis is that there is a critical minimum width for an estuarine mangrove forest strip to maintain its ability to survive. The analysis of available data, both from literature and from satellite observations, supports the hypothesis: an average critical width of approximately 80 m is found for the Mekong estuaries as the critical width. In order to obtain an insight into the efficiency of a mangrove forest in reducing the impact of alongshore flow, the state-of-the-art Delft3D model has been applied. The model results show that the penetration length scale of the shear layer into the mangrove forest requires a certain minimum space to fully develop. It is hypothesized that the minimum width of the mangrove forest, which equals this maximum penetration length scale, plays a crucial role for the health of a mangrove system.

This chapter have been published in Journal of Coastal Research, Volume 33, Issue 4, pages 747–763. Truong, S. H., Ye, Q., and Stive, M. J. (2017). Estuarine mangrove squeeze in the mekong delta, Vietnam.

2

In this chapter of the thesis the squeeze phenomenon is approached based on the observations of the mangrove degradation from the satellite images and the data collection of river bank evolution. A hypothesis of the existence of a critical minimum width for the mangrove forests in particular and for the ecosystem in general is proposed. Then the numerical model was applied to initially examine the hydrodynamic of the mangrove forests.

2.1 Introduction

The Mekong Deltaic River System in Vietnam, located in the southern part of the country, covers an area of 39000 km^2. Near its outlet to the sea, but still in Cambodia, as part of the Mekong delta plain, the Mekong River divides into two branches, the Mekong (Tien River) and the Bassac (Hau River). Before reaching the sea, the Tien River and the Hau River then divide again into nine branches, which flow into nine estuaries of which presently only eight estuaries are left (Tri, 2012). These estuaries with a complex multi-channel system, reach the South China Sea at the eastern zone of the Mekong Delta coast from the Tien Giang province to the Soc Trang province.This estuarine environment is the Study Area (Figure 2.1).

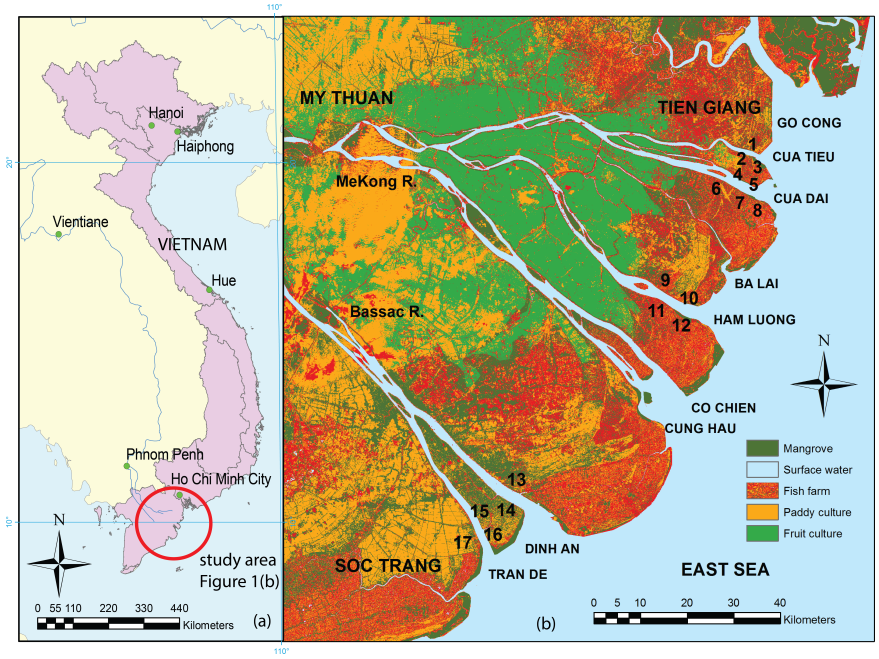

Figure 2.1: (a) Location of the Study Area in South-East Asia. (b) Map of the Mekong Estuarine System captured from a Landsat image showing the major distribution of mangroves, fish farms, fruit and paddy cultures in 2015. Mangroves are mainly located along the river banks and the coastal fringes. The locations numbered from 1 to 17 were chosen to analyse the estuarine river bank evolution trend in relation to the mangrove width (specified in Table 2.1).

The Mekong Delta region in Vietnam is a tropical monsoon region. The dry season is from November to April and the wet season is from May to October. The total mean river discharge of the Mekong is about 15 000 $m^3 s^{-1}$ (Lu and Siew, 2005). The mean high discharge during the flood season is 25 000 $m^3 s^{-1}$ and the mean low discharge during the dry season is 5000 $m^3 s^{-1}$.

According to the report of the Road and Hydraulic Engineering Institute (DWW, 2004) , it is suggested by the local population that the erosion problems have increased from the 1990s in the Mekong Delta in general and in the Mekong Estuarine System (MES) in particular. There are several explanations for the accelerated erosion problems: (1) increasing sea level (Alongi, 2008; Webb et al., 2013), (2) increasing reduced sediment influx as a result of the construction of dams upstream of the Mekong River and sand mining, (3) increasing human induced subsidence and ground water extraction (IUCN, 2011), (4) the clearance of mangrove forests in the 1990s (Gebhardt et al., 2012) and (5) "squeeze" of the coastal mangrove forests. These are the reasons given for accelerated erosion along the coastal region (Phan et al., 2015) and estuarine mangroves probably suffer from the same causes. Together with the accelerated erosion, in many regions along the MES, mangrove have degraded into a narrow strip of less than 50 m. River banks at those locations are usually observed to be suffering from erosion with a rate of 2 m yr^{-1} to 4 m yr^{-1} (Figure 5.1).

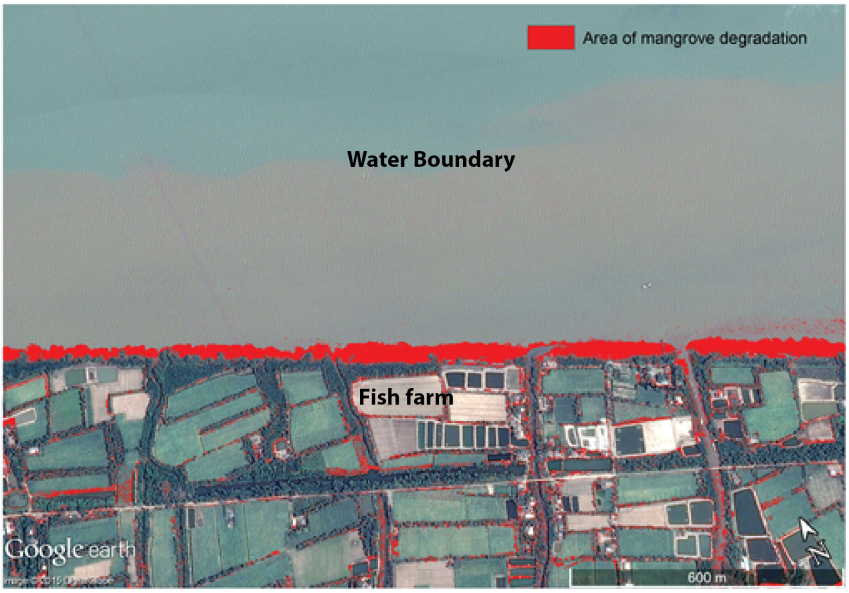

Figure 2.2: Mangrove degradation along a straight part of Dinh An estuary, An Thanh province (location 14). The red area illustrates the area loss of mangrove from 2006 to 2014. Fish farms constructed close to the water boundary push the mangrove into a narrow fringe zone. This area is suffering from erosion with a rate of about 2.5 m yr^{-1}.

During floods, the Mekong Delta carries a large sediment load. The total annual sed-

iment discharge of the whole Mekong Delta river was estimated about 160 $Mt\,yr^{-1}$ in 1995 (Milliman, J.D. and Ren, M.E., 1995) and about 110 $Mt\,yr^{-1}$ in 2011 (Milliman and Farnsworth, 2013) . However, the amount of sediment which finally reaches the South China Sea is less than the total sediment carried by the Mekong river (Kummu and Varis, 2007). Only around 60 % of the total sediment load enters the lower Mekong regions (Manh et al., 2014). This means that the annual amount of sediment entering the lower Mekong basin is about 96 $Mt\,yr^{-1}$ and 66 $Mt\,yr^{-1}$ in 1995 and 2011 respectively. An alternative estimation is based on the average Suspended Sediment Concentrations (SSC), reaching approximately 50 $mg\,L^{-1}$ and 80 $mg\,L^{-1}$ from 1993 to 2000 at Can Tho and My Thuan station, respectively (Lu and Siew, 2005). From the total mean discharge and the SSC, the total annual suspended sediment in the Mekong river can be estimated at about 38 Mt. For a sand- bed river, the bed load fraction may be assumed to be around 30-50 % (Turowski et al., 2010). The total sediment available for the lower Mekong regions, therefore, can range from 54 Mt to 76 Mt. This is almost in line with the estimation of Lu et al. (2014), which is about 50 $Mt\,yr^{-1}$.

Although only part of the above estimated total load of sediment is available for the mangrove forest, it still seems to be enough for the estuarine mangroves. To keep up with the subsidence rate of about 2 $cm\,yr^{-1}$ in the MES (Anthony et al., 2015), the amount of sediment needed for the 16000 ha of estuarine mangrove (100 m width, 200 km length, eight branches) is estimated at only around 8.5 Mt (about 10% of the total, available sediment load). In fact, that amount is probably smaller because the width of mangrove tends to reduce toward the upstream and some branches merge around 30 to 100 km. Hence, the deficiency of sediment sources is not considered as a primary reason for the degradation of estuarine mangrove forest. This study, therefore, focused on the degradation of the estuarine mangrove due to the "squeeze" issue, *i.e.* a limited mangrove width because of the extension of fish farms.

The term "squeeze" was introduced by Doody (2004) in recognition of the threat to the existence of coastal mangroves or tidal wetland habitats caused by the compound impacts of sea-level rise and human activities. The term has since been widely used since (Gilman et al., 2007; Torio and Chmura, 2013). Gilman et al. (2007) noted that, when relative sea-level is rising, a mangrove forest tends to retreat landward. However, the spatial blocking induced by human activities such as urbanization, agriculture, and aquaculture prevents the ecosystem from retreating, pushing the mangroves into narrower and narrower fringes and, finally, to disappear entirely (Feagin et al., 2010). A certain space, therefore, is needed for the ecosystem to be able to retreat to when sea-level rise affects the coast. Phan et al. (2015) adopted the term *squeeze* to determine a "minimum width" required for coastal mangroves to be able to develop sustainably. Nevertheless, in the MES, the situation is even more serious. Mangroves have regularly been cleared for conversion into aquaculture. Fish farms have been constructed intensively, extending toward the foreshore, pushing mangrove to narrow strips. This squeeze phenomenon is a threat to the existence of the mangroves, even when the availability of sediment is not an issue. While sea-level rise is a threat from the water boundary, the destruction of mangroves for conversion to aquaculture is a threat from the land boundary. The latter usually happens in a shorter period and with a larger order of magnitude than the former. Natural sand-dune coasts, salt marsh coasts and mangrove coasts are ecosystems

that form a transition between the open water and the land. There are both abiotic and biotic arguments suggesting that a certain minimal width is required by these ecosystems, and that remains true for fringing estuarine mangroves, as well. Space is required for energetic conditions to be absorbed, and vegetation needs to be able to follow a cyclic evolution. This means that a "minimum width" is required for the survival of the ecosystem, whether the impacts come from relative sea-level rise or from human activities.

2.2 Method

The study area and the mangrove forests in their local and international context are described, followed by an analysis of the observations of estuarine mangrove widths and estuarine bank morphology. Next, to increase understanding about the hydrodynamic forcing in a mangrove forest, a numerical model was applied to study the penetration of flow from the main river channel into the mangrove forest. It was hypothesized that a link existed between "estuarine mangrove squeeze" and the maximum distance in which flow penetration occurs. This hypothesis has not been considered in the international literature.

2.2.1 Study Site in Global and Regional Context

Based on the continental borders, mangroves can be distinguished into six tropical regions: western America, eastern America, western Africa, eastern Africa, Indo-Malaysia and Australia (Duke, 1992). Mangroves in Vietnam belong to the Indo-Malaysian class, the class with the greatest biodiversity (Alongi, 2002). Lugo and Snedaker (1974), based on a functional classification of mangrove forests, categorized mangrove into six classes, namely, fringing, riverine, over wash, basin, scrub and hammock mangroves. Cintron and Novelli (1984) studying topographic landforms, simplified that classification into three main classes: fringing, riverine and basin mangrove. Woodroffe (1992), studying the important role of two physical processes for mangrove forests, namely,the unidirectional river flows and the bidirectional tidal flows, proposed a general classification by referring to mangrove habitats as occupying a broad continuum between tide-dominated mangroves, river-dominated mangroves and those mangrove forests that are isolated from either of those processes, as interior mangrove. Ewel et al. (1998) proposed a hybrid of these systems, combining the classification system of Lugo and Snedaker (1974) with the general system of Woodroffe (1992). Their simplified classification system refers to tide-dominated mangroves as *fringe mangroves*, river-dominated mangroves as *riverine mangroves* and interior mangrove as *basin mangroves*. Riverine mangroves or river-dominated mangroves are flooded by river water as well as by tides. They usually dominate in the river-dominated deltas and are mostly exposed to uni-directional water flows during flood tides. Fringing or tide-dominated mangroves usually dominate low-gradient, intertidal areas of a sheltered coastline. They are usually inundated by daily tides and exposed to strong bidirectional tidal flow. Fringing mangroves facing the open sea (coastal mangrove) can also be exposed to waves. Interior mangroves usually dominate in inland depressions, where they are least exposed to waves and tidal motions (Ewel et al., 1998; Lugo and Snedaker, 1974; Woodroffe, 1992).

All the above state-of-the-art classification systems consider only tides and river flow as the major hydrodynamic indicators, and wave action were not considered. Although the role of mangroves in dissipating wave energy and protecting coastal regions has been well recognized, little attention has been given to the reverse effects of waves on mangroves. Waves have a role in the resuspension of bottom sediments (Wolanski, 2001). There is also a difference in the impact of short waves and long waves on mangroves (Phan et al., 2015).

Neglecting the waves factor makes it more difficult to understand the differences in the setting of coastal mangroves and estuarine mangroves, which is particularly true for the MES. The Mekong Delta is classified as both a wave-influenced and a tide-dominated delta, according to the ternary diagram of Galloway (1975) (Ta et al., 2002). The tide in the region has a semi-diurnal character. The mean tidal range is 2.6 m (Gagliano and McIntire, 1968), whereas the maximum tidal range is 3.2 m to 3.8 m (Nguyen et al., 2000; Wolanski et al., 1996). The average depth of the estuarine branches is typically 5 m to 10 m in the regions between the river mouth and up to 140 km upstream (Wolanski et al., 1996). Because of the relative low elevation and gentle slope of the delta, tide and salt water can intrude deeply into the floodplain through the estuaries of the Mekong and Bassac River (Tri, 2012). In the dry season, tidal variation can be observed as far as Tan Chau and Chau Doc, 228 km upstream from the river mouth (Wolanski et al., 1996). Because of these specific features, mangrove forests in the Mekong Delta dominate a wide range of areas from the coastal to estuary and further upstream. Those differences in the regions where mangrove dominate implies implies differences in the hydrodynamic forces affecting mangrove population Figure 2.3. Although coastal mangroves are distributed alongshore and are often exposed to waves, estuarine mangroves are much less exposed to sea waves and storms. Estuarine mangroves usually dominate in floodplains, which have gently sloping substrates (2-3%), that are exposed at low tide and flooded at high tide. They can also be flooded by river water. Salinity varies during the different flood and dry seasons. Therefore, the mangrove setting is different from that found in coastal to estuarine areas. This was confirmed in the observations of Hong and San (1993). In the coastal area, dense forests are usually found, with trees 15 −25 m tall, composed *Rhizophora*, *Sonneratia* and *Avicennia* species. Coastal mangrove forest width is usually larger than 100 m, with the complex tidal creek systems. In estuarine areas, *Sonneratia* community dominates, along with a mixed community of *Avicennia alba*, *Nypa fruticans* and *Derris trifoliata*. Further inland, along the river, mostly *Avicennia* species and *Nypa fruticans* develop with *Derris trifoliata*. The mangrove forest width along the river is usually less than 50 m.

The simplification of state-of-art classification systems can be challenged. Based on observations of mangrove forest in the Mekong Delta, a new classification is proposed, with three main categories: fringing coastal mangroves (FCs), fringing estuarine mangroves (FEs) and the interior mangrove (I). FCs are the mangrove forests dominating coastal regions, and are primarily exposed to waves and tide. FEs are the mangrove forests dominating in estuarine regions, primarily controlled by tidal forces and the geometric features of the river. The influence of tidal flow, river flow and lateral flow are important for FE mangrove forests. Those mangroves that are protected and least exposed to the forces of waves and tides can be classifeid as I mangroves. In this study,

only FE mangroves were analysed.

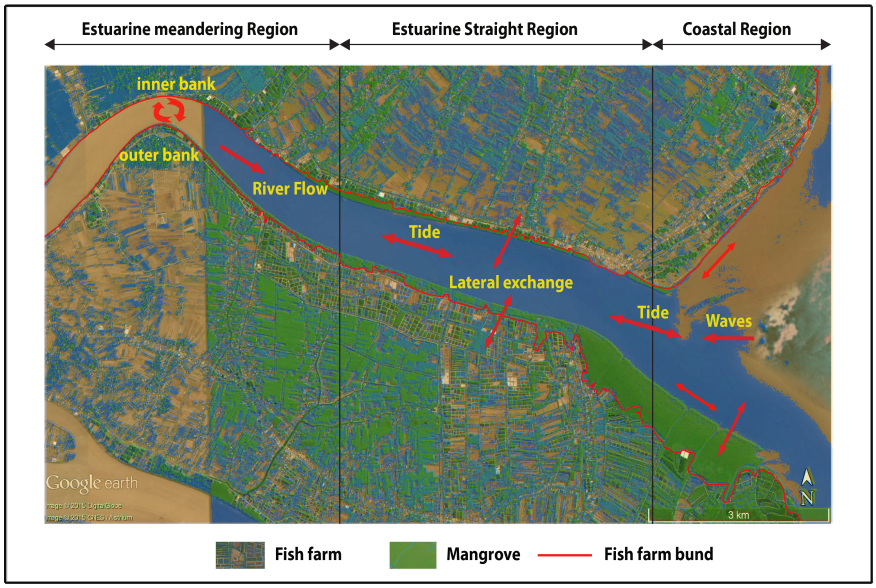

Figure 2.3: Mangroves at Tieu estuary; hydrodynamic forces differ between the river and the sea environment. Coastal mangroves are often exposed to sea waves and storms. Estuarine mangroves are much less exposed to sea waves and storms; these are rather influenced by lateral flow and geometric features of the river (meandering or straight).

The mangrove area in the Mekong Delta, Vietnam, accounts for about 70% of the entire mangrove habitat in Vietnam, about 109 000 ha in 2005 (FAO, 2007). Recently, many changes have been observed in the mangrove forests of the Mekong Delta. During the Vietnam War (1962–71), nearly 40% of the mangrove forests in the region were destroyed (Hong and San, 1993) .Mangrove forests started to recover around 1975 because of natural generation and manual planting. In the 1980s and early 1990s, the mangrove forests were heavily affected by timber overexploitation and the conversion of forest land into aquaculture–fishery farming systems (Christensen et al., 2008). Forest felling bans were imposed by the mid-1990s, but then ceased in 1999. Since then, many mangrove forests have been cleared to create areas for shrimp farming. Currently, many of the eight estuaries of the Mekong Delta are degraded, and the destruction of mangrove forests have been observed. In those regions, only narrows trips of about 10 to 50 m of mangrove forest remain in front of fish farms.

The literature has focused considerably more attention on the loss of coastal mangroves. The effects of wave action are usually blamed as the important cause of mangrove degradation. Anthony and Gratiot (2012), based on an analysis of the impact of land use on coastal mangroves in Guyana, found that the loss of mangroves reduced wave dissipation and promoted net erosion within the mangrove area. According to Winterwerp et al. (2013), there are two main reasons for the unsuccessful rehabilitation of coastal mangrove systems: the reduction in the onshore, fine-sediment flux because

of a decrease in onshore water flux, and local scour in front of structures because of a local increase in wave height due to reflection caused by the implementation of structures within the mangrove forests. In observations of the coastal area of the Mekong Delta, Phan et al. (2015) proposed a relationship between coastal evolution and mangrove width and suggested the important role of long-wave penetration in the sustainability of mangroves.

However, as mentioned, coastal mangroves and estuarine mangroves have different hydrodynamic forces. Whereas coastal mangroves are controlled by wave attenuation, estuarine mangroves are controlled by lateral flow, at least on the bank close to the river. The effects of waves are small in estuarine mangroves. Furthermore, in estuarine regions, several other hydrodynamic factors can lead to the erosion of riverbanks, such as meandering effects and circulation flow. Therefore, the squeeze relationship between mangrove forest width and evolution rate developed for coastal areas cannot readily be applied to mangroves in estuarine regions.

This study focused on the straight part of the estuaries to eliminate the meandering effect. The fundamental hypothesis was that there must be a critical minimum width for an estuarine mangrove forest fringe to exist sustainably exist or, once surpassing the minimum width, to favor sedimentation. The flow penetration into the mangrove forest needs a certain distance to reach an equilibrium-damping value. If the width of the forest is larger than that distance, there will be enough space to absorb the parallel flow energy and to promote sediment deposition, offering a successful environment for both propagules and sedimentation. If the width of the forest is smaller than that distance, the flow energy inside the forest will not have decreased to a reasonable level. Seeds and propagules cannot survive, and sediment cannot be accumulated. A mangrove forest in such a state will degrade, and the riverbank will suffer from more erosion.

2.2.2 Observations of Mangrove Width and River Bank Evolution

IN this section, the estuarine squeeze hypothesis,*i.e.* whenever fish farms or dikes are constructed too close to the nonvegetated foreshore,suggests that erosion trends will dominate and,consequently, the health of the mangrove forest will be threatened.

Optical satellite observations confirm the fact that human intervention, especially the construction of fish-farms, has disturbed mangrove forests in all branches of MES Figure 2.4 shows a part of Tieu estuary with existing mangrove forest. This situation reflects a typical situation of estuarine mangroves in the MES, reflecting a typical situation for the estuarine mangroves in the MES. The fish ponds were extended toward the foreshore. Few mangroves can be observed in front of hard structures, such as dikes. The remaining width of a mangrove forest depends principally on the extent of the fish farms.

In the MES, fish farms have expanded continuously toward the foreshore Figure 2.5. In Figure 2.5, the green line represents the landward boundary in 2006, and the orange line represents the landward boundary in 2010. Between 2006 and 2010, the fish farms extended, with a resulting degradation of the mangrove forest.

In the estuarine regions, at meandering locations, sedimentation can occur on the inner bank of the river, whereas on the outer bank, erosion occurs, and mangroves col-

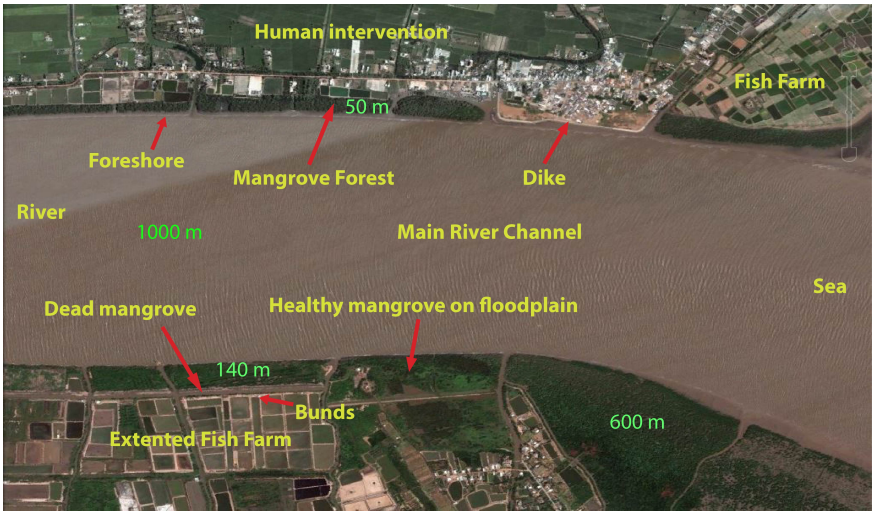

Figure 2.4: Mangroves at Tieu estuary; hydrodynamic forces differ between the river and the sea environment. Coastal mangroves are often exposed to sea waves and storms. Estuarine mangroves are much less exposed to sea waves and storms; these are rather influenced by lateral flow and geometric features of the river (meandering or straight).

lapse if their foundations are eroded. Thus, the meandering locations are more complex, where both natural and human-induced impacts occur. That will be a topic for further study. In this study, to eliminate the meandering effect, observations are focused only on the straight parts of the estuaries. Eight estuaries were reviewed; of which, three were disregarded. In Ba Lai Estuary, the construction of the Ba Lai dam created morphology changes that are different from other branches of the MES, and the resolution of satellite images captured for the Co Chien and Cung Hau estuaries were too low to be used to measure mangrove width. Tieu, Dai, Ham Luong, Dinh An, and Tran De branches offered the most favorable observations, with clear and high-resolution images available. At selected locations, the mangrove width could be measured, the fish ponds could be clearly identified, and data on evolutionary rate were available.

The following assumptions are applied to the observations.Firstly, the area of interest was the area from the landward boundary of the fish ponds to the nonvegetated foreshore. It was assumed that the mangrove width of that area was a representative mangrove width for the entire cross section. Secondly, the mangroves, because of conditions necessary for their survival, usually develop as entire forests, not as individual plants; therefore, the mangrove observations focused on the entire mangrove forest.

An investigation report from the Southern Institute of Water Resources Research (SIWRR, 2010) indicated locations suffering from erosion and accretion. For this study, the mangroves width observed in those areas are represented with minimum widths, maximum widths (mangroves width range), and representative mangroves widths. The observations were taken at different locations that had experienced either erosion or sedimentation on the Tieu, Dai, Ham Luong, Dinh An, and Tran De branches (chosen locations are numbered 1–17 in Figure 2.1; location names can be found in Table 2.1. Ac-

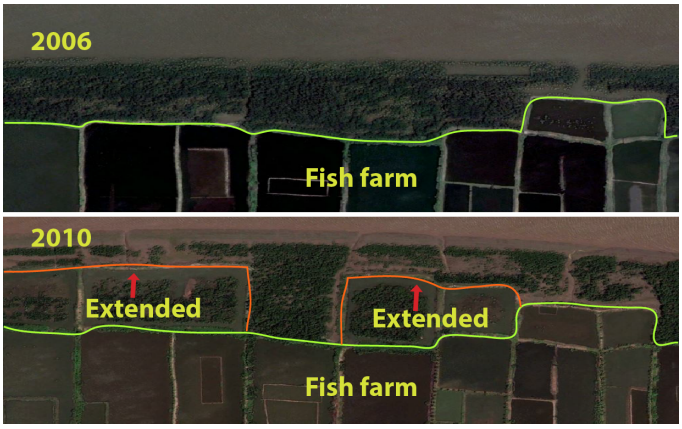

Figure 2.5: Google Earth images showing a typical example of mangrove change between 2006 (a) and 2010 (b) at the Dai estuary due to extended fish farms. Converted mangrove areas play a role as a blocked area, resulting in re-distribution of sediments, the area of unhealthy mangroves seems to increase.

cording to scale classifications of shores and shoreline variability presented by Stive et al. (2002), this study was interested in evolutionary trends based on a timescale of years to decades, with a space scale of 1–10 km. Mangrove widths for each location observed were measured from Google Earth for the year 2006 and are presented in Table 2.1. The rate of riverbank evolution in 2006 is presented in Table 2.1.

The suggested relationship between mangrove width and estuarine-bank evolution is shown in Figure 2.6, which presents the average evolutionary rate as a function of mangrove width in 2006. The uncertainty bars were applied in both vertical and horizontal directions. The uncertainty in the width variability was not due to ground-referencing errors (the location of the primary dike was not influenced by water levels, for instance), but rather, the uncertainty was the result of alongshore variability over the stretches considered and included in the data presentation. The vertical bars indicate the estimated uncertainty in the evolutionary rate given by SIWRR (2010), which, on average, was $0.5\,\mathrm{m\,yr^{-1}}$. A power trend line was fitted that included the 90% confidence interval. Although interpretation of results can be somewhat subjective, from Figure 2.6, it can be deduced that the riverbank will remain stable in the presence of a mangroves width range of approximately 50–150 m, with a representative value of about 80 m. A larger width would lead to a healthier fringe and higher sedimentation potentials. The data set was limited to those locations in which sediment availability was not expected to be a constraint. In general, riverbank evolution depends on many factors, such as local sediment supply, local hydraulic conditions (flow, wave, wind, current), local bathymetry, *etc.* Hence, no unique critical mangrove-width value can be set for all estuarine regions. The quantitative relationship provided, therefore, is only applicable to the Mekong and Bassac estuaries of the Mekong Delta, although the general principle will apply to many other estuarine mangrove regions.

Table 2.1: Average river bank evolution rates reported in 2006 (SIWRR, 2010) and Google-Earth based estimated mangrove widths in 2006 in the MES at different branches.

No	Location	Length (km)	Situation	River bank evolution rate ($m\,yr^{-1}$)	Mangrove Width range (m)	Representative Mangrove width (m)
1	Middle of Tan Hoa –End of Tan Hoa	3	Accretion	1.5	35-60	50
2	Phu Dong	7	Stable	0	100-190	140
3	Phu Tan	5	Accretion	4.5	550-700	600
4	Middle of Phu Thanh to Phu Dong	-	Accretion	2.5	110-290	250
5	Middle of Phu Dong	3	Erosion	-1.5	20-110	85
6	Dinh Trung-Binh Thoi	5	Erosion	-2.5	0-40	25
7	Binh Thoi commune	-	Erosion	-1.5	0-30	20
8	Binh Thang commune	2.5	Accretion	1	45-75	50
9	An Hiep to An Duc	-	Erosion	-2.5	0-60	50
10	An Duc- An Hoa Tay	-	Stable	0	30-170	90
11	An Thanh	4	Accretion	1	50-120	85
12	An Dien	5	Accretion	4	350-600	500
13	Tra Cu Province – Ham Giang	8	Erosion	-3.5	0-75	40
14	An Thanh 2- An Thanh 3	8	Erosion	-2.5	20-120	55
15	Dai An 1	7	Erosion	-1.5	10-60	35
16	Co Tron River -Sea	2.5	Stable	0	50-90	75
17	Dai An 2	-	Erosion	-1.5	20-70	30

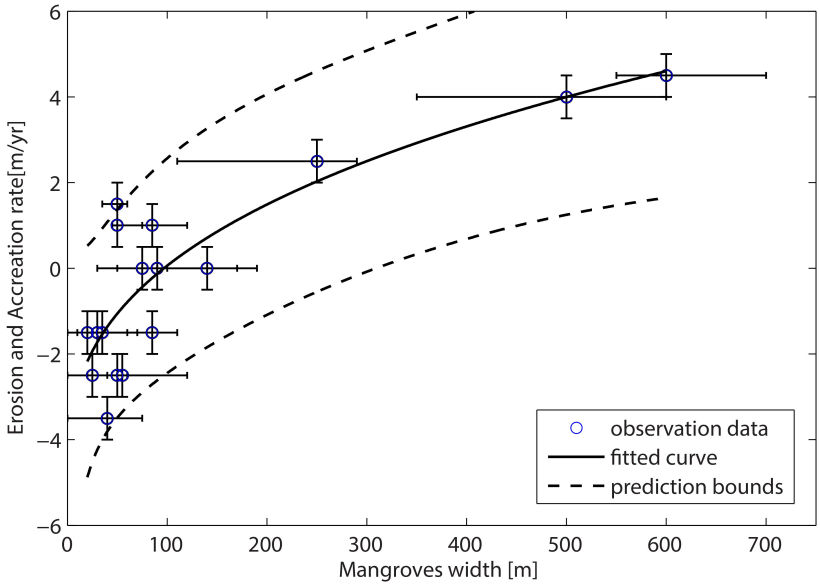

Figure 2.6: Relationship between mangroves width and river bank evolution in the Mekong Delta Estuaries (assuming sediment availability is no constraint; see text)

2.2.3 Flow Attenuation in the Mangrove Forest

To study how far the flow from the river's main channel penetrated into the mangrove forest, and even more specific, the effectiveness of mangroves to attenuate flow en-

ergy as a function of mangrove width, were assessed. A state-of-the-art Delft3D-Flow model with a rigid vegetation simulation was applied. A schematized geometry based on the dimension of the Tieu estuary was used.

Hydrodynamics of Estuarine Mangrove Forest

As mentioned, although the primary hydrodynamic impacts on mangroves in a coastal area are waves, mangroves in estuaries are primarily affected by flow, *i.e.* flow caused by tidal action and by river discharge. Previous studies of the hydrodynamics of mangrove, in general, and in the Mekong Delta Estuaries, in particular, were based on particular field settings. Those studies investigated flow routing *i.e.* the flow in and out of a mangrove swamp. Flooding of the mangrove forest was discovered to have caused by a combination of over-bank flow and creek flow, and ebbing occurred primarily through creek flow (Aucan and Ridd, 2000). The distinction of creek-flow stage and over-bank flow stage was confirmed by comparing the results of a numerical model with data collected from field observations (Horstman, 2014). Flow routing was directly related to hydrodynamic routing of waterborne particles, such as mangrove seeds, nutrients, and fine, suspended sediments through the mangrove systems, which is thought to have an important role in supplying sediment and nutrients to mangrovesn(Furukawa et al., 1997; Mazda et al., 1995; Wolanski et al., 1980, 1990). The significant friction induced by mangroves causes the deceleration of the tidal currents and a delayed discharge into the mangrove forest, resulting in a net input of sediments into the mangrove forest (Wattayakorn et al., 1990). This is known as the tidal asymmetry of tidal currents in both the tidal creeks and mangrove swamps.

That research was implemented principally within healthy riverine mangrove forests, in which mangrove width was not limited and was much larger than the region of the lateral overbank flow. However, in the MES, only a narrow strip of mangrove forest is left because of the human impacts. The mangrove width observed in the MES (approximately 50–600 m) is small when compared with the main estuarine channel width of 1000–2000 m m. Few transversal tidal creeks were observed in the study area. The flow routing in a mangrove forest without tidal creeks is different from that in forests with tidal creeks. By collecting the flow-velocity data along a cross section through a smoothly sloping riverine mangrove fringe without creeks, flow velocities were observed to be parallel to the river at the forest fringe but gradually turned perpendicular to the river further into the forest (Kobashi and Mazda, 2005). That finding accentuates the important role of lateral exchanges in a mangrove forest without creeks. In this sense, the mangrove forests in the MES are similar to vegetated floodplains, which have been explored by several researchers, primarily in laboratory setting. These studies of vegetated floodplains, including a one-dimensional model (Helmiö, 2004; Ikeda et al., 1991; Vionnet et al., 2004) and a two-dimensional model (Pasche and G., 1985), focused on the momentum-exchange mechanism, the distribution of the total discharge, and the distribution of the averaged flow velocity between the main channel and the vegetated floodplain.

In the literature, the similarity in flow hydrodynamics between mangroves and vegetated floodplains has been recognized (Mazda et al., 1997). The shear-layer vortices caused by the Kelvin-Helmholtz instability formed at the interface of the vegetated re-

gions has a significant role in the lateral momentum exchange (Nadaoka and Yagi, 1998; Nezu and Onitsuka, 2001; Tamai et al., 1986; van Prooijen et al., 2005; White and Nepf, 2007, 2008; Xiaohui and Li, 2002; Zong and Nepf, 2010). Nevertheless, those realizations have not been integrated into studies of the hydrodynamics of mangroves. White and Nepf (2007) proposed a model for the vortex-included exchange and the penetration of momentum into a vegetated floodplain. However, that model was based on only one set of flume experiments with rigid, circular cylinders, so whether that result was valid generically has yet to be determined (Nepf, 2012). The exchange of mangrove seeds, nutrients, and fine, suspended sediments through this mechanism can be fundamental for a sustainable mangrove forest.

In summary, because of an estuarine squeeze, the mangrove width in the MES is usually very narrow. In this situation, the hydrodynamics of the mangrove forest is similar to that of a vegetated floodplain. Lateral tidal creeks can be disregarded. The main interaction is the lateral-momentum exchange through the shear-layer vortices between the main river channel and the floodplain region with the mangroves. This momentum exchange is considered to have an important role in the sustainable development of the mangrove forest. The maximum penetration length into the mangrove forest of that momentum exchange during periods of high river discharge were estimated through a depth-averaged velocity profile predicted by a schematized model constructed in Delft3D.

Estuarine Mangrove Distribution

To construct the schematized model for the mangroves in the MES, it was necessary to increase the detail on the mangrove types available within these estuarine regions. Mangroves grow mainly between mean sea level and highest spring tide (Alongi, 2009; Hogarth, 2015) because, below mean sea level, the mangrove seedlings cannot settle, and above the highest spring tide levels, the mangroves cannot compete with the other plants (Schiereck and Booij, 1995). The succession form of the mangrove forest system in the MES, including the mangrove species that dominate land edges and those that dominate water edges, can be described as experiencing the following main stages (Hong and San, 1993). The Pioneer Stage is usually found on tidal flats flooded by the mean tide. Mangrove species, such as *Sonneratia* and *Avicennia*, are able to tolerate the extensive flooding and high salinity. They have the same biological characteristics of pneumatophores roots, which can rapidly establish themselves in the substrate. The Transition Stage is a stage in which the pneumatophore system of *Sonneratia* and *Avicennia* species trap and hold soil and alluvium. After a short time, the mudflats are elevated, *i.e.* when sediment is available as a source. Seedlings of other land edge species, such as *Nypa fruticans*, *Cryptocoryne ciliata*, and *Acanthus ilicifolius* are carried to the flats by tidal water and trapped by the pneumatophore system. The final stage is a Multi-species Community. Because the land is continuously elevated by alluvial deposition, it is usually only flooded at high tide and more land-edge mangrove species, such as *Derris trifoliate*, *Wedelia biflora*, and *Acanthus, ilicifolius* are able to develop.

In contrast to coastal mangroves, estuarine mangroves consist of a variety of mixed types that are able to adapt to a wide range of salinities, such as *Sonneratia Alba*, and *Acanthus ilicifolius*, *Nypa fruticans*, *Cryptocoryne ciliata*, *etc.* In the Mekong Delta Estuaries, the presence of Rhizophora is not often observed, except in the Ba Lai Estuary

(Hong and San, 1993). In the schematized model, the estuarine mangrove forest was considered to consist only of *Sonneratia* species. This type of mangrove is known by its pneumatophores, which are erect, lateral branches of horizontal cable roots that grow underground (De Vos, 2004).

Schematized Model, Different Scenarios and Input Parameters

To obtain insight into the efficiency of a mangrove forest in reducing the impact of alongshore flow, as well as the penetration scale of the shear layer into the forest, a schematized model of mangroves in the Tieu Estuary was constructed in Delft3D. The model covered the first 2 km from the river mouth and half of the estuarine width (1100 m). Default settings in Delft 3D were used as much as possible. Specific settings are explained below and are related to bathymetry, hydraulic boundary conditions, vegetation properties, and numerical choices.

Table 2.2: Vegetation parameters (Ranasinghe et al., 2010).

Parameters	*S. Alba*		
Stem Diameter (m)	0.3		
Root Diameter (m)	0.02		
Canopy Diameter (m)	0.5		
Stem Height (m)	6		
Root Height (m)	0.5		
Canopy Height (m)	2		
Density variations	Spare	Average	Dense
Stem density (m^{-2})	0.5	0.7	1.7
Root density (m^{-2})	25	50	100
Canopy density (m^{-2})	50	100	100

Table 2.3: Different scenario for Tieu Schematised model in Delft 3D- Flow

Schematised model	Floodplain width (m)	mangrove width (m)	Q ($m^3 s^{-1}$)	H (m)
Tieu Estuary	300	300	2848	0.48
$i = 1/5000$	200	200	2848	0.48
$i_f = 1/10$	50	50	2848	0.48
$L = 2$ km, $B = 1.15$ km	300, 200, 50	No mangrove	2848	0.48

The bathymetry and the hydrodynamics were schematized to provide input into the Delft3D-FLOW vegetation model. The model includes a main river and a floodplain in the form of a trapezium-shaped channel. The bathymetry and the slope of the estuary were estimated using topographic maps from the SIWRR (2010) report . Because of the gentle slope of the substrate in a mangrove forest, a mangrove forest slope was not attempted but was taken as being horizontal. Figure 2.7

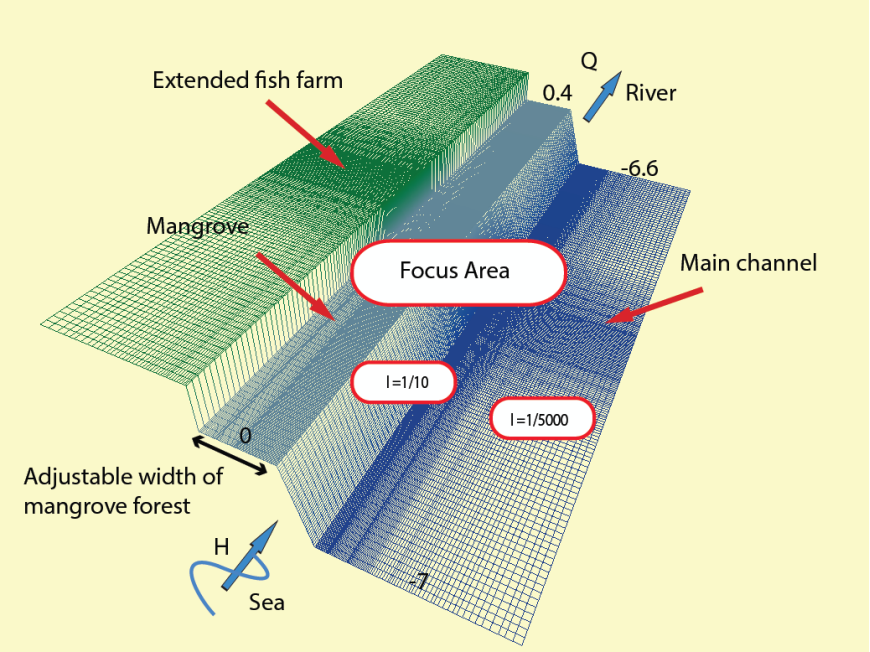

Figure 2.7: Tieu - 3D schematised model. The model includes a main river and a floodplain. It covers the first two kilometers length from the river mouth, and half of the estuarine width.

Hydraulic boundary conditions of the model consisted of river discharge upstream and water level downstream. Because the study area was located in a region of tidal influences, an upstream boundary condition was needed for the model. This was created by extending the model 200 km upstream to the Vam Nao channel, where the tide influence is negligible during the flood season. A constant discharge value could be applied to that location. The water level downstream was recorded by an acoustic Doppler current profiler on 15–30 September 2009. In this extended model, the discharge at 2 km from the river mouth was extracted and applied as the upstream boundary condition for the smaller, nested model. Subsequently, the nested model with a constant boundary condition was set up by considering only a representative time during which the depth averaged velocity in the main river channel was largest because the largest penetration of the flow into the mangrove forest was expected to occur when the depth-averaged velocity in the main river reached its maximum value and was accompanied by the greatest difference between the depth-averaged velocity in the main channel and that in the mangrove forest. A representative moment in time was chosen at 0500 on 20 September 2009 Figure 2.8, when the water level recorded at the river mouth equaled 0.48 m, and the discharge value was 2848 $m^3 s^{-1}$.

As mentioned, only one type of mangrove *Sonneratia* sp. was considered. The characteristics of the *Sonneratia* sp. are described with nine parameters and three different layers by Ranasinghe et al. (2010) for the mangroves in India. The similarities between the mangrove species in the Mekong Delta and those in India were the argument for

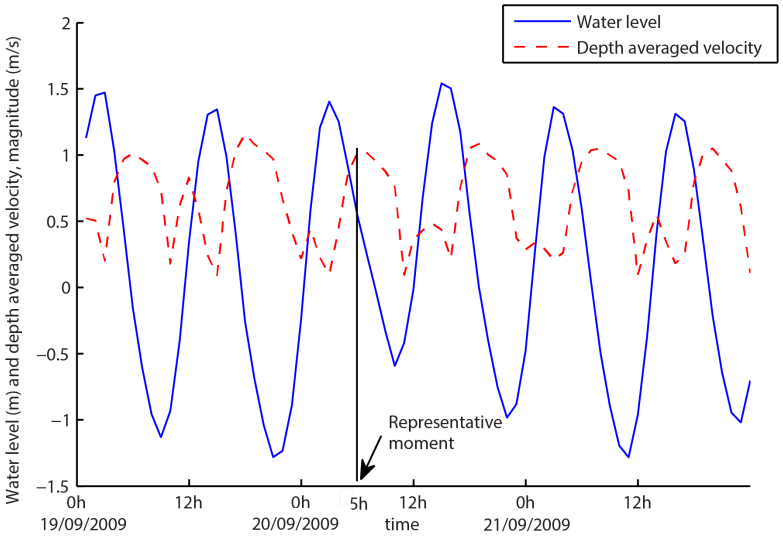

Figure 2.8: Water level and velocity at the Tieu Estuary and a representative moment in time chosen for a constant boundary condition.

using those parameters in the current model (Table 2).

Several mangrove widths, from 50 m to 300 m, were considered. For each case, three scenarios of mangrove density (spare density, average density, and dense density) were examined. The basic setup with the scenarios is presented in Table 3.

To estimate the penetration-length scale of the shear-layer vortices into the mangrove forest, the results focused on the depth-averaged velocity in the middle cross section of the model (the high-resolution area in Figure 2.7), where a fully developed region with stable flow conditions of uniform velocity across the mangrove forest and the main river channel existed.

2.3 Results

The impacts of extending fish farms toward the nonvegetated foreshore were studied by reducing the mangrove width toward the floodplain edge (at x=600 m). The depth-averaged velocity distribution and its reduction trend across the estuary from the main channel to the mangrove forest were examined for no, spare, average, and dense vegetation scenarios. The overall model results are presented in Figure 2.9, showing the reduction trend of the depth-averaged flow velocity from the main channel to inside the mangrove forest. The depth-averaged velocity profiles in the case without mangroves are presented in Figure 2.10. The reduction level in the depth-averaged velocity for different vegetation densities is shown in Figure 2.11. Figure 2.12 focuses on the overall deceleration of the depth-averaged velocity in the region around the last 200 m of the floodplain area (from 450 m to 650 m).

2.3.1 General results

In general, the model results indicated that the depth averaged velocity in the main channel with mangroves was faster than it was without mangroves, and the depth-averaged velocity in a floodplain area with mangroves was much slower than it was without mangroves (Figure 2.9). In other words, the velocity gradient between the main channel and the floodplain increased with the presence of vegetation. This corresponds with the presence of vegetation in the floodplain inducing drag forces, thus reducing the overall flow velocity.

In the case with mangroves, the depth-averaged velocity in the main channel was on the order of magnitude of $0.9\,\mathrm{m\,s^{-1}}$, which quickly reduces to an order of magnitude of $0.015\,\mathrm{m\,s^{-1}}$ inside the mangrove forest ($u_{channel}/u_{mangrove} = 35$), in line with that measured in previous studies (Anthony, 2004; Horstman, 2014; Van Santen et al., 2007). The velocity gradient between the main channel of the river and mangrove forest was about four times larger than that between the adjacent tidal creeks ($0.1\,\mathrm{m\,s^{-1}}$) and the mangrove swamp ($u_{creeks}/u_{mangrove} = 10$). This difference in the velocity gradient again emphasizes the important role of the lateral exchange between the main river channel and mangrove swamp.

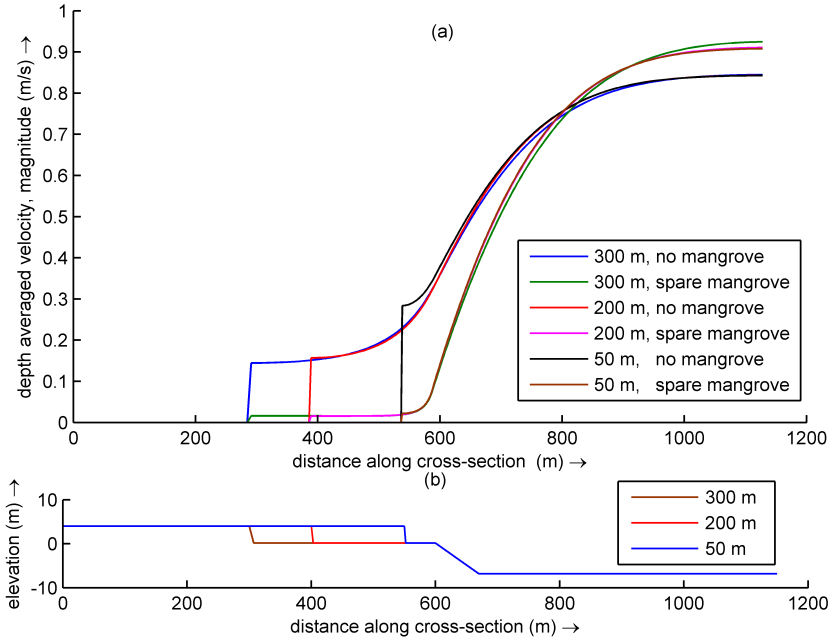

Figure 2.9: Depth averaged velocity along the cross section of Tieu schematised model (a) and corresponding profile with 300 m, 200 m and 50 m width of floodplain (b) (from equilibrium profiles).

2.3.2 No Mangrove

IN the cases without mangrove forests, the magnitude of the velocity within the floodplain region varied with the changes in the floodplain width (Figure 2.10). The smaller the floodplain was, the larger the depth-averaged flow velocity within the floodplain area was. The depth-averaged velocity at the beginning of the floodplain (x=600 m) was about 0.35 m s^{-1}. In the cases of 300 m and 200 m floodplain widths, the depth-averaged velocity reduced and achieved a uniform value of about 0.15 m s^{-1} (43% of that at the start of the floodplain water edge) after about 150 m. With a 50 m floodplain width, the depth-averaged velocity reduced to about 0.3 m s^{-1} (86%) after 50 m. This implies that the depth-averaged flow velocity needs a certain distance from the floodplain edge to achieve a uniform value.

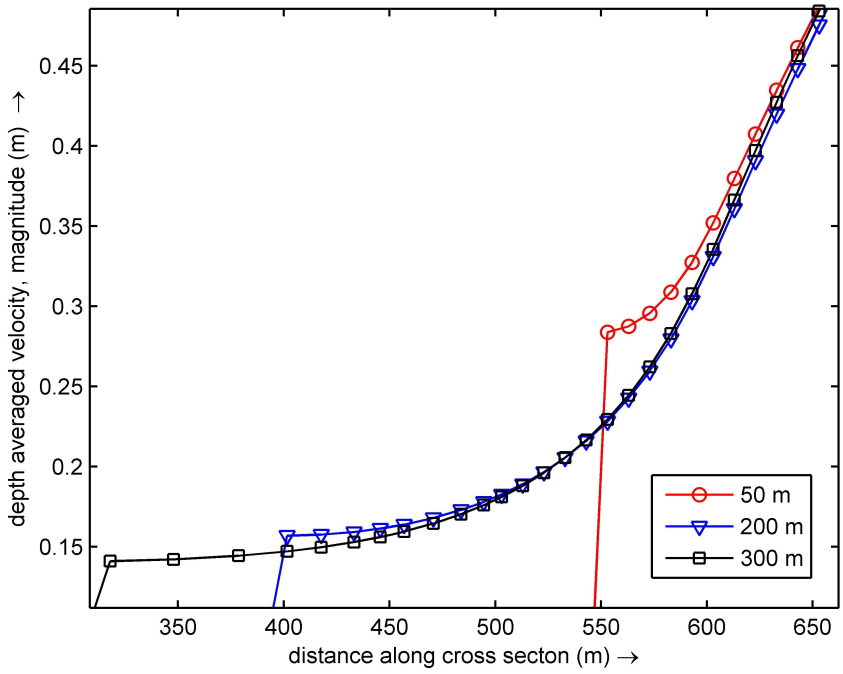

Figure 2.10: Depth averaged velocity along the cross section of Tieu schematised model in case of 50, 200 and 300 m floodplain without mangroves.

2.3.3 Mangroves with different density

THe uniform depth averaged flow velocity within the mangrove forest for Tieu estuary model is anticipated to reach around 0.015 m s^{-1} and this value slightly reduces when the density of mangrove increases Figure 2.11. Another observation in Figure 2.11

is that together with the increasing vegetation density, the depth averaged velocity profiles around the mangrove edge is steeper and requires a shorter distance from the mangrove edge (x=600 m) to achieve uniform values within the mangrove forest. This result implies that if the mangrove forest width is not restricted, the penetration of the exchange into the vegetation regions caused by velocity gradient between the main channel and the vegetated area is principally dependent on the vegetation characteristics.

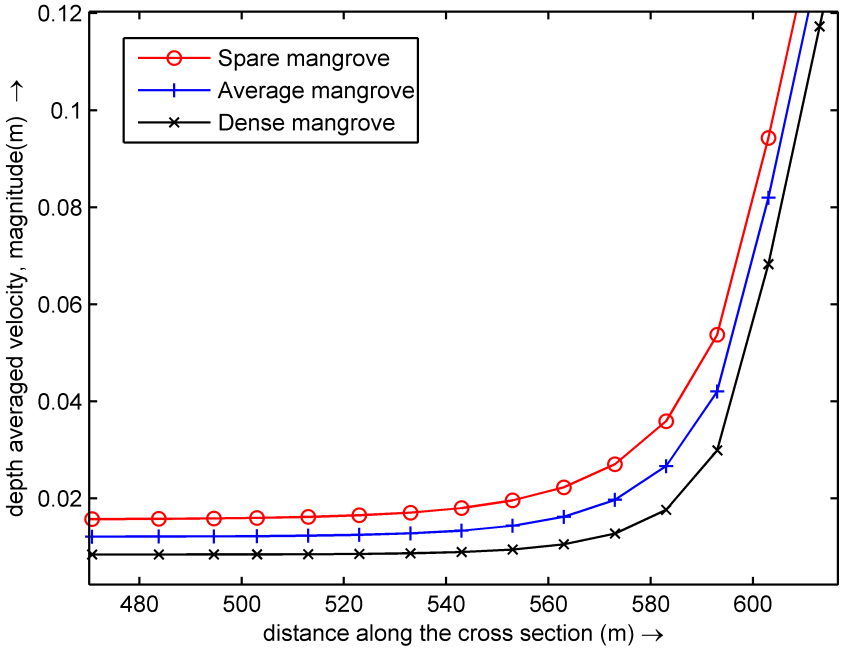

Figure 2.11: Depth averaged velocity with different scenarios of vegetation density at Tieu estuary. The result is zoomed in on the floodplain region.

2.3.4 Mangrove with different width

The trend toward reduced distance from the main channel to the inside of the mangrove forest by the depth-averaged flow velocity was quite similar in cases of 300 m mangrove widths, 200 m mangrove widths, or 50 m mangrove widths for the Tieu Estuary (Figure 2.9). By looking inmore detail into the region around the last 150 m of mangrove edge (from x=450 m to x=600 m) (Figure 2.12), the model indicated that the depth-averaged velocity required about 60 to 80 m to reach a fully uniform value within the mangrove forest (about 0.015 m s^{-1}). That depth-averaged velocity was about 20% of that at the start of the forest (0.08 m s^{-1}). This implies that the length scale of the penetrating shear layer into the mangrove forest was 60–80 m. In other words, the minimum distance from the mangrove edge at which the velocity in the mangrove forest reached

a uniform value of about 0.015 m s^{-1} was about 60 −80 m. Therefore, when floodplain widths were less than 60 −80 m, the depth-averaged velocity profile in the mangrove forest would not reach a uniform value because the penetration length of the mixing layer was larger than the width of the mangrove forest.

In conclusion, these results show that, as long as the riverine mangrove forest width in the MES is larger than approximately 60 −80 m, the uniform depth-averaged flow velocity within the mangrove forest is dependent on mangrove characteristics, rather than on the characteristics of bathymetry and hydraulic conditions in the adjacent main river channel. However, when the riverine mangrove forest width is less than 60 −80 m, the uniform depth-averaged velocity within the mangrove forest is affected by the flow in the main river channel. This is in agreement with the observations that confirm the hypothesis of the existence of a link between critical mangrove width in the estuarine mangrove forest and the maximum penetration of the flow into the forest. An averaged value of 80 m is the minimum width at which the mangrove forest can be maintained, and at that width the forest is sustainable if the construction of fish farms does not reduce that width.

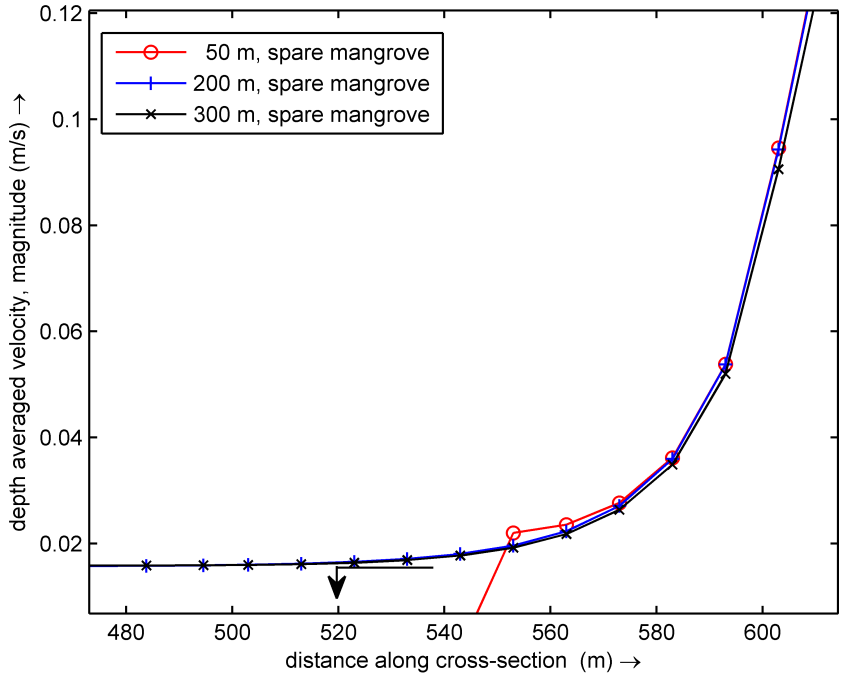

Figure 2.12: Depth averaged velocity in the floodplain region, Tieu estuarine model.

2.4 Discussion

In this section, the physical meaning of a critical mangrove width can be discussed within the context of sedimentation and forest restoration capacity.

2.4.1 Critical mangrove width and sedimentation

THe requirements for a sustainable mangrove forest are very strict. Significant changes in the sediment dynamics within a mangrove forest can do damage to the entire system. Too much sedimentation may bury the mangrove propagules, leading to the death of the aerial mangrove root system of the pioneer species, such as *Sonneratia* and *Avicenna*. However, too little sedimentation may lead to the destabilization of the mangrove trees. The mangrove propagules have a length of 25 −30 cm, so a sediment thickness of around 30 cm is necessary to provide a suitable environment for mangrove aerial roots (Linh, 2012). Nevertheless, only 10 cm of root burial can make *Avicennia* trees die (Ellison, 1999), and 8 cm of sediment burial can reduce growth and increase mortality of *Rhizophora* seedlings (Terrados et al., 1997). In addition, because mangrove roots anchor in only about 0.5 m of the soil, a few decimeters of erosion is sufficient to destabilize a mangrove tree (Winterwerp et al., 2013).

Once fish ponds are constructed too far into the mangrove forest, insufficient mangrove width remains for a proper lateral exchange between the main river channel and the adjacent mangrove forest; this critical width is estimated to be, on average, about 80 m. Widths less than that directly disturb the hydrodynamic conditions, leading to changes in sediment source as well as the available space for sedimentation, reducing the total capacity of the mangrove forest to trap sediment. If there is no accommodation space available, sediment will bypass those sites and be transported to an area in which accommodation space allows the sediment to be deposited (Coe, 2003). Similarly, sediment that cannot be deposited in converted mangrove areas will be transported and deposited in adjacent area, where it may bury mangrove propagules. Therefore, the readjustment of the sedimentation system will have a negative impact on the adaptive capacity of the mangrove system. The loss of mangroves will again reduce the sediment-trapping capacity, resulting in more erosion of the riverbank.

2.4.2 Critical mangrove width and restoration capability

MAngrove forests affected by human intervention landward can sometimes be restored, but only by monocultures of fast growing species, such as Sonneratia, Avicenna, or Rhizophora;rarer species and entire mangrove ecosystems cannot be fully restored. This phenomenon of unsuccessful restoration of mangrove ecosystems, especially that of rare land-edge species, was recently reported by Polidoro et al. (2010).

The reasons for this phenomenon may be explained by the hypothesis about the connection between critical mangrove width and the width of the earlier-stage mangrove species. As mentioned, the primary threats to mangroves are landward human interventions and waterborne sea-level rise. Although human interventions directly affect the mangrove species at the land edges—those established in the final successional stage, the effects of sea-level rise threatens the mangrove species at the water edges—those

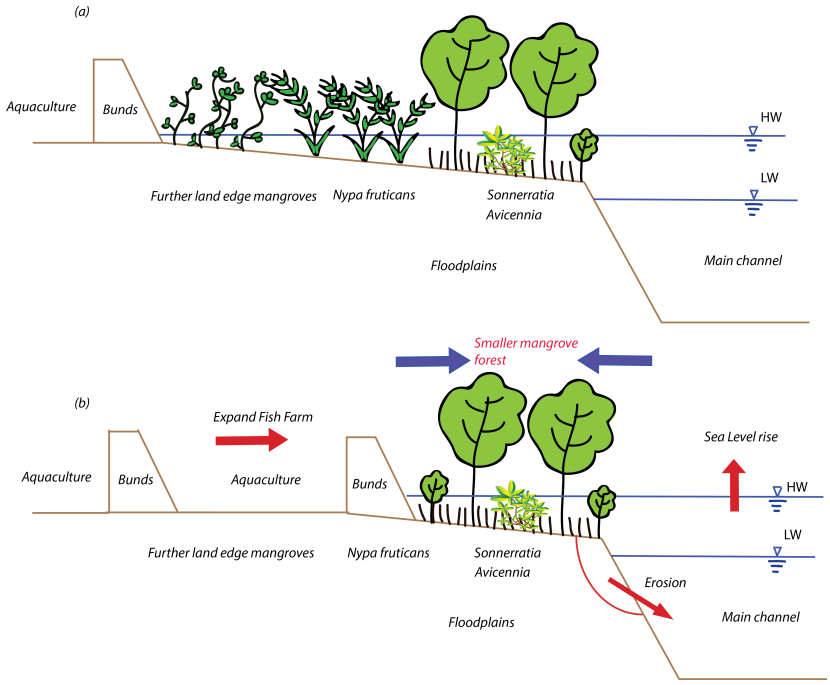

Figure 2.13: Impact of different level of fish farm expansion on the successive stages of mangrove in the MES (after Phan and Hoang, 1990) (a) and estuarine mangrove squeeze issues in Mekong Delta Estuaries (b).

established in the pioneer stage. However, those mangrove species establishing in the later stages are more vulnerable to sea-level rise than are mangrove species that are established at earlier stages because the later-stage mangroves grow slower, have greater difficulty with dispersal, and reproduce slower than do the mangrove species at earlier stages, such as *Sonneratia* and *Avicennia* species (Polidoro et al., 2010). Mangrove species at the water edges of a mangrove forest can be considered a "pioneer protection layer" for land-edge mangrove forests because they cope better with changes at the open-water side, such as sea-level rise, than do the inner mangrove species. Any changes in the open water side first affect the protection layer, and the inner layer has more time to respond to those changes (such as landward retreat). That protection is necessary to the sustainability of the entire mangrove forest ecosystem. The rules for the transition from pioneer species to the species associated with transitional and climax stages are unknown. It was, therefore, hypothesized that there is a link between the critical minimum width and the width of the protection layer for the later stages of mangrove species. In other words, the critical minimum width is also the width that the pioneer mangrove species need for the succession of in the forest to further stages. Once, the human intervention on the land side block mangrove forest reaches and exceeds that width, all the later-stage mangrove species are destroyed (if they already exist) or they do not have space to develop (if they do not already exist) (Figure 2.13), preventing the mangrove forest from reaching its successive stages.

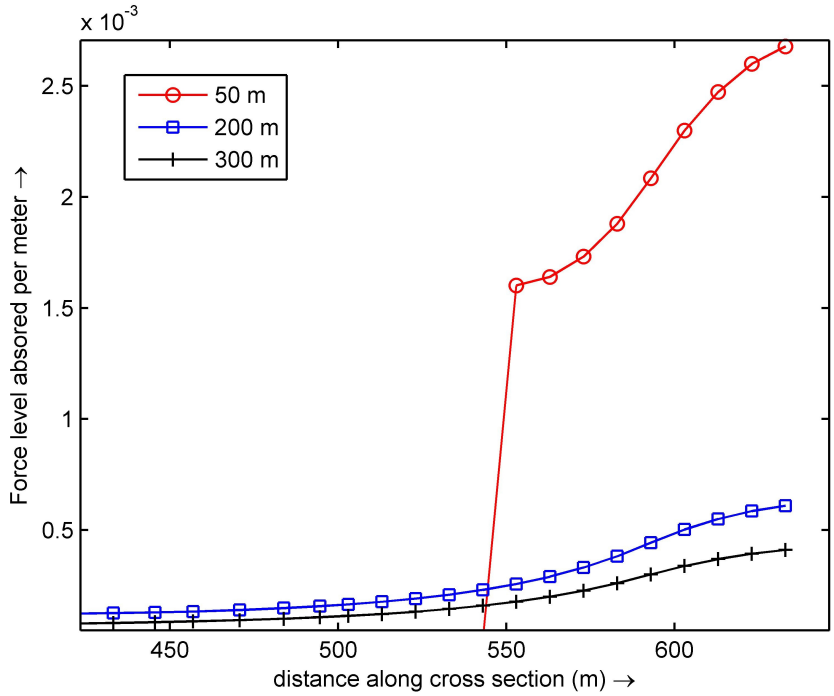

Figure 2.14: Force level required to absorb per meter width of mangrove in cases of different mangrove forest width (Tieu estuary model).

Flow kinetic energy is proportional to the velocity squared. Therefore, the forces absorbed (F_{absorb}) per meter of mangrove forest width can be modeled as followed:

$$F_{absorb} \sim \frac{K_{nomangrove} - K_{mangrove}}{width} \Leftrightarrow F_{absorb} \sim \frac{U^2{}_{nomangrove} - U^2{}_{mangrove}}{width} \quad (2.1)$$

The forces absorbed per meter of mangrove forest width for various different widths are estimated in Figure 2.14. According to that estimation, when reducing from 200 −300 m to 50 −55 m of mangrove width, the magnitude of the forces absorbed per meter of width increases on an order of ten. That means that, for every meter of width, a 50 m mangrove forest absorbs forces that are about ten times greater than those absorbed by every meter of 200 m or 300 m forests to reduce the average velocity to a value suitable for the development of mangroves. Therefore, when a mangrove forest is reduced from 300 m to 50 m, the force per unit meter that the mangrove forest needs to absorb increases about ten times. Under those new conditions, only the pioneer mangrove species can survive and develop. However, many fish farms and other human interventions have been constructed within forests in which the mangrove species are in their final successional stages, which means they are weaker, more vulnerable, and will likely die.

These results mean that if, for some reason, the entire 50 m or 300 m of estuarine mangroves were to be destroyed and the propagules of mangrove species were replanted

in those regions, the force the forest would need to absorb would be ten times greater for the 50 m forest. This implies that the larger the width of a mangrove forest, the easier it is for that forest to recover, especially for the land-edge mangrove species.

2.5 Conclusions

IN this study, mangrove forest degradation and the trends in riverbank evolution affected by the extent of fish farms in the MES were analyzed by adopting a broader definition of the term estuarine squeeze. In that context, a minimum width was derived that the estuarine mangrove ecosystem needs for healthy, cyclic evolution. If mangrove forest widths are less than 80 m in the MES, the riverbank will be less stable and the estuarine mangroves will be more vulnerable. The results were estimated based on an empirical relationship between mangrove forest width and riverbank evolution. Based on the similarity between the hydrodynamics of a narrow mangrove forest and that of a vegetated floodplain channel, the exchange mechanism between the main river channel and the vegetated floodplain could be identified. That mechanism controls such fundamental factors as the transport and deposition of sediment, the supply of nutrients, and the significance of organic outwelling from a mangrove forest. This occurs because of the penetration of shear-layer vortices caused by the velocity gradient and the presence of mangroves on the floodplain. Results from the Delft3D-flow vegetation model for the Tieu Estuary showed the penetration length scale of the shear layer into the mangrove forest. The depth-averaged flow velocity from the main channel was reduced to a uniform value on an order of magnitude of $0.015\,\mathrm{m\,s^{-1}}$ within $60-80$ m inside the mangrove forest. The agreement between field observations and the schematized model confirmed the existence of and estuarine mangrove squeeze and the hypothesis of a critical width linked to the maximum penetration of the flow into the mangrove forest.

Unsuccessful mangrove restoration attempts at the land edge of the forest, which usually contains more rare and vulnerable species compared with pioneer species, can be explained by assuming a link between the critical minimum width and the minimum width of the mangroves at a pioneer stage. The difficulty in the recovering mangrove species in their final stages (the land edge of the mangrove forest) can also be understood from an energetic standpoint.

References

Alongi, D. M. (2002). Present state and future of the world's mangrove forests. *Environmental Conservation*, 29(03).

Alongi, D. M. (2008). Mangrove forests: Resilience, protection from tsunamis, and responses to global climate change. *Estuarine, Coastal and Shelf Science*, 76(1):1 – 13.

Alongi, D. M. (2009). *The energetics of mangrove forests*. SpringerLink: Springer e-Books. Queensland, Australia: Springer.

Anthony, E. J. (2004). Sediment dynamics and morphological stability of estuarine mangrove swamps in sherbro bay, west africa. *Marine Geology*, 208(2):207–224.

Anthony, E. J., Brunier, G., Besset, M., Goichot, M., Dussouillez, P., and Nguyen, V. L. (2015). Linking rapid erosion of the mekong river delta to human activities. *Scientific reports*, 5.

Anthony, E. J. and Gratiot, N. (2012). Coastal engineering and large-scale mangrove destruction in guyana, south america: Averting an environmental catastrophe in the making. *Ecological Engineering*, 47:268–273.

Aucan, J. and Ridd, P. V. (2000). Tidal asymmetry in creeks surrounded by saltflats and mangroves with small swamp slopes. *Wetlands Ecology and Management*, 8(4):223–232.

Christensen, S. M., Tarp, P., and Hjortsø, C. N. (2008). Mangrove forest management planning in coastal buffer and conservation zones, vietnam: A multimethodological approach incorporating multiple stakeholders. *Ocean & Coastal Management*, 51(10):712–726.

Cintron, G. and Novelli, Y. S. (1984). Methods for studying mangrove structure. In *Mangrove ecosystem: research methods*, pages 91–113. Unesco.

Coe, A. L. (2003). *The sedimentary record of sea-level change*. Cambridge University Press.

De Vos, W. (2004). Wave attenuation in mangroves wetlands, red river delta, vietnam. delft, the netherlands: Delft university of technology. Master's thesis, Master's thesis, 107p. http://repository. tudelft. nl/view/ir/uuid% 3A4d8f93b5-8efa-4663-a29a-448a50c45525.

Doody, J. P. (2004). ?coastal squeeze?–an historical perspective. *Journal of Coastal Conservation*, 10(1):129–138.

Duke, N. C. (1992). Mangrove floristics and biogeography. *Tropical mangrove ecosystems*, pages 63–100.

DWW (2004). Report on the Bank erosion in Mekong Delta and along Red River in Vietnam. Technical report, The Hydraulic Engineering Department of the Road and Hydraulic Engineering Institute, Delft, Netherlands : Rijkswaterstaat, Road and Hydraulic Engineering Division, 172p.

Ellison, J. C. (1999). Impacts of sediment burial on mangroves. *Marine Pollution Bulletin*, 37(8):420–426.

Ewel, K. C., Twilley, R. R., and Ong, J. E. (1998). Different Kinds of Mangrove Forests Provide Different Goods and Services. *Global Ecology and Biogeography Letters*, 7(1):83.

FAO (2007). The world's mangroves 1980-2005. *FAO Forestry Paper*, 153:89.

Feagin, R. A., Martinez, M. L., Mendoza-Gonzalez, G., and Costanza, R. (2010). Salt marsh zonal migration and ecosystem service change in response to global sea level rise: A case study from an urban region. *Ecology and Society*, 15(4).

Furukawa, K., Wolanski, E., and Muellerc, H. (1997). Currents and Sediment Transport in Mangrove\rForests. *Estuarine, Coastal and Shelf Science*, 44:301–310.

Gagliano, S. and McIntire, W. (1968). *Reports on the Mekong River Delta*. Technical report (Louisiana State University, Baton Rouge. Coastal Studies Institute). Coastal Studies Institute, Louisiana State University.

Galloway, W. D. (1975). Process Framework for describing the morphologic and stratigraphic evolution of deltaic depositional systems. *Deltas, Models for Exploration*, pages 86–98.

Gebhardt, S., Nguyen, L., and Kuenzer, C. (2012). Mangrove Ecosystems in the Mekong Delta - Overcoming Uncertainties in Inventory Mapping Using Satellite Remote Sensing Data. In Renaud, F. and Kuenzer, C., editors, *The Mekong Delta System: Interdisciplinary Analyses of a River Delta*, pages 315–330. Heidelberg, Germany: Springer.

Gilman, E., Ellison, J., and Coleman, R. (2007). Assessment of mangrove response to projected relative sea-level rise and recent historical reconstruction of shoreline position. *Environmental Monitoring and Assessment*, 124(1-3):105–130.

Helmiö, T. (2004). Flow resistance due to lateral momentum transfer in partially vegetated rivers. *Water Resources Research*, 40(5).

Hogarth, P. J. (2015). *The Biology of Mangroves and Seagrasses, Third Edition*. Oxford University Press, Oxford, 3 edition.

Hong, P. and San, H. (1993). *Mangroves of Vietnam*. IUCN wetlands programme. IUCN.

Horstman, E. (2014). The Mangrove Tangle: Short-term bio-physical interactions in coastal mangroves.

Ikeda, S., Izumi, N., and Ito, R. (1991). Effects of Pile Dikes on Flow Retardation and Sediment Transport. *Journal of Hydraulic Engineering-asce - J HYDRAUL ENG-ASCE*, 117.

IUCN (2011). Why healthy ecosystems matter: the case of mangroves in the Mekong Delta.

Kobashi, D. and Mazda, Y. (2005). Tidal flow in riverine-type mangroves. *Wetlands Ecology and Management*, 13(6):615–619.

Kummu, M. and Varis, O. (2007). Sediment-related impacts due to upstream reservoir trapping, the Lower Mekong River. *Geomorphology*, 85(3-4):275–293.

Linh, P. (2012). The Mekong deltaic coast: past, present and future morphology. Technical report.

Lu, X., Kummu, M., and Oeurng, C. (2014). Reappraisal of sediment dynamics in the Lower Mekong River, Cambodia. *Earth Surface Processes and Landforms*, 39(14):1855–1865.

Lu, X. X. and Siew, R. Y. (2005). Water discharge and sediment flux changes over the past decades in the Lower Mekong River: possible impacts of the Chinese dams. *Hydrology and Earth System Sciences*, 10:181–195.

Lugo, A. E. and Snedaker, S. C. (1974). The Ecology of Mangroves. *Annual Review of Ecology and Systematics*, 5(1):39–64.

Manh, N. V., Dung, N. V., Hung, N. N., Merz, B., and Apel, H. (2014). Large-scale suspended sediment transport and sediment deposition in the Mekong Delta. *Hydrology and Earth System Sciences*, 18(8):3033–3053.

Mazda, Y., Kanazawa, N., and Wolanski, E. (1995). Tidal asymmetry in mangrove creeks. *Hydrobiologia*, 295(1-3):51–58.

Mazda, Y., Wolanski, E., King, B., Sase, A., Ohtsuka, D., and Magi, M. (1997). Drag force due to vegetation in mangrove swamps. *Mangroves and Salt marshes*, 1:193–199.

Milliman, J. and Farnsworth, K. (2013). *River Discharge to the Coastal Ocean: A Global Synthesis*. Cambridge University Press.

Milliman, J.D. and Ren, M.E., . (1995). *River flux ti the sea:impact of human intervention on river systems and adjacent coastal areas*. Taylor & Francis, eisma, d. edition.

Nadaoka, K. and Yagi, H. (1998). Shallow-Water Turbulence Modeling and Horizontal Large-Eddy Computation of River Flow. *Journal of Hydraulic Engineering*, 124(5):493–500.

Nepf, H. M. (2012). Hydrodynamics of vegetated channels. *Journal of Hydraulic Research*, 50(3):262–279.

Nezu, I. and Onitsuka, K. (2001). Turbulent structures in partly vegetated open-channel flows with LDA and PI V measurements. *Journal of Hydraulic Research*, 39(6):629–642.

Nguyen, V., Ta, T., and Tateishi, M. (2000). Late holocene depositional environments and coastal evolution of the Mekong River Delta, Southern Vietnam. *Journal of Asian Earth Sciences*, 18(4):427–439.

Pasche, E. and G., R. (1985). Overbank Flow with Vegetatively Roughened Flood Plains. *Journal of Hydraulic Engineering*, 111(9):1262–1278.

Phan, L. K., van Thiel de Vries, J. S., and Stive, M. J. (2015). Coastal Mangrove Squeeze in the Mekong Delta. *Journal of Coastal Research*, 300:233–243.

Polidoro, B. A., Carpenter, K. E., Collins, L., Duke, N. C., Ellison, A. M., Ellison, J. C., Farnsworth, E. J., Fernando, E. S., Kathiresan, K., Koedam, N. E., Livingstone, S. R., Miyagi, T., Moore, G. E., Nam, V. N., Ong, J. E., Primavera, J. H., Salmo, S. G., Sanciangco, J. C., Sukardjo, S., Wang, Y., and Yong, J. W. H. (2010). The loss of species: Mangrove extinction risk and geographic areas of global concern. *PLoS ONE*, 5(4).

Ranasinghe, R., Narayan, S., Suzuki, T., Stive, M., Ursem, W., and Verhagen, H. (2010). On the effectiveness of mangroves in attenuating cyclone induced waves. In *Proceedings of the 32th International Conference on Coastal Engineering, ICCE 2010, June/July, Shanghai*. ASCE-Texas Digital Library.

Schiereck, G. J. and Booij, N. (1995). Wave transmission in mangrove forests.pdf. In *International Conference on Coastal and Port Engineering in Developing Countries*, pages 1969–1983.

SIWRR (2010). Tien Estuary Investigation Report [in Vietnamese]. Technical report, Southern Institute of Water Resources Research, Ho Chi Minh, Vietnam: Ministry of Agriculture and Rural Development of Vietnam, 180 p.

Stive, M. J., Aarninkhof, S. G., Hamm, L., Hanson, H., Larson, M., Wijnberg, K. M., Nicholls, R. J., and Capobianco, M. (2002). Variability of shore and shoreline evolution. *Coastal Engineering*, 47(2):211–235.

Ta, T. K. O., Nguyen, V. L., Tateishi, M., Kobayashi, I., Saito, Y., and Nakamura, T. (2002). Sediment facies and Late Holocene progradation of the Mekong River Delta in Bentre Province, southern Vietnam: An example of evolution from a tide-dominated to a tide- and wave-dominated delta. *Sedimentary Geology*, 152(3-4):313–325.

Tamai, N., Asaeda, T., and Ikeda, H. (1986). Study on Generation of Periodical Large Surface Eddies in a Composite Channel Flow. *Water Resources Research*, 22(7):1129–1138.

Terrados, J., Thampanya, U., Srichai, N., Kheowvongsri, P., Geertz-Hansen, O., Boromthanarath, S., Panapitukkul, N., and Duarte, C. (1997). The Effect of Increased Sediment Accretion on the Survival and Growth ofRhizophora apiculataSeedlings. *Estuarine, Coastal and Shelf Science*, 45(5):697–701.

Torio, D. D. and Chmura, G. L. (2013). Assessing Coastal Squeeze of Tidal Wetlands. *Journal of Coastal Research*, 290:1049–1061.

Tri, V. K. (2012). Hydrology and Hydraulic Infrastructure Systems in the Mekong Delta, Vietnamong Delta System. In *The Mekong Delta System: Interdiciplinary Analyses of a River Delta*, pages 49–81.

Turowski, J. M., Rickenmann, D., and Dadson, S. J. (2010). The partitioning of the total sediment load of a river into suspended load and bedload: A review of empirical data. *Sedimentology*, 57(4):1126–1146.

van Prooijen, B., A., B. J., and J., U. W. S. (2005). Momentum Exchange in Straight Uniform Compound Channel Flow. *Journal of Hydraulic Engineering*, 131(3):175–183.

Van Santen, P., Augustinus, P. G. E. F., Janssen-Stelder, B. M., Quartel, S., and Tri, N. H. (2007). Sedimentation in an estuarine mangrove system. *Journal of Asian Earth Sciences*, 29(4):566–575.

Vionnet, C. A., Tassi, P. A., and Martín Vide, J. P. (2004). Estimates of flow resistance and eddy viscosity coefficients for 2D modelling on vegetated floodplains. *Hydrological Processes*, 18(15):2907–2926.

Wattayakorn, G., Wolanski, E., and Kjerfve, B. (1990). Mixing, trapping and outwelling in the Klong Ngao mangrove swamp, Thailand. *Estuarine, Coastal and Shelf Science*, 31(5):667–688.

Webb, E. L., Friess, D. A., Krauss, K. W., Cahoon, D. R., Guntenspergen, G. R., and Phelps, J. (2013). A global standard for monitoring coastal wetland vulnerability to accelerated sea-level rise. *Nature Climate Change*, 3:458.

White, B. L. and Nepf, H. M. (2007). Shear instability and coherent structures in shallow flow adjacent to a porous layer. *Journal of Fluid Mechanics*, 593:1–32.

White, B. L. and Nepf, H. M. (2008). A vortex-based model of velocity and shear stress in a partially vegetated shallow channel. *Water Resources Research*, 44(1).

Winterwerp, J. C., Erftemeijer, P. L., Suryadiputra, N., Van Eijk, P., and Zhang, L. (2013). Defining eco-morphodynamic requirements for rehabilitating eroding mangrove-mud coasts. *Wetlands*, 33(3):515–526.

Wolanski, E. (2001). *Oceanographic Processes on Coral Reefs: Physical and Biological Links in the Great Barrier Reef*, volume 22.

Wolanski, E., Huan, N. N., Dao, L. T., Nhan, N. H., and Thuy, N. N. (1996). Fine-sediment dynamics in the Mekong River estuary, Viet Nam. *Estuarine, Coastal and Shelf Science*, 43:565–582.

Wolanski, E., Jones, M., and Bunt, J. S. (1980). Hydrodynamics of a tidal creek - mangrove swamp system. *Aust. J. Mar. Freshwater Res.*, 31(4):431–450.

Wolanski, E., Mazda, Y., King, B., and Gay, S. (1990). Dynamics, flushing and trapping in Hinchinbrook channel, a giant mangrove swamp, Australia. *Estuarine, Coastal and Shelf Science*, 31(5):555–579.

Woodroffe, C. (1992). Tropical mangrove ecosystems. *Coastal and Estuarine Studies*, 41:7–41.

Xiaohui, S. and Li, C. W. (2002). Large eddy simulation of free surface turbulent flow in partly vegetated open channels. *International Journal for Numerical Methods in Fluids*, 39(10):919–938.

Zong, L. and Nepf, H. (2010). Flow and deposition in and around a finite patch of vegetation. *Geomorphology*, 116(3-4):363–372.

Chapter 3

Exchange processes in vegetated compound channels

All of physics is either impossible or trivial;
It is impossible until you understand it, and then it becomes trivial.

Ernest Rutherford

The impact of vegetation on the hydrodynamics of channels with vegetated floodplains has been well recognised. The occurrence of large horizontal coherent structures at the channel-vegetation interface is of primary importance regarding the flow and catchment of sediment and nutrients in the vegetation. However, in a compound channel, the presence of vegetation, coherent structures, their interactions and effects on the exchange processes between the open channel and the adjacent floodplain is still not well examined. A unique laboratory experiment of a vegetated compound channel mimicking estuarine mangroves has been conducted. The results show that in a compound vegetated channel with a very gentle slope, the vegetated shear-layer dynamics resembled that associated with vegetation rather than that associated with a depth differential. Furthermore, the flow field under the effect of the large horizontal coherent structures (LHCSs) shows a spatially and temporally cycloid motion. Sweeping flows induced by LHCSs penetrate into the vegetation region, interact with the cylinder arrays, disturb the slow flow region, significantly decelerate and even become stagnant and reverse, before ejecting from the cylinder arrays at the end of the cycle. Consequently, the coherent structures can have an influence on a broader area than the vegetation area into which the eddy structures can penetrate. In terms of the exchange processes, the momentum transfer and the intensity of transverse fluctuations induced by the LHCSs can be related to this phenomenon. It is shown that decreasing the floodplain width can significantly affect the pattern of the LHCSs and thereby changing the shear-layer, creating unfavourable conditions for sedimentation inside forests and for river bank stability.

A modified version of this chapter is under review as Truong, S.H., Uijttewaal, W.S.J., and Stive, M.J. Exchange processes induced by large horizontal coherent structures in floodplain vegetated channels.*Water Resource Research*. (2018).

In this chapter of the thesis, a physical modeling of the compound channel, with and without vegetation, mimicking the estuarine mangrove at the MES was conducted. The experimental results were analyzed, revealing the physical aspect of the *squeeze* hypothesis.

3.1 Introduction

ALong the Mekong estuaries, mangroves have rapidly been destroyed, largely due to conversion into fishponds. The mangrove areas remaining have been squeezed into narrow strips often as small as 50 m. Riverbanks at those locations are usually suffering from erosion with an average rate of $3\,\mathrm{m\,yr^{-1}}$. Phan et al. (2015) and Truong et al. (2017) recently strengthened the hypothesized correlation between coastal and estuarine mangrove squeeze and shore or bank erosion respectively for the Mekong Delta with the explicit condition that they considered regions where sediment availability is not a restriction. It is hypothesized that a critical minimum width of the mangrove areas is required for the survival of the ecosystem, whether the impacts come from natural causes, such as increasing relative sea-level rise or from human activities, such as spatial squeeze, these causes are highly similar in terms of impact. In a physical sense, active energetic processes require physical space to be able to absorb erosive forces and subsequently restore the impact. Mangroves need these conditions as well to be able to follow a bio-cyclic evolution.

In the estuarine mangrove squeeze areas, the forest width is usually observed to be between about 50 and 600 m, which is small compared to the width of the main channel (about 1000 to 2000 m). Under these conditions, the presence of lateral tidal creeks in those areas is hardly observed and can be ignored. The main interaction is the lateral exchange through the mixing layer between the main river channel and the vegetated floodplain region. In this sense, the hydrodynamics of a mangrove forest is similar to that of a vegetated channel (Mazda et al., 1997; Truong et al., 2017).

Many researchers have studied the flow field and exchange mechanisms in straight and meandering, vegetated and non-vegetated channels, with or without the consideration of a floodplain. In recent decades, the large horizontal coherent flow structures (LHCSs) which are very large compared to the length scale of water depth and caused by the Kelvin-Helmholtz (KH) instability formed at the interface of the low flow and fast flow region have been identified to play a significant role in the lateral momentum exchange (Nadaoka and Yagi, 1998; Nezu and Onitsuka, 2001a; Tamai et al., 1986; van Prooijen et al., 2005; White and Nepf, 2007, 2008; Xiaohui and Li, 2002; Zong and Nepf, 2010).

In non-vegetated compound channels, the presence of the LHCSs is mainly associated with the water depth differences between the floodplain and the open channel region. Based on experiments with transversely steep change in depth and by changing the ratio of the floodplain depth to the main channel depth (D_r) as well as the channel geometry, Knight et al. (2007) suggested that LHCSs on unvegetated floodplains along compound channels are induced by a shear instability and mostly appear where D_r is less than 0.344. As the depth ratio increases ($D_r > 0.344$), the large coherent structures appear less pronounced, and intermittent boils become stronger (Nezu et al., 1999).

However, in a vegetated compound channel, the situation is more complex. Vegetation not only adds to friction, turbulence and drag forces but also restricts the flow space, resulting in interactions between flow and vegetation in different areas, *i.e.* within the canopy or at the interface, which also creates a change in length scales. On the one hand, drag forces induced by vegetation make the velocity difference between slow and fast flow regions significantly larger. This makes it possible for the LHCSs to become more pronounced and stronger. Hence, even in the case of D_r larger than 0.344, large coherent structures in the case of floodplain vegetation can still be observed (Knight et al., 2007). On the other hand, the presence of vegetation contributes enormously to the blocking of the LHCSs inside the forest, inhibiting their evolution. These two processes are coupled, but oppose to each other. By dividing the mixing layer into two different zones, each of which has its own length scale, a new approach has been proposed by White and Nepf (2008). Their model makes it possible to estimate the penetration level of the LHCSs into the vegetated region and should be considered the most up-to-date model for a vegetated channel. However, this model is based on only one set of flume experiments with rigid circular cylinders (Nepf, 2012), and the presence of more shallow floodplains was not considered. Whether this model is generically valid is yet to be determined.

Table 3.1: Some previous experiments with similar configuration

No	Experiment Overall	Author	Year	Feature		
				Vegetation	Floodplain	HCS
1	Compound channel	Knight and Demetriou	1983	N	Y (vertical)	N
2	Overbank flow with vegetated floodplain	Pasche and Rouve	1985	Y	Y (1:1.5)	N
3	Large Eddies in compound channel	Tamai et al.	1986	N	Y (vertical)	Y
4	Flow in main channel and floodplain	Keller and Rodi	1989	N	Y (vertical)	N
5	Turbulent measurements in shear layer-compound channel	Shiono and Knight	1988,1989,1990,1996	Y	Y (1:1)	Y
6	Drag, turbulence and diffusion through emergent vegetation	Nepf	1999	Y	N	N
7	2D solution for straight and meandering flow	Ervine et al.	2000	N	Y (1:1)	N
8	Turbulence structure in vegetated open channel	Nezu and Onitsuka	2001	Y	N	Y
9	Confluence experiment; Compound Channel	Van Prooijen,Uijttewaal and Booij	2000,2004, 2005	N	Y (1:1)	Y
10	Mangrove affect flow in a flume	Struve et al.	2003	Y	N	N
11	Large Coherent Structure in compound channel	Bousmar and Zech	2004	N	Y (vertical)	Y
12	Riprap vegetation on near bank turbulence	McBride et al.	2007	Y	Y (1:1)	N
13	Floodplain Vegetated Channel	Mazurczyk	2007	Y	Y (1:1)	N
14	Vegetated Channel	White and Nepf	2007, 2008	Y	N	Y
15	Vegetated channel -Mean Drag	Tanino and Nepf	2008	Y	N	Y
16	Vegetated Channel -sediment	Zong and Nepf	2009	Y	N	Y
17	Emerged vegetation in compound channel	Jahra et al.	2010-2011	Y	Y (vertical)	N
18	Discharge prediction compound channel	Lambert and Sellin	2010	N	Y (vertical)	N
19	Turbulent kinetic energy in compound channel	Kozioł	2011	Y	Y (1:1)	N
20	Vegetated Channel – flexible plant	Siniscalchi et al.	2012	Y	N	Y
20	Vegetated Channel	Buckman	2013	Y	N	Y
21	Vegetated floodplain channel	Hamidifar and Omid	2013	Y	Y (vertical)	Y
22	Vegetated floodplain channel	Fernandes et al.	2014	Y	Y (vertical)	N
23	Flow structure in vegetated channel	Yan et al.	2016	Y	N	Y
24	Mixing layer development in compound channel flows	Dupuis et al.	2017	Y	Y (vertical)	Y

A vegetated floodplain channel with gentle slope is more natural than a vegetated channel with constant depth or a vegetated floodplain channel with steep or vertical slope which were studied in previous studies. It is known that sediments tend to accumulate more inside the vegetated regions than outside of vegetation (Vargas-Luna et al., 2015). This means that the vegetated regions are usually more elevated than the adjacent areas. In other words, an elevated floodplain appears to create a more natural profile for a vegetated channel than a constant depth (Figure 5.1). In previous studies (Table 3.1), when taking into account the presence of a floodplain, the transition slope of the floodplain is usually as large as 1:1 (FCF experiment data - Knight and Shiono (1990, 1996); Sh-

iono and Knight (1988, 1989, 1990)) or 1:0.9 (Ikeda et al. (2000)). However, in the Mekong Delta Estuary (MDE), the situation is slightly different. The transition areas between the floodplain and the open main river have a very gentle slope of around 1:10. As the transition space from the main channel to the floodplain increases, the flow field has more space to adjust the fast flow in the open channel to the slow flow inside the vegetation. The mixing layer and its penetration into the floodplain are likely to be affected.

Moreover, it is important to note that all studies mentioned above only focused on wide vegetation regions, where the forest width is not a limiting factor and is always much larger than the lateral over-bank flow region. However, in reality, for example along the Mekong Delta estuaries, shrimp farms have increasingly been constructed, pushing mangrove forests into narrow strips. In this context, it is unknown how the flow field, as well as the LHCSs, respond to changes of the forest width and how this so called squeeze effect (Truong et al., 2017) affects the exchange processes. Furthermore, the exchange processes were studied only in the context of the sweep and ejection events, created as the LHCSs move along the interface (White and Nepf, 2007). The transition period between these two successive events, *i.e.* when a sweep is followed by an ejection has received little attentions and thereby, the role of this transformation period on the exchange processes in a vegetated compound channel is unknown.

3.2 Objective

IT is to see that although a number of studies have focused on the hydrodynamics of a floodplain vegetated channel, the flow field and related exchange processes are still unclear, especially in the natural cases of a gentle floodplain slope and squeeze conditions, *i.e.* the conditions in which the width of the vegetation is restricted (Truong et al., 2017). Therefore, the main goals of this chapter are: to (1) evaluate the role and the effects of emerged vegetation on the hydrodynamics of a vegetated floodplain channel with a gentle transition slope, (2) to understand the effects of the LHCSs on the flow field and their related exchange processes; and (3), to relate these investigations to the squeeze effect.

Physical modelling was chosen as a major approach. The experimental setup and measurements are described in the next section. After that, the effects of vegetation are studied by comparing results in similar scenarios, with and without vegetation. Then, the significant role of the LHCSs is described, in relation to the peculiarities of the complex flow field. Finally, the squeeze effect in relation to the width of the forest is shown to play a role as it can directly affect the flows induced the LHCSs.

3.3 Experiment setup and measurements

THe experiment was conducted in a shallow, free-surface flow flume of the Fluid Mechanics Laboratory at the Delft University of Technology. The flume is 20 m long, 3 m wide and the maximum water depth is 0.2 m. For the experiments, the width of the flume was reduced to 2 m. The average water depth-width ratio is about 1:20 and the

depth-length ratio is about 1:130, creating a sufficiently shallow flow (Jirka and Uijttewaal, 2004).

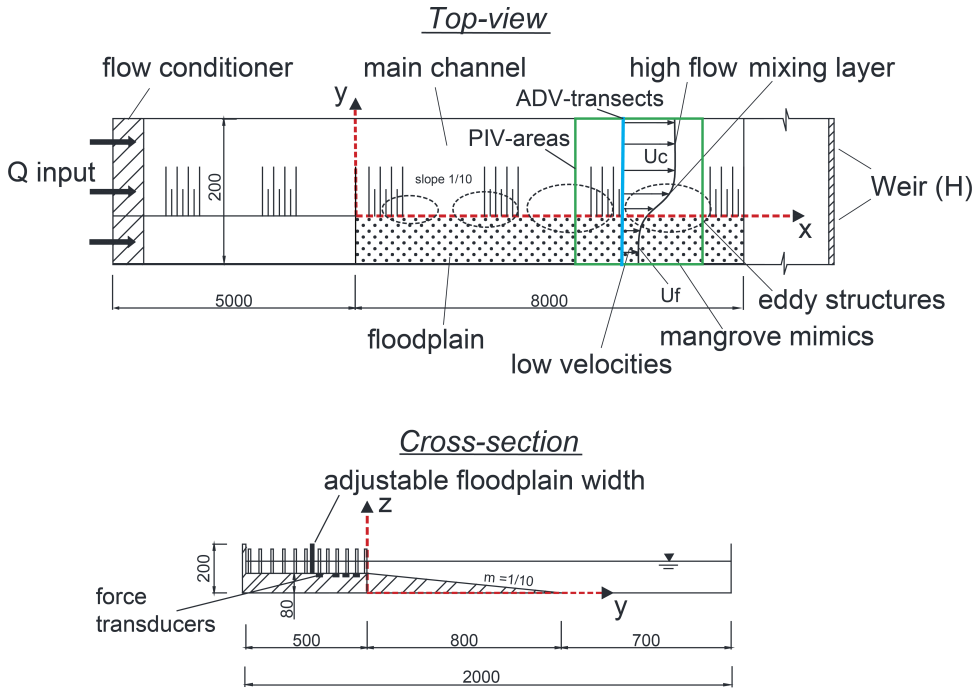

Figure 3.1: Schematic view of the experiment set up (units in mm), the presence of large coherent structures in the flow field. Not to scale.

Figure 3.1 gives a top view and a cross-section of the experimental setup and sketches some flow features observed during the experiment. The floors of the main channel, the slope and the floodplain area consist of glass, concrete and smooth plastic respectively. The sidewalls are all of glass. The cross-sectional profile includes a gentle floodplain slope 1:10 that mimics a typical riverbank slope as found at the Tieu estuary in the Mekong Delta. The squeeze phenomenon will be approached by varying the floodplain width to a small value such that the ratio of floodplain width and channel width $B_f/B < 1/10$. At straight stretches, the rivers usually have two floodplains along both sides of the main channel; however, typically the width of the river is large (1000 to 2000 m) compared to the width of the floodplain (50 to 100 m). This condition justifies the assumption that there is no interaction between the two riverbanks. Hence, the present experiment deployed a single floodplain only.

Water depth and total discharge could be changed by means of a pump and a downstream sharp-crested weir. Upstream from the inflow section, behind the flow straightener, a thin foam board was placed floating on the water surface to suppress small water surface oscillations. Some representative values of the flow quantities are: water depth in test section $H = 11.9\,\text{cm}$; discharge $Q = 45\,\text{L s}^{-1}$; the uniform velocity in the main channel $U_c = 32.15\,\text{cm s}^{-1}$; the uniform velocity in the floodplain $U_f = 20.87\,\text{cm s}^{-1}$ (no vege-

tation), and bottom friction coefficient $c_f = 0.0027$.

The bottom friction parameters were determined separately for the main channel ($c_{f,c}$) and for the floodplain ($c_{f,f}$) according to the formula used by Uijttewaal and Booij (2000) and Chu and Babarutsi (1988): $\frac{1}{\sqrt{cf}} = \frac{1}{k}\left(\ln\left(\mathrm{Re}\sqrt{cf}\right) + 1.0\right)$. In which k is von Karman constant (0.4), and Re is the local Reynolds number. The bottom friction coefficient was then determined according to $c_f = \frac{c_{f,f}+c_{f,c}}{2}$ to represent for the current scenario. With this flume configuration, a large Reynolds number (62,000) can be reached at moderate Froude numbers (0.58). In cases with vegetation (dense cases), the representative values are: water depth $H = 12.2\,\mathrm{cm}$; discharge $Q = 45\,\mathrm{L\,s^{-1}}$; $U_c = 35.58\,\mathrm{cm\,s^{-1}}$; $U_f = 2.14\,\mathrm{cm\,s^{-1}}$.

In order to obtain a proper similarity between the experimental set up and the practical situation of estuarine mangroves, the Reynolds number is also considered. In practical situations, a representative mean velocity measured inside the mangrove swamp is the order of magnitude of $0.02\,\mathrm{m\,s^{-1}}$ (Horstman, 2014) and the representative water depth is the order of magnitude of 0.1 to 0.5 m (Truong et al., 2017). This means that a Reynolds number is the order of magnitude of 1000 to 10000. In the experiment, the Reynolds number in the cylinder arrays was kept as large as possible , in the range of 1000 to 7500, which can be considered to be similar to the real situation. The Froude number is also kept as small as possible (in the range from 0.3 to 0.6) in order to make sure that the variations in the flow do not affect the water surface.

The presence of "mangrove" in the experiment was mimicked based on the "solid volume fraction" of the mangrove. The solid volume fraction is the relation between the total volume of the plants (V_p) and the control volume (V): $\Phi = V_p/V = 1 - n$ for emerged cylinders, the solid volume fraction per unit volume can be then estimated: $\Phi = N \cdot \pi \cdot d^2/4$, where n is the porosity of the plants, d is the diameter of a stem and N is the density of mangroves. In reality, the solid volume fraction of *S.Alba* in the sparse case can be estimated of to be 0.04, including both stems ($d = 0.3\,\mathrm{m}, N = 0.5\,\mathrm{m^{-1}}$) and roots ($d = 0.02m, N = 25\,\mathrm{m^{-1}}$) (Ranasinghe et al., 2010; Truong et al., 2017). The density of the cylinder arrays then was determined based on the "solid volume fraction" of *S.Alba*. Following the configuration in Figure 3.2, the number of cylinders ($d = 0.01\,\mathrm{m}$) per square meter is 556 and 139, yielding a solid volume fraction value of 0.04 and 0.01 respectively. The cylinder diameter was kept relatively large in order to keep the Reynolds number based on this diameter sufficiently large. In this way, the densest scenarios in the experiment are similar to the sparse cases of mangroves in reality.

Because of the water depth difference between the floodplain and the main channel, the flow over the shallower floodplain is slower than in the deeper main channel. As a consequence of this velocity difference, a mixing layer develops between the floodplain and the channel. In shallow water over a flat bottom, the bottom friction affects the mixing layer as it decreases the velocity differences and the KH instability develops downstream (Uijttewaal and Booij, 2000). The transverse depth difference sustains the velocity difference and the bed friction limits the growth of the mixing layer. As the mixing layer develops, it achieves a constant width after 7 to 8 m in comparable laboratory case with depths < 0.1 m such as a confluence with different velocities (Uijttewaal and Booij, 2000), 7.5 m in cases of a compound channel profile (Fernandes et al., 2014), and about 4 m in cases of a partly vegetated channel profile (White and Nepf, 2007). In the

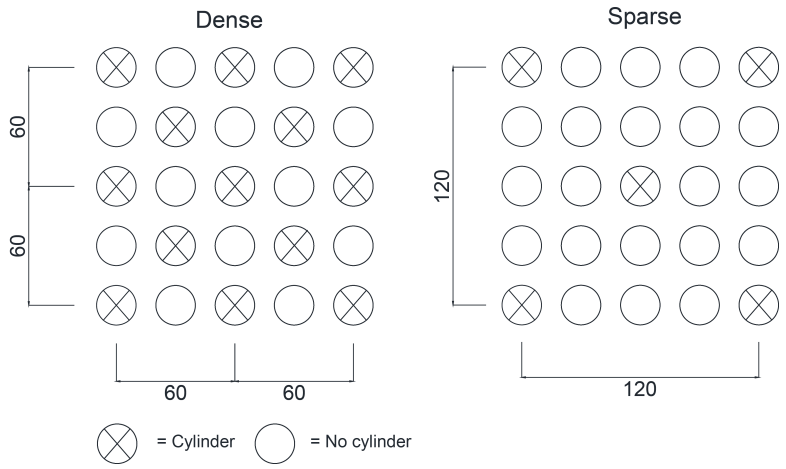

Figure 3.2: Staggered distribution of the cylinder arrays (units in mm) representative for the dense and sparse scenarios.

present experiments, in order to ensure the velocity measurements were taken at the location where the mixing layer is fully developed, an Acoustic Doppler Velocity meter (ADV) was placed at 10 m downstream from the floodplain starting point. This means that in cases with the presence of vegetation, the ADV was located at 5 m from the first row of cylinders. It was checked that at this location, a fully developed flow field can be safely achieved despite the slight non uniformity due to the horizontal bed and the sloping free surface(see Figure 3.3).

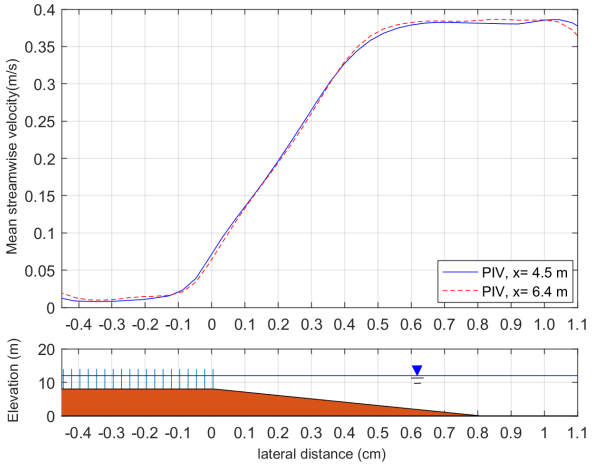

Figure 3.3: A representative comparison of mean streamwise velocity measured from PIV between locations $x = 4.5$ m and $x = 6.4$ m.

As the water free surface is considered to not vary much over the cross-section, both

the stream in the floodplain area and in the main channel are subject to the same forcing from the free surface water slope. The velocity was measured using a Nortek Acoustic Doppler Velocity meter (ADV) at a sampling rate of 25 Hz. Velocity measurements were taken over a time interval of 10 minutes in order to achieve representative statistical data. Besides, in order to obtain a good particle seeding in the flowing water, an electrolyzer with 0.1 mm thick wires was placed about 15 cm ahead from the ADV. Very small oxygen bubbles produced by the electrolyser significantly improved the quality of the ADV signal. In the experiments, the correlations are larger than 85-95%, and the dimensionless signal-to-noise ratios (SNR) exceed 18 dB in all measurement scenarios. In order to eliminate the formation of calcium carbonate, the electrolyzer was cleaned every two hours. The final data were collected applying Nortek software for the Vectrino. With the purpose of capturing a velocity profile over the cross-section, in the slope region with changed water depth, at least 10 points were taken at mid-depth, while in the region with constant water depth, at least three points were to be measured.

Particle Image Velocimetry (PIV) was used to measure the movement of flow. In order to achieve sufficient contrast between the particles and the flume bottom, floating black polypropylene tracer particles with a diameter of around 2 mm were used. Besides, the flume bottom at the capture area was also painted with high contrast white paint. In the present experiments, a sampling frequency of 10 Hz was used. A RedLake 1 MegaPixel digital camera with a resolution of 1008 x 1018 pixels has been used to capture frames and was installed on the very top of a frame build on a movable platform constructed over the flume. In order to minimize distortion effects, the digital camera was carefully directed vertically downward. For each measurement with a different water level, a careful check of image distortion was employed. In order to capture most of the features of the water surface flow, a large number of tracer particles was used (Muste et al., 2008). They are expected to follow the surface flow sufficiently well. Their distribution over the water surface was relatively homogeneous. A preprocessing step was applied to enhance the quality of the images. All images were subtracted from a representative background image in order to eliminate undesirable effects of the background information. Then all pairs of sequential camera frames were loaded in PIV Lab 1.4 software package and subsequently spatially correlated (Thielicke and Stamhuis, 2014). All sets of 2 consecutive particle-frames have been analysed. A two-stage square interrogation windows size of 128 pixels and 32 pixels respectively have been used with a spatial overlap of 50% in both x and y-direction. The measurement duration was 300 s. This means that with a 10 Hz frequency, 3000 frames were recorded for each case. The average particle displacement has been computed to acquire the instantaneous surface velocity fields.

Furthermore, direct measurement of the force on a single cylinder in streamwise direction was conducted to examine the drag coefficient C_d. Four sensitive force sensors were mounted under the cylinder located at different locations inside the vegetation region ($y = -0.18, -0.06\,\text{m}, -0.12\,\text{m}$, and $0\,\text{m}$).

Following the setup described above, experiments have been performed for scenarios with different discharges, water depths and floodplain widths (Table 3.2). The detailed settings can be found in the Table A.1 in the appendix. The role of vegetation, LHCSs, floodplain width and their corresponding effects on the flow fields in a compound channel with a gentle slope are the major interests and are analysed in terms of

the mean streamwise velocities, the Reynolds' shear stresses (RSs), the power density spectra (PDSs), and the auto correlation functions (R_{vv}) for configurations of different mangrove densities and widths. These values were determined from the data measurement according to their definitions (Pope, 2000; Uijttewaal and Booij, 2000). While the mixing layer properties can be determined from the mean streamwise velocity profiles, the RSs contain information regarding the momentum exchange between these regions.

Table 3.2: Experiment scenarios

ϕ	Density 1 (no vegetation)	Density 2 (sparse vegetation)	Density 3 (dense vegetation)
$Cylinder/\mathrm{m}^2$	0	139	556
$C_d \cdot a[\mathrm{cm}^{-1}]$	0	0.014	0.056
$Q_{input}[\mathrm{Ls}^{-1}]$	45, 60, 80	45, 60, 80	45, 60, 80
$H_{control}$[cm]	12,13,14 cm	12,13,14 cm	12,13,14 cm
Floodplain Width [m]	0,5 m ; 0.25m ; 0.1 m	0,5 m ; 0.25 m; 0.1 m	0,5 m ; 0.25 m; 0.1 m

3.4 Results

This section of the chapter presents the experimental results. The effects of vegetation in a compound channel with a gentle slope the floodplain on the shear-layer dynamics at the vegetation edge were evaluated by comparing scenarios with and without vegetation. The presence of LHCSs and their influences on the flow field were clarified in terms of their flow events. Furthermore, the transverse exchange of momentum was examined and area affected by the LHCSs are deduced. Finally, the squeeze effect *i.e* the changes in the hydrodynamics of a compound vegetated channel as a result of a decreased floodplain width was analysed.

3.4.1 Role of vegetation

The effect of vegetation on the flow field and turbulence structures is analysed by comparing the mean streamwise velocities, the Reynolds' shear stresses (RSs) and the power density spectra (PDSs) for different configurations, with and without vegetation. While the mixing layer and its penetration from the main channel into the floodplain can be determined from the mean streamwise velocity profiles, the RSs contain information regarding the momentum exchange between these regions. Besides, the PDSs contain information regarding the distribution of the turbulent kinetic energy over the range of frequencies.

The influence of vegetation on decreasing the flow inside the floodplain can be clearly recognized. In the cases of a non-vegetated floodplain channel (Figure 3.4a), the velocity profiles can be divided into three main regions closely corresponding to their water depths, which are the floodplain area (from $y = -0.5$ to 0 m), the main channel (from $y =$ 0.8 to 1.5 m) and the transition area (from $y = 0$ to 0.8 m).

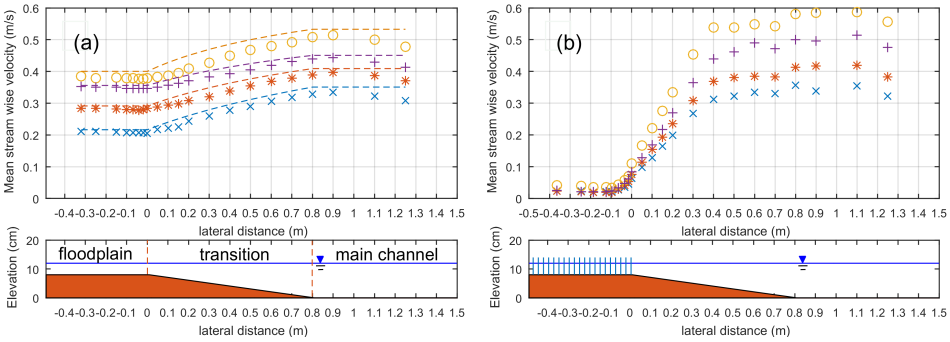

Figure 3.4: Scenarios for a 50 cm wide floodplain with no cylinders (a) and densely placed cylinders (b) configuration for different discharges and water levels. Legend qxxhyy refers to a discharge of xx l/s and a water depth of yy cm. Crosses: q45h12 , stars: q60h13, plusses: q80h14, circles: q80h12. Dashed lines in (a) correspond to the water depth fraction $gS_oD(y)/C_f$ of the same scenarios.

In all cases with a 0.5 m floodplain width, from the main channel towards the floodplain, the mean streamwise velocity gradually reduces over the transition slope region. Laterally-uniform values of the mean streamwise velocity are achieved right at the floodplain edge (location $y = 0$ m in Figure 3.4a). This implies that the penetration of the main stream momentum into the floodplain region is zero. As the discharge and water depth increase, the order of magnitude of the mean streamwise velocity also increases. However, the penetration of the mixing layer into the floodplain region does not increase and the velocity gradient remains almost the same. If the transverse exchange is small in the mixing layer, the governing momentum equation can be written as: $-gS_o \approx -\frac{1}{2}\overline{u}_d{}^2\left(\frac{C_f}{D}\right) \Leftrightarrow \overline{u}_d{}^2 \approx \frac{gS_oD}{C_f}$. where $\overline{u}_d$ is a time and depth-averaged streamwise velocity, $D(y)$ is Water depth, S_o is pressure gradient term and C_f is bed friction coefficient. As the water slope is the same along the cross-section, the time and depth-averaged streamwise velocities are approximately proportional to the ratio between the water depth and the bottom friction. The results of Figure 3.4a confirm this.

With vegetated floodplain channels (Figure 3.4b), it is observed that the presence of cylinders boosts the magnitude of the velocity gradient about 4 times, from around $0.2\,s^{-1}$ in scenarios without vegetation to $0.8\,s^{-1}$ in scenarios with vegetation. Instead of gradually decreasing, following the transition slope (from $y = 0.8$ to 0 m) as in the cases without vegetation, the mean streamwise velocity slowly reduces from the main channel before a sudden significant decrease at the location of 0.4 m (the middle of the transition slope). Also, a penetration of the shear-layer into the cylinder arrays of about 0.1 m can be observed through the lateral distribution of the mean streamwise velocity. A laterally-uniform value of the mean streamwise velocity is maintained at locations $y < -0.1$ m. The strong presence of the large horizontal coherent structures induced by the presence of vegetation is the main reason for these differences of the penetration of the shear-layer into the floodplain region. Furthermore, although the velocity gradient across the vegetated floodplain edge increases with the increase of the discharge, the mean streamwise velocity and the penetration of the shear layer into the canopy remain unchanged.

Solely in the regions where there are no cylinders, including transition slope and main channel, the mean streamwise velocity was significantly affected.

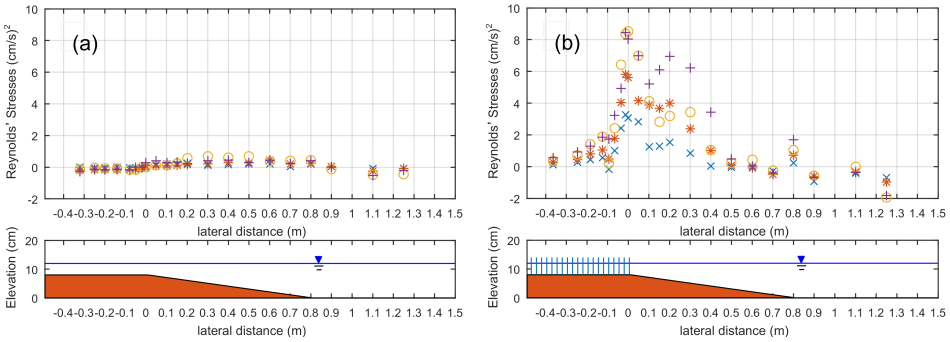

Figure 3.5: Reynolds shear stress ($-\overline{u'v'}$) no cylinder cases (a) and dense cases (b), 50 cm width; different input discharge and water level. Legend qxxhyy refers to a discharge of xx l/s and a water depth of yy cm. Crosses: q45h12 , stars: q60h13, plusses: q80h14, circles :q80h12.

Figure 3.5 show the transverse profiles of the Reynolds' Stresses (RSs) ($-\overline{u'v'}$) in different scenarios with and without the cylinders. The positive values of the RSs indicate that the momentum is transferred towards the floodplain area. Increasing the input discharge Q and water level H does increase the RSs. In cases without vegetation, the maximum values of RSs are located around the middle ($y = 0.4$ m) of the transition region (from $y = 0$ to 0.8 m). This means that the momentum exchange happens mostly at this location. However, in cases with vegetation, the maximum value of RSs significantly shifts towards the vegetation edge (location $y = 0$ m). The results also show that the magnitude of the RSs in the cases without vegetation is quite small relative to that in cases with vegetation by an order of magnitude. This demonstrates the role of vegetation in drawing greater momentum flux towards the floodplain vegetation region.

In order to obtain more insight into the distribution of the turbulent kinetic energy, the time-varying components have been analysed in the frequency domain. The presence of the LHCSs at the channel-vegetation interface and the influences of vegetation on their characteristics can be clearly identified in the PDSs of the lateral fluctuation velocity v' at different locations along the cross-section Figure 3.6. The results suggest that in cases without and with vegetation, there is a definite peak region in the power density spectrum typically in the range of 0.05 Hz to 0.1 Hz, corresponding to an eddy period of 10 s to 20 s, but with much higher amplitude with vegetated case.

In cases without vegetation (Figure 3.6a), although only around the floodplain edge (y=0 m), peaks can be recognized at the frequency of around 0.07 Hz corresponding to 14 s period structures. The signals of the presence of large coherent structures are generally weak and hardly observed. Inside and outside the floodplain, the decrease of PDSs approximately follows the $-5/3$ slope that is known from flows with a large inertial subrange.

In cases with vegetation (Figure 3.6b), there is a definite peak region in the power density spectrum. The high-frequency side of the peak has a slope of approximately -3

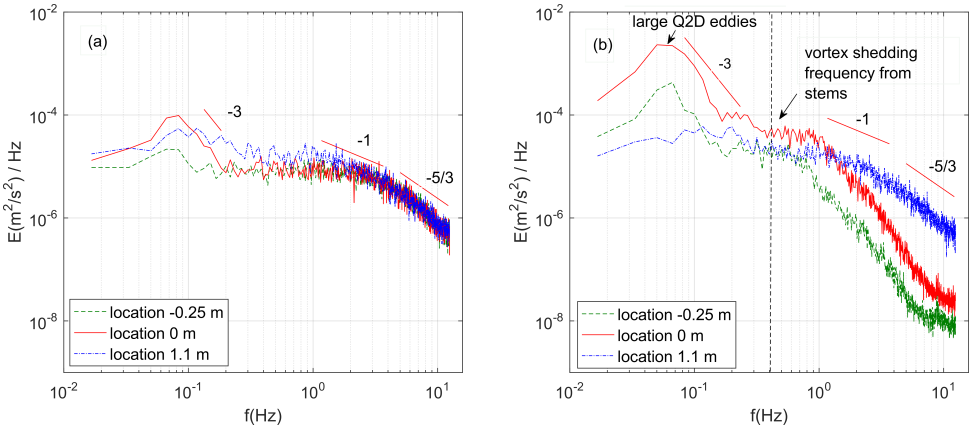

Figure 3.6: Power density spectra of lateral velocity fluctuations at different locations from the wall – No and Dense vegetation scenario, 50 cm width, discharge =45 l/s, water level =12 cm; y= -0.25 m located inside the vegetation, y=0 m located at the vegetated floodplain edge, y=1.1 m location outside in the main channel.

indicating the large turbulence structures possess two-dimensional characteristics (Uijttewaal and Booij, 2000). These peaks with slope -3 can be clearly distinguished in the PDSs at a frequency in the range of 0.05 Hz to 0.1 Hz, corresponding to an eddy period of 10 s to 20 s. The energy density then seems to follow a -1 slope character (Nikora, 1999; Perry and Li, 1990), which indicates that the large structures no longer possess the two-dimensional characteristic. This can be explained by the effect of the bottom friction in the floodplain region. The peaks have virtually disappeared at location 1.1 m. This implies the disappearance of the LHCSs at that position. It can also be seen that the LHCSs in cases with dense vegetation are stronger, more pronounced and contain more energy than in cases without vegetation.

At the high-frequency side of the spectra, a gradual decrease of the energy density can also be observed. However, it is observed that there are differences in the high-frequency regions of the energy density at locations inside and outside the vegetation regions. The decrease in energy density at the locations outside the floodplain region (1.1 m) almost follows a slope -5/3 that is indicative of flows with a large inertial sub-range. Inside the floodplain region ($y = -0.25m$ and $y = 0m$), the decrease of the energy density does not properly follow this rule. This is possibly due to the effect of the vortex shedding associated with the wakes behind the stems. Because of the presence of the vegetation, between the cylinder arrays, the large turbulence scale structures are more quickly transformed into smaller scale turbulent structures. Estimating the Strouhal number to be about 0.2 for flow around a circular cylinder (Sumer et al., 2006), the frequency of vortex shedding in this scenario is derived from being approximately 0.4 Hz ($T = 2.5$ s) (Figure 3.6b).

Together with the PDSs of v', Figure 3.7a and b shows the Cross Power Energy Density Spectra (CPEDSs) using u' and v' data measured at a single point located in the vegetated floodplain (location $y = -0.065m$) and at the floodplain edge ($y = 0m$) inside the mixing layer. It can be seen that the peaks in the $u'v'$ spectra reach their maximum at the almost

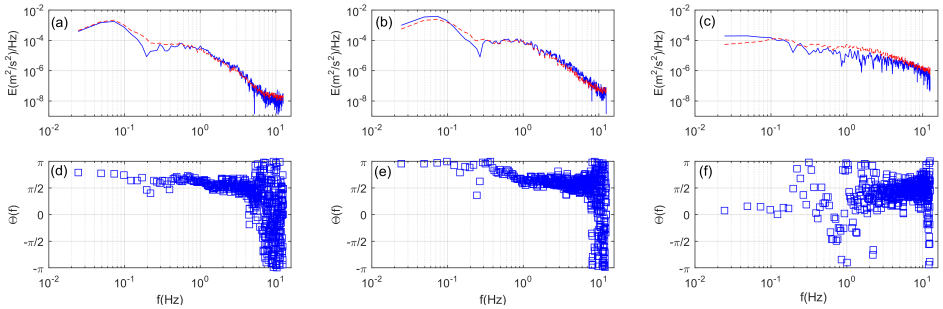

Figure 3.7: Dense case – Cross Power density spectral, case 50 cm width, and discharge = 45 l/s, water level =12 cm: location y=-0.065 m (inside the vegetation) (a) , location y =0 m (at the edge) (b) and y= 1.1 m (in the main channel) (c) - Blue line (u'v' spectrum); Red line (v' spectrum). The phase relation between u' and v': location y=-0.065 m (d), location y=0m (e) and y=1.1 m (f).

same frequencies as in the v' spectra. This demonstrates that the main contributions to the transferring momentum over the mixing layer are from the LHCSs. This feature cannot be observed at locations outside the mixing layer (location $y = 1.1m$) (Figure 3.7c).

In addition to the CPEDSs for the different frequency components, the phase relation between u' and v' has been determined (Figure 3.7d, e, f). It can be seen that the phase relation between u' and v' for the low frequencies yields a value of around $3/4\pi$ at location -0.065 m (in the vegetation, inside the mixing layer) and at the vegetated floodplain edge ($y = 0m$) (Figure 3.7d, e). At the higher frequencies, the phase angles are distributed randomly. The point beyond which the phase relation becomes random is directly linked to the position in the spectrum where small 3D turbulence prevails (Uijttewaal and Booij, 2000). Figure 3.7f shows the phase relation outside the mixing layer (location 1.1 m), indicating that the phase relation is much more random along the frequencies axes.

It is known that the exchange of mass and momentum between the open channel and the vegetated region is significantly connected to the phase relation between u' and v'. The exchange is maximized if u' and v' are in antiphase ($\theta = \pm\pi$). If $\theta = \pm\pi/2$, the inward and outward components are equal, but in opposite directions (Yossef and de Vriend, 2010). This means that the net exchange is almost 0. For locations near the vegetated floodplain edge (around $y = 0cm$), the phase difference between u' and v' yields values of around π . These phase relations reduce toward $\pm\pi/2$ when moving further outside the channel or inside the floodplain. This indicates that the maximum momentum exchange is happening at the vegetated floodplain edge location and continues to reduce further along two sides, toward the inner and outer sides of the mixing layer.

3.4.2 Role of Large horizontal coherent structures

The differences in the average streamwise velocities, RSs as well as PDSs described in the previous section are mainly due to the stronger presence of the LHCSs, especially in cases with vegetation. Therefore, it is necessary to study the LHCSs in more detail. The

presence of LHCSs, their associate flow events and the impacts of them on the flow field are the major interests of this part.

The presence of the LHCSs

A regular pattern of the LHCSs in the mixing layer can be identified through autocorrelation of the transverse velocity signals obtained by the ADV. Figure 3.8a and b show the representative profiles of the autocorrelation function of the transverse velocity signals at different locations in cases without and with vegetation, respectively. In cases with vegetation, it can be seen that at first the autocorrelation function decreases sharply down to 0.7, representing the smaller scales, three-dimensional effects in the turbulence spectrum. Then, the correlation falls off slower and its amplitude extrapolated to $t = 0$ indicates that the large coherent structures contribute about 60 - 70% to the total normalized turbulent kinetic energy. The effects of larger coherent structures are seen in the modulation of the auto-correlation function beyond this point.

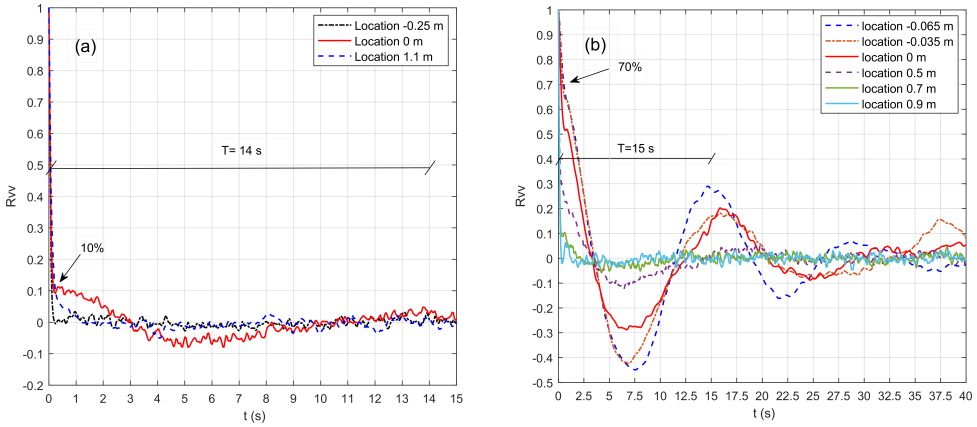

Figure 3.8: Autocorrelation function Rvv, 50 cm width, discharge =45 l/s, water level =12 cm; (a) No vegetation, (b) Dense vegetation.

By comparing the autocorrelation function obtained at different locations across the flume, it can be observed that the further away from the mixing layer, the smaller the modulation and the faster the decrease of the autocorrelation function. The strong modulation that remains significant for several tens of seconds is totally lost at location $y =$ 0.7 or 0.9 m. In this sense, the correlation shows no signs of large scale coherence structures. Besides, a clear transition can be observed at small values of t. This indicates the disappearance of the contribution of the small-scale turbulence for the locations close to the mixing layer. The major contributions are from the large-scale turbulence. The different time scales of the small- and large-scale turbulence, of the order of 0.1 and 20 s respectively, are noticeable. This demonstrates that the mixing layer contains on average much larger structures than the free stream outside the mixing layer. The characteristic time of the autocorrelation modulation is related to the width of the LHCSs (Uijttewaal and Booij, 2000). At location −0.065 m, a period of about 15 s is observed between peaks

at 0 and 15 s. The oscillation is greatly reduced beyond this point. This result is in line with the PDSs, as the period T of large coherence structures is about 16.7 s (Figure 3.7 a, b).

Nevertheless, these signals of the LHCSs are hard to recognize in cases without the vegetation (Figure 3.8 a). Quasi-two-dimensional structures contribute only to about 10% of the total normalized energy as the autocorrelation function at the floodplain edge falls off faster to around 0.1 after 0.1 s. The modulation can also be seen to be much weaker. This result demonstrates that the presence of vegetation does produce definitely stronger LHCSs in the compound channel.

The effects of the LHCSs on the flow field

In order to get an insight into how the LHCSs affect the flow field, it is necessary to understand the movement of the structures themselves. Although it is not always straightforward to visualize the LHCSs by simply looking at the velocity vector field in the PIV data set, the motion of the LHCSs along the vegetation interface leaves an important trace, which is the presence of stagnation areas moving along together with the LHCSs. Capturing these stagnation areas and their movement within the vegetated floodplain area in the instantaneous velocity field (Figure 3.9) reveals a cycloid motion.

As the large coherent structures move along the interface between cylinder arrays and the open channel, they create inflows, which we term sweeps ($u' > 0$, $v' < 0$). In the beginning, the sweeps accelerate outside the vegetation as the depth decreases in the transverse direction. However, when the sweeps enter the vegetation regions, due to the surrounding slow flow and the drag forces of the vegetation, they are strongly disturbed and decelerated significantly, even become stagnant and reverse direction before flowing out from the cylinder arrays through the ejection events at the end of the cycle. It is also observed that the regions where the flows are almost stagnant ($u, v \sim 0$), which are termed stagnation areas are found along the streamwise direction next to the LHCSs.

As the LHCSs move along the vegetation area, these regions of stagnation points appear, increasing local pressure which then can counteract the overall free surface water slope to becoming the main force driving the flow inside the vegetation reversing its direction. The transverse velocity is hindered by the vegetation and the vertical wall which according to the Bernoulli's principle lead to the elevated free surface at the stagnation points. This drives the reverse flows as it is apparently larger than the mean gradient from water slope. Further away from the stagnation areas, as this pressure becomes weaker, the reverse flow becomes weaker and its interaction with the streamwise flow creates other stagnation areas. In this way, to the extend the flow induced by the increased local pressure can reach, the surrounding areas are also affected by the LHCSs. Hence, the transverse distance affected by the LHCSs is larger than the distance in which the mean profile of the mixing layer can penetrate. Figure 3.9 confirms these analyses. It can be seen that the vegetation area affected by the LHCSs is of the size of around $0.35 - 0.4$ m which is about four times larger than the distance over which the mean streamwise velocity profile achieves its constant value (about 0.1 m) (Figure 3.4b).

In order to obtain further insight into this flow events, the data measured from the ADV were also combined in the analyses. The motion of the LHCSs along the interface of vegetation generates fluctuations in the time signal of the mean streamwise velocities

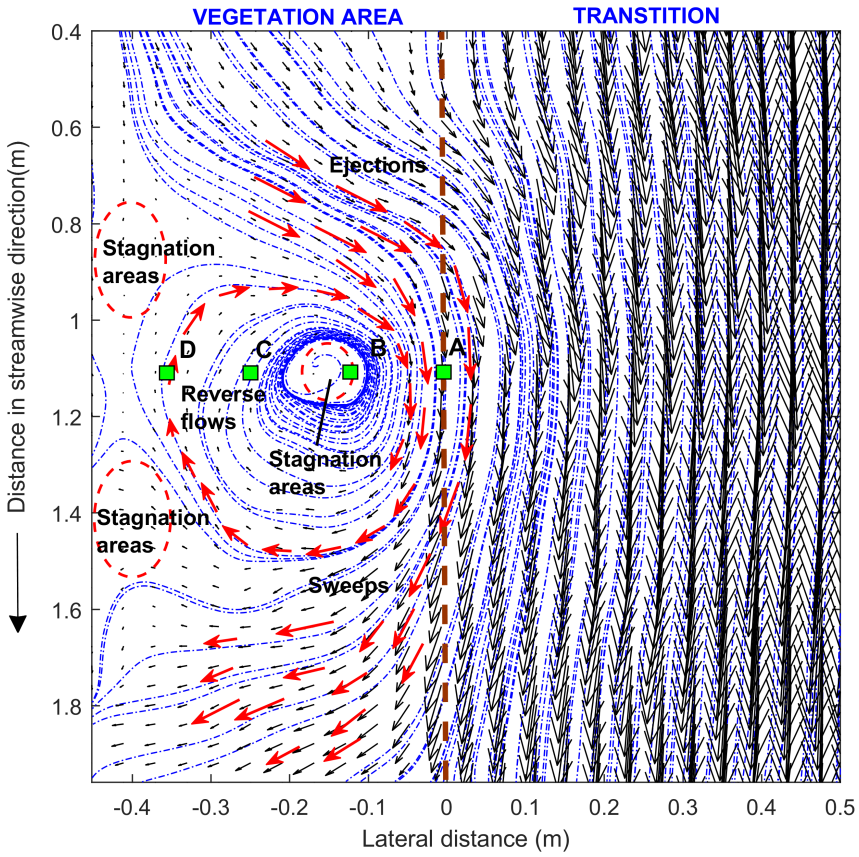

Figure 3.9: Representative ejections, sweeps, stagnation areas and reverse flows captured in instantaneous velocity field at free surface measured by PIV, case of dense density, 50 cm width, discharge Q : 45 Ls^{-1}, water level H : 12 cm (y<0 indicates regions inside vegetated floodplain). There are also four representative locations A (y=0 m), B (y=−0.125 m), C (y=−0.255 m) and D (y=−0.365 m) where the separate measured data from the ADV were employed to analyse the phenomenon. The red arrows and the stagnation areas illustrate experimental observations interpolated from the instantaneous streamlines (blue-dot lines) of the instantaneous flow field.

(u), lateral velocities(v) and their corresponding shear stress ($\overline{u'v'}$). The stagnation areas and reverse flow observed above can clarify the zero and negative values of the streamwise velocity signal measured by the ADV at locations B ($y = -0.125m$) , C ($y = -0.255m$) and D ($y = -0.365m$) inside the vegetation region (Figure 3.12 b, c, d). The negative values are hard to observe in the streamwise velocity signal at location A at the edge of floodplain (Figure 3.12 a). This means that the stagnation areas and reverse flow mainly occurs further inside the vegetation. It also can be seen in the Figure 3.12a that the sweep events corresponding to the peaks of the product $u'v'$ which indicate that the maximum

transverse momentum exchange occurs during these events. The product $u'v'$ is relatively small inside the vegetation at location B, C, D (Figure 3.12 b, c, d). Hence, the sweep events are hardly observed at this location. In this sense, the sweep and ejection events appear to dominate the edge region of vegetation, while the stagnation areas and reverse flows are likely to occur in the further inner region. The result also suggested that although the shear stresses are small inside the vegetation, the fluctuation of lateral velocity (v) is still large.

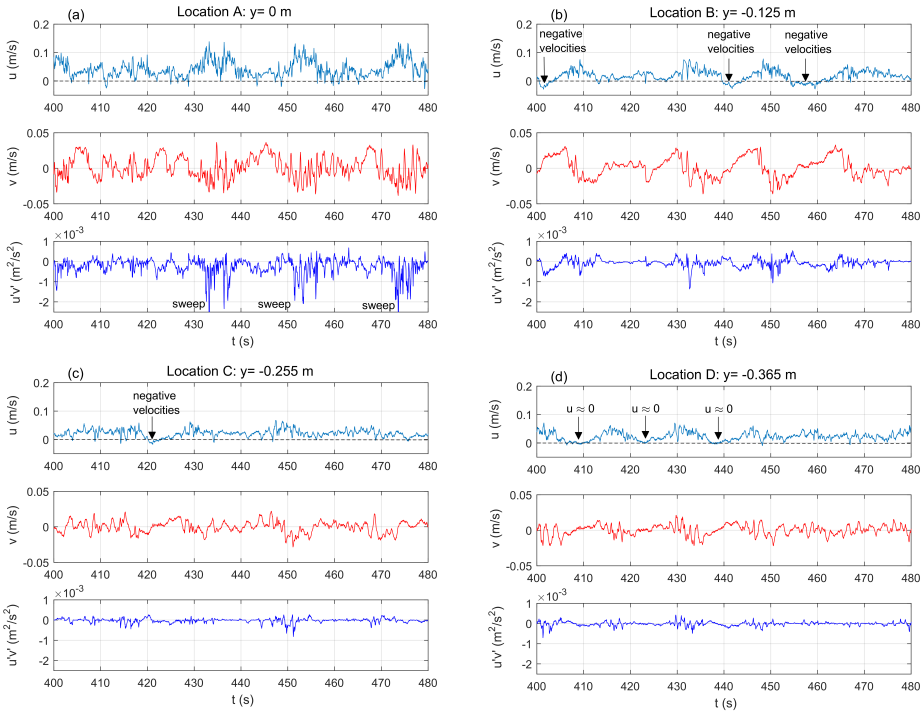

Figure 3.10: Time series of streamline velocity u (solid line), lateral velocity v (dash line) and the shear stress (u' v') (dot-dash line) at locations A: y=0 m (a) ; B: y = -0.125 m (b) ; C: y = -0.255 m (c) and D: y = -0.365 m (d) in case of dense vegetation, 50 cm floodplain width, discharge =45 l/s and water level =12 cm.

This implies that the influences of LHCSs on the flow inside vegetation can remain significant even when there is virtually an insignificant amount of momentum exchange induced by the LHCSs at this location. While the former is related to the lateral fluctuation velocity v' and thereby is proportional to the normal stresses $-\overline{v'v'}$, the latter is proportional to the Reynolds shear stresses (RSs=$-\overline{u'v'}$). A comparison between these two stresses (Figure 3.11b), along with the results of Figure 3.9 demonstrate that the region inside the vegetation affected by the LHCSs can be much larger than the area where the transverse momentum exchange induced by LHCSs can occur.

Furthermore, it is noted that as the LHCSs move, they cause velocity fluctuations resulting in the fluctuation of the forces (see Figure 3.12). The fluctuation is strongest at the floodplain edge and become weaker further inside the vegetation. The negative val-

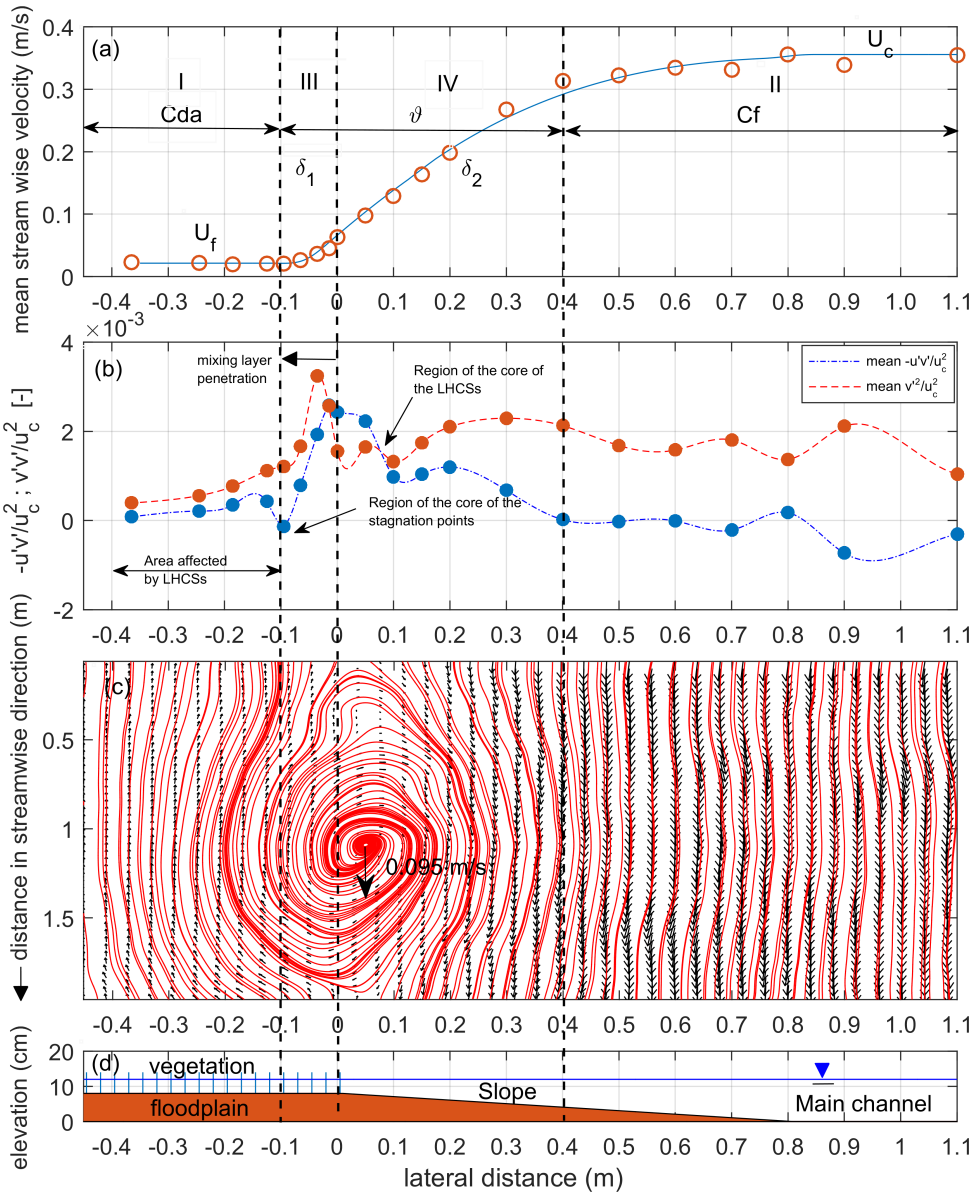

Figure 3.11: Representative Mean streamwise velocity in cases with vegetation (a). Representative comparison between the normal stresses and the Reynolds shear stresses in the vegetated compound channel induced by the LHCSs (b). The representative LHCSs captured through the streamlines of the instantaneous fluctuating velocity field and its corresponding effect on the mean streamwise velocity (c). Dense scenario, 50 cm floodplain width, discharge = 45 Ls^{-1}, water depth = 12 cm.

ues of the streamwise forces can also be clearly observed. These negative values caused by the stagnant and reverse flow events are not observed at the edge of floodplain. In this

context, it is suggest that the sweep and ejection events appear to dominate the edge region of vegetation, while the stagnation areas and reverse flows are likely to occur further into the vegetated region.

Figure 3.12a shows the distribution of measured streamwise stem forces F_x by box plots at these different locations. The mean value is given by the red line with the box

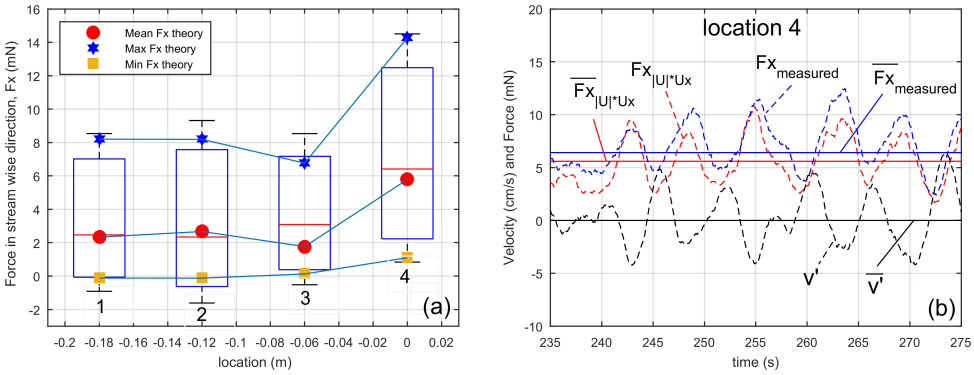

Figure 3.12: Representative distribution of measured stem forces on cylinder 1, 2, 3, 4 (location $y = -0.18\,\text{m}, -0.06\,\text{m}, -0.12\,\text{m}$, and $0\,\text{m}$), together with forces estimated from the theory, *i.e.* the forces estimated from measured streamwise velocity U_x combined with drag coefficient C_d equal 1 (a). Directly measured streamwise force, F_x on 4th cylinder (floodplain edge), compared with the forces estimated from the theory. Corresponding lateral velocity fluctuation also included (b). Sparse scenario, 25 cm floodplain width, discharge = $80\,\text{L s}^{-1}$, water depth = 14 cm.

indicating the 25th and 75th percentiles. The mean values of the streamwise forces based on the measured velocity U are also included in the figure (solid red circles). $F_{xtheory} = \frac{1}{2}\rho C_d dH|U|U_x$ where ρ is water density, C_d is drag coefficient and equal 1, d is the diameter of the cylinder, H is water depth, $|U| = \sqrt{U_x^2 + U_y^2}$ and U_x, U_y are the mean streamwise and lateral velocity inside the vegetation.

Figure 3.12b shows the time series of the streamwise force (F_x) measured on the 4th cylinder together with the predicted one ($F_{x,theory}$) and the lateral fluctuation velocity (v'). It is suggested that the force achieves its maximum value together with the minimum lateral fluctuation velocity ($v' < 0$). This indicates that the force on the cylinder is largest during the sweeps and smallest during the ejections. Furthermore, it is also suggested that a good estimation for the force on the cylinder can be achieved with the value of the drag coefficient C_d equal 1 combined with the local velocity.

It is noted from the Table 3.3 that there is a large difference between the values of the vegetation drag ($Cda_{measured}$) derived from a balance between total array drag and the pressure gradient due to the free surface slope (see (White and Nepf, 2008), $Cda_{measured} \approx -2gS/U_1^2$; where U_1 is the cross-sectionally averaged velocity within the vegetation array; and $S = dh/dx$ is the water slope) and that derived based on the theory ($Cda_{theory} = Cd_{theory} \cdot N \cdot d$; $Cd = 1$ proved by directly measured forces). This difference can be explained in terms of (1) the presence of reverse flows and stagnant flows which may reduced the averaged streamwise velocity inside the vegetation; (2) mean force is not propotional to the mean velocity squared ; and (3) the uncertainty in the measurement

of the water slope which is about 20%. This difference can be improved using $Cda_{|U|Ux} = \frac{-2gS}{\sqrt{U_x^2+U_y^2}\cdot U_x}$.

Table 3.3: A comparison of the vegetation drag

	White and Nepf (2007)		Current study	
Φ	0.02	0.045	0.01	0.04
$N(number/m^2)$	603	1356	137	550
$d(m)$	0.0065	0.0065	0.01	0.01
Cda_{theory}	0.039	0.088	0.014	0.056
$Cda_{measured}$	0.092	0.285	0.029	0.094
$Cda_{\|U\|Ux}$	-	-	0.023	0.049

It is noted that similar phenomenon of the interaction of the LHCSs and cylinder arrays was described by White and Nepf (2007), but in terms of the phase difference between u' and v'. The interaction of the LHCSs and stagnation points inside the vegetation region discussed in this study is related to the Lagrangian coordinate system. Hence, the latter provides a different view on the phenomenon. For example, it is worth noting that while the effects of the sweeps and ejections have been well recognised (White and Nepf, 2007), the reverse flow and stagnation areas inside vegetation region have not been observed in cases with a flat bed. The presence of a transverse slope appears to play an important role in this behaviour, see *e.g.* van Prooijen et al. (2005). It is seen from the experiment that the reverse flow and stagnation areas inside vegetation region are a relevant factor potentially affecting the sedimentation and nutrient deposition within the cylinder arrays.

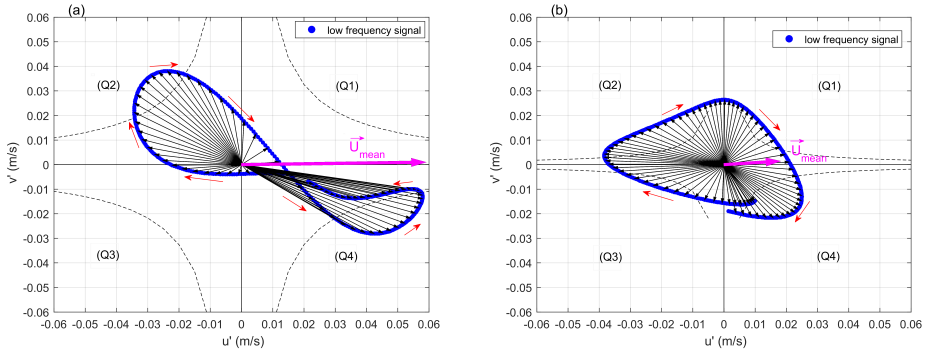

Figure 3.13: The representative motion (red arrows) of the quadrant analysis of the horizontal fluctuations associated with low-frequency signal (blue circles) in a period of 15 seconds, location A at the edge of vegetated floodplain (y=0 m) (a) and location B at y=−0.125 m inside the vegetation (b). Black arrows indicate the instantaneous fluctuation velocity; the pink arrows indicate the mean flow velocity at those locations. The dashed lines in the figure represent hyperbolas corresponding to $|u'v'| = 2\left(-\overline{u'v'}\right)$.

Studying the quadrant analysis of the RSs at two different locations A and B (see Fig-

ure 3.9) makes it possible to understand how the stagnation areas and reverse flow events can occur and why they are barely observed in the literature. Figure 3.13 shows a quadrant analysis in a period of 15 s of the horizontal fluctuations associated with low frequency signal (blue circles), which correspond to the LHCSs at the edge of the vegetated floodplain (location A: $y = 0m$) and inside the vegetation (location B: $y = -0.125m$). Although the stagnation areas and reverse flow events observed in the flow field do not directly appear in quadrant analysis of the RSs (u', v'), however, these flow events can be recognized by adding in the quadrant analysis the mean flow velocity (pink arrows) together with instantaneous fluctuation velocities (in the form of vectors) corresponding to the distribution of (u', v') in time (black arrows). In this way, there are two main components in the quadrant analysis of the RSs, the fluctuation motion caused by the LHCSs and the mean flow motion caused by the mean free surface water slope. The essential conditions so that the stagnation areas or reverse flow events can occur can be stated as follows :

"the LHCSs need to be strong enough, and the mean flow velocity needs to be small enough so that the fluctuation motions induced by the LHCSs become equal or larger than the mean flow velocity".

Following the dye tracer in the flume, the flow field in a Eulerian coordinate system can be observed. The observation suggests that the tracer path of the dye does follow a

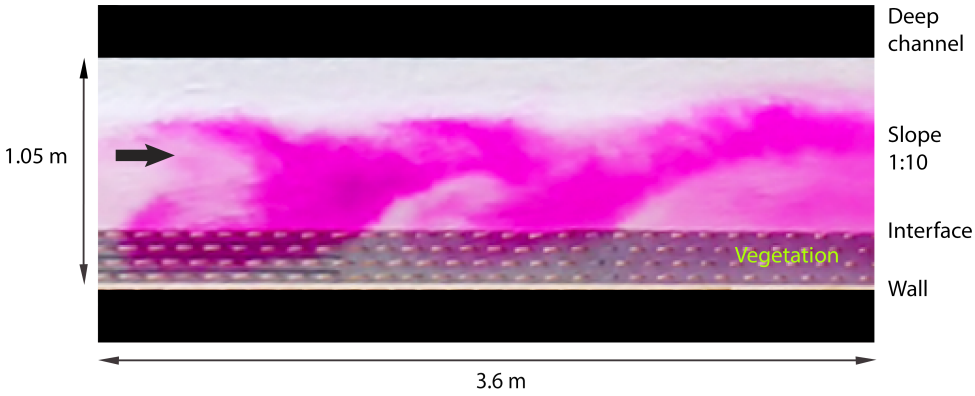

Figure 3.14: Cycloid Flow field under the effect of the LHCSs visualized by the colour dye for sparse density scenarios and respectively 25 cm floodplain width. The LHCSs as it moves along the cylinder arrays shows a "cycloid motion" property.

prolate cycloid curve (Figure 3.14). The observations confirm the presence of the LHCSs and the flow events caused by the motion of the LHCSs along the vegetated floodplain. The flow field under the effect of the LHCSs appears to have cycloid characteristics.

The LHCSs then can be identified by subtracting the advection velocity at the centre of the stagnation areas from the instantaneous velocity field (Figure 3.11c). It is shown that when moving along the interface, the LHCSs clearly split the mean streamwise velocity into three different regions (Figure 3.11a), *viz.* the uniform region inside the floodplain (region I) controlled by the drag from vegetation, outside in the main channel (region II) controlled by the bottom friction and water depth, and the mixing layer region

(region III and IV). These results suggest that in a compound vegetated channel with a very gentle slope, for the conditions tested ($\frac{Cda}{C_f/D} \geq 60$), the vegetated shear-layer dynamics resembled to that associated with vegetation alone which was described in White and Nepf (2007, 2008), rather than that associated only with a depth differential.

It is clear that the presence of LHCSs is the most important factor in the mixing layer forcing the momentum exchange between the main channel region and the floodplain region. As described in the previous section, the transverse momentum exchange in this region is increased 20 times due to the presence of vegetation and associated LHCSs. In this sense, the horizontal eddy viscosity plays a key role in understanding and describing the momentum exchange mechanism in these regions. Dealing with the horizontal eddy viscosity is treated in the next separate Chapter 4.

3.4.3 Role of vegetation width or Squeeze effect

Finally, the "squeeze" effect has been experimentally studied by varying the width of the floodplain region. Figure 3.15 shows the mean streamwise velocity for different floodplain widths. In cases without vegetation, 50 cm floodplain width (Figure 3.15a), the mean streamwise velocity achieved uniform values of 34.9 cm s^{-1} right at the floodplain edge ($y = 0$ m). When reducing the width of the floodplain from 50 cm to 25 cm and 10 cm, the mean streamwise velocity does not achieve a transverse uniform value at the floodplain edge, and keeps decreasing further inside the floodplain region. This means that the penetration of the mixing layer increases together with the decrease of the width of the floodplain. In other words, the width of the floodplain does affect the penetration of the mixing layer into the floodplain area.

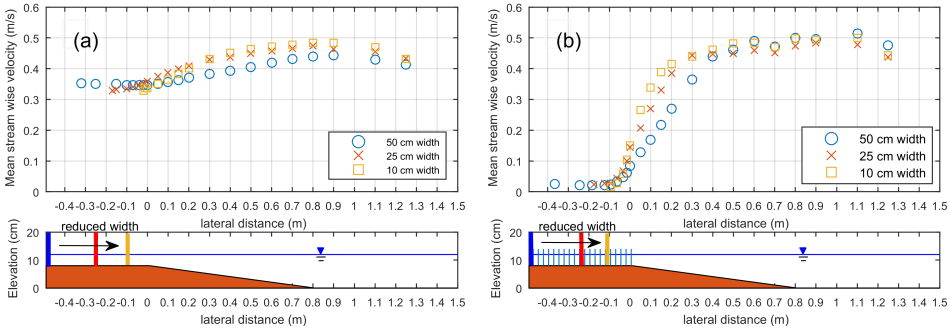

Figure 3.15: Mean streamwise velocity profile in non-vegetated floodplain scenarios and dense vegetation scenarios, discharge Q=80 L s^{-1}, water level H=14 cm, different floodplain widths – circles: 50 cm; crosses: 25 cm; squares: 10 cm.

In the case of dense vegetation (Figure 3.15b), the response of mean streamwise velocity within the floodplain region is less sensitive. As the width of the floodplain reduces from 50 cm to 25 cm, the mean streamwise velocity shows different trends only in the outer region (from location $y = 0$ to around $y = 0.5m$) where the velocity gradient significantly increases. This means that the velocity gradient around the vegetation interface

can be increased by decreasing the floodplain width. These changes in the velocity can be explained in terms of the increased velocity gradient at the vegetated edge which was induced by the changes in the pattern of the LHCSs.

It can be seen that the increased velocity gradient together with the presence of vegetation does not lead to a larger penetration of the shear layer into the vegetated floodplain. In both cases (50 cm and 25 cm floodplain width), the mean streamwise velocity decreases inside the floodplain region and achieves a transversely uniform value beyond about 10 cm penetration. This indicates that the mean streamwise velocity does require a certain distance such that a uniform velocity within the forest can be achieved. In these scenarios, the distance required is about 10 cm. Differences can be noted when further reducing the width of the floodplain from 25 cm to 10 cm, the mean streamwise velocity within the vegetated floodplain starts "feeling" the side wall and is being affected. The mean streamwise velocity cannot achieved a transverse uniform value as it keeps decreasing until the end of the floodplain region. This means that the mixing layer appears to penetrate the whole floodplain region.

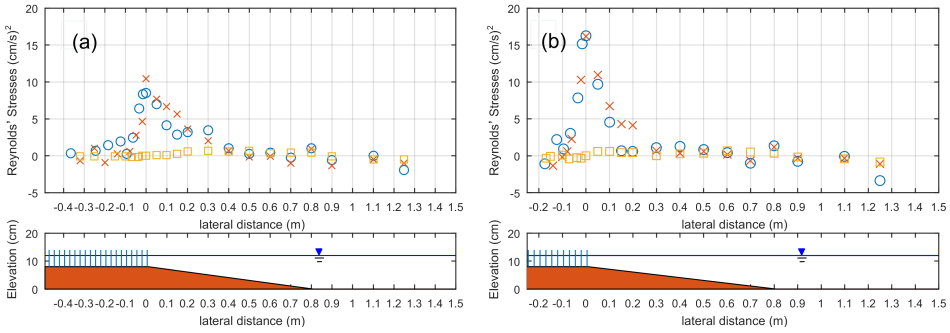

Figure 3.16: Lateral profiles of Reynold stress in case of 50 cm floodplain width (a) and 25 cm floodplain width (b) ; no cylinder (squares), sparse cylinder (crosses), and dense cylinders (circles); discharge Q=80 L s^{-1}, water level H=12 cm.

Figure 3.16 a shows the transverse profiles of the RSs in cases of different density and different width. Although strong peaks of RSs can be clearly observed in cases with the presence of cylinders (sparse and dense scenarios), in cases without vegetation, it is less obvious as the maximum values tend to spread more along the transition slope region. It is also observed that the more vegetation, the less spreading of the RSs. When the width of the floodplain is reduced to 25 cm (Figure 3.16b), the RSs around the floodplain edge (location $y = 0m$) increase. As the order of magnitude of the RSs is related to the momentum exchange in the mixing layer, this implies an increase in the momentum exchange between these two regions when the floodplain width is restricted.

The LHCSs are important drivers forcing the flow field in the vegetated floodplain region. Therefore, comparing the autocorrelation function and PDSs in scenarios of different widths is informative as they contain information related to large coherent structures. The autocorrelation functions of lateral velocity in different floodplain width scenarios are shown in Figure 3.17. Reducing the width of the floodplain also reduces the period of the quasi-2D structure, from 11.5 s to 8.5 s. Besides, the normalized en-

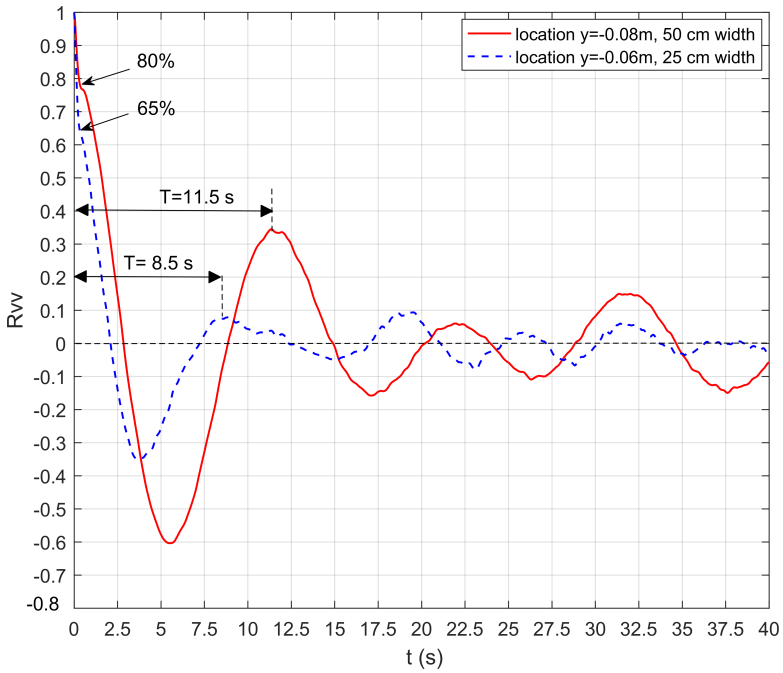

Figure 3.17: Autocorrelation function Rvv in cases of sparse density, floodplain width = 50 cm and 25 cm; discharge $Q = 45\,\mathrm{L\,s^{-1}}$, water level $H = 12$ cm.

ergy contribution also reduces from 80% to 65%. These results show that squeezing the floodplain does increase the frequency of the LHCSs. This is probably due to the smaller LHCSs and faster advection velocity. In terms of K-H instability, the results suggest that decreasing the floodplain width results in a smaller wavelength and wave period. The results of Figure 3.18a,b confirm this.

Finally, the response of the structures themselves to the "squeeze effect" is addressed. Figure 3.18a shows the representative LHCSs (solid red lines) in cases of 50 cm floodplain width. The corresponding LHCSs in cases where the width of vegetated floodplain has been reduced to 25 cm, is shown in Figure 3.18b. It can be seen that the LHCSs seems to be contracted in the streamwise and lateral direction in the narrower floodplain scenarios. As a result, the LHCSs in "squeeze" cases are likely to be smaller than the cases with non-restricted floodplain.

It is noted that reducing the floodplain width (from 50 cm to 25 cm) diminish the width of the area affecterd by the LHCSs where fluctuation motions can occur. The combined impact of the LHCSs and the narrower space of the floodplain area may cause an increase in the increased local pressure, induced by the stagnation areas and reverse flows. As a result, the reverse flow and the RSs in the vegetation region in cases of narrower 25 cm floodplain width are larger than that in the scenario of 50 cm floodplain width (Figure 3.18c, d). Additionally, the more frequent LHCSs means that the flow events occur more frequently and region of stagnation areas move faster. In this sense,

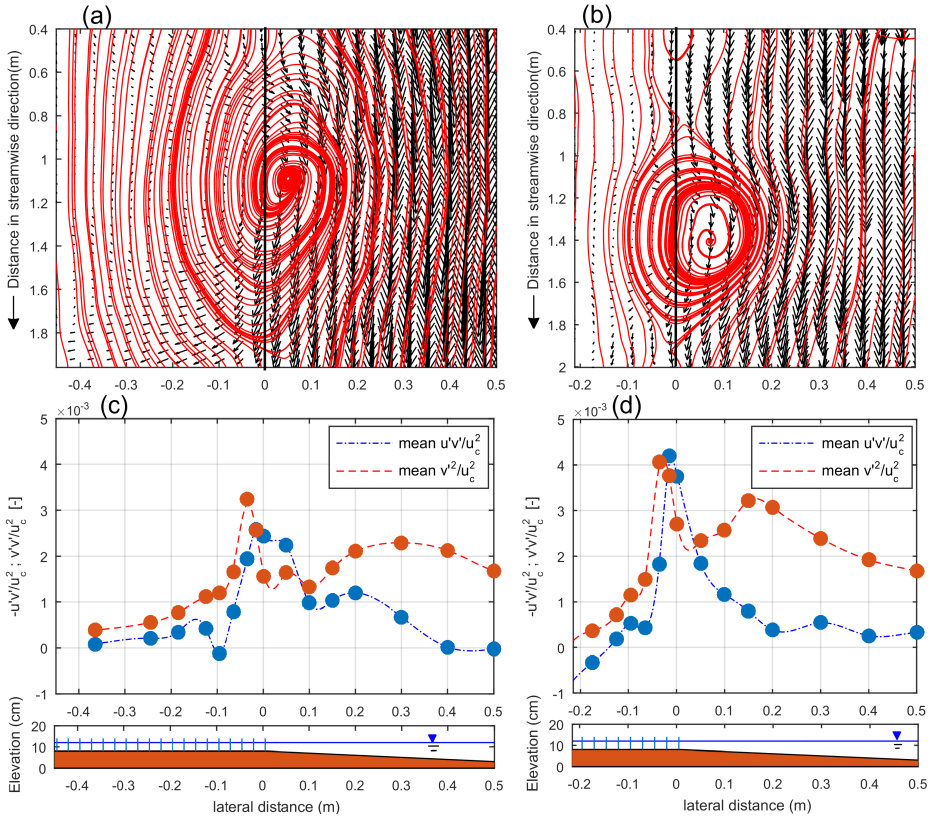

Figure 3.18: The Large Horizontal coherent structure (red-solid lines) in cases of 50 cm width (a) and 25 cm width (b) and the corresponding shear and normal stresses in cases of 50 cm width (c) and 25 cm width (d). Dense scenarios, discharge =45 l/s, water level =12 cm.

sedimentation processes may be significantly affected in such a way that there is less time and space for the sediment to be deposited, while the momentum fluxes are larger.

3.5 Discussion

So far, the results of our work indicate that vegetation, in general, and mangroves , in particular, have a strong role in determining the strength and direction of flow in river channels with vegetated floodplains. Large differences in the mean streamwise velocity and Reynolds shear stresses between the scenarios with and without vegetation can be observed. It is important to note that these differences are not only caused directly by the presence of vegetation in the floodplain region (*i.e.* vegetation disturbs, diverts and reduces the flow velocities), but also due to the presence of the LHCSs, generated by the vegetation-induced shear layer. Therefore, differences were observed to occur not only at the vegetation interface, but also deeper inside the vegetation area, and in the

adjacent transition slope. The phenomenon in which areas deeper inside the vegetation, or outside in the transition slope are affected by the flow events generated by LHCSs as they moving along the vegetation interface can be conceptually explained through the cycloid characteristic of the flow field (Figure 3.19)

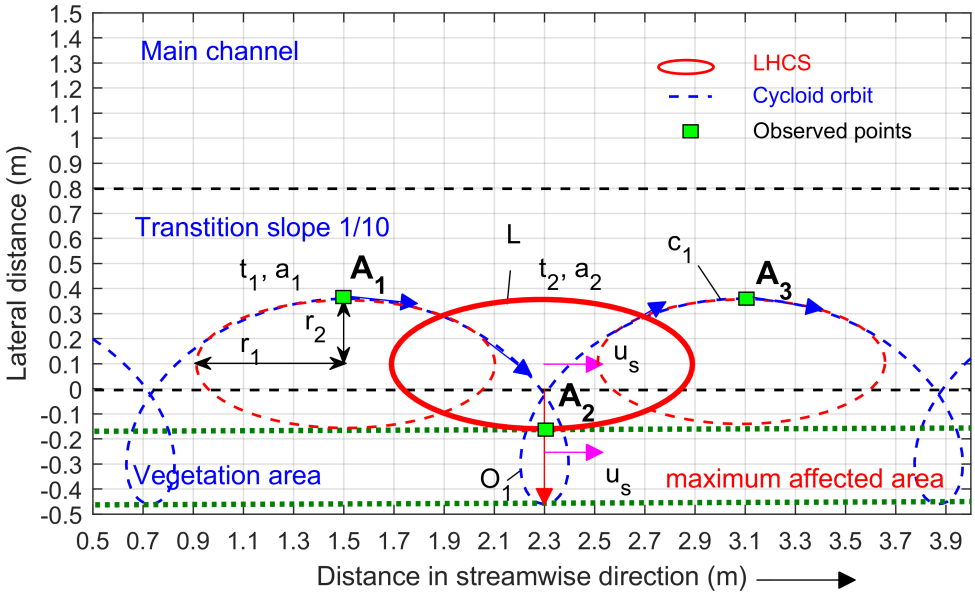

Figure 3.19: Schematic view of cycloid motion under the effect of the LHCSs as they are moving along the vegetated interface. The maximum affected area is larger than the penetration of the LHCSs.

Based on the observation of the particle movement in the PIV data set and the previous analyses, it is seen that the LHCSs (L) in this case have the ellipse form with two radii corresponding to the length $r_1 = 0.6\,\text{m}$, and to the width $r_2 = 0.25\,\text{m}$ (Figure 3.18*a*). At the moment t_1, the LHCSs is at location a_1, and an observed point A_1 located at its edge tends to follow the orbit of a prolate cycloid curve c_1. At the moment t_2, the LHCSs is at location a_2, and an observed point A_1 follow the orbit of a prolate cycloid curve c_1 to the location A_2. In the vegetation region outside the mixing layer, areas surrounding the prolate cycloid curve $c1$ appear to be affected by the motion of the LHCSs and tend to follow the motions of the observed point (A1-A2-A3). This results in a stagnant area. As the LHCSs are moving along the interface between vegetation and open region, these stagnation areas also move with the same velocity u_s. In this sense, the region of the stagnation area captured by PIV measurement is likely to link to the cycloid loop (O_1) at the time t_2. The corresponding LHCSs at this moment at location a_2 can be deduced by subtracting the instantaneous velocity field to the advection velocity u_s at the centre of stagnation areas (O_1). According to this explanation, it is suggested that the maximum affected area is likely to connect to the width of the outer layer of the LHCSs. In practical engineering, this means that a structure which directly interferes with the vegetated river bank should be carefully considered, especially in terms of the changes of the hydrodynamics and exchange processes induced by the modification of the LHCSs.

The stability of the river bank in squeezed condition *i.e.* the mangrove width is restricted is discussed in terms of the changes in the bed shear stress. Based on the results

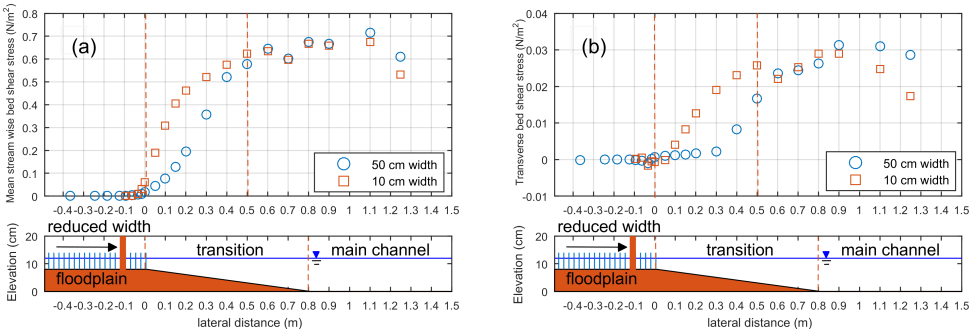

Figure 3.20: Streamwise bed shear stress comparison(a) and transverse bed shear stress comparison(b) in scenarios of 50 cm and 10 cm floodplain width, discharge $Q = 80\,\mathrm{L\,s^{-1}}$, water level $H = 14\,\mathrm{cm}$.The positive values of the transverse bed shear stress indicate that it is directed away from the floodplain.

of the experiment, the bed shear stress, which are representative for the applied forces induced by the flow water, including the LHCSs can be determined (Figure 3.20). It can be clearly seen that, when the mangrove width is reduced, although the bed shear stress in the inner layer almost remain the same, the bed shear stress in the outer layer (both streamwise and transverse) increase significantly.

It can be seen that the outer layer appears to be the most vulnerable area in term of river bank stability. It is suggested that significant variation in the bed shear stresses induced by changes in the LHCSs can be expected when decreasing the forest width. Therefore, the width of the vegetation area does play a role in the stabilization of a vegetation compound channel, especially for the transition slope. In normal condition, there should be a certain width so that the applied bed shear stresses to the river bank can be counteracted by the advanced shear stresses induced by the presence of the vegetation.

3.6 Conclusions

The effect of vegetation on the hydrodynamics of a compound channel, the presence of the LHCSs and their effect on the flow field as well as “squeeze” effects were investigated through experiments. It is shown that in a compound vegetated channel with a gentle transverse slope, the shear layer properties are dominated by the presence of vegetation, rather than by the water depth difference. The vegetation significantly increases the gradient of the mean streamwise velocity, drawing more exchange toward the vegetation edge and pushing more flow into the floodplain region. It is also very effective in damping and shielding the flow within the forest from external boundary conditions. Furthermore, the presence of vegetation does enhance the occurrence of LHCSs, which is a dominant factor in forcing the exchange mechanism at the vegetation interface. The presence of LHCSs, which is much more pronounced in cases with vegetation, is the major factor contributing to the momentum exchange between the

vegetated floodplain regions and the adjacent open channel. The experimental results also reveal that the region affected by the LHCSs where large transverse fluctuations can occur is much larger than the region of transverse momentum exchange which is connected to the penetration of the LHCSs into the vegetated floodplain region. The moving of the LHCSs along the vegetation interface is associated with the sweeps, the ejections, as well as the stagnant and the reverse flows forming a so called cycloid motion. While the sweeps and ejections dominate the momentum exchange region and appear to link to the import and export mechanism of nutrients and sediments, the stagnant and reverse flows appear to dominate the region further inside the vegetation and are important for the deposition processes. The streamwise forces is maximum during the sweeps and smallest during the ejections. Moreover, due to the presence of stagnant and reverse flows, negative streamwise forces can be recorded.

It is important to note that although the vegetation is very effective in damping and protecting the hydrodynamic conditions within the forest, the “squeeze effect” makes this protection much less successful. Reducing the forest width does influence the hydrodynamics in and around the cylinder arrays, especially the shear layer at the vegetation interface. Furthermore the mean flow velocity needs a certain space to reach its uniform value inside the floodplain area and the vegetated region affected by the LHCSs can be even larger than the region which the mixing layer can penetrate into. Hence, a too narrow floodplain may diminish the affected area directly and makes it impossible for the flow field inside the vegetation to be able to reach its equilibrium state. As a result, the LHCSs in “squeeze” condition occur more frequently, but less regularly and the transverse exchange processes induced by these LHCSs can be strongly disturbed. The momentum fluxes are larger, and the time and space for the sediment to be deposited is restricted. These are hypothesized to not create favourable conditions for the nutrient or sediment deposition within the forest. It is also seen that the denser the vegetation, the less sensitive the mangrove forest is to the squeeze effects. This again shows the vegetation function in the protection of the river banks.

References

Bousmar, D. and Zech, Y. (2004). Large-scale coherent structures in compound channels. In *Shallow Flows: Research Presented at the International Symposium on Shallow Flows, Delft, Netherlands, 2003*, page 347. Taylor & Francis.

Buckman, L. (2013). Hydrodynamics of partially vegetated channels: stem drag forces and application to an in-stream wetland concept for tropical, urban drainage systems. Master's thesis.

Chu, V. H. and Babarutsi, S. (1988). Confinement and bed-friction effects in shallow turbulent mixing layers. *Journal of hydraulic engineering*, 114(10):1257–1274.

Dupuis, V., Proust, S., Berni, C., and Paquier, A. (2017). Mixing layer development in compound channel flows with submerged and emergent rigid vegetation over the floodplains. *Experiments in Fluids*, 58(4):30.

Ervine, D. A., Babaeyan-Koopaei, K., and Sellin, R. H. (2000). Two-dimensional solution for straight and meandering overbank flows. *Journal of Hydraulic Engineering*, 126(9):653–669.

Fernandes, J., Leal, J., and Cardoso, A. (2014). Improvement of the lateral distribution method based on the mixing layer theory. *Advances in Water Resources*, 69:159–167.

Hamidifar, H. and Omid, M. H. (2013). Floodplain vegetation contribution to velocity distribution in compound channels. *Journal of Civil Engineering and Urbanism*, 3(6):357–361.

Horstman, E. (2014). *The Mangrove Tangle: Short-term bio-physical interactions in coastal mangroves*. PhD thesis.

Ikeda, S., Kawamura, K., Fukumoto, M., and Sano, T. (2000). Organized horizontal vortices and lateral sediment transport in compound open channel flows with bank vegetation. *PROCEEDINGS OF HYDRAULIC ENGINEERING*, 44:795–800.

Jahra, F., Kawahara, Y., Hasegawa, F., and Yamamoto, H. (2011). Flow–vegetation interaction in a compound open channel with emergent vegetation. *International journal of river basin management*, 9(3-4):247–256.

Jirka, G. and Uijttewaal, W. (2004). Shallow flows: A definition. pages 3–11.

Keller, R. and Rodi, W. (1988). Prediction of flow characteristics in main channel/flood plain flows. *Journal of Hydraulic research*, 26(4):425–441.

Knight, D., Aya, S., Ikeda, S., Nezu, I., and Shiono, K. (2007). *Flow and sediment transport in compound channels, the experiences of Japanese and UK Research*, chapter 2:Flow structure, pages 5–113. CRC Press.

Knight, D. and Shiono, K. (1990). Turbulence measurements in a shear layer region of a compound channel. *Journal of hydraulic research*, 28(2):175–196.

Knight, D. and Shiono, K. (1996). River channel and floodplain hydraulics. *Floodplain processes*, pages 139–181.

Knight, D. W. and Demetriou, J. D. (1983). Flood plain and main channel flow interaction. *Journal of Hydraulic Engineering*, 109(8):1073–1092.

Kozioł, A. (2011). Turbulent kinetic energy of water in a compound channel. *Annals of Warsaw University of Life Sciences-SGGW. Land Reclamation*, 43(2):193–205.

Lambert, M. and Sellin, R. (1996). Discharge prediction in straight compound channels using the mixing length concept. *Journal of Hydraulic Research*, 34(3):381–394.

Mazda, Y., Wolanski, E., King, B., Sase, A., Ohtsuka, D., and Magi, M. (1997). Drag force due to vegetation in mangrove swamps. *Mangroves and Salt Marshes*, 1(3):193–199.

Mazurczyk, A. (2007). Scales of turbulence in compound channels with trees on floodplains. *Publs. Inst. Geophys. Pol. Acad. Sc*, (401):169–176.

McBride, M., Hession, W. C., Rizzo, D. M., and Thompson, D. M. (2007). The influence of riparian vegetation on near-bank turbulence: A flume experiment. *Earth Surface Processes and Landforms*, 32(13):2019–2037.

Muste, M., Fujita, I., and Hauet, A. (2008). Large-scale particle image velocimetry for measurements in riverine environments. *Water Resources Research*, 44(4):n/a–n/a. W00D19.

Nadaoka, K. and Yagi, H. (1998). Shallow-Water Turbulence Modeling and Horizontal Large-Eddy Computation of River Flow. *Journal of Hydraulic Engineering*, 124(5):493–500.

Nepf, H. (1999). Drag, turbulence, and diffusion in flow through emergent vegetation. *Water resources research*, 35(2):479–489.

Nepf, H. M. (2012). Hydrodynamics of vegetated channels. *Journal of Hydraulic Research*, 50(3):262–279.

Nezu, I. and Onitsuka, K. (2001a). Turbulent structures in partly vegetated open-channel flows with LDA and PI V measurements. *Journal of Hydraulic Research*, 39(6):629–642.

Nezu, I. and Onitsuka, K. (2001b). Turbulent structures in partly vegetated open-channel flows with lda and pi v measurements. *Journal of hydraulic research*, 39(6):629–642.

Nezu, I., Onitsuka, K., and Iketani, K. (1999). Coherent horizontal vortices in compound open-channel flows. *Hydraulic Modeling (ed. VP Singh, IW Seo & JH Sonu)*, pages 17–32.

Nikora, V. (1999). Origin of the ?- 1? spectral law in wall-bounded turbulence. *Physical Review Letters*, 83(4):734.

Pasche, E. and Rouve, G. (1985). Overbank Flow with Vegetatively Roughened Flood Plains. *Journal of Hydraulic Engineering*, 111(9):1262–1278.

Perry, A. and Li, J. D. (1990). Experimental support for the attached-eddy hypothesis in zero-pressure-gradient turbulent boundary layers. *Journal of Fluid Mechanics*, 218:405–438.

Phan, L. K., van Thiel de Vries, J. S., and Stive, M. J. (2015). Coastal Mangrove Squeeze in the Mekong Delta. *Journal of Coastal Research*, 300:233–243.

Pope, S. (2000). *Turbulent Flows*. Cambridge University Press.

Ranasinghe, R., Narayan, S., Suzuki, T., Stive, M., Ursem, W., and Verhagen, H. (2010). On the effectiveness of mangroves in attenuating cyclone induced waves. In *Proceedings of the 32th International Conference on Coastal Engineering, ICCE 2010, June/July, Shanghai*. ASCE-Texas Digital Library.

Shiono, K. and Knight, D. (1988). Two-dimensional analytical solution for a compound channel. In *Proc., 3rd Int. Symp. on refined flow modeling and turbulence measurements*, pages 503–510.

Shiono, K. and Knight, D. (1989). Transverse and vertical reynolds stress measurements in a shear layer region of a compound channel. In *Proc. 7th Symp. Turb. Shear Flows*, volume 28, pages 1–6.

Shiono, K. and Knight, D. (1990). Mathematical models of flow in two or multi stage straight channels. In *Proc. Int. Conf. on River Flood Hydraulics*, pages 229–238. Wiley New York, NY.

Siniscalchi, F., Nikora, V. I., and Aberle, J. (2012). Plant patch hydrodynamics in streams: Mean flow, turbulence, and drag forces. *Water Resources Research*, 48(1).

Struve, J., Falconer, R. A., and Wu, Y. (2003). Influence of model mangrove trees on the hydrodynamics in a flume. *Estuarine, Coastal and Shelf Science*, 58(1):163–171.

Sumer, B. M. et al. (2006). *Hydrodynamics around cylindrical strucures*, volume 26. World scientific.

Tamai, N., Asaeda, T., and Ikeda, H. (1986). Study on Generation of Periodical Large Surface Eddies in a Composite Channel Flow. *Water Resources Research*, 22(7):1129–1138.

Tanino, Y. and Nepf, H. M. (2008). Laboratory investigation of mean drag in a random array of rigid, emergent cylinders. *Journal of Hydraulic Engineering*, 134(1):34–41.

Thielicke, W. and Stamhuis, E. (2014). Pivlab–towards user-friendly, affordable and accurate digital particle image velocimetry in matlab. *Journal of Open Research Software*, 2(1).

Truong, S. H., Ye, Q., and Stive, M. J. (2017). Estuarine mangrove squeeze in the mekong delta, vietnam. *Journal of Coastal Research*, pages 747–763.

Uijttewaal, W. and Booij, R. (2000). Effects of shallowness on the development of free-surface mixing layers. *Physics of fluids*, 12(2):392–402.

Van Prooijen, B. (2004). *Shallow mixing layers*. PhD thesis.

van Prooijen, B., Battjes, J. A., and Uijttewaal, W. (2005). Momentum Exchange in Straight Uniform Compound Channel Flow. *Journal of Hydraulic Engineering*, 131(3):175–183.

Vargas-Luna, A., Crosato, A., and Uijttewaal, W. S. (2015). Effects of vegetation on flow and sediment transport: comparative analyses and validation of predicting models. *Earth Surface Processes and Landforms*, 40(2):157–176.

White, B. L. and Nepf, H. M. (2007). Shear instability and coherent structures in shallow flow adjacent to a porous layer. *Journal of Fluid Mechanics*, 593:1–32.

White, B. L. and Nepf, H. M. (2008). A vortex-based model of velocity and shear stress in a partially vegetated shallow channel. *Water Resources Research*, 44(1).

Xiaohui, S. and Li, C. W. (2002). Large eddy simulation of free surface turbulent flow in partly vegetated open channels. *International Journal for Numerical Methods in Fluids*, 39(10):919–938.

Yan, X.-F., Wai, W.-H. O., and Li, C.-W. (2016). Characteristics of flow structure of free-surface flow in a partly obstructed open channel with vegetation patch. *Environmental fluid mechanics*, 16(4):807–832.

Yossef, M. F. and de Vriend, H. J. (2010). Flow details near river groynes: Experimental investigation. *Journal of Hydraulic Engineering*, 137(5):504–516.

Zong, L. and Nepf, H. (2010). Flow and deposition in and around a finite patch of vegetation. *Geomorphology*, 116(3-4):363–372.

Chapter 4

Analytical modelling of transverse momentum exchange

Mathematics is not about number, equations, computations, or algorithms;
It is about understanding.

William Paul Thurston

In floodplains of vegetated channels, transverse exchange processes of mass and momentum are of primary importance as these are directly linked to the river bank stability, sedimentation and nutrient transport. Despite its importance, knowledge about this phenomenon is still incomplete especially in the context of the presence of the large horizontal coherent structures (LHCSs). As a result, although various exchange models have been developed, their applicability in different circumstances is still unclear as their validity is usually restricted to a narrowly ranging experiment data set. A proper model for this exchange in a compound channel geometry with or without vegetation is lacking. In order to obtain more insight, a laboratory experiment of a shallow flow field in a compound vegetated channel has been conducted. A quadrant analysis of the Reynolds shear stresses has been applied to study the connection between the cycloid flow events induced by the LHCSs and transverse momentum exchange in the channel. It is suggested that local variability leads to differences in the transverse exchange of momentum. Furthermore, the experimental data were used to verify state-of-the-art momentum exchange models. As the limitations of those models were analysed, for the first time a hybrid eddy viscosity model based on the occurrence of LHCSs and the presence of vegetation was proposed and validated using a variety of experimental data sets. The results suggest that the transverse momentum exchange can be well modelled with the new eddy viscosity model for quite a range of different set-ups and scenarios by varying only a coefficient of proportionality β which is related to the transverse slope between the main channel and the floodplain.

This chapter is under review as Truong, S.H., and Uijttewaal, W.S.J., Transverse Momentum Exchange induce by large coherent structures in vegetated compound channels. *Water Resource Research* (2018).

In this chapter of the thesis, the mathematical models of the transverse momentum exchange between the vegetation region and the adjacent open channel were studied. The governing equations were derived for the vegetated compound channel. A quadrant analysis of the Reynold shear stress was applied to gain more insight into the contribution of the LHCSs in the momentum exchange processes. Moreover, the most up to date analytical models were reviewed and verified with the experimental results in Chapter 3. Finally, a new model based on the LHCSs has been proposed and validated with the data from various experimental data sets.

4.1 Introduction

In the Mekong Delta Estuaries, mangroves usually dominate the floodplain regions with a gentle slope of about 1 : 10. Due to the human impacts in many large mangrove forests, only a narrow strip of about 50 to 200 m is left. The river banks at those locations are usually eroding at a rate of two to four meters per year (Figure 5.1). This degradation of mangrove forests together with the accelerated river bank erosion has been studied in the context of the "squeeze" phenomenon (Phan et al., 2015; Truong et al., 2017). In a squeezed mangrove forest, the presence of lateral tidal creeks is hardly observed and the main interaction is the lateral exchange through the mixing layer developed at the vegetation interface. In this condition, the hydrodynamics of a squeezed estuarine mangrove forest is similar to that of a compound vegetated channel (Mazda et al., 1997; Truong et al., 2017).

A compound channel usually consists of floodplains, transition slopes and a main open channel. In appropriate conditions, ecological systems such as mangroves or salt marshes can develop in the floodplain region, and the compound channel becomes a compound vegetated channel, also called floodplain vegetated channel. There are also cases in which the channels are partially covered with vegetation and the presence of the floodplain is negligible. The cross sections of these natural channel systems can schematically be depicted, see Figure 4.2.

In compound channels, the flow over the shallower floodplain is slower than in the deeper main channel because of the difference in bed friction. As a result, a mixing layer develops between the floodplain and the channel (van Prooijen et al., 2005). A shallow flow field in this condition is considered as a parallel shear flow (Drazin and Reid, 2004) between the floodplain and adjacent open region that can trigger velocity-shear instability, so called the Kelvin-Helmholtz (K-H) instabilities (Bousmar, 2002). The K-H instabilities then induces the flow to develop a kind of self-organizing flow structures with horizontal length scale larger than the water depth, which is termed "large horizontal coherent flow structures" (LHCSs) (Adrian and Marusic, 2012; Bousmar, 2002; White and Nepf, 2008). It is considered to be the fundamental factor controlling the structure of these turbulent flows. The presence of LHCSs was well observed not only at the interface of open compound channel, but also in cases of flow past river groynes Talstra (2011), the confluence of two flows (Uijttewaal and Booij, 2000; Van Prooijen, 2004; van Prooijen et al., 2005), in the wakes of islands (Chen and Jirka, 1997), along the edge of vegetation (Nezu et al., 1999; Nezu and Sanjou, 2008). They usually appear in the mixing layer, where there is a large gradient in velocities.

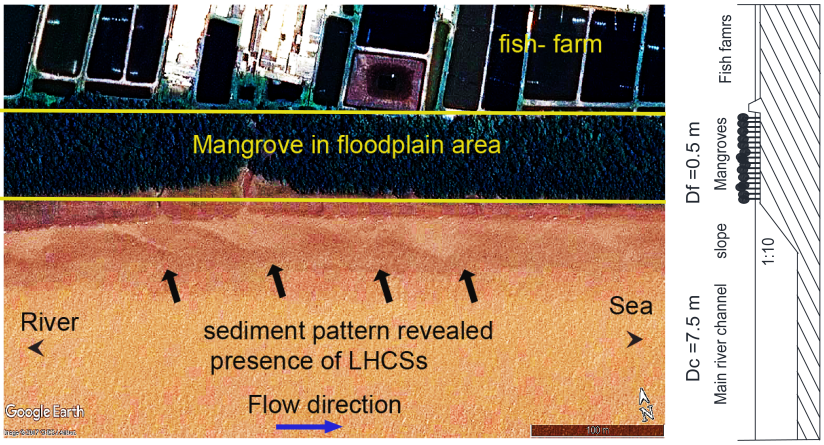

Figure 4.1: Typical mangroves distribution along a straight part of Tieu estuary, Vietnam and the associated schematised bathymetry. Fish farms constructed close to the water boundary push the mangrove into a narrow fringe zone. This area is suffering from erosion with a rate of about 2.5 m yr^{-1} (Truong et al., 2017).

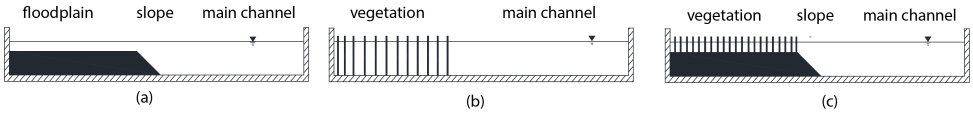

Figure 4.2: Typical schematised profiles of natural systems of a straight river channel including compound channel (a), partially vegetated channel (b) and vegetated floodplain channel (c).

In cases of shallow water over a flat bottom, the bottom friction affects the mixing layer and LHCSs as it decreases the velocity differences and the growth of KH instability downstream (Uijttewaal and Booij, 2000). However, in compound channels, the transverse depth difference sustains the velocity difference and the bed friction limits the growth of the mixing layer. Consequently, the mixing layer can achieve an equilibrium width and the flow field is fully developed after a certain width, for example 7.5 m in cases of a compound channel profile (Fernandes et al., 2014), and 4 m in cases of a partially vegetated channel profile (White and Nepf, 2007). As a result, the presence of LHCSs can be sustained in this fully developed region.

In a vegetated compound channel, a similar shear layer is generated. However, the presence of vegetation adds to friction, turbulence and drag forces, greatly damping the flow in this region, and significantly boosting the magnitude of the velocity gradient between the vegetation and open channel region (White and Nepf, 2007, 2008). As a result, the K-H instabilities increase and the LHCSs formed at the vegetation interface, observed in floodplain vegetated channels are more pronounced than in cases without vegetation. These pronounced LHCSs then, promote more transverse momentum exchange into the vegetation region (Nepf, 1999). The transverse exchange of momentum from “fast” regions to “slow” regions, mediated by the strong presence of the LHCSs is the major interest of this study.

4.2 Objectives

In recent decades, numerous studies on compound channels have been published, particularly focusing on understanding and quantifying the lateral momentum exchange processes in the mixing layer of a compound channel, with or without vegetation (Helmiö, 2004; Ikeda et al., 1991; Nadaoka and Yagi, 1998; Nezu and Onitsuka, 2001; Pasche and Rouve, 1985; Tamai et al., 1986; van Prooijen et al., 2005; Vionnet et al., 2004; White and Nepf, 2007, 2008; Xiaohui and Li, 2002; Zong and Nepf, 2010). However, these studies either did not take into account the presence of LHCSs, or the presence of the vegetation on the floodplain. Furthermore, those models have primarily been based on laboratory studies, and each model refers to a particular set-up. Therefore, whether or not they are generically valid for different configurations and at different scale are yet to be determined. It is unclear how and to what extend the presence of the large horizontal coherent structures (LHCSs) affects the flow field and the transverse exchange of momentum of a compound vegetated channel. Therefore, the main objectives of this research are: (1) to obtain insight into the transverse momentum exchange in the shallow flow field between the open channel and the vegetated region induced by the LHCSs and (2) to verify and extend the momentum exchange model for compound vegetated channels based on the effective eddy viscosity model of van Prooijen et al. (2005).

4.3 Methodology

Momentum exchange in a compound channel flow can be expressed as a turbulent shear stress ($\overline{u'v'}$) or using the concept of an eddy viscosity (v_t): $\tau_{xy} \approx -\rho \cdot \overline{u'v'} \approx -\rho \cdot v_t \cdot \frac{\partial u}{\partial y}$ (van Prooijen et al., 2005). While the former is important for understanding the mechanisms contributing to the transverse exchange of momentum, the later plays a key role in modelling it. In this study, in order to achieve the research objectives.B both aspects are addressed in this study.

The governing equations are introduced (Section 4.4), and existing modelling approaches of transverse exchange of momentum are reviewed (Section 4.5). A laboratory study was chosen as a major source of data(Section 4.6). Subsequently, a quadrant analysis of the Reynolds shear stress is applied (Section 4.7). Then, a hybrid model of the eddy viscosity (v_t) is proposed (Section 4.8). The model is then verified using 39 different experimental settings (Section 4.9), including the experiments of the current study (Table A.1 in the appendix), three representative cases of White and Nepf (2007) for partially vegetated channels and the experimental results of Lambert and Sellin (1996) and Ervine et al. (2000) which were also used to validate the effective eddy viscosity model of van Prooijen et al. (2005). Finally, conclusions are drawn in the Section 4.10.

4.4 Governing Equations

In compound vegetated channels (Figure 4.2c), near a porous vegetation interface, the equations of fully developed stationary flow motion can be derived by applying the time-, spatially- and depth- averaged properties to the 2D shallow water equations,

which is similar to that used by White and Nepf (2007) for partially vegetated channels. In this way, a simplified momentum exchange equation for the floodplain vegetated channel, with streamwise uniform flows can be written as:

$$0 = -gD\frac{\partial n\zeta}{\partial x} + \frac{1}{\rho}\frac{\partial nD\left\langle \overline{T_{xy}} \right\rangle_d}{\partial y} - D \cdot D_x \tag{4.1}$$

In which:

- $D = D(y)$ is the water depth , $D \cdot D_x$ is the drag force exerted on the fluid in the x (streamwise direction).
- n is porosity, ρ is mass density and ζ is water level above an arbitrary horizontal reference plane.
- The term $\frac{1}{\rho}\frac{\partial nD\left\langle \overline{T_{xy}} \right\rangle_d}{\partial y}$ accounts for the transverse exchange of streamwise momentum between the open channel and the floodplain vegetated regions.
- $\left\langle \overline{T_{xy}} \right\rangle_d$ is the sum of depth, time and space averaged transverse shear stress.
- The term $-gD\frac{\partial n\zeta}{\partial x} - D \cdot D_x$ is the difference of the flow from an equilibrium channel flow without transverse exchange (due to slope and vegetation)
- $\frac{\partial n\zeta}{\partial x}$ is the pressure gradient term
- D_x is drag force exerted on the fluid in the x-direction (streamwise direction) where:

$$D_x = \begin{cases} \frac{1}{2}\langle \overline{u} \rangle_d^2 \left(\frac{C_f}{D} + C_D \cdot a \right) & y < 0 \quad \text{“in vegetation”} \\ \\ \frac{1}{2}\langle \overline{u} \rangle_d^2 \left(\frac{C_f}{D} \right) & y > 0 \quad \text{“no vegetation”} \end{cases} \tag{4.2}$$

Where:

- C_f is the Bed friction coefficient
- C_d is the drag coefficient of the array element,
- a is the average solid frontal area per unit volume in the plane perpendicular to the flow (White and Nepf, 2007), $a = N \cdot d$, where N is the density of cylinders (cylinder area) and d is the cylinder diameter.

In cases of high Reynolds numbers, the contribution of viscous stress ($\mu\frac{\partial U}{\partial y}$) is small compared to depth averaged Reynolds stress. Thus, the viscous term has been neglected in these equations. It is noticed that this momentum equation can be globally applied to study the transverse momentum exchange in various scenarios of constant depth, or

with different depth along the channel (in the presence of the floodplain) and with or without vegetation. In cases of a partially vegetated channel (of constant depth) (Figure 4.2b), equation (4.1) reduces to:

$$0 = -g\frac{\partial n\zeta}{\partial x} + \frac{1}{\rho}\frac{\partial n\left\langle \overline{T_{xy}} \right\rangle_d}{\partial y} - D_x \tag{4.3}$$

In cases of a non-vegetated floodplain ($Cda = 0$) (Figure 4.2a), due to the absence of vegetation, equation (4.1) reduces to:

$$0 = -gD\frac{\partial \zeta}{\partial x} + \frac{1}{\rho}\frac{\partial D\overline{T_{xy}}_d}{\partial y} - D \cdot D_x \tag{4.4}$$

Equation (4.3) was studied by White and Nepf (2007). It was applied to different regions of the channel, finding separate scaling of the inner and outer layers of the mixing layer in a partially vegetated channel (Figure 4.2b). Equation (4.4) was studied by van Prooijen et al. (2005). They proposed a constant mixing length across the compound channel and studied the mixing layer as a whole (Figure 4.2a). These two equations are special cases of the equation (4.1). In floodplain vegetated channels (Figure 4.2c), due to the presence of both the floodplain and the vegetation, equation (4.1) needs to be considered in which the time and depth-averaged transverse shear stress or so-called transverse exchange of downstream momentum ($\left\langle \overline{T_{xy}} \right\rangle_d$) is the most significant term left that needs to be modelled. It is the sum of time, space and depth averaged transverse shear stress due to advective dispersion, turbulence, and viscosity, respectively:

$$\left\langle \overline{T_{xy}} \right\rangle_d = -\rho\left\langle \left(\langle \overline{u} \rangle - \langle \overline{u} \rangle_d\right)\left(\langle \overline{v} \rangle - \langle \overline{v} \rangle_d\right)\right\rangle_d - \rho\left\langle \overline{u'v'} \right\rangle_d - \rho\left\langle \overline{u''v''} \right\rangle_d. \tag{4.5}$$

Where:

- $\langle \overline{u} \rangle_d$,$\langle \overline{v} \rangle_d$ are time, spatially and depth averaged streamwise and transverse velocities.
- u', v' are streamwise and transverse velocity temporal fluctuations, $u' = u - \overline{u}$, $v' = v - \overline{v}$
- u'', v'' are streamwise and transverse velocity spatial fluctuations, $u'' = \overline{u} - \langle \overline{u} \rangle$, $v'' = \overline{v} - \langle \overline{v} \rangle$
- $-\rho\left\langle \left(\langle \overline{u} \rangle - \langle \overline{u} \rangle_d\right)\left(\langle \overline{v} \rangle - \langle \overline{v} \rangle_d\right)\right\rangle_d$ is advective dispersion stresses due to depth variation in the mean flow, $-\rho\left\langle \overline{u'v'} \right\rangle_d$ is Turbulent Reynolds stresses and $-\rho\left\langle \overline{u''v''} \right\rangle_d$ is dispersive stress due to spatial fluctuations.

For flow through and around vegetated regions, at high Reynolds number, the Reynolds stress is the main shear stress. Since the stress contributed from secondary circulations is for most conditions small (van Prooijen et al., 2005) and for the dense arrays, $ad > 0.01$ (Poggi et al., 2004a,b) dispersive stresses are also relatively small. So the time, spatially

and depth-averaged Reynolds shear stress are assumed to account for the total momentum exchange between the open channel and vegetated floodplain area. This means that:

$$\left\langle \overline{T_{xy}} \right\rangle_d \approx -\rho \left\langle \overline{u'v'} \right\rangle_d \tag{4.6}$$

The eddy viscosity concept or Boussinesq approach is usually used to model this turbulent shear stress:

$$\left\langle \overline{T_{xy}} \right\rangle_d \approx -\rho \left\langle \overline{u'v'} \right\rangle_d = \nu_t \frac{d\langle \overline{u} \rangle_d}{dy} \tag{4.7}$$

In this sense, the determination of the transverse exchange of momentum is replaced by the finding of a proper eddy viscosity (ν_t) model.

4.5 Existing Models of Transverse Exchange of Momentum

As quoted in previous sections, numerous momentum exchange models have been developed, in which the LHCSs have been considered as a fundamental element in the lateral momentum exchange between the slow flow and fast flow regions (Nadaoka and Yagi, 1998; Nezu and Onitsuka, 2001; Tamai et al., 1986; Uijttewaal and Booij, 2000; van Prooijen et al., 2005; White and Nepf, 2007, 2008; Xiaohui and Li, 2002; Zong and Nepf, 2010). However, it is not our main aim to discuss all of those here, only the most recent two insightful models of van Prooijen et al. (2005) and White and Nepf (2008) are chosen to be discussed. While the former was developed for the un-vegetated compound channels, the latter is the most up-to-date model developed for the partially vegetated channel without considering the lateral depth variations.

Table 4.1: Two insightful models for the transverse exchange of streamwise Momentum

Model concept	Author	$T_{xy} \approx -\rho \cdot \upsilon_t \cdot \frac{\partial u}{\partial y}$	Note
Effective eddy viscosity concept	van Prooijen et al. (2005)	$\upsilon_t = \alpha\sqrt{c_f}\langle \overline{u} \rangle_d D + \frac{Dm}{D(y)}\beta^2\delta^2 \left\lvert \frac{d\langle \overline{u} \rangle_d}{dy} \right\rvert$	$\alpha = 0.1$ $\beta = 0.07$
Vortex based model	White and Nepf (2008)	$\upsilon_{t\_outer} = 0.7 \cdot u_*^2 \cdot \frac{\delta_2}{U_c - U_m}$ $\upsilon_{t\_inner} = u_*^2 \cdot \frac{\delta_1}{U_0 - U_f}$	$U_m = U(y_m)$

The transverse momentum exchange model, proposed by van Prooijen et al. (2005) including the physics of the LHCSs, appears to be one of the most insightful models for the compound channel without vegetation. In that model, the contribution from the LHCSs and bottom turbulence, as well as the effect of transverse depth variation are considered. Nevertheless, there is no vegetation and the mean streamwise velocity gradient is only caused by the shallowness due to the floodplain region. As a result, in scenarios with vegetation, the model cannot capture the significant reduction in the turbulent length scale due to the high resistance from vegetation and may overestimate the penetration of the flow into the vegetation region (White and Nepf, 2008).

By dividing the mixing layer into different layers (inner layer δ_1, and outer layer δ_2), each has its own length scale and is connected by the matching point (y_m) where continuity of the velocity profile is required, a vortex based model had been proposed by

White and Nepf (2008). That model allows to estimate the maximum penetration of the mixing layer into the cylinder arrays and is considered to be the most advanced model for the channel with partial vegetation. It is also suggested that the penetration scale of the momentum into the vegetation region mainly depends on the vegetation characteristic (or $C_d a$). Other effects are minor and can be neglected. However, in that study, the floodplain was not considered. This means that the shallowness or water depth variations have not been taken into account. The velocity gradient and corresponding LHCSs are only caused by the resistance from the presence of vegetation. As mentioned in previous sections, the vegetated channel without floodplain is only a special case of floodplain vegetated channels with depth ratio equal 1 ($D_r = D_f/D_c = 1$). Neglecting the presence of a floodplain may significantly affect the physical exchange processes. In this sense, which of these models is suitable for vegetated floodplain channel is yet to be determined.

4.6 Experiment set up and general results

An experiment was conducted in the shallow, free-surface flow facility of the Fluid Mechanics Laboratory at the Delft University of Technology. A top view and a cross-section of the experimental setup and some flow features observed during the experiment are shown in Figure 3.1. The detailed experimental configurations, parameters and analyses can be seen in Chapter 3. The main data set is the time-series data of the streamwise velocity $U(y)$ and lateral velocity $V(y)$ along the cross section, which is obtained from a Nortek Acoustic Dopper Velocity meter (ADV). It was used to determined the transverse momentum exchange between the main channel and floodplain.

The experimental results suggested that the increased drag due to vegetation can substantially reduce the local flow velocity, thereby increasing the velocity gradient between the adjacent open channel and the vegetation region, withdrawing more momentum towards the floodplain vegetated region. As a result, the LHCSs formed at the vegetation interface, discovered in vegetated floodplain channels are more pronounced than in cases without vegetation. As the LHCSs move along the vegetation interface, they generate cycloid flow events, which are sweeps, ejections, stagnant and reverse flows.

Figure 4.3 illustrates the represenative experimental results. It is suggested that the increased drag due to vegetation can substantially reduce the local flow velocity, thereby increasing the velocity gradient between the adjacent open channel and the vegetation region, withdrawing more momentum towards the floodplain vegetated region (see Figure 4.3a,b). As the LHCSs move along the vegetation interface, they generate cycloid flow events, which are composed of sweeps, ejections, stagnant and reverse flows. These flow events then divide the shallow flow field of a vegetated compound channel with a gentle slope into three main different regions, which are driven by different physical parameters and have different length scales (Figure 4.3). The uniform region in the main channel (region II) is controlled by the bottom friction (C_f), the corresponding length scale is the water depth (D_c). The uniform region inside the floodplain (region I) is controlled by drag force ($C_d \cdot a$) from the vegetation. The relevant length scales are the cylinder diameter (d) and the distance between cylinders (s), and the water depth (D_f). In between these regions the mixing layer (region III and IV) is governed by the LHCSs. The

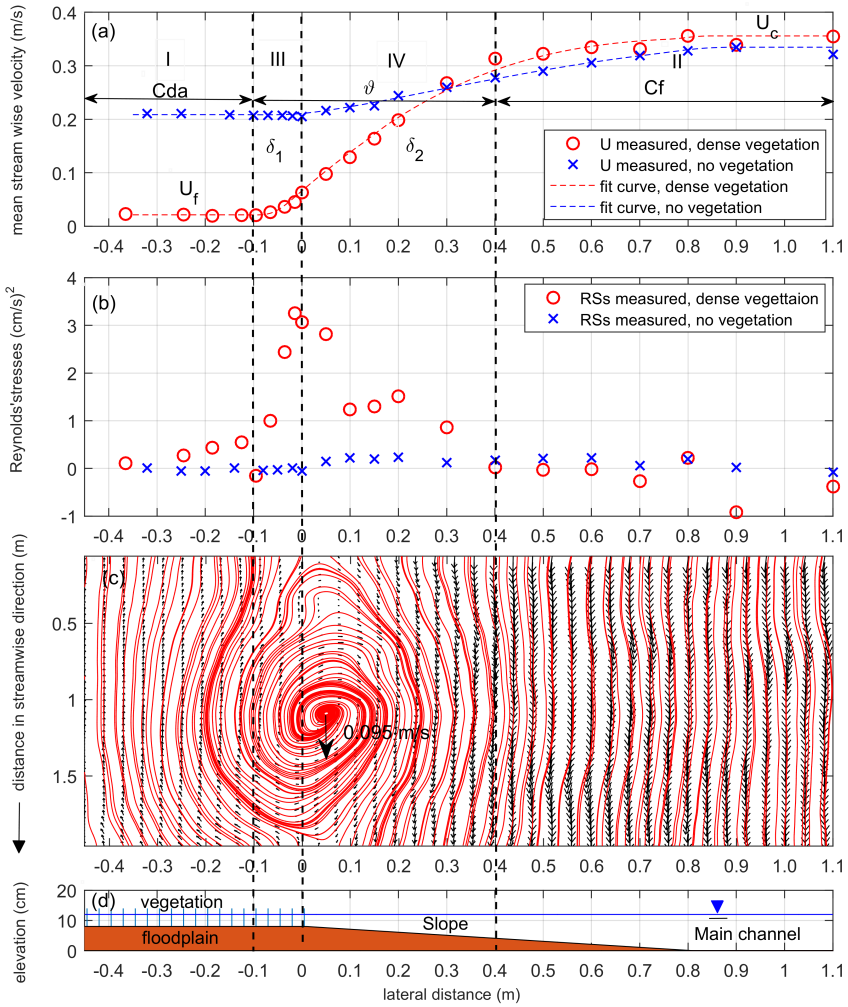

Figure 4.3: Representative mean streamwise velocity (a) and Reynold shear stresses (b) in cases with and without vegetation. The representative LHCSs captured through the streamlines of the instantaneous fluctuating velocity field and its corresponding effect on the mean streamwise velocity (c). Corresponding profile of a vegetated compound channel with a gentle slope (d). Dense scenario, 50 cm floodplain width, discharge = 45 L s^{-1}, water depth =12 cm. The vegetated floodplain starts from y=0 in the negative direction.

corresponding length scales in this region are the width of the penetration into the vegetation (δ_1), the outer layer width (δ_2) and the water depth ($D(y)$). The presence of LHCSs is the key factor in the mixing layer determining the transverse exchange of momentum between the open region (II, IV) and the vegetated region (I, III).

4.7 Quadrant analysis of the cycloid flow field under the effects of LHCSs

A quadrant analysis of the Reynolds shear stress is a simple but useful turbulence data processing technique which is able to provide insightful information on the contribution to the turbulent shear stress from various events in the flows (Kim et al., 1987; Wallace et al., 1972; Willmarth and Lu, 1972). This quadrant analysis technique can also be used to study the organized structures in the channel flow (Kim and Moin, 1986). Therefore, in this section of the paper, the quadrant analysis of the Reynolds shear stresses was performed to examine the connection between the motion of the LHCSs and the associated cycloid flow events as well as their contribution to the total transverse exchange of momentum.

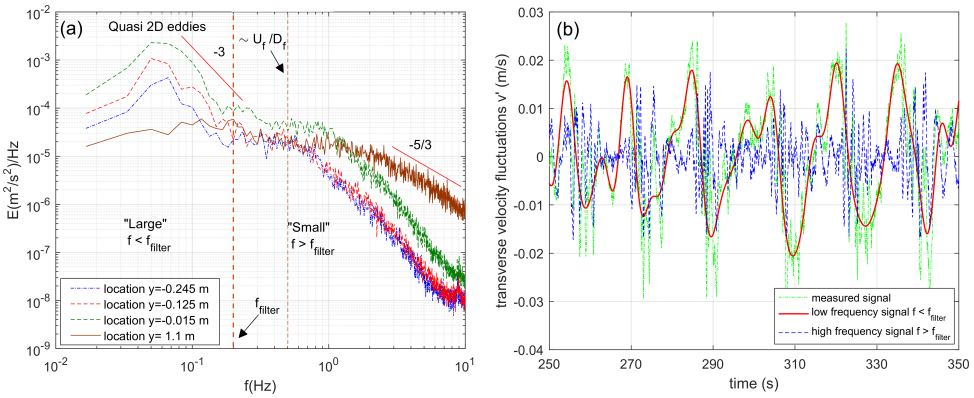

Figure 4.4: (a) Representative power density spectra at different locations along the cross-section. (b) Separation of the "large" and "small" transverse velocity signal by using a filter frequency (f_{filter}=0.2 Hz), location y=−0.125 m for dense scenarios. Case of dense vegetation, floodplain width H=50 cm, discharge Q=45 l/s and water level H=12 cm.

Figure 4.4a illustrates the power density spectra (PDSs) of the lateral fluctuation velocity v' at different locations of the cross-section. It can be clearly seen that in the high-frequency regions of the PDSs at a location in the main channel (y=1.1 m), the decrease in energy density almost follows a slope −5/3 that is indicative of flows with a large inertial subrange. However, inside the vegetation (y=−0.245 m, −0.125 m,−0.015 m) the decrease of the energy density does not properly follow this rule. The presence of vegetation is likely to affect the energy cascade. as the large turbulence structures are more quickly transformed into smaller scale turbulent structures. Additionally, the Reynolds number in this region is not so high (in the range of 1000 to 7500) that a large inertial range is formed. Furthermore, the large-scale structures make the flow to vary over timescales larger than the timescale of the 3D-turbulence. These interactions are likely to cause deviations from the standard Kolmogorov spectrum.

The power density spectra of the transverse fluctuation velocity show definite peaks with a slope -3 corresponding to the quasi 2D large horizontal coherent structures ($f < f_{filter} = 0.2$ Hz) (Uijttewaal and Booij, 2000). These peak regions are associated with the

low frequencies signals (LHCSs) and were separated from the high frequencies signals (Figure 4.4b) using a low pass filter defining the low frequencies ($f < f_{filter}$) and the high frequencies ($f > f_{filter}$). In this way, the Reynolds shear stresses induced by LHCSs (low frequency signal) can be filtered and compared with the total Reynolds shear stresses (Figure 4.5).

Results confirm the dominant contribution of the LHCSs to the total turbulent shear stress. For instance, at the edge of the floodplain vegetated region, Reynolds shear stresses induced by LHCSs contribute more than 90% to the total the Reynolds shear stresses. It is noticed that there is a significant decrease in the value of the Reynolds shear stresses at location $y = -0.1$ m which can be interpreted as the distance of the penetration of the LHCSs into the vegetation area . The remarkable result for y=0.9 m is most likely related to the transition from the sloped bed to the horizontal bed, providing a different role for the smaller scales compared to the large scales. It is noted that the absolute value of RSs induced by the LHCSs ($f < f_{filter}$) may be larger than the absolute value of the total RSs. This means that small scale motions in the flow are correlated differently and thereby may reduce the Reynold shear stress induced by large scale motions. A quadrant analysis of the turbulent fluctuations will therefore shed more light on this behaviour.

The separate low-frequency signals are plotted in the quadrants together with the original measured signals (Figure 4.6 a to d). In this way, the contribution of LHCSs and their associated flow events to the total turbulent stresses can be clearly apprehended. Figure 4.6 shows results, for different locations in the cross sections of the vegetated compound channel; from the vegetated floodplain edge (a) to inside the vegetation (c) and in the main open channel (d). According to the sign of u' and v', the quadrant analysis divides the Reynolds shear stresses into four quadrants (I-Q1, II-Q2, III-Q3, IV-Q4).

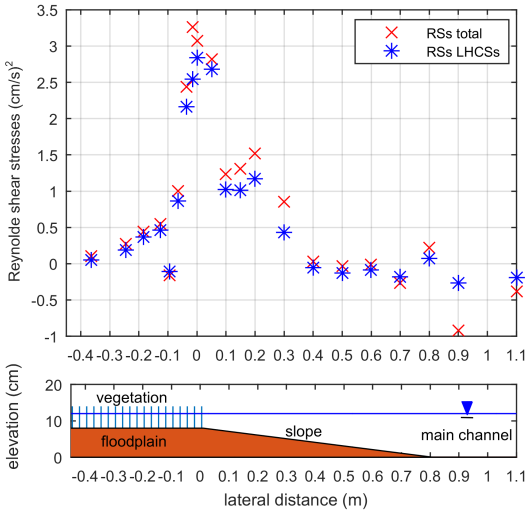

Figure 4.5: RSs induced by the LHCSs compared to total RSs in the case of dense vegetation, floodplain width H=50 cm, discharge Q=45 l/s and water level H=12 cm..

These four quadrants are associated with four different events,namely outward interactions ($u' > 0, v' > 0$) , ejections ($u' < 0, v' > 0$), inward interactions ($u' < 0, v' < 0$) and sweeps ($u' > 0, v' < 0$), respectively. While the Q2 and Q4 motions, which are related to the ejection and sweep events can be clearly visualized, the Q1 and Q3 motions, which are linked to the outward and inward interactions are lacking a descriptive terminology and are less obviously visualized (Wallace, 2016).

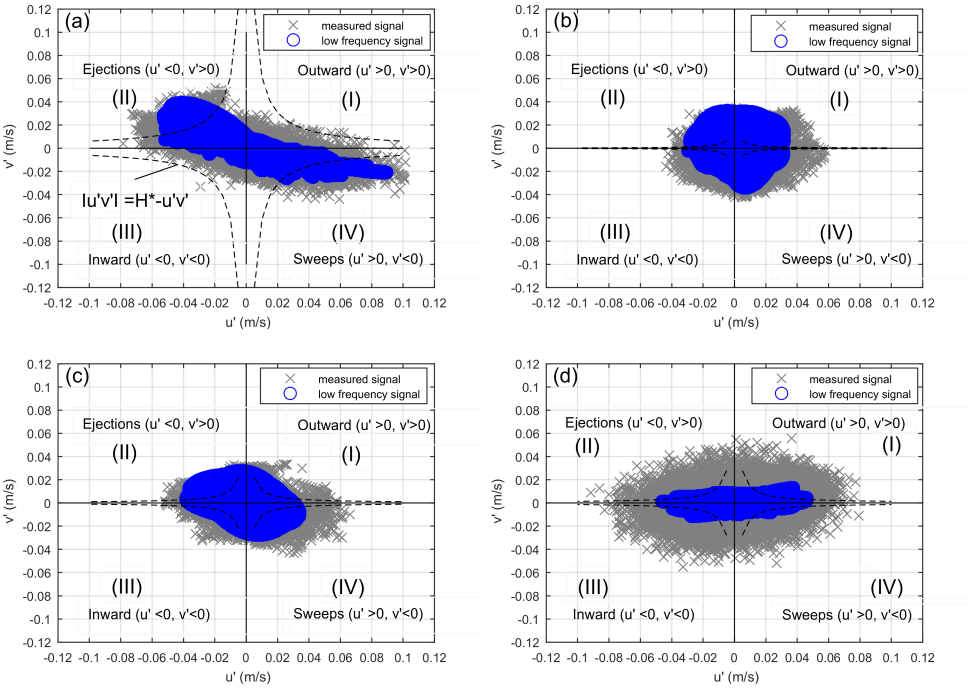

Figure 4.6: The representative distribution of (u',v') measured the low frequency signal for dense scenarios, q45h12 : at location $y = 0$ m (at the vegetation interface) , $H = 2$ (a) ; $y = -0.015$ m , H=2 (b) ; $y = -0.065$ m (inside the vegetation), H=2 (c) ; $y = 1.25$ m (in the main open channel), H=5 (d); The dashed lines in the figure represent hyperbolas corresponding to $|u'v'| = H \cdot (-\overline{u'v'})$.

It is clear that the distribution in the quadrants of flow events associated with the LHCSs (low-frequency signals) are different from the floodplain edge toward the region inside the vegetation. At the edge of the vegetated floodplain (Figure 4.6a) the distribution of (u',v') corresponding to the "large" structures is mainly found in Q2 and Q4. This means that the dominant events are the ejection (Q2) and the sweep (Q4) implying that the exchange of momentum happens strongest at the edge of the floodplain, mediated by sweeps and ejections. This result is also in line with the observations in the partially vegetated channel of White and Nepf (2007, 2008). However, deeper inside the vegetation (Figure 4.6b,c), the contributions of the signal in Q2 and Q4 become smaller, and those in Q1 and Q3 larger. This means that the momentum exchange at these locations or the effect of LHCSs is smaller. In the main channel (Figure 4.6d), as there is no LHCSs at this location, the presence of LHCSs associated with sweep and ejection events cannot

be observed. Although there are many events associated with large u'v', their average is almost zero which implies that there is virtually no transverse momentum exchange at this location.

4.8 Modelling Transverse Momentum Exchange in Vegetated Floodplain Channel

As described in previous sections, the total momentum exchange between the open channel and vegetated floodplain area is mainly represented by the time, depth and spatially-averaged turbulence shear stress: $\left\langle \overline{T_{xy}} \right\rangle_d \approx -\rho \left\langle \overline{u'v'} \right\rangle_d$. In this study, by following footprints of the effective eddy viscosity model of van Prooijen et al. (2005) and the concept of eddy viscosity model inside the cylinder arrays given by Kean and Smith (2013), a new hybrid eddy viscosity model to estimate $\left\langle \overline{T_{xy}} \right\rangle_d$ is proposed and validated using different experimental data sets.

The eddy viscosity model that was proposed for a compound channel without vegetation is used as a starting point. According to van Prooijen et al. (2005), the eddy viscosity is the contribution of two separate components, the eddy viscosity related to the bottom turbulence (v_t') and the eddy viscosity associated with the LHCSs (v_t'') and $v_t = v_t' + v_t''$. Both contributions are modelled as the product of a typical length and velocity scale LU related to their underlying mechanisms. The Elder formulation is adopted for the contribution by the bottom turbulence part (van Prooijen et al., 2005):

$$v_{t_p}'(y) = \alpha D \sqrt{c_f} \langle \overline{u} \rangle_d \tag{4.8}$$

Where α is a constant of the order of 0.1 (Fischer et al., 1979). The Prandtl's mixing length model is used to model the contribution of LHCSs to the total momentum exchange. Moreover, an extra factor which depends on the local water depth is incorporated in the model for the eddy viscosity related to the LHCSs (van Prooijen et al., 2005). The expression of the eddy viscosity linking to the LHCSs' part then reads:

$$v_{t_p}''(y) = \frac{Dm}{D(y)} \beta^2 \delta^2 \left| \frac{d\langle \overline{u} \rangle_d}{dy} \right| \tag{4.9}$$

In which β is a proportionality constant and δ is the mixing length. $D(y)$ is local water depth; D_m is the mean water depth; $D_m = \frac{D_c + D_f}{2}$; D_c is water depth in the channel , D_f is water depth in the floodplain channel.

In non-vegetated floodplain channels, the role of water depth ratio ($D_r = D_f / D_c$) has been acknowledged as it is shown to be associated with an increased shear rate and the consequent appearance of the LHCSs (Knight et al., 2007; Nezu et al., 1999). In vegetated channels, as the presence of vegetation appears to control the velocity gradient and thus the appearance of the LHCSs, the role of the water depth ratio D_r has received much less attention. It is noted that LHCSs originally arise from the Kelvin-Helmholtz (KH) instability caused by the velocity gradient in the flow field. The differences in water depth or the drag from vegetation are elements contributing to this. Furthermore, the water

depth ratio (D_r) is directly related to the vertical compression of the LHCSs, and thereby may have an influence on the spreading of the LHCSs. These effects of the water depth ratio on the manifestation of the LHCSs can be accounted for by multiplying with D_r^2. The eddy viscosity associated with the manifestation of LHCSs then can be expressed as:

$$v_t{}''(y) = \frac{Dm}{D(y)}(D_r\beta)^2\delta^2\left|\frac{d\langle\overline{u}\rangle_d}{dy}\right| \tag{4.10}$$

It is noted that vt'' depends on the velocity gradient (du/dy). In a single channel without floodplain and vegetation ($du/dy = 0$), the LHCSs cannot be generated and thereby $vt'' = 0$. Finally, the total eddy viscosity in non-vegetated compound channels can be written as:

$$v_t = \alpha\sqrt{c_f}\langle\overline{u}\rangle_d D + \frac{Dm}{D(y)}D_r{}^2\beta^2\delta^2\left|\frac{d\langle\overline{u}\rangle_d}{dy}\right| \tag{4.11}$$

In studied scenarios, *i.e.* compound channel, compound vegetated channel and partially vegetated channel, the K-H instabilities are triggered primarily in the velocty gradient due to the water depth difference between the floodplain and adjacent channel region or the presence of the vegetation. The bottom friction only limits the growth of the mixing layer. Therefore the interaction between the two terms in Equation (4.11) is neglected and they can be considered independent.

In the literature, the mixing layer width can be estimated from the experimental data as the velocity difference between the main channel and the floodplain divided by the velocity gradient at the centre of the velocity profile (Uijttewaal and Booij, 2000): $\delta = \frac{U_c - U_f}{(\partial U/\partial y)_{\max}}$. In order to take into account the asymmetry in the velocity profile, the mixing layer width is determined from the distance between position $y_{90\%}$ and $y_{10\%}$ (Pope, 2000): $\delta = y_{90\%} - y_{10\%}$. or position $y_{25\%}$ and $y_{75\%}$ (van Prooijen et al., 2005): $\delta = 2\cdot\left(y_{75\%} - y_{25\%}\right)$ where $U(y_{x\%}) = U_f + x\%\cdot(U_c - U_f)$. However, these ways of determining the mixing layer width still do not well capture the asymmetrical feature of the mean streamwise velocity profile as there is usually a sharp decrease in the flow velocity near the vegetation edge (White and Nepf, 2007). Moreover, the penetration of the mixing layer into the vegetation region is not determined. Therefore, separating the mixing layer into two layers appears to be a better approach. In this way, the mixing layer width includes the penetration length scale of the mixing layer into the vegetation and the outer layer width can be calculated according to: $\delta_I \approx \max(0.5\cdot Cda^{-1}, 1.8\cdot d)$ and $\delta_o = \frac{U_c - U_m}{(dU/dy)_{ym}}$, where y_m is the matching point and $U_m = U(y_m)$ (White and Nepf, 2008). Still, the determination of the mixing layer width in this way is not likely to be consistent, and it is also unclear to what extent the accuracy of the penetration was considered.

In compound vegetated channels, the mean streamwise velocity profiles are also asymmetrical. At the edge of the vegetated floodplain, there is a sharp decrease corresponding to an inflection point in the velocity profile, which implies the effect of the shallower floodplain area and the presence of vegetation. Therefore, the mixing layer is divided into 2 layers, corresponding to the penetration layer and the outer layer: $\delta = \delta_1 + \delta_2$ (Figure 4.7). The penetration width of the mixing layer into the vegetation is defined as the distance required for the flow velocity to achieve a constant value inside the floodplain (U_f) plus an error of 5%. In other words, the penetration is the distance from

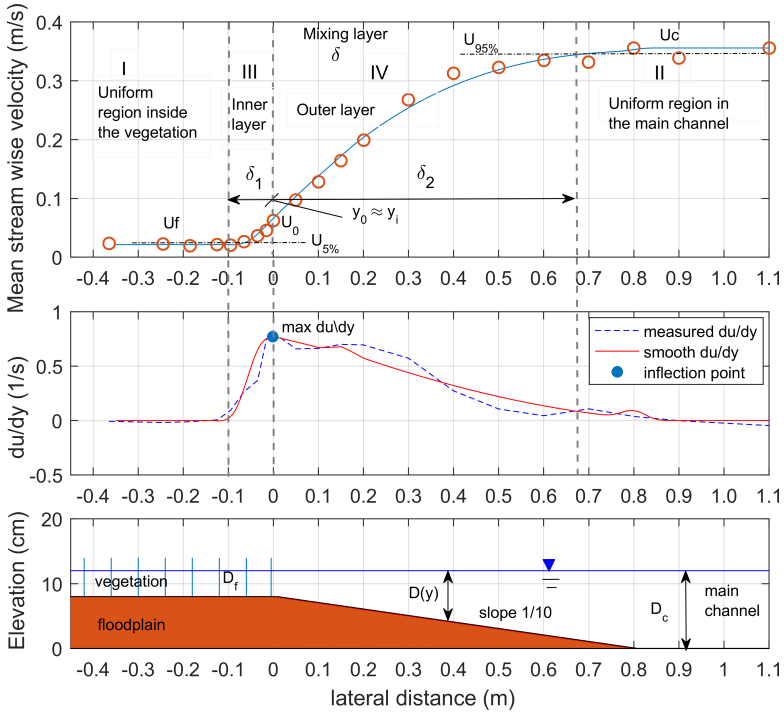

Figure 4.7: Representative mean streamwise velocity profile in cases with the consideration of vegetation. The most interesting region is the mixing layer, including the penetration (δ_1) or inner layer part and the outer layer part (δ_2). Q=45 L s^{-1}, H=12 cm, width= 50 cm.

the position where the mean stream wise velocity is 5% different from the uniform mean stream wise velocity further inside the floodplain (U_f) to the vegetated floodplain edge: $\delta_1 = y_0 - y_{5\%}$ and $U_{5\%} = U_f + 5\% \cdot U_f$. A similar rule is also applied for the outer layer width: $\delta_2 = y_{95\%} - y_0$ and $U_{95\%} = U_c - 5\% U_c$. This definition of the mixing layer width is consistent and allows to determine the penetration precisely without any ambiguity. A typical streamwise velocity distribution is shown in Figure 4.7. y_0 is the point at the edge of the vegetated floodplain ($y = 0$ m). The point where the velocity gradient dU/dy reach its maximum value is the inflection point y_i. As y_i and y_0 are almost the same in all cases in the presence of vegetation, it can be considered that $y_i \approx y_0$.

The presence of vegetation can be taken into account by following the work of Kean and Smith (2013). Inside the vegetation, the eddy viscosity associated with the presence of vegetation (υ_{tv}) is determined from the production of turbulent kinetic energy by the flow through the stems and can be determined as:

$$\upsilon_{tv}(y) = \frac{1}{8} {C_t}^{-2} C_d d \langle \overline{u} \rangle_d \tag{4.12}$$

Where C_t is a constant of proportionality, the value of it depends on the shape of the streamwise velocity profile, usually $C_t = 1$; C_d is the drag coefficient of a single stem,

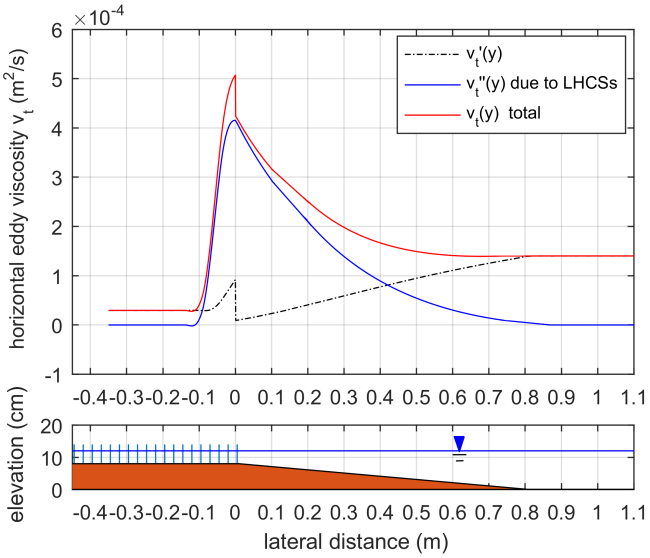

Figure 4.8: Eddy viscosity profile determined according to the hybrid eddy viscosity model and based on the measured velocity profile, in case of dense cylinder, Q=45 L s^{-1}; H=12 cm and floodplain width W=50 m.

theoretically $C_d = 1$. In this way, the eddy viscosity within the vegetation region including the part due to bottom friction, can be determined as:

$$v_t'(y) = \alpha\sqrt{c_f}\langle\overline{u}\rangle_d D + \frac{1}{8}{C_t}^{-2} C_d d\langle\overline{u}\rangle_d \tag{4.13}$$

Finally, with the presence of vegetation and LHCSs the total eddy viscosity can be calculated according to equation (4.14). It is also noticed that in cases without vegetation, equation (4.14) becomes equation (4.11). Figure 4.8 illustrates the eddy viscosity determined theoretically from equation (4.14) in cases of dense vegetation, floodplain width H=50 cm, discharge Q=45 L s^{-1} and water level H=12 cm.

$$v_t = \begin{cases} \alpha\sqrt{c_f}\langle\overline{u}\rangle_d D + \frac{Dm}{D(y)} {D_r}^2\beta^2\delta^2\left|\frac{d\langle\overline{u}\rangle_d}{dy}\right| & \text{(outside vegetation)} \\ \underbrace{\alpha\sqrt{c_f}\langle\bar{u}\rangle_d D}_{Elder} + \underbrace{\frac{1}{8}{C_t}^{-2} C_d d\langle\bar{u}\rangle_d}_{vegetation\ drag} + \underbrace{\frac{D_m}{D(y)} {D_r}^2\beta^2\delta^2\left|\frac{d\langle\bar{u}\rangle_d}{dy}\right|}_{LHCSs} & \text{(inside vegetation)} \end{cases} \tag{4.14}$$

4.9 Comparison with the experimental data

IN this section, the hybrid eddy viscosity model is validated using different experimental data sets, including the current experiment of compound channels with and with-

out vegetation, three representative experimental cases of White and Nepf (2007) in partially vegetated channels and the experimental results of Lambert and Sellin (1996) and Ervine et al. (2000) in compound channels without vegetation. Additionally, the transverse shear stresses determined from the hybrid eddy viscosity model was compared with that calculated from the eddy viscosity models of White and Nepf (2008) and van Prooijen et al. (2005). The results show the applicability of the hybrid eddy viscosity model.

To begin with, as the measured and collected data include the Reynolds shear stresses ($-\left\langle \overline{u'v'} \right\rangle_d$), the measured momentum transfer is determined by:

$$T_{xymeasure} = -\rho \cdot \left\langle \overline{u'v'} \right\rangle_d. \tag{4.15}$$

Furthermore, as described in the previous sections, the theoretical eddy viscosity model (υ_t) was determined from equation (4.14). In all scenarios, the depth average mean streamwise velocity profiles along the cross section of the flume were plotted. Within the vegetation area, the velocity was spatially averaged to remove cylinder-scale spatial fluctuations in the arrays. A 4th order polynomial line was drawn through the measurement points. Then, following the definitions in the previous section, the velocity gradient, the inner layer width, outer layer width and the width of the mixing layer were determined. Finally, the transverse shear stresses based on the hybrid eddy viscosity model (T_{xy1}) were determined using:

$$T_{xy1} = -\rho \cdot \upsilon_t \cdot \frac{\partial U}{\partial y}. \tag{4.16}$$

Moreover, the transverse shear stresses were also determined from the vortex based model of White and Nepf (2008) (T_{xy2}) in scenarios with vegetation, and from the effective eddy viscosity concept of van Prooijen et al. (2005) for cases of compound channel flows without vegetation (T_{xy3}) (definitions in Table 4.1). Figure 4.9 illustrates the validation and comparison of the transverse momentum exchange determined from the different eddy viscosity models. Representative results for different scenarios are presented in the Appendix (Figure B.1 to Figure B.10). The complete set is presented in the supplementary material of this paper.

In cases of compound vegetated channels, it is shown is that the model of White and Nepf (2008) produces a relatively good result of the transverse momentum exchange. However, it is likely to overestimate the peak of the lateral momentum transfer, the momentum transfer inside the vegetation, and the momentum transfer in the outer layer. In cases of compound channels, the model of van Prooijen et al. (2005) significantly overestimates the lateral momentum exchange.

It is suggested that by changing only the values of the proportional coefficient (β) with an average value of 0.0625 for mild slopes, the depth-averaged transverse momentum exchange determined from the hybrid eddy viscosity model can be made to fit with different experimental data sets, including the 32 scenarios of the current experiment and three representative scenarios of partially vegetated channels. In the scenarios of unvegetated compound channels of Lambert and Sellin (1996) and Ervine et al. (2000), the β values increased to about 0.42 The difference in the transition slope is likely to

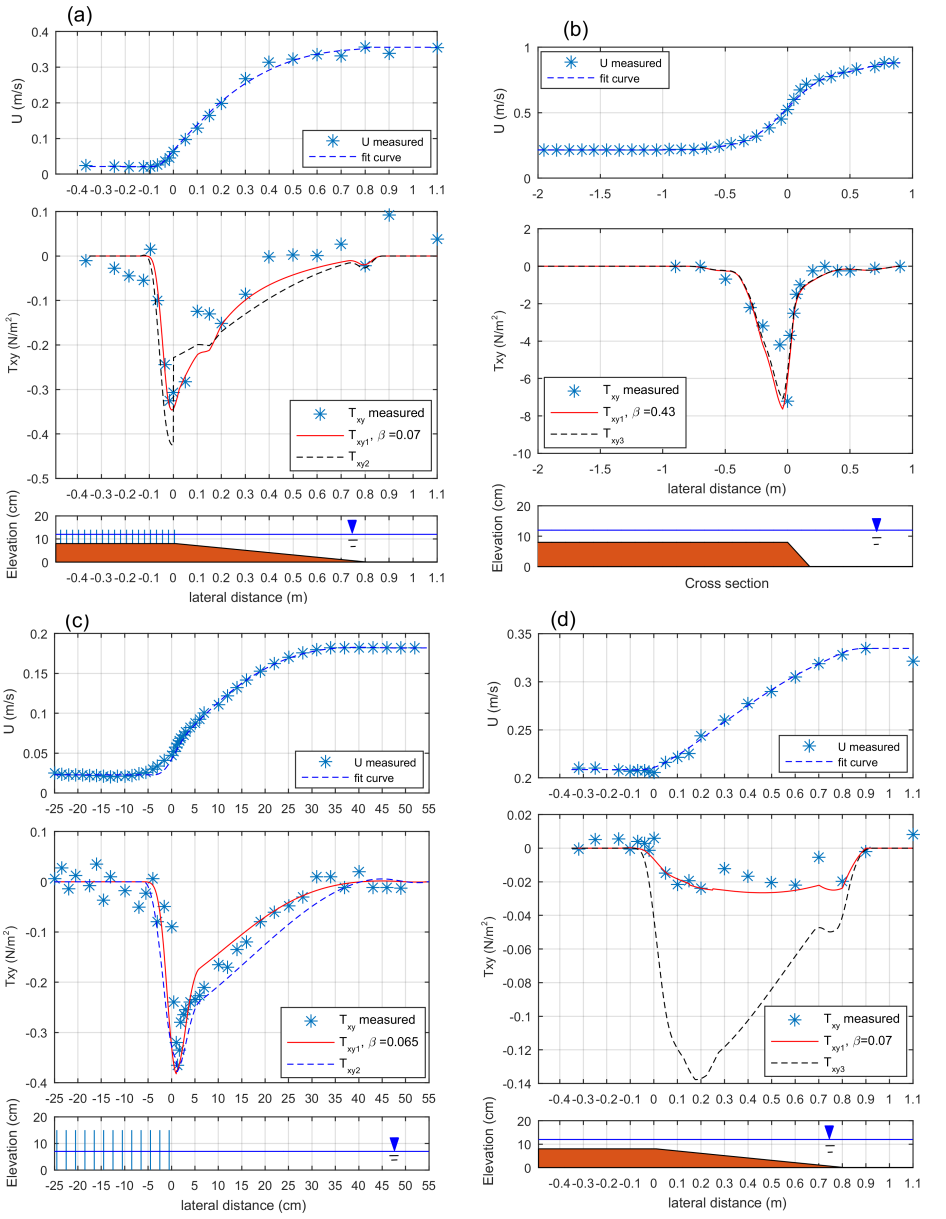

Figure 4.9: Comparison of transverse momentum exchange between the measurement data ($T_{xy}measured$), eddy viscosity model of White and Nepf (2008) (T_{xy2}), the new hybrid eddy viscosity model (T_{xy1}) and the effective eddy viscosity of van Prooijen et al. (2005) (T_{xy3}) in the current experiment, case Ad1 and An1: dense and no vegetation, Q=45 Ls^{-1}; H=12 cm and floodplain width W=50 m (left upper panel and right lower panel, respectively); in the experiment of Lambert and Sellin (1996) (right upper panel); and in the experiment of White and Nepf (2007), case I (left lower panel).

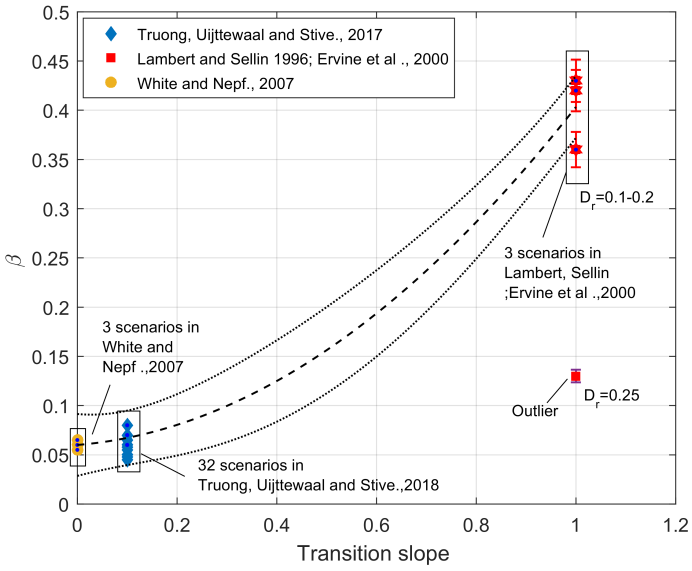

Figure 4.10: A possible relationship between the beta and the transition slope based on the three representative scenarios from White and Nepf (2007), 32 scenarios from the current study and 3 scenarios from Lambert and Sellin (1996) and Ervine et al. (2000) (in total 38 scenarios), dash line: fitted curve; dot line: prediction bound.

be the main reason for the increase of the β value. A possible relationship between the β value and the transition slope can be seen in Figure 4.10, with only one scenario of a compound channel without vegetation (slope 1:1, D_r=0.25), in which the value of β significantly drops to about 0.13. It is noticed that for a steep slope, as the water depth increases, the contribution of secondary circulations to the momentum exchange increases, and becomes dominant over the contribution of the turbulent mixing (Tominaga and Nezu, 1991; Vermaas et al., 2011). Therefore, this outlier of the β value is likely to be due to the effect of the secondary flow triggered by the increased water depth, which was not included in the current hybrid model.

4.10 Conclusions

In a vegetated compound channel, the transverse exchange of mass and momentum between the open main channel and the region of vegetation governs the sediment and nutrient transport, which has lots of ecological implications. The presence of the LHCSs and their associated cycloid flow events are the major factors contributing to this momentum exchange. However, the understanding of this phenomenon is still incomplete. As a result, the momentum exchange models developed in previous studies appear to be not applicable for different scenarios as their validity is usually restricted to a particular experiment data set.

In this study, with the purpose of getting insight into the transverse momentum ex-

change, a unique experiment has been conducted. Based on the results of the experiment, a quadrant analysis of the Reynolds shear stresses has been performed. The results revealed the connection between the LHCSs, their associated flow events and the transverse momentum exchange. Moreover, the appearances of the cycloid flow events as well as the way in which different locations in the flow field are affected by the LHCSs were analysed. The most up-to-date momentum exchange models were reviewed and verified with the data from the experiment. A new hybrid eddy viscosity model is proposed and validated using different experiment data sets. The results suggested that by varying only a coefficient of proportionality β related to the forcing of the mixing layer, which significantly depends on the transition slope, the transverse momentum exchange can be well modelled for quite a range of different set-ups and scenarios of compound channels with or without vegetation. Limitations are still found for steep slope cases where secondary circulation can play a significant role in the momentum transport.

Now the generic applicability of the viscosity estimation has been demonstrated, it can be used as a turbulent model representing the large scale structures in numerical simulations of compound channel flow. The numerical model can be run first with traditional eddy viscosity model such as Elder formulation. Based on the simulation results, the presence of LHCSs can be checked, and the shear-layer width can be determined. This value can be used to iteratively calculate the eddy viscosity according to the hybrid eddy viscosity model and imposed again into the constructed model to improve the results in terms of velocity and especially the Reynold shear stress. This will be the subject of Chapter 5.

References

Adrian, R. J. and Marusic, I. (2012). Coherent structures in flow over hydraulic engineering surfaces. *Journal of Hydraulic Research*, 50(5):451–464.

Bousmar, D. (2002). Flow modelling in compound channels. *Uniré de Génie Civil et Environnemental*.

Chen, D. and Jirka, G. H. (1997). Absolute and convective instabilities of plane turbulent wakes in a shallow water layer. *Journal of Fluid Mechanics*, 338:157–172.

Drazin, P. G. and Reid, W. H. (2004). *Hydrodynamic stability*. Cambridge university press.

Ervine, D. A., Babaeyan-Koopaei, K., and Sellin, R. H. (2000). Two-dimensional solution for straight and meandering overbank flows. *Journal of Hydraulic Engineering*, 126(9):653–669.

Fernandes, J., Leal, J., and Cardoso, A. (2014). Improvement of the lateral distribution method based on the mixing layer theory. *Advances in Water Resources*, 69:159–167.

Fischer, H. B., List, E. J., Koh, R., Imberrger, J., and Brooks, N. (1979). In *Mixing in Inland and Coastal Waters*. Academic Press, San Diego.

Helmiö, T. (2004). Flow resistance due to lateral momentum transfer in partially vegetated rivers. *Water Resources Research*, 40(5).

Ikeda, S., Izumi, N., and Ito, R. (1991). Effects of Pile Dikes on Flow Retardation and Sediment Transport. *Journal of Hydraulic Engineering-asce - J HYDRAUL ENG-ASCE*, 117.

Kean, J. W. and Smith, J. D. (2013). *Flow and Boundary Shear Stress in Channels with Woody Bank Vegetation*, pages 237–252. American Geophysical Union.

Kim, J. and Moin, P. (1986). The structure of the vorticity field in turbulent channel flow. part 2. study of ensemble-averaged fields. *Journal of Fluid Mechanics*, 162:339–363.

Kim, J., Moin, P., and Moser, R. (1987). Turbulence statistics in fully developed channel flow at low reynolds number. *Journal of fluid mechanics*, 177:133–166.

Knight, D., Aya, S., Ikeda, S., Nezu, I., and Shiono, K. (2007). *Flow and sediment transport in compound channels, the experiences of Japanese and UK Research*, chapter 2:Flow structure, pages 5–113. CRC Press.

Lambert, M. and Sellin, R. (1996). Discharge prediction in straight compound channels using the mixing length concept. *Journal of Hydraulic Research*, 34(3):381–394.

Mazda, Y., Wolanski, E., King, B., Sase, A., Ohtsuka, D., and Magi, M. (1997). Drag force due to vegetation in mangrove swamps. *Mangroves and Salt marshes*, 1:193–199.

Nadaoka, K. and Yagi, H. (1998). Shallow-Water Turbulence Modeling and Horizontal Large-Eddy Computation of River Flow. *Journal of Hydraulic Engineering*, 124(5):493–500.

Nepf, H. (1999). Drag, turbulence, and diffusion in flow through emergent vegetation. *Water resources research*, 35(2):479–489.

Nezu, I. and Onitsuka, K. (2001). Turbulent structures in partly vegetated open-channel flows with LDA and PI V measurements. *Journal of Hydraulic Research*, 39(6):629–642.

Nezu, I., Onitsuka, K., and Iketani, K. (1999). Coherent horizontal vortices in compound open-channel flows. *Hydraulic Modeling (ed. VP Singh, IW Seo & JH Sonu)*, pages 17–32.

Nezu, I. and Sanjou, M. (2008). Turburence structure and coherent motion in vegetated canopy open-channel flows. *Journal of hydro-environment research*, 2(2):62–90.

Pasche, E. and Rouve, G. (1985). Overbank Flow with Vegetatively Roughened Flood Plains. *Journal of Hydraulic Engineering*, 111(9):1262–1278.

Phan, L. K., van Thiel de Vries, J. S., and Stive, M. J. (2015). Coastal Mangrove Squeeze in the Mekong Delta. *Journal of Coastal Research*, 300:233–243.

Poggi, D., Katul, G., and Albertson, J. (2004a). A note on the contribution of dispersive fluxes to momentum transfer within canopies. *Boundary-layer meteorology*, 111(3):615–621.

Poggi, D., Porporato, A., Ridolfi, L., Albertson, J., and Katul, G. (2004b). The effect of vegetation density on canopy sub-layer turbulence. *Boundary-Layer Meteorology*, 111(3):565–587.

Pope, S. (2000). *Turbulent Flows*. Cambridge University Press.

Talstra, H. (2011). *Large-scale turbulence structures in shallow separating flows*. PhD thesis.

Tamai, N., Asaeda, T., and Ikeda, H. (1986). Study on Generation of Periodical Large Surface Eddies in a Composite Channel Flow. *Water Resources Research*, 22(7):1129–1138.

Tominaga, A. and Nezu, I. (1991). Turbulent structure in compound open-channel flows. *Journal of Hydraulic Engineering*, 177(1):21–41.

Truong, S. H., Ye, Q., and Stive, M. J. (2017). Estuarine mangrove squeeze in the mekong delta, vietnam. *Journal of Coastal Research*, pages 747–763.

Uijttewaal, W. and Booij, R. (2000). Effects of shallowness on the development of free-surface mixing layers. *Physics of fluids*, 12(2):392–402.

Van Prooijen, B. (2004). *Shallow mixing layers*. PhD thesis.

van Prooijen, B., Battjes, J. A., and Uijttewaal, W. (2005). Momentum Exchange in Straight Uniform Compound Channel Flow. *Journal of Hydraulic Engineering*, 131(3):175–183.

Vermaas, D., Uijttewaal, W., and Hoitink, A. (2011). Lateral transfer of streamwise momentum caused by a roughness transition across a shallow channel. *Water resources research*, 47(2).

Vionnet, C. A., Tassi, P. A., and Martín Vide, J. P. (2004). Estimates of flow resistance and eddy viscosity coefficients for 2D modelling on vegetated floodplains. *Hydrological Processes*, 18(15):2907–2926.

Wallace, J. M. (2016). Quadrant analysis in turbulence research: history and evolution. *Annual Review of Fluid Mechanics*, 48:131–158.

Wallace, J. M., Eckelmann, H., and Brodkey, R. S. (1972). The wall region in turbulent shear flow. *Journal of Fluid Mechanics*, 54(1):39–48.

White, B. L. and Nepf, H. M. (2007). Shear instability and coherent structures in shallow flow adjacent to a porous layer. *Journal of Fluid Mechanics*, 593:1–32.

White, B. L. and Nepf, H. M. (2008). A vortex-based model of velocity and shear stress in a partially vegetated shallow channel. *Water Resources Research*, 44(1).

Willmarth, W. and Lu, S. (1972). Structure of the reynolds stress near the wall. *Journal of Fluid Mechanics*, 55(1):65–92.

Xiaohui, S. and Li, C. W. (2002). Large eddy simulation of free surface turbulent flow in partly vegetated open channels. *International Journal for Numerical Methods in Fluids*, 39(10):919–938.

Zong, L. and Nepf, H. (2010). Flow and deposition in and around a finite patch of vegetation. *Geomorphology*, 116(3-4):363–372.

Chapter 5

Numerical modelling

At it's heart,
Engineering is about using science to find creative practical solutions.

Queen Elizabeth II

The presence of large horizontal coherent structures (LHCSs) at the vegetation interface was shown to be of primary importance with regards to the transverse exchange processes. However, most advanced knowledge obtained in this field is primarily based on laboratory studies and numerical models that can well reproduce the physics at prohibitive computational cost in terms of practical engineering. Although depth averaged numerical models (2DH models) have been applied widely to model quasi-steady flow patterns in rivers, estuaries and coasts, the extent to which a 2DH model can be trustworthy in the context of the presence of the LHCSs is not yet determined. In this paper, the capability of 2DH models in modelling the shallow flows in a compound vegetated channel was studied. The shallow water solver of Delft3D was used. Based on that, a 2DH numerical model mimicking a physical model of a compound vegetated channel was constructed. The model results were then compared with the experimental results, showing the limitation of the 2DH models. Then, the numerical model was improved by adopting a semi-analytical hybrid eddy viscosity model including the occurrence of the LHCSs. Finally, the utilization of the 2DH model for real scenarios of vegetated compound channel was examined and the philosophies learned at small laboratory scales were applied.

This chapter is in preparation to submit to Journal of Hydraulic Engineering. Truong, S.H., Uijttewaal, W.S.J., and Stive, M. J. (2018). A numerical study of cycloid flow field induced by Large horizontal coherent structures in vegetated compound channels.

In this chapter of the thesis, a numerical study of the hydrodynamics in a vegetated compound channel flow, mimicking the laboratory experiment was performed. The numerical results were extracted and analysed, indicating the applicability of the 2DH model on a larger real scale.

5.1 Introduction

Estuarine mangrove forests along the Mekong river have been squeezed into narrow strips of about 50 m. In this squeeze condition, the hydrodynamics of a mangrove forest is similar to that of a compound vegetated channel (see Figure 5.1)(Truong et al., 2017). The average water depth-width and the depth-length ratio are as small as 1:100 (Truong et al., 2017), the flow field in this condition can be considered as a shallow flow field (Jirka and Uijttewaal, 2004).

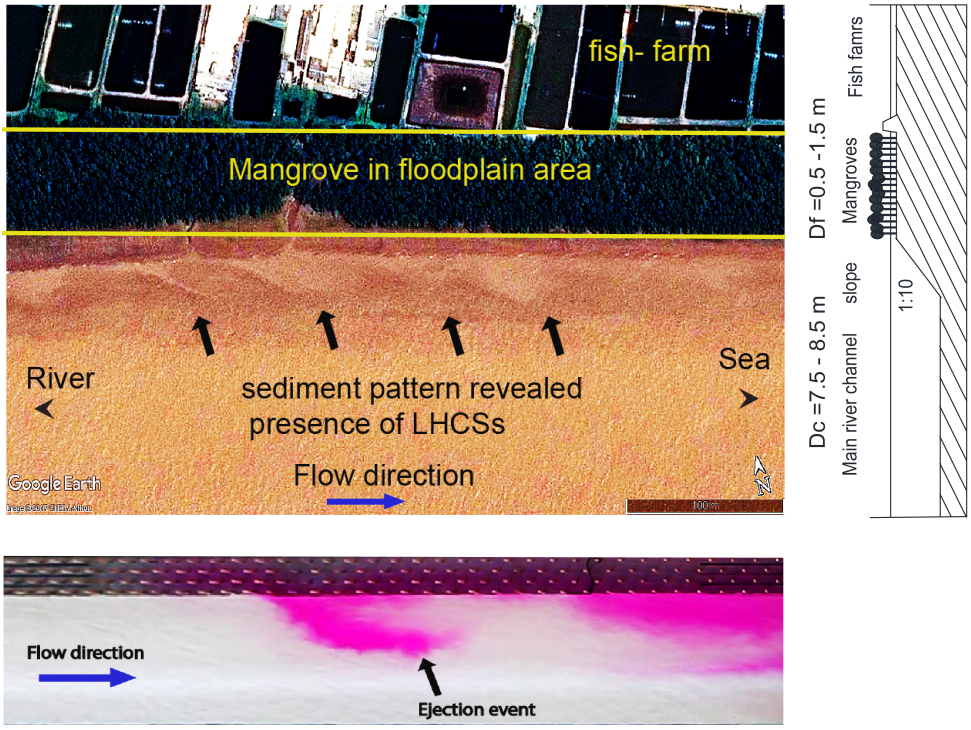

Figure 5.1: Typical mangroves distribution along a straight part of Tieu estuary, Vietnam and the associated schematised bathymetry. Fish farms constructed close to the water boundary push the mangrove into a narrow fringe zone. This area is suffering from erosion with a rate of about 2.5 myr^{-1}(Truong et al., 2017). The flow events in the mixing layer which were observed in the experiment can also be seen in real scale through the pattern of sediment.

In a compound vegetated channel, the presence of large horizontal coherent structures (LHCSs) at the vegetation interface is of primary importance in terms of river bank stability, sedimentation, and nutrient transport (White and Nepf, 2007). The presence

of vegetation in the floodplain area adds to friction and drag forces, and significantly reduces the flow velocity inside the forest. As a result, the magnitude of the velocity gradient between the vegetation and open channel region substantially increases, and a mixing layer develops at the vegetation interface. A shear instability, the Kelvin-Helmholtz (K-H) instability, then can be triggered, inducing LHCSs (Nezu and Onitsuka, 2001; Tamai et al., 1986; van Prooijen et al., 2005; White and Nepf, 2007, 2008; Zong and Nepf, 2010). As these LHCSs move along the vegetation interface, they generate cycloid flow events, namely sweeps, ejections, stagnant and reverse flows. These events then determine the behaviour of the surrounding flow field, and promote significant transverse exchange of momentum between the vegetation and adjacent open channel (Truong et al., 2018).

Nevertheless, studies and knowledge obtained on this topic, mostly have been restricted to a laboratory scale, in which rules of similitude were violated apart from the obvious Reynolds number limitation. For instance, in the experiment of Truong et al. (2018), although the vegetation drag ($C_d.a$) and the transition slope (m) in the experiment were almost the same as in the reality, the ratio of the water depth between the floodplain and main channel region (D_r) was different. While in the reality, the D_r is as small as 0.06 (Truong et al., 2017), that in the flume is about 0.33. Consequently, although the presence of LHCSs in the compound vegetated channel on a small experimental scale is confirmed, the existence of these LHCSs in the real estuarine river channel is still uncertain.Therefore, whether or not knowledge obtained from the small scale is still valid for a vegetated channel on the large scale of an estuarine river channel has not yet been determined (Nepf, 2012).

In the literature, well validated numerical models provide an effective tool to fullfill this knowledge gap. The presence of LHCSs was successfully captured at the interface of a porous layer in a numerical simulation (Jimenez et al., 2001), and at the vegetation interface in two-dimensional Large Eddy Simulation (LES) models (Nadaoka and Yagi, 1998; Xiaohui and Li, 2002). In principle, these models then can be scaled up to a real scale, in which the presence of LHCSs can be evaluated. However, it is noticed that the utilization of such detailed models on a large scale *e.g.* river channel, coasts and estuaries is computationally costly in the context of normal design of civil engineering. As far as practical engineering is concerned, a depth average model (2DH model) appears to be a proper option. However, whether or not a 2DH model can well simulate and reproduce the complex shallow flow field of a compound vegetated channel regarding the presence of the LHCSs is unknown.

5.2 Objectives and Methodology

THe main objectives of this paper are (1) to assess the capability of the 2DH model in the simulation of the shallow flow field in a vegetated floodplain channel, particular focusing on the role of LHCSs, profiles of mean streamwise velocity and transverse shear stresses; (2) to evaluate different background eddy viscosity models in the 2DH simulation of the hydrodynamics of vegetated floodplain channels; and (3) to approach the complex shallow flow field in and around a vegetated floodplain in reality by means of an improved 2DH viscosity model. In other words, the potential is assessed of the 2DH model in combination with different models of the background eddy viscosity to predict

the flow field in a compound vegetated channel at different scales. There is a particular focus on the role of the LHCSs in transverse exchange processes.

In order to achieve these objectives, the shallow-water solver of Delft3D, a state-of-the-art model that can includes vegetation (and also sediment transport processes) was used. A 2DH numerical geometry mimicking the experiment of a compound vegetated channel was constructed. The results of the numerical model in which different models of background eddy viscosity were imposed then were compared with experimental results of Truong et al. (2018). Finally, a real-scale 2DH model of the Tieu estuary in the Mekong Delta with schematised bathymetry was constructed and examined. The presence of LHCSs on a larger real scale and their effects on the flow field and transverse exchange processes were investigated.

5.3 Physical model

In order to obtain a data set for the model validation and calibration, a laboratory study was conducted in a shallow, free-surface flow flume of the Fluid Mechanics Laboratory at the Delft University of Technology. A top view and cross-section of the experiment can be seen in Figure 5.2. Details of the experimental configurations, parameters and results are described in Chapters 3 and 4.

The main data set of the physical model includes the time-series data of the streamwise velocity $U(y)$, lateral velocity $V(y)$ along the cross section, which are obtained from a Nortek Acoustic Dopper Velocity meter (ADV) located at 5 m from the first row of cylinders. It also includes the instantaneous flow field obtained from the Particle Image Velocimetry measurements (PIV). Both data sets in the chosen scenario were compared with the numerical results. The details of the 2DH model set-up are described in the following section. In this study, a representative scenario is considered for further detail numerical analyses (dense vegetation: density N = 556 cylinder/m^2, diameter d=1 cm, floodplain width W =50 cm, Water discharge Q=0.045 $m^3\,s^{-1}$, and water level in the flume H = 12 cm).

5.4 2DH model set-up

As mentioned in the previous section, a 2DH numerical model was constructed in Delft3D Flow. The geometry includes a main channel and a floodplain in the form of a trapezium-shaped channel, mimicking the physical model with a horizontal bed, see Figure 5.2. The dimensions of the numerical model are as same as that of the physical model. In this way, the numerical results can be directly compare with the measurements in the physical model. Default settings were used as much as possible, the detail input parameters can be seen in Table 5.1. Specific settings are described below and are related to numerical choices, boundary conditions and vegetation properties, see also in Figure 5.3.

The minimum grid cell size is 0.01 m x 0.02 m inside the vegetation region. This is smaller than the water depth (0.04 m)and results in about 100000 active grid points. The time step was chosen as small as 0.0001 s. The hydraulic boundary conditions of the

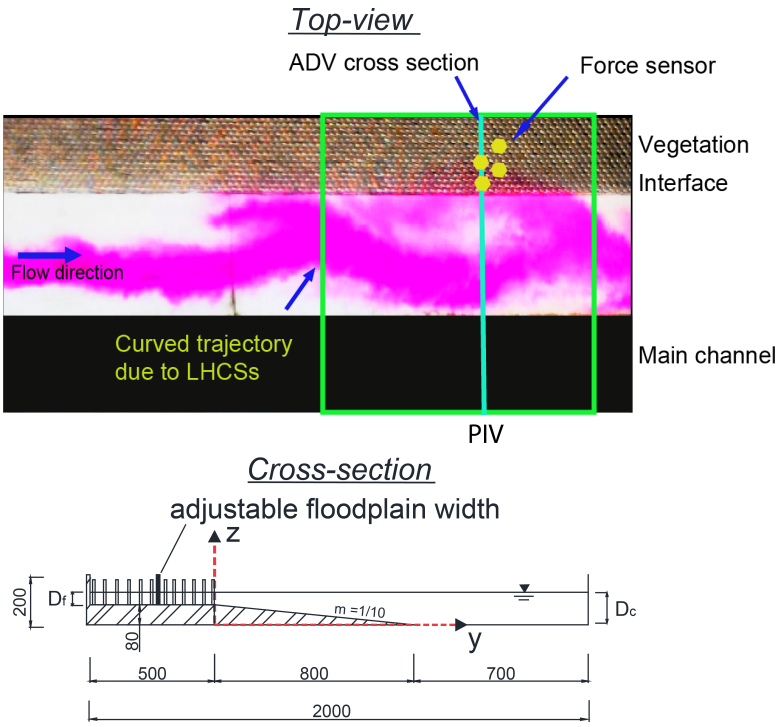

Figure 5.2: Physical model set up and measurements including top view and cross section of the experiment, dense cases, 50 cm floodplain width. The presence of LHCSs can be clearly observed through color dye. It can be seen that the penetration of the dye into the cylinder array is about 20 cm which is similar to that in Figure 3.14: sparse case, 25 cm floodplain width. The similarity between the shear-layer dynamics of sparse and dense cases can also be seen in Figure A.1 in the appendix.

Table 5.1: Properties for the 2DH numerical model of a compound vegetated channel

2DH numerical set up	Value
Layer	1 (2DH model)
smallest grid size (cm)	1 cm x 2 cm
timestep Δ_t (s)	0.0001
Boundary condition upstream: Discharge Q ($m^3\,s^{-1}$)	0.045
Boundary condition downstream: Water level H (cm)	12
Bottom roughness n_b (Manning's equation)	0.0098
Drag coefficient C_d (derived from measured forces, see Figure 3.12b)	1
Boundary is weakly reflective α	10 s
Slope i_b	0
Simulation time (T)	20 min
Computational time	6 hours

numerical model were defined as in the physical model in which the upstream boundary has constant input discharge $Q = 0.045\,\mathrm{m^3\,s^{-1}}$ and the downstream boundary condition is a constant water level $H = 12$ cm.

The experimental results suggest that a good estimation for the force on the cylinder can be achieved with the value of the drag coefficient C_d equal 1 combined with the local velocity. It is noted that if the drag coefficient increases, the vegetation drag also increases. As a result, a decrease of flow velocity within the vegetation patch is expected. This means that a larger drag coefficient, Cd will lead to a smaller flow velocity in the vegetation and a higher flow velocity in the main channel (the same total discharge) (Zhu, 2017).

Based on the experimental configuration, the bottom roughness (n_b) can be specified according to the Manning equation (Equation (5.1)).

$$n_b = K\frac{A}{Q}R^{\frac{2}{3}}S^{\frac{1}{2}} \tag{5.1}$$

in which K is a constant and depends on the units used (K =1 in metric unit), A is the cross-sectional area of flow or wet cross-section (A=0.168 m^2), R is hydraulic radius: $R = A/P$ (R=0.0776 m), P is wetted perimeter (P=2.164 m), and S is the slope of the free surface at the measurement point ($\approx 2\cdot10^{-4}$). This results in a Manning coefficient n_b of about 0.0098.

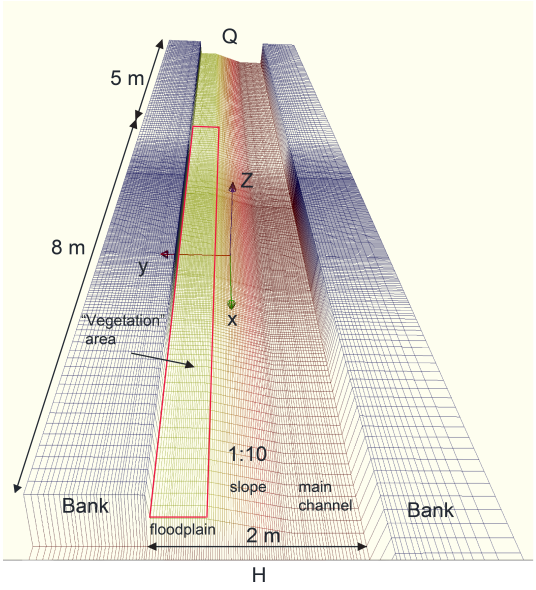

Figure 5.3: Computational grid of the 2DH numerical model at the vegetation region. The numerical model mimicking the physical model.

A rigid vegetation module has been developed and successfully implemented in Delft3D Flow (Baptist, 2005). It was validated for different applications from experiments (Meijer, 1998; Oberez, 2001) to field measurements including salt-marsh vegetation (Bouma

et al., 2007; Temmerman et al., 2005) and mangrove forests (Horstman, 2014). In this study, as all cylinders are emergent, the implementation of vegetation resistance can also be applied for the 2DH computation (Deltares, 2014).

5.5 Eddy viscosity models

IN 2DH models, a closure model of the turbulent shear stresses *i.e.* the horizontal eddy viscosity (υ_t) need to be prescribed so that the depth averaged equations of continuity and momentum can be solved numerically. The horizontal eddy viscosity represents flow events that are not resolved (Gerritsen et al., 2007). The magnitude of the horizontal eddy viscosity can therefore vary from $0\,m^2\,s^{-1}$ to $100\,m^2\,s^{-1}$ (Deltares, 2014) .

The background horizontal eddy viscosity can be modelled with different complexity levels. Firstly, the simplest one is a space and time constant horizontal eddy viscosity which depends on the numerical grid size (Deltares, 2014). As a rule of thumb, an initial horizontal background eddy viscosity of $1\,m^2\,s^{-1}$ was used and then it was reduced (or increased) continuously until the model can be run smoothly without any errors. In this way, for the constructed computational grid, a constant horizontal background eddy viscosity can be determined of $10^{-4}\ m^2\,s^{-1}$. Secondly, space varying and time constant horizontal eddy viscosity models were prescribed for the 2DH model. Based on experimental results, the horizontal eddy viscosity models were determined according to two viscosity models which are the Elder formulation (equation 5.2) and the hybrid eddy viscosity model (equation 5.3).

The Elder formulation can be adopted in which the water depth D is the length scale and the friction velocity ($u_* = \sqrt{c_f}\langle\overline{u}\rangle_d$) is the velocity scale (van Prooijen et al., 2005) :

$$\nu_t = \alpha u_* D = \alpha D\sqrt{c_f}\langle\overline{u}\rangle_d \tag{5.2}$$

Where $\alpha = 0.1$ is a constant (Fischer et al., 1979), c_f is the bottom friction coefficient, and $\langle\overline{u}\rangle_d$ is the depth, time and spatially averaged streamwise velocity.

The total horizontal eddy viscosity determined according to the hybrid eddy viscosity model based on the experimental data (Truong and Uijttewaal, 2018):

$$\upsilon_t = \begin{cases} \alpha\sqrt{c_f}\langle\overline{u}\rangle_d D + \frac{Dm}{D(y)} {D_r}^2\beta^2\delta^2\left|\frac{d\langle\overline{u}\rangle_d}{dy}\right| & \text{(outside vegetation)} \\ \underbrace{\alpha\sqrt{c_f}\langle\bar{u}\rangle_d D}_{Elder} + \underbrace{\frac{1}{8}{C_t}^{-2}C_d d\langle\bar{u}\rangle_d}_{vegetation\ drag} + \underbrace{\frac{D_m}{D(y)}{D_r}^2\beta^2\delta^2\left|\frac{d\langle\bar{u}\rangle_d}{dy}\right|}_{mixing\ layer} & \text{(inside vegetation)} \end{cases} \tag{5.3}$$

Where $D(y)$ is local water depth, D_m is mean water depth, $D_m = \frac{D_c+D_f}{2}$, D_c is water depth in the channel, and D_f is water depth in the floodplain channel. β is proportionality constant, depends on the transition slope and δ is the total mixing length. D_r is the water depth ratio, $D_r = D_f/D_c$. C_t is a constant of proportionality, the value of it depends on the shape of the streamwise velocity profile, usually $C_t = 1$ and C_d is the drag coefficient of a single stem, theoretically $C_d = 1$.

Figure 5.4 illustrates the horizontal eddy viscosity models considered in the 2DH model. They are determined theoretically based on the experimental data in case of dense vegetation, floodplain width H=50 cm, discharge Q=45 L s^{-1} and water level H=12 cm. It is noticed that in a compound vegetated channel, the hybrid eddy viscosity model is composed of three separate components, the eddy viscosity related to the bottom turbulence part determined with the Elder formulation, the eddy viscosity linked to the presence of vegetation determined by the model of (Kean and Smith, 2013), and the eddy viscosity associated with the LHCSs (Truong and Uijttewaal, 2018).

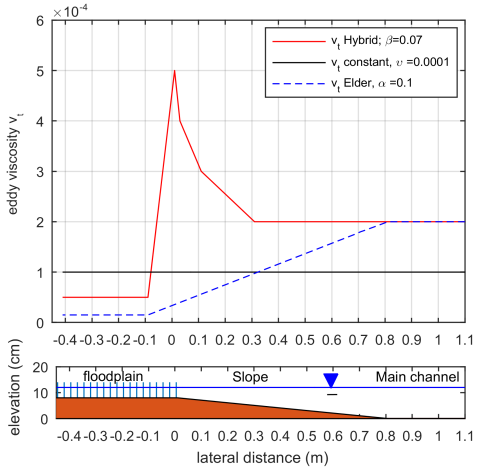

Figure 5.4: Different background eddy viscosity models prescribed in the 2DH model, the results were extracted from the 2DH model.

5.6 Results

In this section, the simulation results are compared with the experimental results, particularly focusing on the mean streamwise velocity profile, transverse shear stresses and the flow pattern related to the LHCSs.

5.6.1 2DH model results with different eddy viscosity models

By including the presence of the LHCSs in the background eddy viscosity by means of the hybrid eddy viscosity model of equation (5.3), it is shown that the 2DH model can well predict experimental data. Experimental and numerical data of the depth and time streamwise velocity are compared in the upper panel of figure 5.5. The middle panel of figure 5.5 shows the depth and time averaged transverse shear stresses measured in the experiment and that determined from the 2DH models. It demonstrates that when the hybrid eddy viscosity model is prescribed in the 2DH model, the transverse shear stress also is well reproduced.

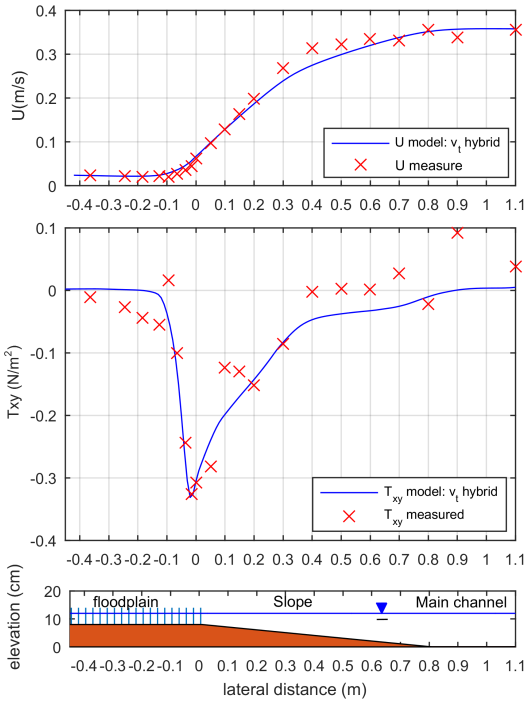

Figure 5.5: Comparison of results between the numerical model and physical model: the depth and time averaged velocities (upper panels) and the transverse shear stresses (lower panels). The hybrid eddy viscosity model was prescribed into the 2DH model.

The differences between the measurement and the numerical simulation can be clearly recognized when the background horizontal eddy viscosity model was prescribed as a constant value or determined from the Elder formulation only. Figure 5.6 illustrates the mean streamwise velocity profile measured in the experiment and the corresponding results computed by the 2DH models. It is suggested that the 2DH model appears to underestimate the mean streamwise velocity inside the vegetation region. Furthermore, it significantly overestimates the transverse shear stresses.

It is noticed that the transverse shear stresses calculated from the 2DH model results have two main parts, which are the part calculated from the eddy viscosity model (T_{xy_v}) and the part resolved by the model (T_{xy}resolved) (see equation (5.4)).

$$T_{xy} = \underbrace{\rho \nu_t \frac{d\langle \bar{u} \rangle_d}{dy}}_{\substack{T_{xy_v} \\ \text{Calcualted from the } \nu_t}} + \underbrace{\rho \left\langle \overline{u'v'} \right\rangle_d}_{\substack{T_{xy}\text{resolved} \\ \text{Extracted from the resolved turbulence structures}}} \tag{5.4}$$

The middle panel of Figure 5.6 also illustrates these different parts of the transverse shear stresses determined from the numerical model (see equation (5.4)) in which the hybrid eddy viscosity model and Elder eddy viscosity model were imposed.

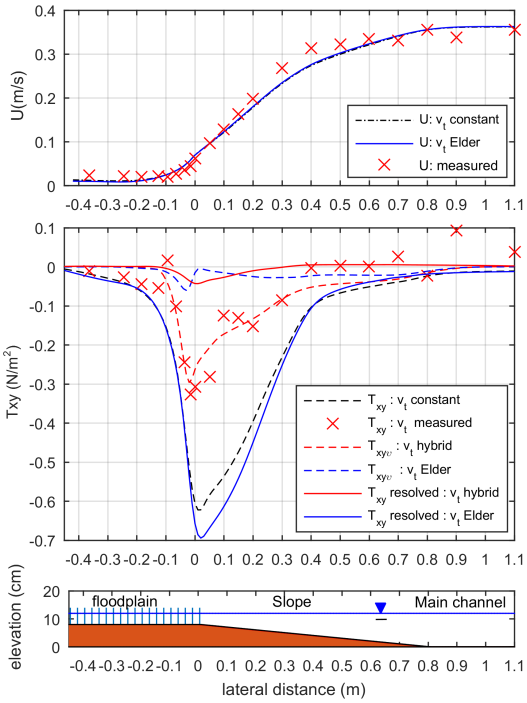

Figure 5.6: Comparison of results between the numerical model and physical model: the depth and time averaged velocities and the transverse shear stresses in case with different eddy viscosity models. Different components of transverse shear stresses including the resolved part extracted from the numerical simulation (solid lines) and the part determined from the eddy viscosity model (dashed lines). They are extracted from the numerical simulation in which the background horizontal eddy viscosity model was determined from the Elder formulation (blue line) and from the hybrid eddy viscosity model (red line).

On the one hand, it can be clearly seen that when the Elder eddy viscosity model was prescribed, the transverse shear stresses determined from the eddy viscosity model (dashed blue line) are much smaller than those extracted from the resolved Reynolds shear stresses of the model (solid blue line). The resolved Reynolds shear stresses are about two times larger than those measured in the experiment. This means that the quasi two dimensional structures were resolved as too strong by the 2DH model when the background eddy viscosity determined according to the Elder formulation was prescribed.

On the other hand, when the hybrid eddy viscosity model was imposed, it is suggested that the transverse shear stresses determined from the eddy viscosity model (dashed blue line) are much larger than the resolved transverse shear stresses (solid red line). This means that the “true” LHCSs substituting for the one resolved too strong by the model, were included in the model of background eddy viscosity. Therefore, the numerical results were improved.

5.6.2 The presence of LHCSs

When the Elder viscosity model (or a constant background eddy viscosity model) was imposed into the 2DH model, the presence of LHCSs can be observed in the results (Figure 5.7b). Qualitatively, the vorticity field reveals the large horizontal coherent structures at the vegetation interface. Moreover, the penetration of the LHCSs into the vegetation region of about 0.1 m was also observed. The length and width of the structure can also be determined of about 1 m and 0.6 m, respectively. These results appear to be well in-line with those observed in the experiment of Truong et al. (2018). When the presence of the LHCSs was included in the background eddy viscosity using the hybrid eddy viscosity model of equation (5.3), the LHCSs resolved by the model seen in the vorticity field previously cannot be observed in the vorticity field (Figure 5.7a).

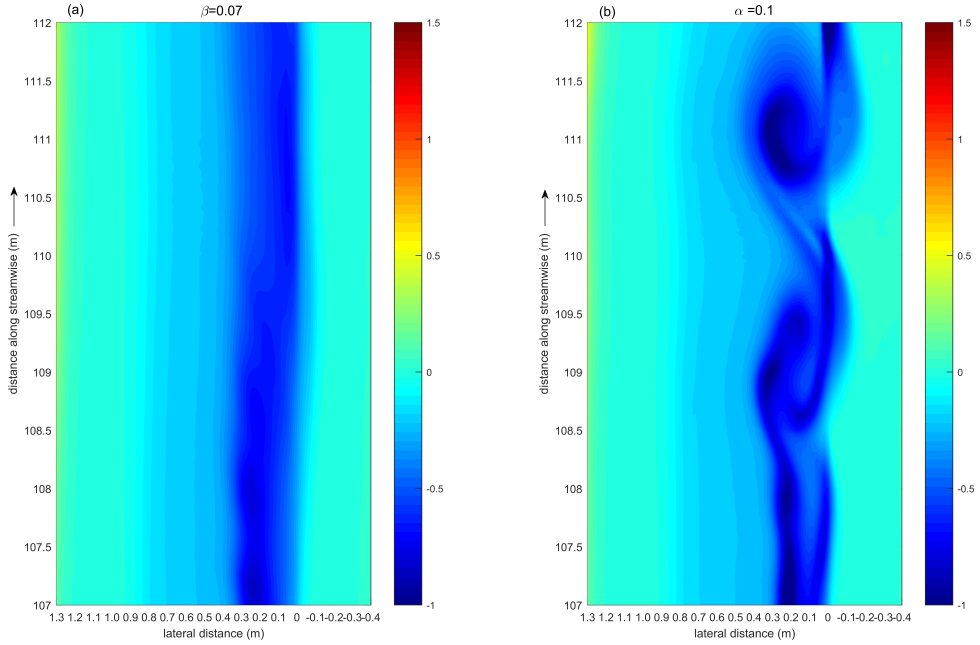

Figure 5.7: Representative vorticity resolved by the model in which the eddy viscosity was determined by the hybrid eddy viscosity model (left panel), and by Elder formulation (right panel). The presence of LHCSs can be observed as their influences were not included in the Elder model (fight panel), but can not be observed as their influences were included in the hybrid viscosity model (left panel).

So far, it can be seen that when the Elder viscosity model was prescribed, although the numerical simulation can capture the presence of the LHCSs (Figure 5.7b), it fails to predict the transverse shear stresses (Figure 5.6) and their calculations can be improved if the LHCSs are included in the hybrid eddy viscosity model (Figure 5.5 and Figure 5.7a). In this sense, it is noticed that the parameter α in Elder formulation and β in the hybrid eddy viscosity model are useful tools to calibrate the 2DH model regarding the LHCSs and transverse shear stresses. Therefore, they can be tuned in such a way that the transverse shear stresses were in fair agreement with the measured data when the Elder for-

mulation was imposed and over-predicted when the hybrid eddy viscosity model was prescribed (Figure 5.8).

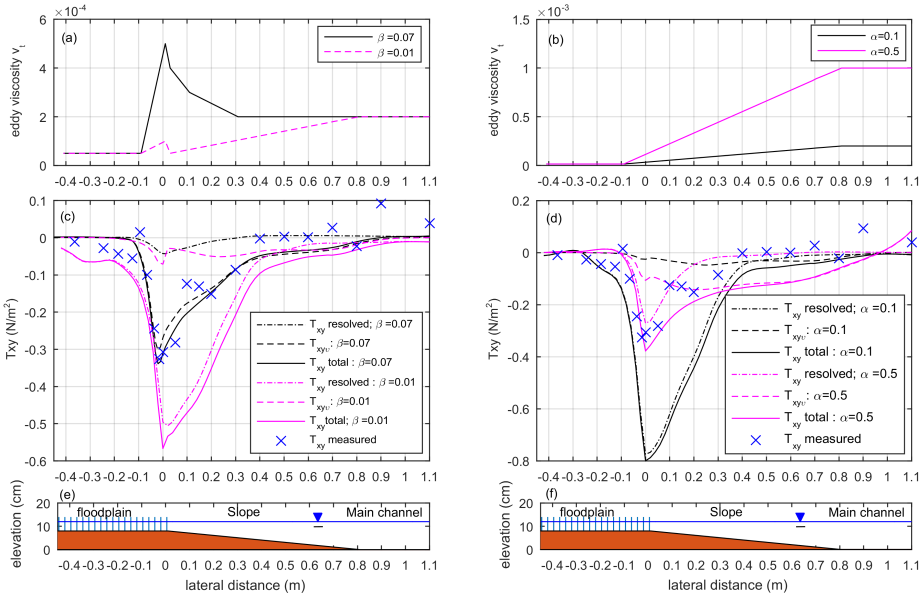

Figure 5.8: Sensitive analysis of the β and α in terms of the transverse shear stresses. Transverse shear stresses were over predicted when β was reduced from 0.07 to 0.01 (a) and are in fairly agreement with the measured data when α was increased from 0.1 to 0.5 (b).

The results suggest that when β reduces, the 2DH model resolved stronger LHCSs (see Figure 5.9a) and T_{xy} resolved increases, but then the T_{xyv} decrease so that the total transverse shear stresses is over predicted (see Figure 5.8c). Furthermore, it can be seen that when α increases, the 2DH model resolved less LHCSs (see Figure 5.9b) and thereby T_{xy} resolved significantly decreases. The total transverse shear stresses reduced and their magnitude is in fairly agreement with the measured data Figure 5.8d.

On the one hand, it can be seen that the total transverse shear stresses (in case when α is tuned) still appear to be overestimated for the open region ($y > 0$ m) because T_{xyv} in this region (pink dashed line in Figure 5.8b) is significantly increase. It is to see that by tuning α in Elder formulation, the 2DH model can better predict the presence of the LHCSs as well as the transverse shear stresses. However, in this case, it is still quite difficult to obtain a good agreement with the measured data as can be seen when using the hybrid eddy viscosity model. By including the role of LHCSs in the model of viscosity, the presence of the LHCSs and their associated transverse shear stress resolved by the model is expected to be totally eliminated. In this sense, it is more simple to calibrate the 2DH model in terms of transverse shear stresses by adjusting the bottom friction (C_f) only. On the other hand, it is noticed that when the hybrid eddy viscosity model was prescribed, the presence of the LHCSs is not expected in the 2DH model. This makes it impossible to assess the LHCSs, in terms of their appearance for different scenarios.

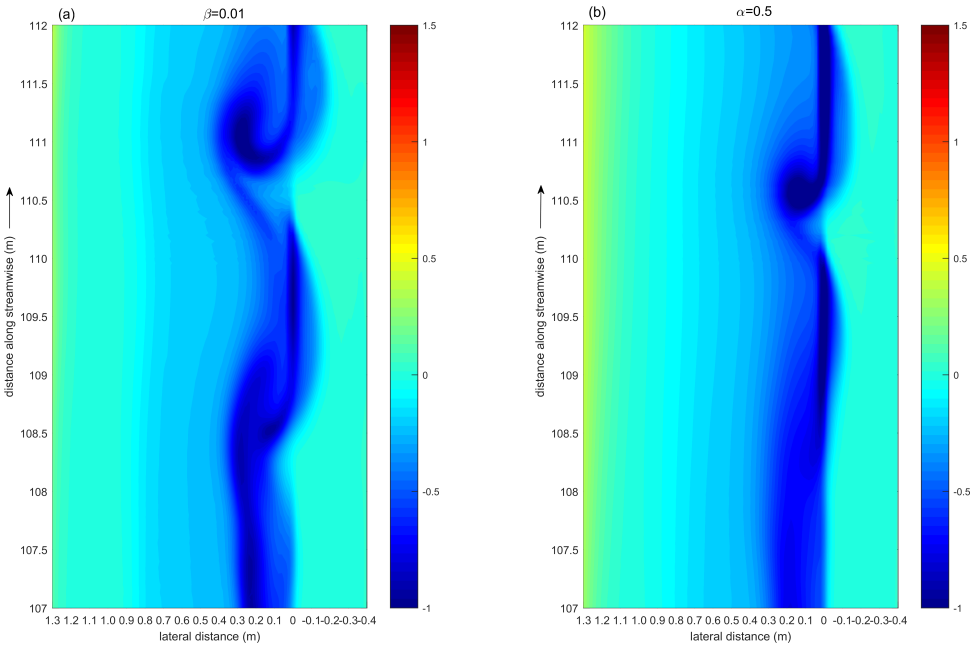

Figure 5.9: Representative vorticity resolved by the model in which the eddy viscosity was determined by the hybrid eddy viscosity model (left panel, $\beta = 0.01$), and by Elder formulation (right panel $\alpha = 0.5$).

In cases when the LHCSs were resolved (Elder viscosity model was imposed into the 2DH model), the instantaneous velocity flow field was extracted from the numerical simulation and compared with that captured by the PIV measurement in the experiment (see Figure 5.10). The results show that there is a good agreement between the two flow fields. The flow events such as sweeps, ejections and even the stagnant and reverse flows can be clearly identified in the instantaneous flow field computed by the 2DH model (Figure 5.10a), and is similar to that captured in the experiment (Figure 5.10b). These events caused by the LHCSs as they are moving along the vegetation interface then determine the surrounding flow motion, contributing for an important part to the transverse momentum exchange between the vegetation region and the adjacent open channel region (Truong et al., 2018).

5.7 Discussions

5.7.1 A 2DH model of schematised Tieu estuary river channel

As far as practical engineering is concerned, understanding to what extend the philosophies learned in this topic can be applied on a larger real scale is a demand. Therefore, a 2DH model of the compound vegetated channel mimicking the Tieu estuary in the Mekong Delta with schematised bathymetry (see Figure 5.1) was constructed. In which, the hydraulic boundary conditions of the model was defined as same as that used in

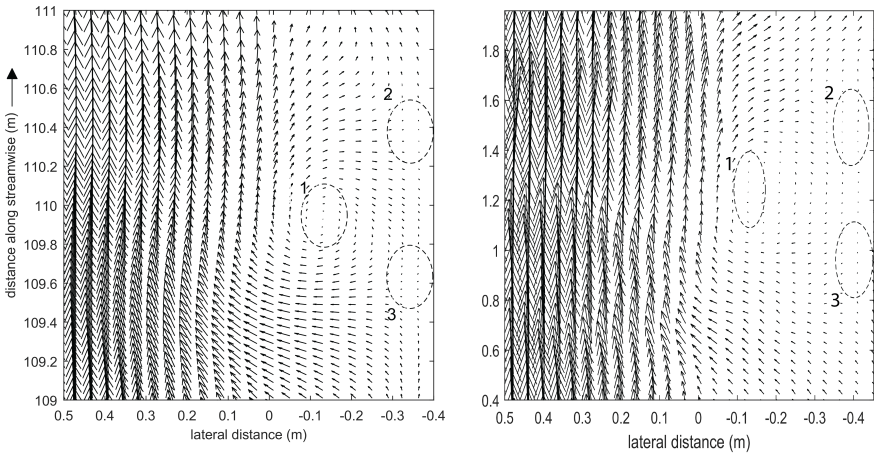

Figure 5.10: Instantaneous velocity field in and around vegetation region computed by the numerical model (a) and that measured by PIV in the experiment (b). The stagnation areas (1,2,3) that observed in the experiment can be well captured by the 2DH model.

the nested model of Truong et al. (2017). The upstream is a constant input discharge $Q = 2848\,\mathrm{m^3\,s^{-1}}$ and the downstream boundary condition is a constant water level (H = 0.48 m - 1.5 m) . The time step was chosen as small as 0.0001. The detail input parameters of this "scaled up" 2DH model can be seen in Table 5.2.

Figure 5.11 shows the computational grid with associated length scales of the 2DH schematised Tieu estuarine model. The minimum grid size is 2 m x 4 m inside the vegetation region. Because the densest scenarios in the experiment correspond with the sparse cases in reality (Truong et al., 2018), in this study, only the cases with sparse vegetation were considered. Following the footprint of Truong et al. (2017), the estuarine mangrove forests in the Mekong Delta was assumed to be consist of only *Sonneratia sp.* The characteristic of the *Sonneratia sp.* prescribed in the model can be seen in Table 5.2.

The schematised model was at first run with a space and time constant background horizontal eddy viscosity. Based on the result of the numerical model, the eddy viscosity can be determined according to the Elder formulation, or the hybrid eddy viscosity model and then imposed again into the model. By applying this iteration methodology, the numerical results would be converged. While 2DH models prescribed with the elder formulation can be used to assess of the appearance of the LHCSs, the hybrid eddy viscosity model can be used to improve the calculation results regarding the transverse shear stresses.

Figure 5.12 shows the possible relationship between the water depth ($D_r = D_f / D_c$) and the maximum transverse shear stress predicted by the numerical simulations. The presence of LHCSs observed in the field of vorticity was also described in this figure. It is suggested that as the water level increases (D_r increases), the maximum transverse shear stresses at the vegetation interface reduces. Moreover, the numerical results predict that the LHCSs appear to occur in the Tieu estuary (see Figure 5.13) only when the water

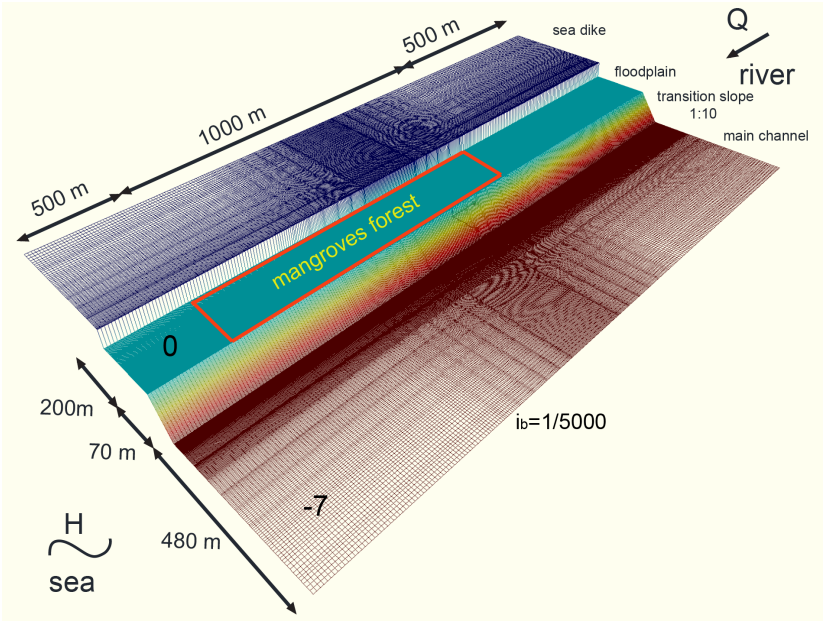

Figure 5.11: A computational grid of the “scaled up" 2DH model with the schematised bathymetry of the Tieu Estuary. The model includes a floodplain with mangroves, transition slope (1:10) and a main river channel. It covers the first 2 km stretch from the river mouth and half of the estuarine width.

Table 5.2: Properties for the scaled up 2DH numerical model of Tieu Estuary and Vegetation parameters

2DH numerical set up	Value	Vegetation parameters	S.Alba
Layer	1 (2DH model)	Steam diameter (m)	0.3
smallest grid size (cm)	2 m x 4 m	Root diameter (m)	0.02
timestep Δ_t (s)	0.0001-0.005	Canopy diameter (m)	0.5
Discharge Q ($m^3 s^{-1}$)	2848	Stem height (m)	6
Water level H (m)	D_f= 0.48-1.5 m; D_c= 7.48 m	Root height (m)	0.5
Bottom roughness n_b	0.02 (default value)	Canopy height (m)	2
Drag coefficient C_d	1	Density	Sparse
Boundary is weakly reflective	100 s	Stem density (m^{-2})	0.5
Slope i_b	1/5000	Root density (m^{-2})	25
Simulation time	6 hours	Canopy density (m^{-2})	50
Computational time	8 hours		

level in the floodplain is larger than 1.1 m (the hybrid eddy viscosity was not prescribed in these simulations). The length of the LHCSs is up to 100 m, the outer layer width is about 60 m, and the penetration of the mixing layer into the vegetation is about 6 to 10 m. It is noticed that as the structure moves along the vegetation interface, the region inside the vegetation affected by the LHCSs is up to 200 m inside the forest, which is much further than the penetration of the mixing layer into the vegetation region. This can be

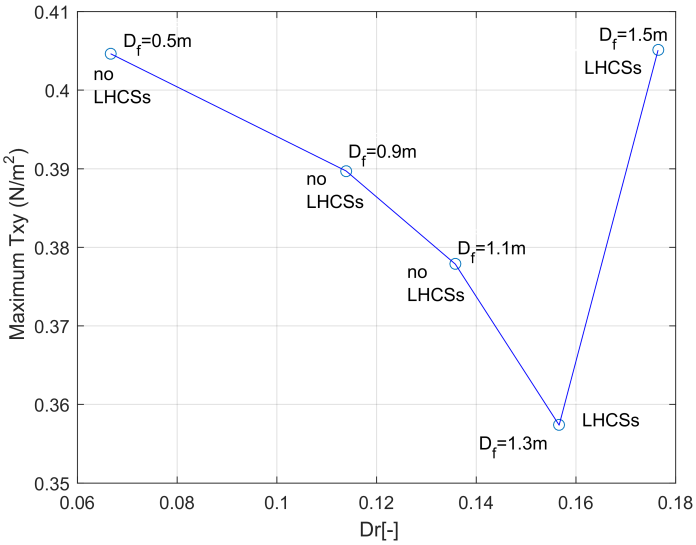

Figure 5.12: The relationship between the maximum transverse shear stress, water depth and the presence of LHCSs predicted by the simulations.

recognised through the stagnant and reverse flows observed inside the region of vegetation. This phenomenon was also observed in the laboratory and explained by Truong

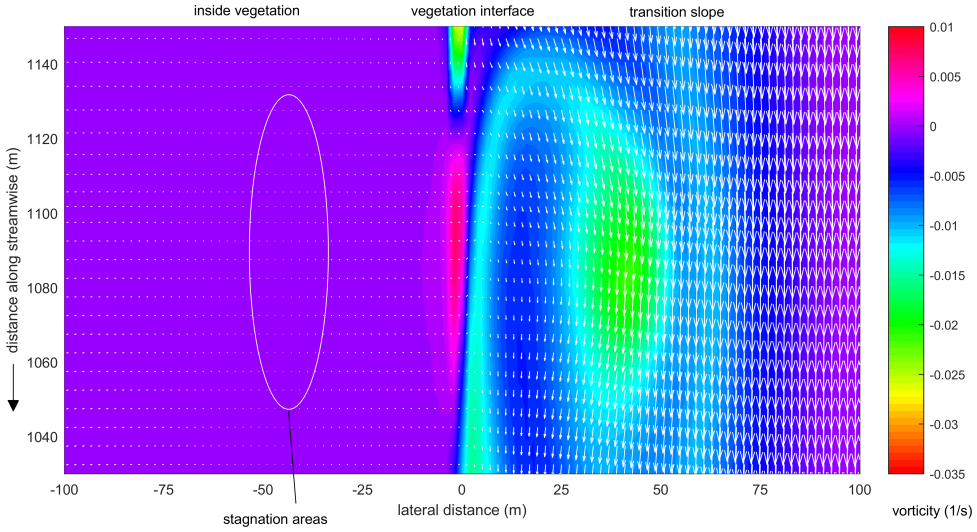

Figure 5.13: The field of vorticity and the corresponding velocity field reveals and presence of the LHCSs and its effects on the flow field at real scale.

et al. (2018). It is suggested that as the LHCSs move along the vegetation interface, they

generate flow events which are the sweeps, ejections and stagnation area and reverse flows (Figure 5.13). These flow events, then determine the surrounding flow field and become the governing factor driving the motion of the surrounding water inside the forest. This means that the numerical simulations predict that the influences of the LHCSs in reality appear to be the same as that described in the physical model.

Nevertheless, as mentioned above, although the 2DH model can predict the presence of LHCSs, it is difficult to control the contribution to the total transverse momentum exchange from different parts. By including the LHCSs in the hybrid eddy viscosity model, the model results appear to be more reliable. As the presence of LHCSs in the field of vorticity cannot be observed (Figure 5.14), the presence of LHCSs is well prescribed in the hybrid eddy viscosity model.

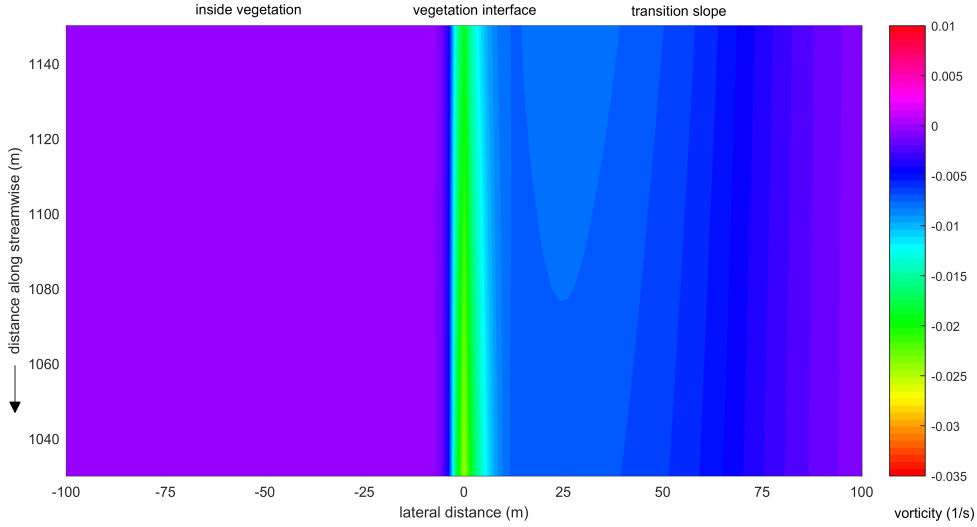

Figure 5.14: The field of vorticity in which the presence of LHCSs can not be observed as their influences were included in the hybrid viscosity model .

The result suggested that the numerical results on a large scale are quite sensitive with the eddy viscosity imposed into the model, especially the transverse shear stresses (T_{xy}). Figure 5.15 illustrates the mean streamwise velocity profile and the associated transverse shear stresses computed by the 2DH model prescribed by different eddy viscosity models. The results zoomed into the 200 m around the vegetation interface was extracted at the middle of the mangrove forest (*i.e.* 500 m from the beginning of the mangrove forest) where the mixing layer was fully developed. It can be seen that there is a significant difference in the mean streamwise velocity and transverse shear stress predicted by different models of background eddy viscosity. As analysed in previous sections, in this study the numerical results with the hybrid eddy viscosity model were considered to be the most reliable one in which the uniform mean streamwise velocity inside the mangrove forest is about 0.01 m s^{-1}. Moreover, the penetration of the mean streamwise velocity into the vegetation region is about 6 m to 10 m. It is noticed that this penetration is smaller than that estimated previously in Truong et al. (2017), in which only a

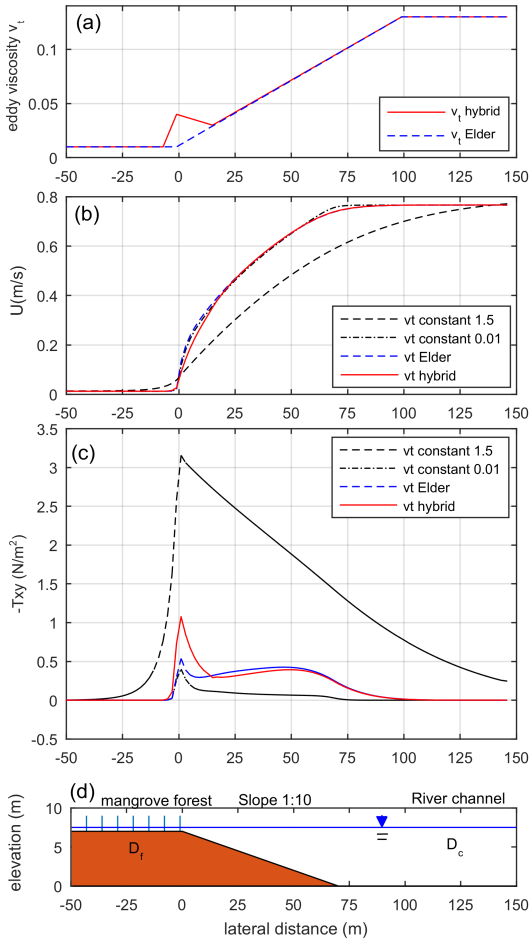

Figure 5.15: Sensitivity analysis of the background eddy viscosity imposed into the 2DH model of the Tieu estuary river channel in the Mekong Delta with schematised bathymetry. Eddy viscosity models (a) considered include the eddy viscosity ν_t determined according to Elder formulation, hybrid eddy viscosity model and a constant value of eddy viscosity of 1.5. The differences in (b) the profile of mean streamwise velocity (U) and (c) the transverse shear stresses (T_{xy}) are significant.

space and time constant background eddy viscosity was prescribed. Furthermore, it can be seen that the transverse shear stresses achieve its maximum value of about $1\,\mathrm{N\,m^{-2}}$ at the edge of the vegetated floodplain, indicating that the momentum transfer occurs strongest at this location. The mixing length is about 80 m to 100 m which is similar to that observed and measured by sediment patterns in Figure 5.1.

5.7.2 Squeeze effects

IN this section, the stability of the river bank in squeezed condition *i.e.* the mangrove width is restricted is discussed in terms of the changes in the bed shear stress. As far as the fluvial process is concerned, the most widely known and generally accepted cause of fluvial erosion mechanism is that flowing water applies a force (T_a) to the stream bank that exceeds a critical shear stress (T_c) specified for the particular material of that stream bank. This also occurs in cases of shear stress on cohesive stream banks caused by fast-moving water during peak flows. The riverbank or bed erosion rate induced by the flow is usually modelled by the excess stress equation (Partheniades, 1965):

$$\varepsilon = k_d \cdot (T_a - T_c)^a \tag{5.5}$$

Where: ε is the erosion rate (m), k_d is soil erodibility coefficient, T_a is applied shear stress on the soil ($\mathrm{N\,m^{-1}}$), T_c is soil critical shear stress ($\mathrm{N\,m^{-1}}$), and a is a coefficient, usually assumed equal one.

It is essential to distinguish two different mechanisms, which are the mechanism cause the failure of stream banks and the mechanism through which vegetation affects the river bank processes. While the former relates to the direct removal of bank material by the water flow (fluvial entrainment/ fluvial erosion), and the geotechnical instability, which are the primary mechanisms responsible for river bank failure processes (Thorne, 1982). The latter deals with the impacts of vegetation on the erosion processes of river banks by affecting those main failure mechanisms. For instance, the presence of vegetation on the floodplain, on the one hand, strengthen the soil, increasing critical shear stress (increase T_c) and reduce the soil erodibility coefficient k_d. On the other hand, vegetation diverts the flow direction, damping the flow velocity together with the exerted force (reduce T_a). In this way, the vegetation can be considered as a mean to reduce the erosion of the river bank.

It is noticed that it is difficult to determine T_a, T and k_d even in cases without vegetation. In this section, only the hydrodynamics aspect is considered, thereby only the impact of vegetation on the fluvial processes, in which vegetation increases flow resistance and diverges flows direction, changing velocity field and bed shear stresses are discussed. In other words, only the changes of T_a induced by changing flow properties, which is caused by the presence of vegetation are considered, k_d and T_c are assumed to be constant and only depend on the characteristic of the cohesive soil.

In vegetated floodplain channel, the applied force on stream bank or bed in vegetated floodplain channel (T_a) can be related to the bed shear stress τ_b. The bed shear stress then can be split into transverse bed shear stress τ_{bt} and streamwise bed shear stress τ_{bs}, however, the numerical simulation suggested that in the real scale of the Tieu estuary, the transverse bed shear stress τ_{bt} is two orders of magnitude smaller than the streamwise bed shear stress τ_{bs} ($0.03\,\mathrm{N\,m^{-2}}$ compared to $3\,\mathrm{N\,m^{-2}}$). In this sense, the influence of the transverse bed shear stress on the total bed shear stress can be neglected, and the total bed shear stress can be expressed as:

$$\tau_b = \sqrt{\left(\rho C_f U^2\right)^2 + \left(\rho C_f UV\right)^2} \approx \rho C_f U^2 \tag{5.6}$$

In which the $\rho C_f UV$ is the transverse bed shear stress and $\rho C_f U^2$ is the streamwise bed

shear stress, ρ is the density of water, C_f is bottom friction coefficient, U and V is the depth-averaged velocity in streamwise and lateral direction.

Figure 5.16 illustrates the difference in total bed shear stress in scenarios of 200 m width (dash black line) and 50 m width (solid red line) which are predicted by the numerical model. It can be seen that the outer layer (from $y = 0$ to $y = 80$m) appears to

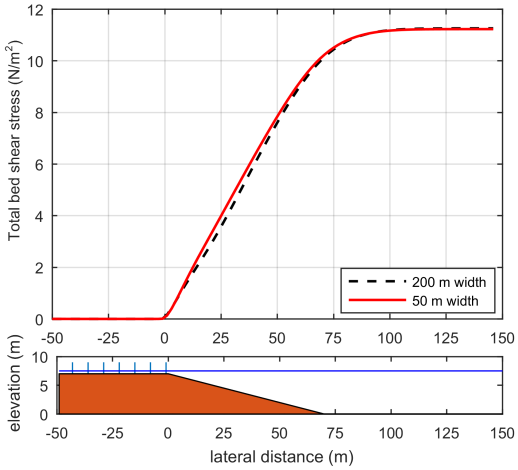

Figure 5.16: Comparison of the total bed shear stress predicted by the numerical simulation in scenario of 50 m width and 200 m width.

be the most affected area when the mangrove width is reduced. Moreover, these results can be generalized for the rough assessment of the role of vegetation in a compound vegetated channel (see Figure 5.17).

The total difference of the total bed shear stress (A_{τ_b}) in the outer layer when reducing the floodplain width (from w_2 to w_1) can be determined as:

$$A_{\tau_b} = \int_{y=0}^{y=\delta_2} \left(\tau_{bw_1} - \tau_{bw_2}\right) dy \tag{5.7}$$

where τ_{bw_1} and τ_{bw_2} are the total bed shear stresses corresponding to floodplain with the width of w_1 and w_2, respectively. Subsequently, the averaged advanced bed shear stress generated per meter of the vegetation in the floodplain can be estimated according to:

$$\overline{A_{ad}} = \frac{A_{\tau_b}}{w_2 - w_1} \tag{5.8}$$

The degradation of the mangrove forest or the limitation of the floodplain width appears to affect the outer layer of the mixing layer. According to the equation (5.7) and (5.8), the total advanced bed shear stress created per meter of cylinder arrays in the real scale of river channel is determined of about 8 N m^{-2}. The advanced bed shear stress created per meter of vegetation in the estuarine river channel can be estimated of around

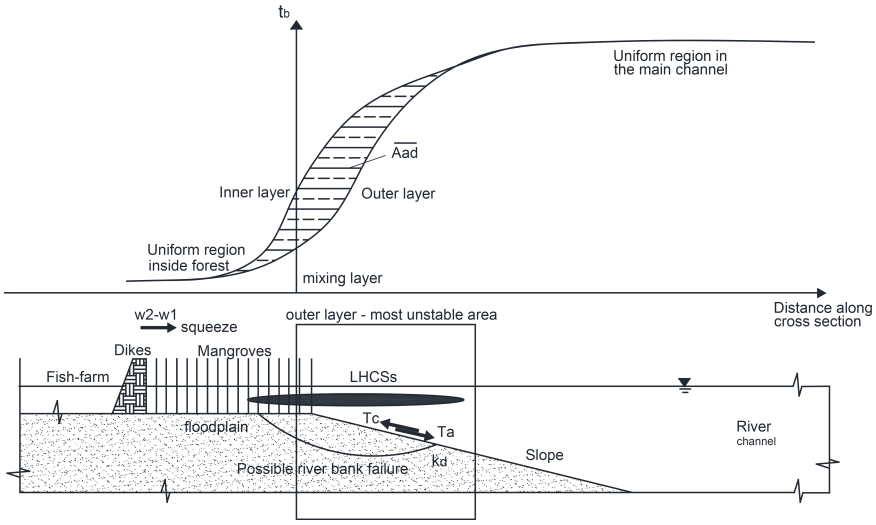

Figure 5.17: Schematised failure mode of the river bank caused by the squeezed effect in a vegetated compound channel. The averaged applied bed shear stresses increases as the region of vegetation decreases, leading to the possible erosion in the outer layer width of the mixing layer.

$0.05\,\mathrm{N\,m^{-2}}$ ($\approx 0.5\,\mathrm{kg\,m^{-2}}$). Finally, the influences of vegetation and their available width (w) on the fluvial processes can be added into the model of riverbank/bed erosion rate induced by the flow by a modified applied bed shear stress:

$$\varepsilon = k_d[(T_a - w \cdot 0.05) - T_c]^a \tag{5.9}$$

5.8 Conclusions

THe vegetation in general and mangroves, in particular, have drawn more focuses in recent decades as their defensive role for the protection of coastal and estuarine areas was recognized. Nevertheless, advanced knowledge obtained in this topic was mostly based on the laboratory studies. For instance, the presence of the LHCSs at the vegetation interface and their associated cycloid flow events were described in the vegetated compound channel at the laboratory scale. As a result, to what extent these philosophies learned from a small experimental scale are still valid on a larger real scale is unknown, especially in the context of the presence of the LHCSs and their effects on the flow field.

Numerical models provide a useful tool to handle this knowledge gap. However, detail simulations such as DNS or LES for these complex phenomena are usually computational costly. Currently, in term of practical engineering, a 2DH model still appears to be the most applicable one. In this study, the capability of the 2DH models in the simulation of the complex cycloid flow field in and around the vegetation region was studied, particularly focus on the sensitivity of the horizontal eddy viscosity. The ability of the model was quantitatively examined by means of the presence of the LHCSs

and the associated flow events and qualitatively examined by means of the profile of the mean streamwise velocity and transverse shear stresses. The results suggested that although the 2DH model can resolve the presence of the LHCSs and their corresponding cycloid flow events, it appears to underestimate the mean streamwise velocity inside the mangrove forest and overestimate the transverse shear stresses induced by the LHCSs. Nevertheless, by imposing into the 2DH model the hybrid eddy viscosity model in which the presence of the LHCSs was included, it is shown that the numerical results can be improved.

Finally, a real-scale 2DH model mimicking the mangrove forest in the Tieu estuary with schematised bathymetry was constructed and examined in terms of the mean streamwise velocity, transverse shear stress and the LHCSs. The hybrid eddy viscosity model was considered to improve its capability in the prediction of the mean streamwise velocity and transverse shear stress. According to the numerical result, the presence of the LHCSs and the cycloid flow events appears to occur in the large scale of Tieu estuary when the water depth in the vegetation region is larger than 1.1 m. Furthermore, it is also observed that although the penetration of the mixing layer into the vegetation region, in reality, is only about 10 m, the areas located much further inside the vegetation are still affected by the LHCSs. In a squeezed condition, the area affected the most is the outer layer of the mixing layer where there is a slight increase in the total bed shear stress. In this context, the advanced bed shear stress created per meter of vegetation can be determined of about $0.05\,\mathrm{N\,m^{-2}}$.

References

Baptist, M. (2005). Modelling floodplain biogeomorphology, phd diss.

Bouma, T., Van Duren, L., Temmerman, S., Claverie, T., Blanco-Garcia, A., Ysebaert, T., and Herman, P. (2007). Spatial flow and sedimentation patterns within patches of epibenthic structures: Combining field, flume and modelling experiments. *Continental Shelf Research*, 27(8):1020–1045.

Deltares, D. (2014). Delft3d-flow user manual: Simulation of multi-dimensional hydrodynamic flows and transport phenomena. Technical report, including sediments. Technical report.

Fischer, H. B., List, E. J., Koh, R., Imberrger, J., and Brooks, N. (1979). In *Mixing in Inland and Coastal Waters*. Academic Press, San Diego.

Gerritsen, H., De Goede, E., Platzek, F., Genseberger, M., van Kester, J., and Uittenbogaard, R. (2007). Validation document delft3d-flow; a software system for 3d flow simulations. *The Netherlands: Delft Hydraulics, Report X*, 356:M3470.

Horstman, E. (2014). *The Mangrove Tangle: Short-term bio-physical interactions in coastal mangroves*. PhD thesis.

Jimenez, J., Uhlmann, M., Pinelli, A., and Kawahara, G. (2001). Turbulent shear flow over active and passive porous surfaces. *Journal of Fluid Mechanics*, 442:89–117.

Jirka, G. and Uijttewaal, W. (2004). Shallow flows: A definition. pages 3–11.

Kean, J. W. and Smith, J. D. (2013). *Flow and Boundary Shear Stress in Channels with Woody Bank Vegetation*, pages 237–252. American Geophysical Union.

Meijer, D. (1998). Modelproeven overstroomde vegetatie (tech. rep. no. pr121. 10). *HKV lijn in water*.

Nadaoka, K. and Yagi, H. (1998). Shallow-water turbulence modeling and horizontal large-eddy computation of river flow. *Journal of Hydraulic Engineering*, 124(5):493–500.

Nepf, H. M. (2012). Hydrodynamics of vegetated channels. *Journal of Hydraulic Research*, 50(3):262–279.

Nezu, I. and Onitsuka, K. (2001). Turbulent structures in partly vegetated open-channel flows with LDA and PI V measurements. *Journal of Hydraulic Research*, 39(6):629–642.

Oberez, A. (2001). Turbulence modelling of hydraulic roughness of submerged vegetation. IHE.

Partheniades, E. (1965). Erosion and deposition of cohesive soils. *Journal of the Hydraulics Division*, 91(1):105–139.

Tamai, N., Asaeda, T., and Ikeda, H. (1986). Study on Generation of Periodical Large Surface Eddies in a Composite Channel Flow. *Water Resources Research*, 22(7):1129–1138.

Temmerman, S., Bouma, T. J., Govers, G., Wang, Z. B., De Vries, M. B., and Herman, P. M. J. (2005). Impact of vegetation on flow routing and sedimentation patterns: Three-dimensional modeling for a tidal marsh. *Journal of Geophysical Research: Earth Surface*, 110(4).

Thorne, C. (1982). Processes and mechanisms of river bank erosion. *Gravel-bed rivers*, pages 227–271.

Truong, H. and Uijttewaal, W. (2018). Transverse momentum exchange induced by large coherent structures in a vegetated compound channel. *Water Resources Rearch (under review)*.

Truong, H., Uijttewaal, W., and Stive, M. (2018). Exchange processes induced by large horizontal coherent structures in floodplain vegetated channels. *Water Resources Rearch (under review)*.

Truong, S. H., Ye, Q., and Stive, M. J. (2017). Estuarine mangrove squeeze in the mekong delta, vietnam. *Journal of Coastal Research*, pages 747–763.

van Prooijen, B., Battjes, J. A., and Uijttewaal, W. (2005). Momentum Exchange in Straight Uniform Compound Channel Flow. *Journal of Hydraulic Engineering*, 131(3):175–183.

White, B. L. and Nepf, H. M. (2007). Shear instability and coherent structures in shallow flow adjacent to a porous layer. *Journal of Fluid Mechanics*, 593:1–32.

White, B. L. and Nepf, H. M. (2008). A vortex-based model of velocity and shear stress in a partially vegetated shallow channel. *Water Resources Research*, 44(1).

Xiaohui, S. and Li, C. W. (2002). Large eddy simulation of free surface turbulent flow in partly vegetated open channels. *International Journal for Numerical Methods in Fluids*, 39(10):919–938.

Zhu, Y. (2017). Flow patterns in partially vegetated channels : Combining physical experiments and numerical modelling. Master's thesis.

Zong, L. and Nepf, H. (2010). Flow and deposition in and around a finite patch of vegetation. *Geomorphology*, 116(3-4):363–372.

Chapter 6

Conclusions and recommendations

One finished task carried to a successful conclusion
is better than 100 half-finished tasks.

This is a concluding chapter, in which the research findings of the present study are summarised, following the story line of the research. Conclusions stemming from previous chapters are introduced in a synthetic way. Finally, a number of suggestions and recommendations are presented for future research.

This thesis concerns the issue of mangrove degradation along the Mekong delta estuaries in the context of hydrodynamics and human intervention. Different approaches and methodologies were applied. The main findings of the research can be summarised as follows:

6.1 Mangrove Squeeze phenomenon

THe degradation of mangrove forests and the erosion of river banks associated with the restricted width of the vegetation area induced by human interventions was studied in terms of the squeeze phenomenon. Along the Mekong delta estuaries, the degradation of mangrove forests is observed together with an increasing erosion rate of the river banks. The width of the estuarine mangroves is in the range of 10 m to 600 m. An erosion rate is recorded of up to $4\,\mathrm{m\,yr^{-1}}$. However, based on an empirical relationship between mangrove forest width and riverbank evolution, it is suggested that a riverbank still can remain dynamically stable in the presence of mangroves with a representative width of about 60 m to 80 m. Hence the squeeze phenomenon was approached in a new sense, it is hypothesized that there is a critical minimum width that a mangrove forest in the Mekong Delta needs for healthy, cyclic evolution, whether the alternations come from relative sea-level rise or from human activities. In other words, even when the availability of sediment is not an issue, the sustainable development of mangroves still can be threatened if there is not enough available space for them.

As far as physical processes are concerned, the dominant mangrove forests in estuarine regions are fringing estuarine mangroves (FEs), primarily controlled by tidal forces, river flows and the geometric features of the river. In a squeezed condition, tidal creeks can be neglected, the hydrodynamics of a narrow mangrove forest and that of a vegetated floodplain channel was recognized to be similar. In this sense, the influence of transverse exchange processes between the main river channel and the vegetated region is important for FEs. This exchange occurs primarily due to the mixing layer at the interface of the vegetation and adjacent open channel flow. It is a fundamental factor, controlling the import, export and deposition of sediment, nutrients, as well as organic matter in a mangrove forest.

A schematized model for the estuarine mangroves at Tieu Estuary in the Mekong delta, Vietnam was constructed with the Delft3D-flow vegetation model. The results of the model showed that the depth-averaged flow velocity from the main channel was reduced to a uniform value on an order of magnitude of $0.015\,\mathrm{m\,s^{-1}}$ within about 60 m to 80 m inside the mangrove forest. This implies that the mixing layer can have impacts on a maximum region up to 80 m inside the vegetation. However, the numerical results have been shown to overestimate the penetration of the mixing layer into the forest. This means that in reality, the actual penetration of the shear layer into the vegetation is smaller, estimated around 10 m. Still, the results from physical model suggest that the large horizontal coherent structures(LHCSs) can have a strong influence on a much larger area than the penetration of the mixing layer into the forest. This area was termed the maximum affected area, and was related to the region of intensive transverse fluctuations which can be connected the above critical minimum width in the hypothesis of mangrove squeeze. These conclusions address the key question 1 and 2.

6.2 Physical mechanisms

Once the hypothesis of the squeeze phenomenon was proposed, it is important to discover the major physics lying behind it. This is not a trivial step, especially in the sense that numerous physics can be involved. For instance, sediment dynamics, morphodynamics, eco-biology and hydrodynamics, *etc.*. Among these, hydrodynamics play a fundamental role, connecting all others processes. However, understanding the hydrodynamics of an estuarine mangrove is still limited. Hence, a physical modelling of a compound channel, mimicking an estuarine mangrove forest was set up.

Firstly, the role of vegetation was examined. It is suggested that vegetation is very effective in damping the flow inside the mangrove forest. Vegetation greatly increases the velocity gradient between the vegetation regions and the adjacent open regions, drawing more exchange toward the vegetation edge and pushing more flow into the floodplain region. For example, in case with dense vegetation, the velocity gradient increases about 3-5 times compared with the scenarios without vegetation. Consequently, the K-H instability also increase, and the LHCSs formed at the interface of the vegetation become more pronounced. As a result, the LHCSs emerge in the mixing layer, promoting more exchange towards the vegetation area. For instance, in dense scenarios, the transverse momentum exchange increases about 20 times in comparison with the non-vegetation scenarios. Secondly, the LHCSs and their influences on the shallow flow field in and around the vegetation area were investigated. It is suggested that as a LHCS moves, it generates flow events, namely sweeps, ejections, stagnant and reverse flows. These flow events occur periodically and dominate the flow field, especially the mixing layer. They were termed cycloid flow events. Under the effect the LHCSs, the shallow flow field in and around the region of vegetation shows cycloidal properties.

In terms of exchange processes, while the sweeps and ejections contribute a large part to the input and output of the nutrients and sediment, the stagnant and reverse flow play an important role in the deposition processes. Moving along the vegetation interface, the LHCSs cause momentum exchange. While the sweeps and ejections dominate the region of momentum exchange, which is related to the penetration of the mixing layer, the stagnant and reverse flows dominate the further region inside the vegetation, where large lateral fluctuations still may occur. It is suggested that the LHCSs can affect a larger area than the region into which the mixing layer can penetrate.

In summary, On the one hand, due to the LHCSs, the presence of vegetation can have strong influences on a large region, even outside the vegetation. On the other hand, due to the cycloid flow events, the LHCSs can have strong effects on a large area, event further than their penetration into the mangrove forests.

Squeezing the mangrove forest causes changes in the pattern of LHCSs, and thereby changing the exchange processes. Once the width of a mangrove forest is reduced, the LHCSs become smaller but more frequently and less regularly. In cases when the width of the mangrove forest is smaller than the region affected by the LHCSs, the mixing layer can penetrate into the whole forest, the region affected by the LHCSs is diminished. Furthermore, the flow penetrating into the vegetation can not achieve a stable uniform value. In this way, there is less time, place and proper flow condition for the deposition of the suspended sediment and nutrient. These conclusions address the key question 3

and 4.

6.3 Transverse momentum exchange - analytical model

ALthough this study has not yet considered sediment processes, understanding the transverse momentum exchange facilitates modelling the transport of sediments and nutrients in and around the region of vegetation. In order to get an insight into the transverse momentum exchange, the governing equations for the vegetated floodplain channel based on a simplified depth-integrated, time-averaged and spatially-averaged form of the 2D shallow water equations were derived and utilized. After that, the momentum equations were studied where the transverse momentum exchange (T_{xy}) is the most significant term left need to be modelled. The transverse momentum exchange (T_{xy}) can be expressed in term of physical meaning ($\overline{u'v'}$) and modelling (υ_t). In this study, these terms were studied separately.

A quadrant analysis was applied for the Reynolds' shear stresses. It shows the strong connection between the LHCSs, their associated flow events and the transverse momentum exchange. By separating the LHCSs from the quadrant analysis, the main contribution to the total momentum exchange of the LHCSs at the vegetation interface was confirmed. Different locations inside the mangrove forest experience cyclic flow events differently, and thereby the transverse momentum exchange are also different. Furthermore, the results suggest that the stagnant and reserve flows can be observed only in cases the fluctuation motions induced by LHCSs are larger than the mean flow motion.

State-of-the-art eddy viscosity models (υ_t) were reviewed and validated with the experimental results. It is suggested that they are not globally applicable as their validity is usually restricted to a narrowly ranging experiment data set. Additionally, the penetration of the LHCSs into the vegetation, which appears to relates to the appearance of the LHCSs was also analysed. It is not only depend on the vegetation drag but also on the outer layer width, the width of the vegetated floodplain and the water depth ratio. Based on the previous eddy viscosity models and on the presence of the LHCSs, a new hybrid eddy viscosity model was proposed and validated with different experiment data sets. It is suggested that the transverse momentum exchange can be well modelled by varying only a coefficient which is related to the spreading of the mixing layer. These conclusions address the key question 4.

6.4 Numerical simulations

FInally, the hybrid eddy viscosity model representing the LHCSs was used as a turbulence model in numerical simulations of compound channel flow. A 2DH model, mimicking the experiment was constructed. The results were compared with the experimental data regarding the mean streamwise velocity, transverse shear stresses and the patterns of the LHCSs. In this way, the applicability of the 2DH models with different eddy viscosity models in the simulation of the complex cycloid flow field in and around the vegetation region can be examined. It was quantitatively examined by means of the presence of the LHCSs and the associated cycloid flow events, and qualitatively

examined by means of the profile of the mean streamwise velocity and transverse shear stresses. The results suggest that when a constant eddy viscosity model or eddy viscosity model determined according to the Elder formulation were prescribed, the 2DH model tends to overestimate the presence of the LHCSs. Consequently, the mean streamwise velocity inside the mangrove forest appears to be underestimated and the transverse shear stresses induced by the LHCSs appears to be overestimated. Nevertheless, the numerical simulations of compound channel flow can be much improved by imposing into the model a hybrid eddy viscosity model as developed in Chapter 4, in which the presence of the LHCSs was included.

Last but not least, having in mind all the philosophies obtained, the real-scale 2DH model mimicking the mangrove forest in the Tieu estuary with schematised bathymetry was re-considered. The numerical results suggested that the presence of the LHCSs and the cycloid flow events can occur on the large scale of Tieu estuary when the water depth in the vegetation region is larger than 1.1 m. In order to improve the capability of the 2DH model in the prediction of the mean stream wise velocity and transverse shear stress, the hybrid eddy viscosity model was prescribed in the model. The numerical simulation suggests that the outer layer width of the mixing layer is about 60 m, and the penetration of the mixing layer into the vegetation is about 6 to 10 m.

It is noted that although the penetration of the LHCSs into the vegetation areas is only about 6 to 10 m, the area affected by the LHCSs can be much larger. Because the maximum area affected by the LHCSs appears to connected to the outer layer width of the mixing layer, it can be seen that the minimum width required for a sustainable development of the estuarine mangrove forest (estimated of about 60 to 70 m) appear to link to this length scale, in which the lateral fluctuations induced by the LHCSs is the dominant. These conclusions address the key question 5.

6.5 Recommendations

At the end of this study, still, it is recognized that certain knowledge gaps are remained. Among which, large scale validation and more complicated numerical simulation in terms of mass exchange are the two most challenges, but most important to clarify the squeeze phenomenon, it is suggested as follows:

- Large scale measurement: this study is based on a small scale laboratory experiment. Therefore, whether or not all the new physics learned can remain the same at a larger real scale is still questionable. This is particularly true for the LHCSs. A data set acquired at the field scale or a comparable large scale enables to understand and overcome this main challenge. Once understanding the hydrodynamics of vegetated compound channel at real scale can be achieved, field scale measurement also allows to approach and study the sediment processes.

- Transverse exchange of mass: A detailed numerical simulation which allows to include the vegetations, sediment but still can produce the LHCSs is essential for the practical applications. However, it is not a trivial topic. On the one hand, the Large eddy simulations (LES), or direct numerical simulations (DNS) can be able

to resolve correctly the LHCSs. However, including sediment processes and consider such that model on a large real scale is still not practical. On the other hands, although the vegetation and sediment can be imposed into the 2DH model, the LHCSs at the vegetation interface resolved appear to be not reliable. Although the numerical results can be improved in terms of mean streamwise velocity and transverse exchange of momentum with the hybrid eddy viscosity model representing for the large turbulent structures, a proper model for the exchange of mass induced by the LHCSs is still unknown. While transverse momentum exchange induced by the LHCSs is necessary to understand the import and export of the sediment and nutrients at the vegetation interface, transverse exchange of mass may be the dominant process inside the forest, determining the deposition processes.

Appendix A

Experimental Results

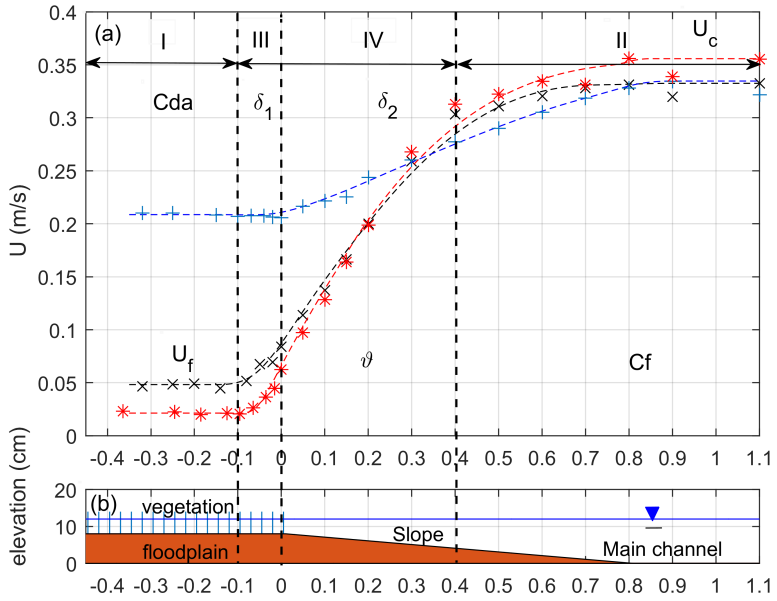

Figure A.1: Representative mean streamwise velocity profiles in cases with no vegetation (blue-plusses), sparse vegetation (blacked-crosses) and dense vegetation (red-stars). Corresponding profile of a vegetated compound channel with a gentle slope (b). 50 cm floodplain width, discharge = 45 Ls^{-1}, water depth =12 cm. The vegetated floodplain starts from y=0 in the negative direction.

Figure A.1 shows that the larger the vegetation drag (the larger the cylinder density) the smaller the flow velocity within the cylinder array and the higher the flow velocity in the main channel. However, the vegetated shear-layer dynamic of the sparse scenario appears to resemble that of the dense scenario. The penetration of the mixing layer into the vegetation is about 10 cm (in both sparse and dense cases).

Table A.1: Experiment configurations and major results.

Cases	**An1**	**An2**	**An3**	**An4**	**Bn1**	**Bn2**	**Bn3**	**Bn4**	**As1**	**As2**	**As3**	**As4**	**Bs1**	**Bs2**	**Bs3**	**Bs4**
$N(number/m^2)$	0	0	0	0	0	0	0	0	139	139	139	139	139	139	139	139
Φ	0	0	0	0	0	0	0	0	0	0	0	0	0.01	0.01	0.01	0.01
$C_D \cdot a$	0	0	0	0	0	0	0	0	0.029	0.025	0.028	0.027	0.019	0.019	0.017	0.019
$Width$(m)	50	50	50	50	25	25	25	25	50	50	50	50	25	25	25	25
$Q(\mathrm{Ls}^{-1})$	45	60	80	80	45	60	80	80	45	60	80	80	45	60	80	80
D_f(cm)	3.9	4.84	6.26	4.4	4.13	5.12	6.47	4.11	4.76	5.17	6.47	4.59	4.82	5.59	6.28	4.66
D_c(cm)	11.9	12.84	14.26	12.4	12.13	13.12	14.47	12.11	12.76	13.17	14.47	12.59	12.82	13.59	14.28	12.66
$Dr = D_f/D_c$	0.33	0.38	0.44	0.35	0.34	0.39	0.45	0.34	0.37	0.39	0.45	0.36	0.38	0.41	0.44	0.37
Fr	0.33	0.41	0.44	0.58	0.32	0.38	0.41	0.59	0.29	0.36	0.4	0.5	0.27	0.32	0.39	0.47
$R_{ec}(\times 10^3)$	39.83	49.55	61.57	62.05	39.93	51.23	65.3	64.87	41.03	53.53	69.09	69.49	38.87	49.79	66	65.95
$R_{ef}(\times 10^3)$	8.02	13.64	21.81	16.7	8.32	13.62	21.38	15.29	2.27	3.57	4.86	4.63	2.3	3.35	4.6	4.28
$U_f(\mathrm{cms}^{-1})$	20.9	28.2	34.9	38	20.2	26.6	33.2	37.3	4.8	6.9	7.9	9.8	3.99	5.29	6.27	8.39
$U_c(\mathrm{cms}^{-1})$	33.5	39.8	44.4	51.5	34.9	41.3	47.4	56.3	33.3	42.06	49.56	56.91	33.24	40.34	50.33	56.5
$U_o(\mathrm{cms}^{-1})$	20.9	28.2	34.9	38	22.5	29.6	35.8	41.3	8.7	11.3	13.02	15. 5	9.41	12.32	15.53	18.04
$U_s(\mathrm{cms}^{-1})$	0	0	0	0	2.4	3	2.6	4.1	3.9	4.4	5.12	5.65	5.42	7.03	9.26	9.65
u_*	0.24	0.45	0.45	0.7	0.3	0.45	0.83	0.66	3.9	5.08	8.23	10.41	5.5	7.88	12.96	16.15
y_i(cm)	72	89	89.8	83.9	50	50	50	50	50	50	50	50	50	50	50	50
δ_1	0	0	0	0	6.6	6.6	4	5.4	9.8	8.8	8.9	8.1	9.2	9.2	9.3	8.9
δ_2(cm)	47.5	28.7	22.5	31	66.3	58.6	51.2	61.6	57.5	56.7	54.2	56.8	60.9	57.2	52.4	54
δ(cm)	69.5	67.7	62.3	64.9	72.9	65.2	55.2	67	67.3	65.5	63.1	64.9	70.1	66.4	61.7	62.9
β	0.07	0.065	0.07	0.07	0.065	0.065	0.07	0.07	0.08	0.08	0.08	0.08	0.065	0.065	0.065	0.065
Cases	**Cs1**	**Cs2**	**Cs3**	**Cs4**	**Ad1**	**Ad2**	**Ad3**	**Ad4**	**Bd1**	**Bd2**	**Bd3**	**Bd4**	**Cd1**	**Cd2**	**Cd3**	**Cd4**
$N(number/m^2)$	139	139	139	139	556	556	556	556	556	556	556	556	556	556	556	556
Φ	0.01	0.01	0.01	0.01	0.04	0.04	0.04	0.04	0.04	0.04	0.04	0.04	0.04	0.04	0.04	0.04
$C_D \cdot a$	0.019	0.013	0.012	0.012	0.094	0.153	0.132	0.106	0.124	0.115	0.127	0.089	0.117	0.084	0.054	0.059
$Width$(m)	10	10	10	10	50	50	50	50	25	25	25	25	10	10	10	10
$Q(\mathrm{Ls}^{-1})$	45	60	80	80	45	60	80	80	45	60	80	80	45	60	80	80
D_f(cm)	4.4	5.11	6.49	4.44	4.22	5.21	6.42	4.64	4.33	5.43	6.74	4.53	4.47	5.75	6.49	4.47
D_c(cm)	12.4	13.11	14.49	12.44	12.22	13.21	14.42	12.64	12.33	13.43	14.74	12.53	12.47	13.75	14.49	12.47
$Dr = D_f/D_c$	0.35	0.39	0.45	0.36	0.35	0.39	0.44	0.37	0.35	0.4	0.46	0.36	0.36	0.42	0.45	0.36
Fr	0.26	0.32	0.35	0.45	0.31	0.36	0.42	0.52	0.29	0.33	0.36	0.47	0.31	0.34	0.41	0.51
$R_{ec}(\times 10^3)$	34.92	47.36	61.23	62.3	41.4	53.7	71.48	72.83	39.42	51.3	64.41	64.98	42.37	53.75	70.1	71.03

$R_{ef}(\times 10^3)$	2.83	4.38	6.69	5.59	0.9	1.03	1.39	1.7	0.95	1.42	1.79	2.01	1.83	3.02	4.62	3.44
$U_f(\mathrm{cms}^{-1})$	3.5	2.6	7.2	8.9	2.1	2.06	2.17	3.65	2.19	2.61	2.65	4.45	0.99	1.02	1.55	2.5
$U_c(\mathrm{cms}^{-1})$	34.17	42.51	49.56	58.42	35.6	41.9	51.5	58.7	34.9	41.23	48.3	58.53	35.01	40.15	50.04	59.25
$U_o(\mathrm{cms}^{-1})$	11.7	13.2	16.6	19.7	6.6	7.8	8.6	11.11	8.9	11.65	14.3	16.36	8.93	12	15.8	17.1
$U_s(\mathrm{cms}^{-1})$	8.2	10.6	9.4	10.8	4.5	5.75	6.4	7.5	6.7	9.04	11.67	11.9	7.94	10.98	14.2	14.6
u_*	3.1	5.8	9.4	11	3.3	5.8	8.5	8.5	5.1	9.3	13.2	16.27	4.8	8.2	14.8	15.8
$y_i(\mathrm{cm})$	50	50	50	50	50	50	50	50	50	50	50	50	50	50	50	50
δ_1	10	10	10	10	7.6	8.4	8.7	7	8.3	8.1	8.4	6.8	10	10	10	10
$\delta_2(\mathrm{cm})$	51.4	41.7	38	40.6	61.3	64	62.8	59.7	60.1	56.5	54.4	59.3	48.5	45.9	43.2	47.7
$\delta(\mathrm{cm})$	61.4	51.7	48	50.6	68.9	72.4	71.5	66.7	68.4	64.6	62.8	66.1	58.5	55.9	53.2	57.7
β	0.045	0.045	0.048	0.045	0.07	0.065	0.06	0.07	0.058	0.06	0.055	0.055	0.048	0.05	0.045	0.055

Appendix B

Hybrid eddy viscosity model validation

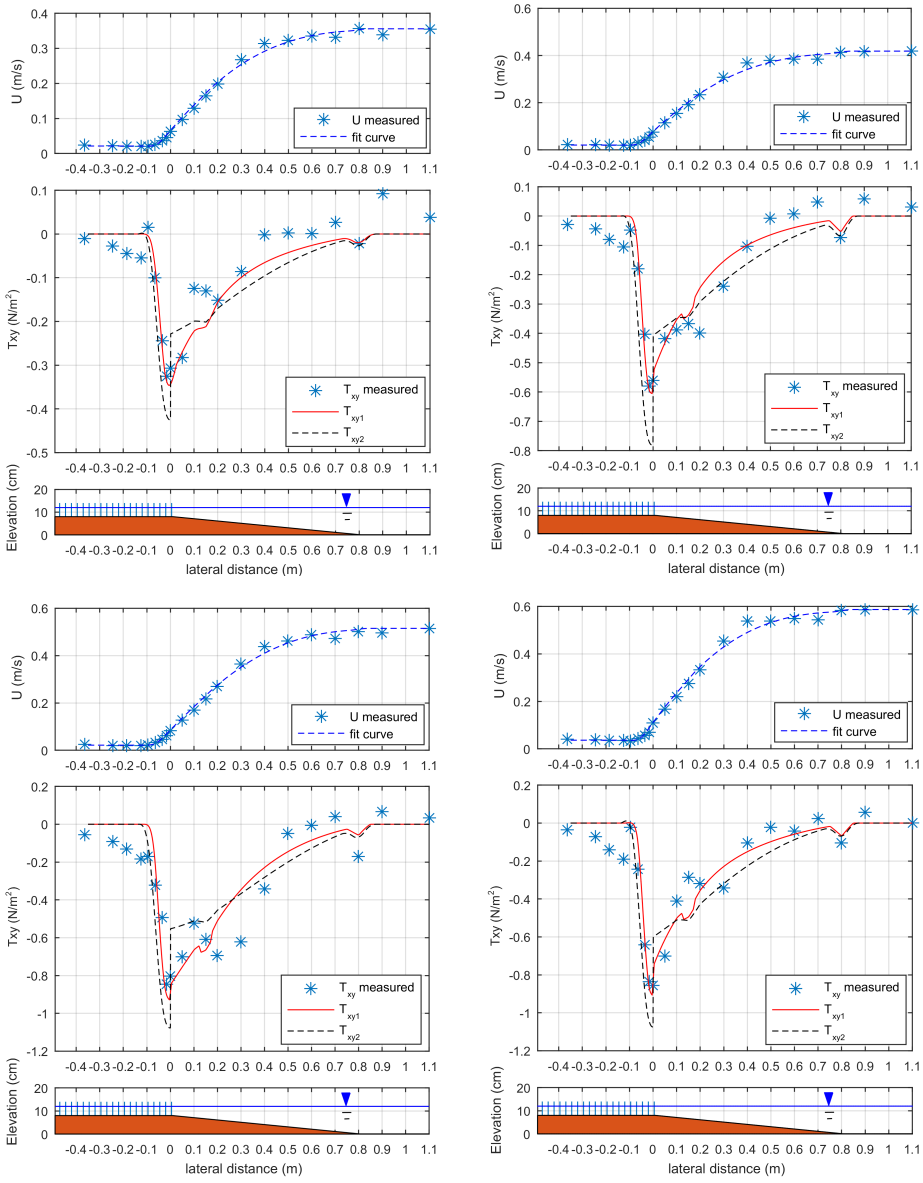

Figure B.1: Profile of mean streamwise velocity, and the comparison of modelled transverse shear stress according to the eddy viscosity model of this study Txy1, in cases Ad1, Ad2, Ad3, Ad4 (left upper panel, right upper panel, left lower panel, right lower panel, respectively), and Txy2 [White and Nepf, 2008].

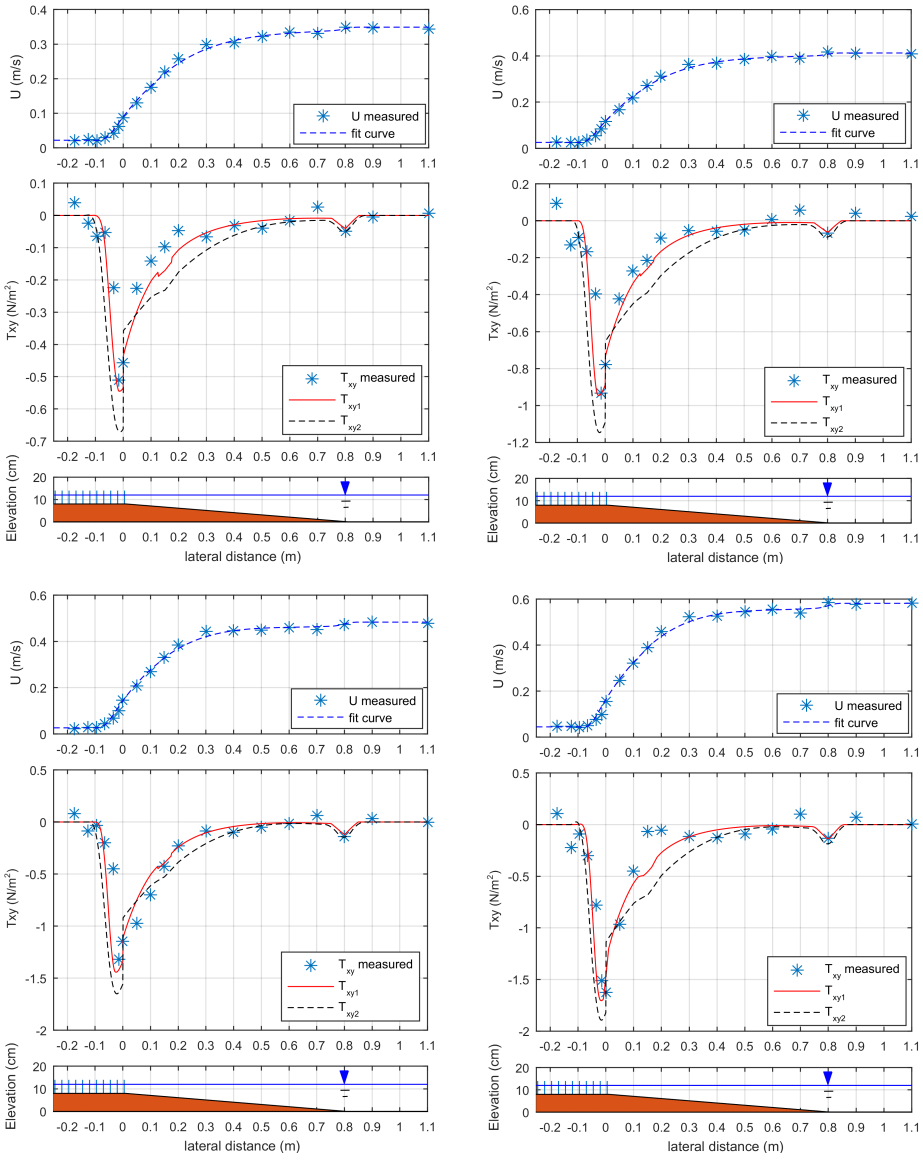

Figure B.2: Profile of mean streamwise velocity, and the comparison of modelled transverse shear stress according to the eddy viscosity model of this study Txy1, in cases Bd1, Bd2, Bd3, Bd4 (left upper panel, right upper panel, left lower panel, right lower panel, respectively), and Txy2 [White and Nepf, 2008].

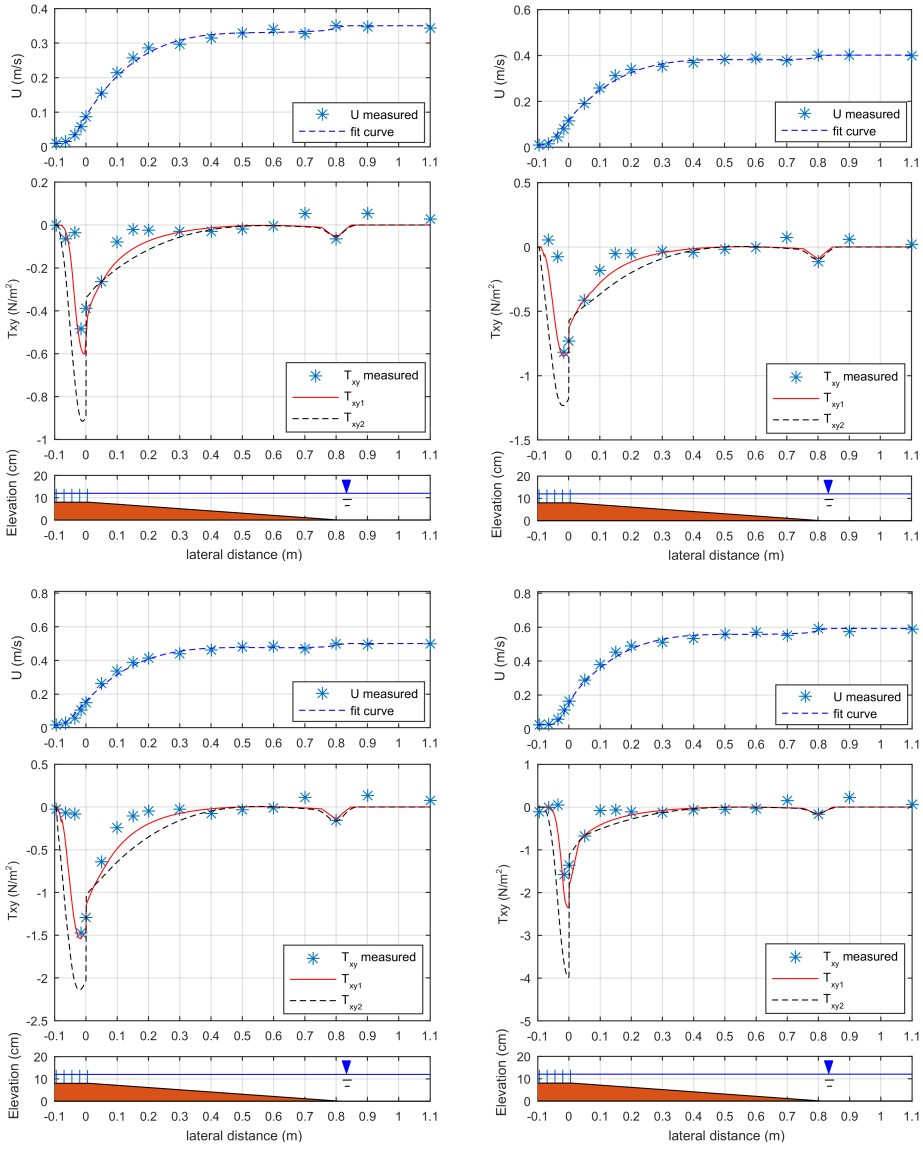

Figure B.3: Profile of mean streamwise velocity, and the comparison of modelled transverse shear stress according to the eddy viscosity model of this study Txy1, in cases Cd1, Cd2, Cd3, Cd4 (left upper panel, right upper panel, left lower panel, right lower panel, respectively), and Txy2 [White and Nepf, 2008].

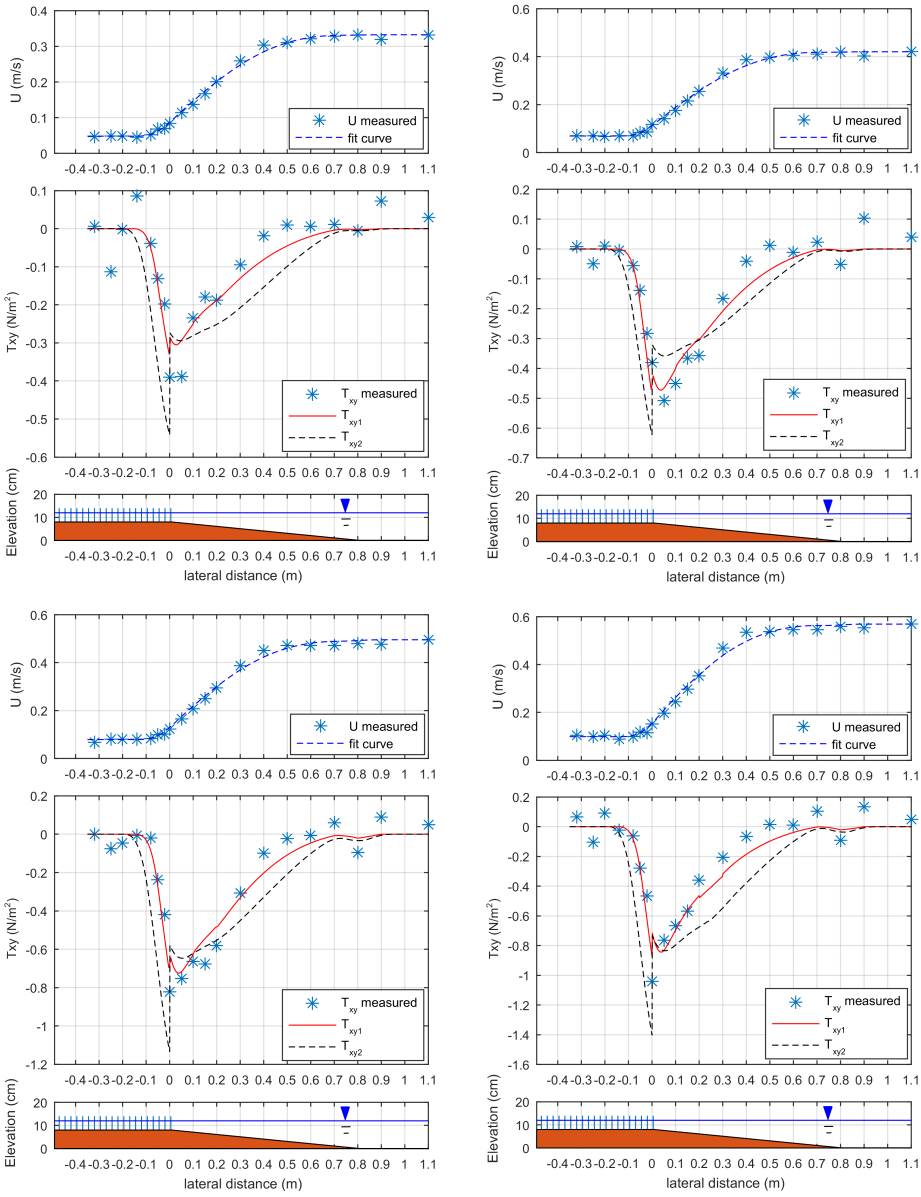

Figure B.4: Profile of mean streamwise velocity, and the comparison of modelled transverse shear stress according to the eddy viscosity model of this study Txy1, in cases As1, As2, As3, As4 (left upper panel, right upper panel, left lower panel, right lower panel, respectively), and Txy2 [White and Nepf, 2008].

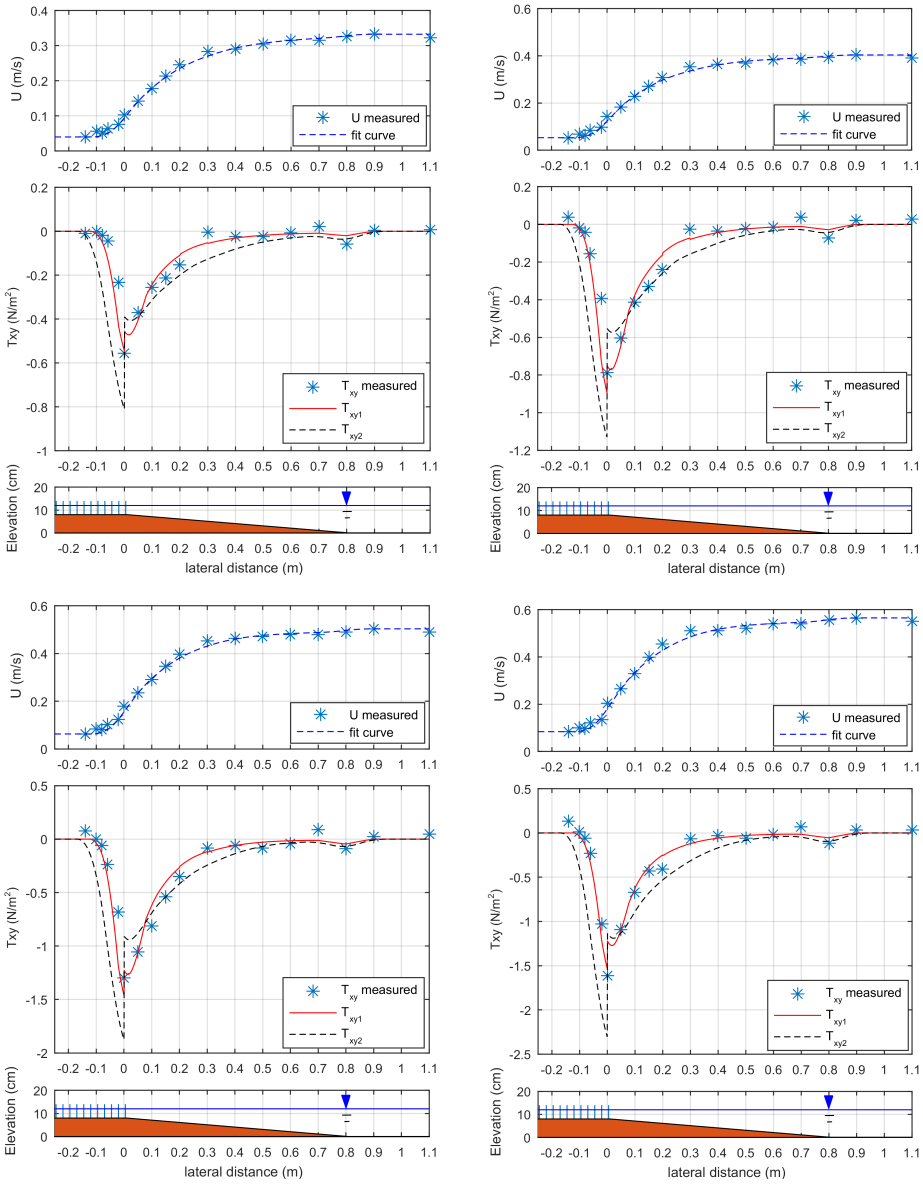

Figure B.5: Profile of mean streamwise velocity, and the comparison of modelled transverse shear stress according to the eddy viscosity model of this study Txy1, in cases Bs1, Bs2, Bs3, Bs4 (left upper panel, right upper panel, left lower panel, right lower panel, respectively), and Txy2 [White and Nepf, 2008].

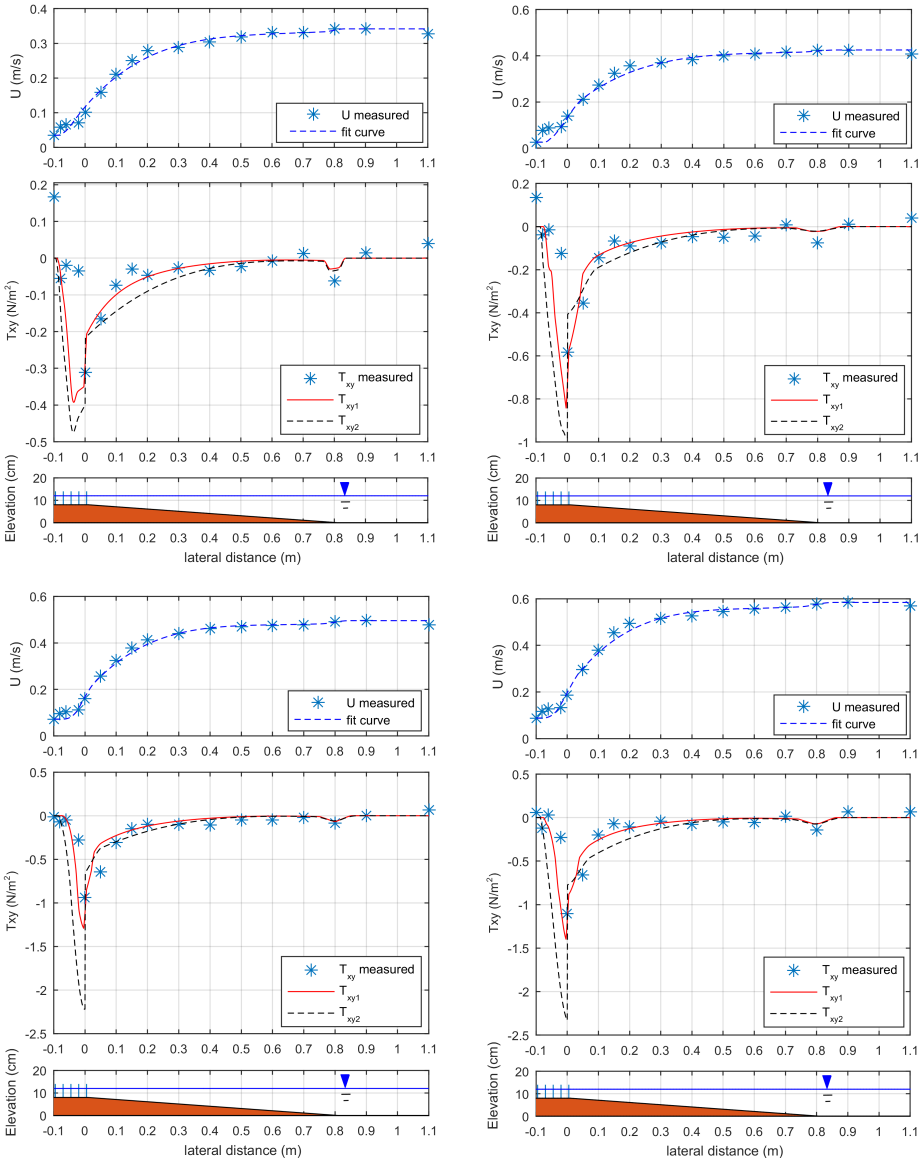

Figure B.6: Profile of mean streamwise velocity, and the comparison of modelled transverse shear stress according to the eddy viscosity model of this study Txy1, in cases Cs1, Cs2, Cs3, Cs4 (left upper panel, right upper panel, left lower panel, right lower panel, respectively), and Txy2 [White and Nepf, 2008].

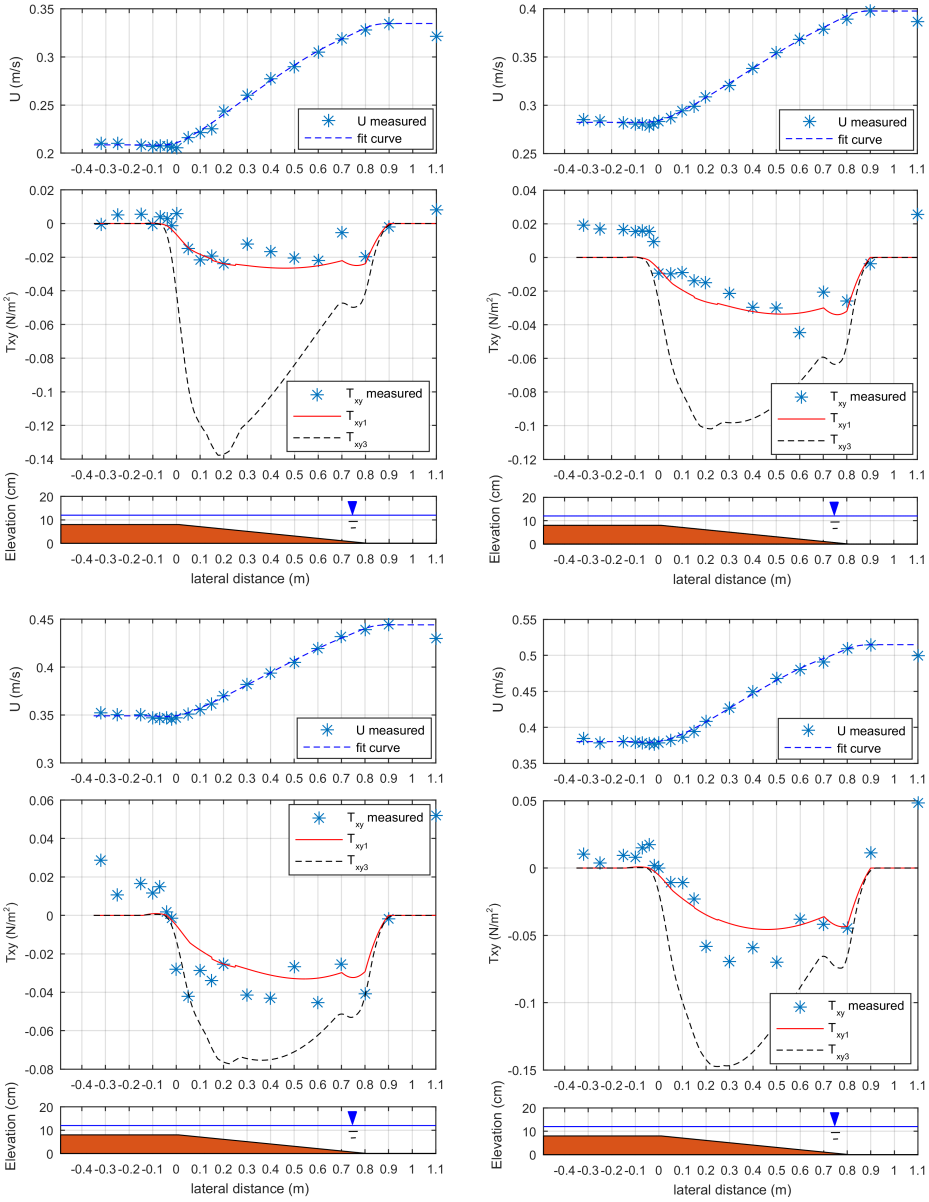

Figure B.7: Profile of mean streamwise velocity, and the comparison of modelled transverse shear stress according to the eddy viscosity model of this study Txy1, in cases An1, An2, An3, An4 (left upper panel, right upper panel, left lower panel, right lower panel, respectively), and Txy3 [van Prooijen et al, 2005].

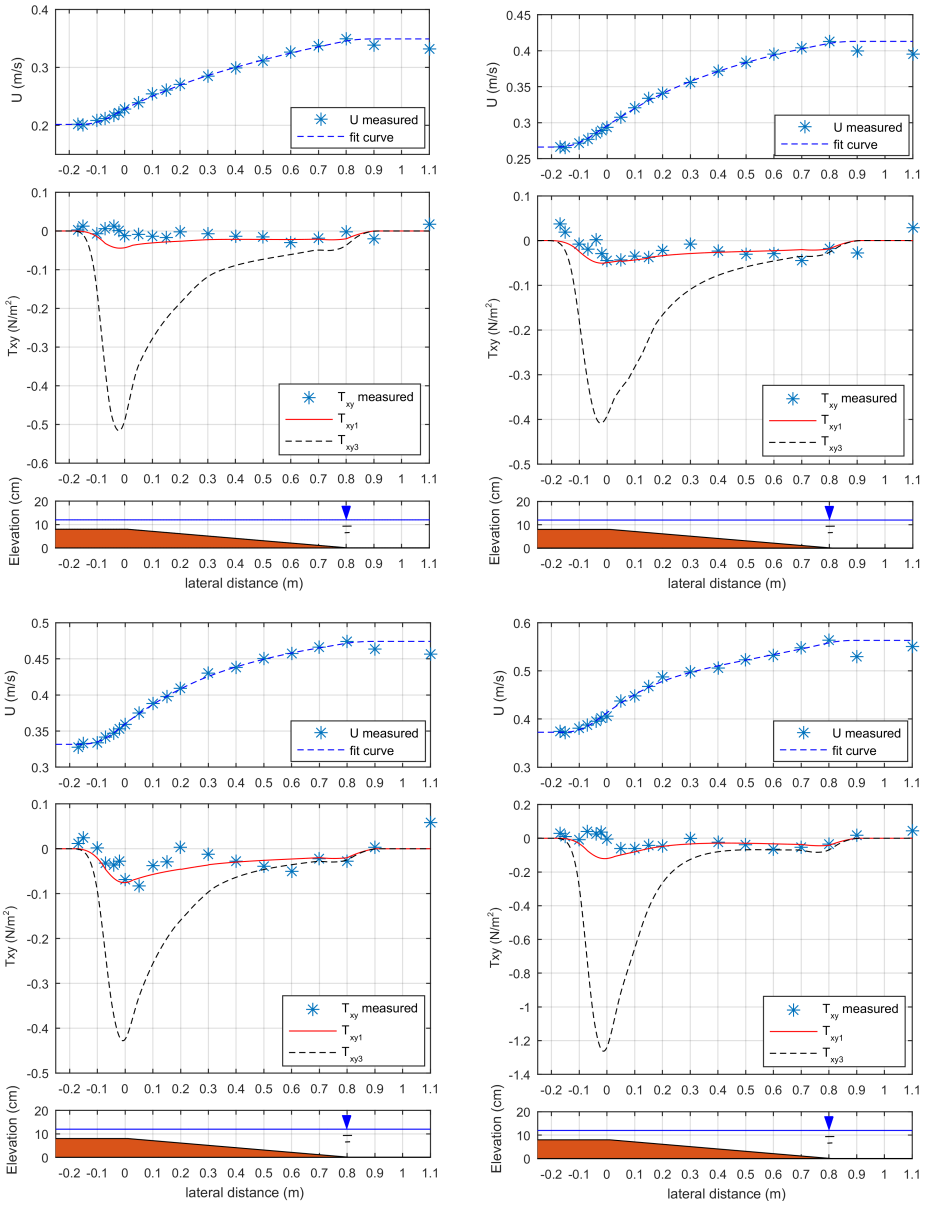

Figure B.8: Profile of mean streamwise velocity, and the comparison of modelled transverse shear stress according to the eddy viscosity model of this study Txy1, in cases Bn1, Bn2, Bn3, Bn4 (left upper panel, right upper panel, left lower panel, right lower panel, respectively), and Txy3 [van Prooijen et al, 2005].

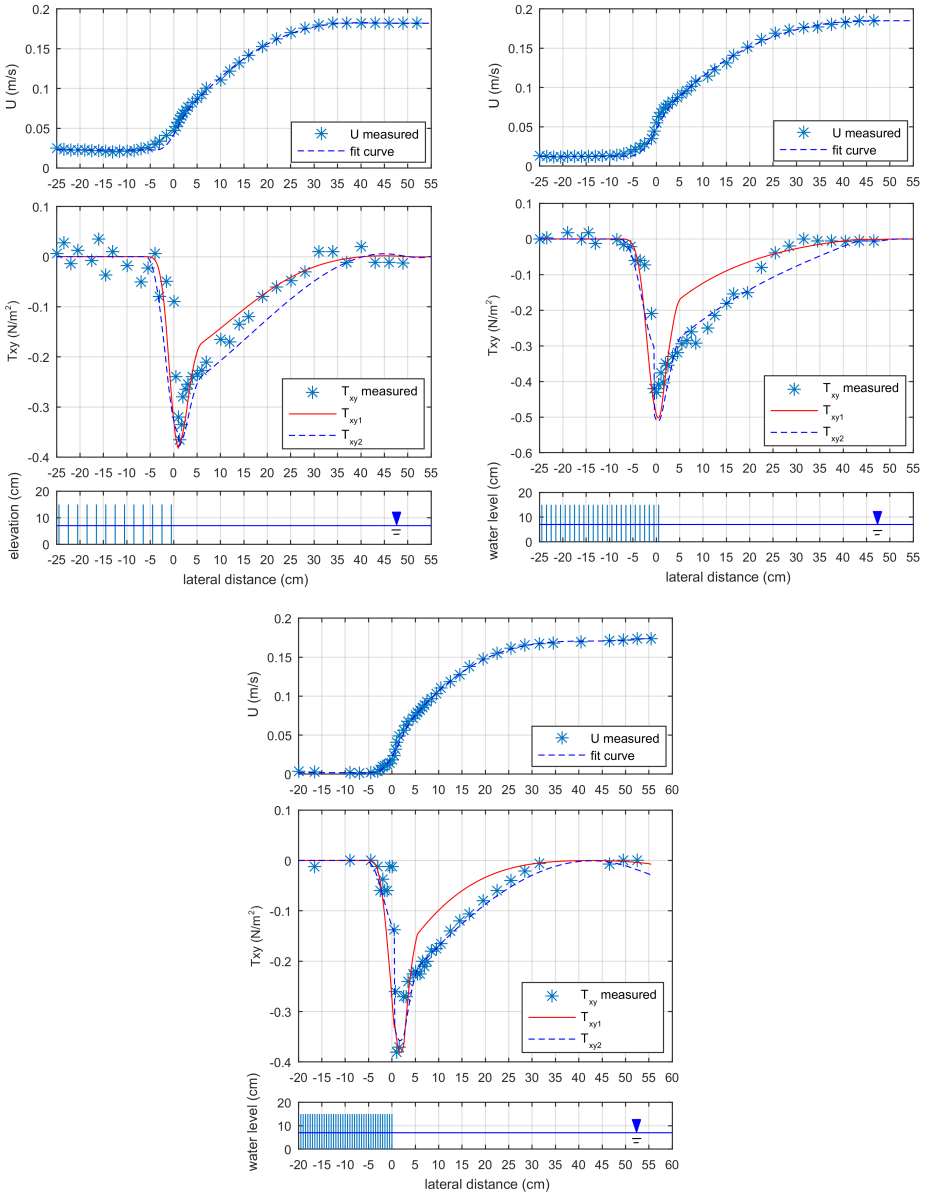

Figure B.9: Profile of mean streamwise velocity, and the comparison of modelled transverse shear stress according to the eddy viscosity model of this study Txy1, in cases I, IV, VII of White and Nepf [2008] (left upper panel, right upper panel, lower panel, respectively), and Txy2 [White and Nepf, 2008].

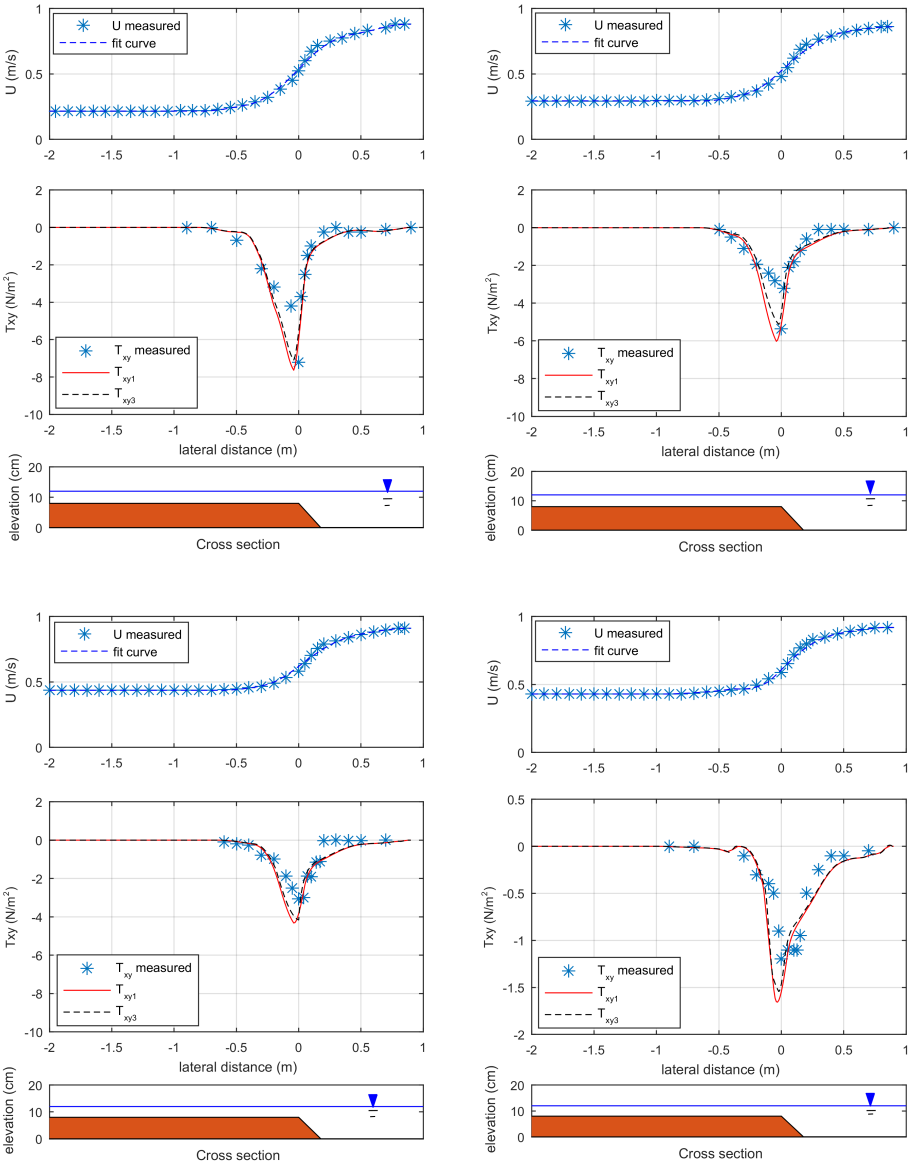

Figure B.10: Profile of mean streamwise velocity, and the comparison of modelled transverse shear stress according to the eddy viscosity model of this study Txy1, in cases Dr =0.11, 0.15, 0.20 and 0.25 (left upper panel, right upper panel, left lower panel, right lower panel, respectively) of Lambert and Sellin [1996] and Ervine et al. [2000], and Txy3 [van Prooijen et al., 2005].

Acknowledgements

All of the work in this dissertation was achieved in cooperation with others, especially with prof Marcel and prof Wim. So, at the end of the story, I am grateful to the people who have guided, accompanied and supported me during the past 5 years and who have significantly contributed to this thesis.

I am extremely grateful to professor Wim Uijttewaal (TU Delft), who has been involved from the beginning of my research, not only as my promoter, but also as a "super" daily supervision. Your unstoppable questions and enthusiasm, looking for the "true" facts and mechanisms have stimulated me a lot in putting this work together. Despite your busy schedule, I could always find your door open and we had many interesting discussions on the topic of experiments, flow and turbulence. We wrote three journal papers together in one year, leading to an increased quality and decrease in the time it took me to write new manuscripts. I learned a lot from you, from your detailed reviews and your feedback on my work. I am eternally grateful for everything you have taught me!

I want to thank to professor Marcel Stive (TU Delft), who, as my "super" promoter, was the initiator of this Ph.D. project. Your profound knowledge and broad vision have guided me, while your work and living style inspired me throughout this work. You gave me not only the challenges and possibility, but also freedom, to find my own way in the research field of hydraulic engineering. This helped me a lot to become a proactive and independent researcher. How can I ever thank you enough!

I want thank Mr. Sander de Vree and his colleagues at the water lab: Mr. Frank Kalkman, Mr. Arno Thorn, and Mr. Jaap van Duin, who have all enthusiastically supported my experimental work. The experiment in the water lab forms the basis of this research, generating new data, results, imaginings and adding more knowledge. I really appreciate the help of Mr. Sander and your colleagues to set up my measurement. I also want to express my gratitude to Dr. Quinghua, for his help with the vegetation model in Delft 3D.

I really appreciate all the hard work you have done to help me! The Vietnam International Education Cooperation Department and The Delft University of Technology are gratefully acknowledged for their financial support.

I also want to mention my good friends in Delft. I am grateful for having you as friends! Finally, I give my heartfelt appreciation to my family, my parents, my wife, my son and my daughter. When trouble comes, it's your family that supports you !
Delft, 16th Octorber 2018.

Curriculum Vitæ

Hong Son TRUONG

07-04-1985 Born in Ha Noi, Viet Nam.

Education

2004–2009 Bachelor of Hydraulic structure in Civil Engineering.
B.Sc. cum laude.
Thuy Loi University, Vietnam

2010–2012 Master in Coastal and Marine Engineering and Management.
M.Sc. Eramus mundus.
University of Science and Technology (NTNU),
University of Southampton (Soton),
Delft University of Technology (Tu Delft).

2013-2018 PhD. in environmental fuid mechanics
Thesis: Hydrodynamics of vegetated compound channels; Model representations of estuarine mangrove squeeze in the Mekong Delta.
Promotor: Prof. dr. M. J.F Stive
Prof. dr. W. S.J Uijttewaal

Awards

2008 Third prize in National Mechanics Olympic in soil mechanics.
2008 Third prize in "Innovation Technology in Vietnam" (VIFOTEC).
2009 ADB world bank research fellowships.
2010 Huygens scholarship, The Netherlands.
2010 Erasmus Mundus Scholarship, EU.
2013 VIED Scholarship.

List of Publications

1. **H.S Truong**., W.S.J. Uijttewaal., J.F Marcel., *"Exchange processes induced by large horizontal coherent structures in vegetated compound channels."*, Water resources research, Under review, 2018.
2. **H.S Truong**., W.S.J. Uijttewaal., *"Transverse momentum exchange induced by Large Coherent Structures in Vegetated Compound Channel."*, Water resources research, Under review, 2018.
3. **H.S Truong**., W.S.J. Uijttewaal., *"Numerical simulation of the hydrodynamics in estuarine mangrove forest"*, Journal of hydraulic engineering, in preparation to submit, 2018.
4. **H.S Truong**., Y., Qinghua., J.F Marcel., *"Estuarine Mangrove squeeze in the Mekong Delta VietNam"*, Journal of Coastal Research, 33(4),pp 747-763, 2017.
5. P.K Linh., J.F Marcel., **H.S Truong**., M. Zijlema., *"The effects of wave non-linearity on wave attenuation by vegetation"*, Coastal Engineering, Under review, 2018.
6. P.K Linh., J.F Marcel., M.F.S Tissier., **H.S Truong**., S.G.J Aarninkhof *"A laboratory study of infragravity wave attenuation by vegetation"*, Coastal Engineering, in preparation to submit, 2018.
7. **H.S Truong**., W.S.J. Uijttewaal., *"Cycloid flow field in vegetated floodplain channel."*, International conference, River flow, 2018.
8. **H.S Truong**., P.K Linh., J.F Marcel., W.S.J. Uijttewaal., *"A Laboratory study of the shallow flow field in a vegetated compound channel."*, International Conference on Estuaries and Coasts (ICEC), 2018.
9. P.K Linh., **H.S Truong**., J.F Marcel., *"A Laboratory study of wave attenuation through mangrove"*, International Conference, Coastal Lab, 2018.
10. **H.S Truong**., W.S.J. Uijttewaal., J.F Marcel., *"Shallow flow field and large coherent structures in a vegetated floodplain channel"*, International Symposium on shallow flows (ISSF 4th), Eindhoven, The Netherlands 2017.
11. **H.S Truong**., J.K. Vrijling., J.F Marcel., *"The Innovative structure solution for preventing salt intrusion and retaining freshwater in Mekong Delta Vietnam"*, 35th IAHR World congress, Chengdu, China 2013.
12. T.D Du., **H.S Truong**., P.K Linh., D.V Khoa., *"The application of hydraulic automatic gate in caisson sluice to prevent salt intrusion in Mekong delta Vietnam"*, Proceedings of the 4th International Conference on Estuaries and Coasts, Vietnam, volume 2, pp.260-264, 2013.